Spray Deposition of 2D MoS_2 and MXene ($Ti_3C_2T_x$) Nanosheets as Anodes for Li and Na Ion Batteries

Zur Erlangung des akademischen Grades eines
DOKTORS DER NATURWISSENSCHAFTEN
(Dr. rer. nat.)

von der KIT-Fakultät für Chemie und Biowissenschaften
des Karlsruher Instituts für Technologie (KIT)

genehmigte

DISSERTATION

von

M. Sc. Tianzhu Liu

aus Anhui, China

1. Referent: Prof. Dr. Helmut Ehrenberg
2. Korreferent: T.T.-Prof. Dr. Helge S. Stein

Tag der mündlichen Prüfung: 18.07.2022

Selbstständigkeitserklärung

Hiermit versichere ich, die vorliegende Arbeit selbstständig verfasst und keine anderen als die angegebenen Quellen und Hilfsmittel verwendet sowie Zitate kenntlich gemacht zu haben. Die Dissertation wurde bisher an keiner anderen Hochschule oder Universität eingereicht.

Karlsruhe， den 31. 05. 2022

Tianzhu Liu

Acknowledgments

First of all, I would like to acknowledge my supervisor Prof. Dr. Helmut Ehrenberg, who allowed me to do research work at the Institute of Applied Materials-Energy Storage Systems (IAM-ESS), Karlsruhe Institute of Technology (KIT). Next, I would like to express my sincere gratitude to my supervisor Dr. Mendoza Beatriz Sanchez for her guidance, scientific support, supervision and encouragement throughout my PhD work. I would like to thank co-supervision from Dr. Michael Knapp who helped with the XRD course, XRD scientific support and thesis corrections. In addition, I would like to express my deep appreciation to our collaborators Dr. Christopher Shuck and Prof. Yury Gogotsi (Drexel University) for providing us with MAX materials and fruitful discussions. And I would like to thank Prof. Dr. Helge Stein (HIU) as the second Referent for his valuable comments and suggestions.

I would like to express my great gratitude to all the people at IAM-ESS/ Institute of Nanotechnology (INT) for their scientific support and fruitful discussions: Dr. Anna-Lena Hansen (XRD), Dr. Oleksander Dolotko (XRD), Mrs. Liuda Mereacre (Raman), Mr. Udo Geckle (SEM/EDS), Dr. Kai Wang and Dr. Georgian Melinte (TEM). Equally, I would like to thank administrative and technical support from Mr. Heinz-Robert Goebel (equipment support), Mrs. Almut Kriese (administrative support) and Luis Sanchez (IT support). Additionally, the kind help from Chinese colleagues at IAM-ESE and HIU, Dr. Yueming Wang, Dr. Yanchen Wu, Dr. Guiying Tian, Dr. Zijian Zhao, Dr. Weibo Hua, Dr. Qiang Fu, Dr. Jiangong Zhu, Dr. Lihua Zhu, Dr. Xianlin Luo, Dr. Yuan Ma, Bijian Deng, Yinghan, Zhao, Yifan Wang, Hang Li, Hao Liu, Jiali Peng, etc., are highly appreciated.

It is a great pleasure to thank the financial support of the China Scholarship Council (CSC, No.: 20180833089).

Finally, I would like to express deep gratitude to my parents, my brother, and my sister for their endless love, confidence, encouragement, and support during my Ph.D. life.

Table of Contents

Abstract

With the ever-increasing demand for renewable and clean energy, lithium-ion batteries (LIBs) are one of the most important technologies of energy storage systems that have been extensively investigated owing to their advantages of high energy density and relatively long life span. Thanks to these, LIBs have already made great commercial success in portable electronics, electric vehicles (EVs), and hybrid electric vehicles (HEVs). However, the current graphite-based anodes have a low capacity (372 mAh g^{-1}) and unsatisfied rate capability, which leads to the current LIBs systems that struggle to meet the rapidly increasing energy consumption. As a result, the exploration and design of novel anode materials are extensively urgent. Two-dimensional (2D) molybdenum disulfide (MoS_2), a typical material of layered transition metal dichalcogenides (TMDs), featuring with unique properties such as high specific area and short length of ion transfer due to the reduced dimension, are considered as a promising anode material for LIBs because of the high theoretical capacity (~ 670 mAh g^{-1}) and large availability. Nonetheless, the commercial application of MoS_2-based anodes has been restricted so far by the shortcomings of low electronic conductivity, and fast capacity degradation resulting from the inevitable volume expansion of the electrodes during the repetitive charge/discharge process. To this end, compositing MoS_2-based electrodes with highly conductive and robust materials was proposed to solve the abovementioned issues.

Transition metal carbides and nitrides (termed as MXenes), a new family of 2D materials, were produced from their ternary carbide or nitride precursors (MAX phase) by selective etching of the A (group 4, 5 and 6 element) layer in hydrofluoric (HF) or HF-containing etchants. The general formula of MXenes is $M_{n+1}X_nT_x$ (n= 1, 2, and 3), where M represents an early transition metal (e.g. Ti, V, and Mo), X is carbon and/or nitrogen and T_x stands for the surface termination groups (such as –OH, -O, and -F). Extensive experimental and theoretical studies have shown that MXenes are promising candidates for lithium storage due to their attractive features such as excellent mechanical flexibility and low ion diffusion barriers as well as superior conductivity. However, like the limitations of other conventional 2D materials, MXenes have demonstrated only moderate capacity (e.g. $Ti_3C_2T_x$, 320 mAh g^{-1}) due to the pseudocapacitive mechanism.

In this context, 2D heterostructures were created by stacking different 2D materials to construct electrodes that would combine the advantages of the individual building blocks while eliminating the associated drawbacks. Up to

date, many techniques have been performed such as vacuum deposition, dipping, or spinning to engineer the 2D heterostructures, which are highly efficient for electronic applications, but not practical for creating battery electrodes due to the scalability concerns. Therefore, this thesis mainly focuses on the manufacture of 2D MoS_2, $Ti_3C_2T_x$ (MXene) electrodes, and their 2D heterostructures via a facile and scalable layer-by-layer (LBL) spray deposition technique, which is then used as anode materials for LIBs. More importantly, their lithium storage performance is intensively studied, including the corresponding reaction mechanism and the effect of various heterostructures and compositions, utilizing several *ex-situ* techniques such as Raman, SEM, XRD, and XPS.

Firstly, few-layers 2D MoS_2 nanosheets were synthesized through a facile liquid-phase exfoliation (LPE) synthesis method. Thereafter, conductive additives-free thin-film 2D MoS_2 electrodes were manufactured by using spray deposition. Compared to bulk MoS_2, the 2D MoS_2 electrode exhibits improved Li storage capacity and rate capacity due to the exfoliated nanosheets that have increased the interlayer distance and specific surface area. The reversible conversion reaction mechanism of the 2D MoS_2 electrode has been unravelled by *ex-situ* Raman, studies revealing that, in 2D MoS_2 electrodes, conversion processes are indeed reversible, where nanostructure played a key role. Surprisingly, the 2D MoS_2 electrode shows continuous capacity increase and stabilization after initial capacity fading (ca. after 100 cycles) at high various rates (0.75-3.0 C), and this so-called reactivated electrode can still deliver an exceptional rate capability in the subsequent prolonged cycles. *Ex-situ* SEM was employed to track the structural and morphological change of the cycled electrode, and the electrode reaction kinetics was evaluated by electrochemical impedance spectroscopy (EIS). These results reveal that the 2D MoS_2 electrodes can be reconstructed and/or reactivated, due to the volume expansion when cycling at high rates, to generate a robust porous electrode structure with an abundance of tiny needle-like nanosheets. Consequently, the nano-scaled diffusion length of the activated electrode facilitates mass and charge transports; meanwhile, a self-optimized static SEI layer during long-term cycling also endows the electrodes to deliver exceptional stable rate capability and extended lifespan.

The 2D MoS_2 electrode also exhibited an unexpected lithiation activation at high rates due to the volume expansion. To address this, several different types of the 2D MoS_2/$Ti_3C_2T_x$ heterostructures with and without carbon nanotubes (CNTs) were engineered by a large-scale alternative LBL spray deposition technique, aiming to combine the high redox activity of MoS_2 with $Ti_3C_2T_x$ and

CNTs because of their exceptional electronic conductivity and mechanical strength. Concretely, three types of 2D $MoS_2/Ti_3C_2T_x$ heterostructures were engineered and denoted as $(Ti_3C_2T_x/MoS_2)$xn (n = 1, 2, 3, 4, and 8), where n is the number of the $Ti_3C_2T_x/MoS_2$ bilayers, $(MoS_2/Ti_3C_2T_x)$x3, and $MoS_2/Ti_3C_2T_x$-mixed heterostructures, which are featured with the terminal layer of MoS_2, $Ti_3C_2T_x$, and mixed $MoS_2/Ti_3C_2T_x$ nanosheets, respectively. When they were used as anodes for LIBs, all of the as-prepared heterostructures exhibited enhanced electrochemical performance compared to single MoS_2 or $Ti_3C_2T_x$ electrodes. In particular, only the $(MoS_2/Ti_3C_2T_x)$x3 electrode achieved high and stable capacities at various rates (0.05-1.0 A g^{-1}), while it still requires a high number of cycles for achieving pre-activation when compare to $(MoS_2/Ti_3C_2T_x)$x3 and $MoS_2/Ti_3C_2T_x$-mixed heterostructures. Hence, to further improve the electrochemical performance, single-wall carbon nanotubes matrix (CNTs) were incorporated to obtain the $(MoS_2/Ti_3C_2T_x/CNTs)$x3 heterostructure. It delivers high reversible capacities of 891, 630, 578, 532, and 347 mAh g^{-1} at current densities of 0.05, 0.5, 1.0, 2.0, and 5.0 A g^{-1}, respectively, showing excellent capacity retention above 90% over thousands of cycles (ca.1000-2000). This is owing to the fact that continuous large-area layers of face-to-face contacts are created between 2D MoS_2 and $Ti_3C_2T_x$ nanosheets that can better buffer the severe volume expansion of MoS_2 during the lithiation/delithiation process, particularly at high rates. Meanwhile, the CNT matrix acting as conductive additive for the heterostructure, not only facilitates faster reversible transport of electrons and ions at the interfaces between adjacent $MoS_2/Ti_3C_2T_x$ nanosheets but also prevents the terminal $Ti_3C_2T_x$ layer from aggregation, thereby enabling the formation of robust solid-electrolyte interfaces (SEI) during long-term cycling. The structural evolution of the SEI and CNTs are further confirmed by electrochemical impedance spectroscopy (EIS) and *ex-situ* SEM. In addition, the $(MoS_2/Ti_3C_2T_x/CNTs)$x3 heterostructure delivers comparable specific capacities of 180 (0.1 C) and 158 mAh g^{-1} (1.0 C) when coupled in a full cell with the commercial $LiNi_{0.6}Co_{0.2}Mn_{0.2}O_2$ (NCM622) cathode.

Despite LIBs having been extensively applied for energy storage applications, concerns over the cost and availability of lithium reserves for large-scale applications involving renewable energy integration have to be answered. In this regard, sodium-ion batteries (SIBs) have drawn increasing attention because of the drastically lower cost and the abundance of sodium sources. Inspired by the above studies of 2D MoS_2 and $Ti_3C_2T_x$ electrodes and the different 2D $MoS_2/Ti_3C_2T_x$ heterostructures with and without CNTs as anodes for LIBs, which were applied directly as anodes for SIBs to determine if the combination

of $Ti_3C_2T_x$ and 2D MoS_2 can result in enhanced electrochemical performance for sodium storage. Firstly, the influence of fluoroethylene carbonate (FEC) electrolyte additive on the sodium storage of 2D MoS_2 and $Ti_3C_2T_x$ electrodes was explored. It is found that the capacity and cycling stability of both electrodes were remarkably improved by the FEC additive due to it modifying the surface passivation layer (more various organic compounds, less inorganic salts), including the SEI film. Next, three types of $MoS_2/Ti_3C_2T_x$ heterostructures that have been used as anodes for LIBs, which are $MoS_2/Ti_3C_2T_x$-mixed, $(MoS_2/Ti_3C_2T_x)x3$, and $(MoS_2/Ti_3C_2T_x/CNTs)x3$ heterostructures, as anodes for SIBs in FEC-containing electrolyte. Similar to the case of LIBs, the well-defined stacking $(MoS_2/Ti_3C_2T_x)x3$ heterostructure exhibits improved specific capacity and cycling stability, which is significantly superior to the $MoS_2/Ti_3C_2T_x$-mixed electrode that features with a random stacking of MoS_2 and $Ti_3C_2T_x$ nanosheets. Finally, the $(MoS_2/Ti_3C_2T_x/CNTs)x3$ heterostructure was constructed and aims to further improve the rate capability of the above $(MoS_2/Ti_3C_2T_x)x3$ electrode. The $(MoS_2/Ti_3C_2T_x/CNTs)x3$ heterostructure cannot be used as an anode for SIBs, different to LIBs, which might be because the large radius of Na^+ (1.02 Å) cannot be intercalated comfortably into the CNTs or into the engineered $Ti_3C_2T_x/CNTs$ layer structure.

The study in this thesis demonstrates that 2D $MoS_2/Ti_3C_2T_x$ heterostructures are promising anodes for LIBs. Importantly, the 2D heterostructures strategies developed here may offer a facile and efficient approach for addressing the low conductivity and volume expansion issues of other metal oxides/sulfides-based electrodes.

Zusammenfassung

Angesichts der ständig steigenden Nachfrage nach erneuerbarer und sauberer Energie sind Lithium-Ionen-Batterien (LIBs) eine der wichtigsten Technologien für Energiespeichersysteme, die aufgrund ihrer hohen Energiedichte und relativ langen Lebensdauer ausgiebig untersucht wurden. Dank dieser Vorteile haben LIBs bereits einen großen kommerziellen Erfolg in tragbarer Elektronik, Elektrofahrzeugen (EVs) und Hybrid-Elektrofahrzeugen (HEVs) erzielt. Die derzeitigen graphitbasierten Anoden haben jedoch eine relativ niedrige Kapazität (372 mAh g^{-1}) und eine unzureichende Stromratenbeständigkeit, was dazu führt, dass die derzeitigen LIBs-Systeme Schwierigkeiten haben, den schnell steigenden Energieverbrauch zu decken. Daher ist die Erforschung und Entwicklung neuartiger Anodenmaterialien von großer Dringlichkeit. Zweidimensionales (2D) Molybdändisulfid (MoS_2), ein typisches Material der geschichteten Übergangsmetalldichalkogenide (TMDs), das sich durch einzigartige Eigenschaften auszeichnet, wie z. B. eine hohe spezifische Fläche und eine verkürzte Länge des Ionentransfers aufgrund der reduzierten Dimension, wird aufgrund der hohen theoretischen Kapazität (~ 670 mAh g^{-1}) und der großen Verfügbarkeit als vielversprechendes Anodenmaterial für LIBs angesehen. Dennoch bleibt die kommerzielle Anwendung von MoS_2-basierten Anoden bisher wegen der Nachteile der geringen elektronischen Leitfähigkeit und des schnellen Kapazitätsverlusts aufgrund der unvermeidlichen Volumenausdehnung der Elektroden während des wiederholten Lade-/Entladeprozesses eingeschränkt. Daher wurde vorgeschlagen, MoS_2-basierte Elektroden mit hochleitfähigen und robusten Materialien zu kombinieren, um die oben genannten Probleme zu lösen.

Übergangsmetallcarbide und -nitride (als MXene bezeichnet), eine neue Familie von 2D-Materialien, wurden aus ihren ternären Carbid- oder Nitridvorläufern (MAX-Phase) durch selektives Ätzen der A-Schicht (Element der Gruppen 4, 5 und 6) in Flusssäure (HF) oder HF-haltigen Ätzmitteln hergestellt. Die allgemeine Formel von MXenen lautet $M_{n+1}X_nT_x$ (n= 1, 2 und 3), wobei M für ein frühes Übergangsmetall (z. B. Ti, V und Mo), X für Kohlenstoff und/oder Stickstoff und Tx für die Oberflächenabschlussgruppen (wie -OH, -O und -F) steht. Umfassende experimentelle und theoretische Studien haben gezeigt, dass MXene aufgrund ihrer attraktiven Eigenschaften wie hervorragende mechanische Flexibilität und niedrige Ionendiffusionsbarrieren sowie hervorragende Leitfähigkeit vielversprechende Kandidaten für die Lithiumspeicherung sind. Wie bei anderen konventionellen 2D-Materialien wurden jedoch auch bei MXenen aufgrund des pseudokapazitiven Mechanismus nur mäßige Kapazitäten nachgewiesen (z. B. $Ti_3C_2T_x$, 320 mAh g^{-1}).

In diesem Zusammenhang wurden 2D-Heterostrukturen durch Stapeln verschiedener 2D-Materialien geschaffen, um Elektroden zu konstruieren, die die Vorteile der einzelnen Bausteine kombinieren und gleichzeitig die damit verbundenen Nachteile beseitigen. Bis heute wurden viele Techniken wie Vakuumabscheidung, Tauch- oder Rotationsbeschichtung zur Herstellung von 2D-Heterostrukturen angewandt, die für elektronische Anwendungen hocheffizient sind, aber für die Herstellung von Batterieelektroden aufgrund von Bedenken hinsichtlich der Skalierbarkeit nicht praktikabel sind. Daher konzentriert sich diese Arbeit hauptsächlich auf die Herstellung von 2D MoS_2, $Ti_3C_2T_x$ (MXene) Elektroden und deren 2D Heterostrukturen durch eine einfache und skalierbare Schicht-für-Schicht (LBL) Sprühabscheidungstechnik, die dann als Anodenmaterialien für LIBs verwendet werden können. Darüber hinaus wird ihr Lithiumspeichervermögen intensiv untersucht, einschließlich des entsprechenden Reaktionsmechanismus und der Auswirkung verschiedener Heterostrukturen und Zusammensetzungen. Dabei kommen mehrere ex-situ-Techniken wie Raman, SEM, XRD und XPS zur Anwendung.

Zunächst wurden 2D MoS_2 Nanoschichten mit wenigen Lagen durch eine einfache Flüssigphasenexfoliation (LPE)-Synthesemethode synthetisiert. Danach wurden leitfähige, additivfreie 2D MoS_2 Dünnfilmelektroden durch Sprühabscheidung hergestellt. Im Vergleich zu herkömmlichen MoS_2-Elektroden weist die 2D-MoS_2-Elektrode eine verbesserte Li-Speicherkapazität und -Rate auf, was auf die exfolierten Nanobschichten zurückzuführen ist, die den Zwischenschichtabstand und die spezifische Oberfläche vergrößert haben. Der Mechanismus der reversiblen Umwandlungsreaktion der 2D-MoS_2-Elektrode wurde durch Ex-situ-Raman-Studien untersucht, die zeigten, dass die Umwandlungsprozesse in 2D-MoS_2-Elektroden tatsächlich reversibel sind, wobei die Nanostruktur eine Schlüsselrolle spielte. Überraschenderweise zeigt die 2D-MoS_2-Elektrode einen kontinuierlichen Kapazitätsanstieg und eine Stabilisierung nach anfänglichem Kapazitätsabfall (ca. nach 100 Zyklen) bei unterschiedlichen hohen Raten (0,75-3,0 C). Diese so genannte reaktivierte Elektrode kann in den nachfolgenden längeren Zyklen immer noch eine außergewöhnliche Ratenfähigkeit aufweisen. Die strukturellen und morphologischen Veränderungen der zyklierten Elektrode wurden mit Hilfe von Ex-situ-SEM untersucht, und die Reaktionskinetik der Elektrode wurde durch elektrochemische Impedanzspektroskopie (EIS) bewertet. Die Ergebnisse zeigen, dass die 2D-MoS_2-Elektroden aufgrund der Volumenexpansion beim Zyklieren mit hohen Raten rekonstruiert und/oder reaktiviert werden können, um eine robuste poröse Elektrodenstruktur mit einer Fülle von winzigen nadelartigen Nanoblättern zu erzeugen. Infolgedessen erleichtert die nanoskalige Diffusionslänge der aktivierten Elektrode den Massen- und Ladungstransport; eine selbstoptimierte statische SEI-Schicht während der

Langzeitzyklen verleiht den Elektroden außerdem eine außergewöhnlich stabile Ratenfähigkeit und eine längere Lebensdauer.

Die 2D-MoS_2-Elektrode weist aufgrund der Volumenexpansion eine unerwartete Lithiierungsaktivierung bei hohen Raten auf. Um dies zu beheben, wurden verschiedene Arten von 2D-MoS_2/$Ti_3C_2T_x$-Heterostrukturen mit und ohne Kohlenstoffnanoröhren (CNTs) durch eine groß angelegte alternative LBL-Sprühdepositionstechnik hergestellt, um die hohe Redoxaktivität von MoS_2 mit $Ti_3C_2T_x$ und CNTs aufgrund ihrer außergewöhnlichen elektronischen Leitfähigkeit und mechanischen Festigkeit zu kombinieren. Konkret wurden drei Arten von 2D-MoS_2/$Ti_3C_2T_x$-Heterostrukturen entwickelt, die als ($Ti_3C_2T_x$/MoS_2)xn (n = 1, 2, 3, 4 und 8) bezeichnet werden, wobei n die Anzahl der $Ti_3C_2T_x$/MoS_2-Doppelschichten ist, (MoS_2/$Ti_3C_2T_x$)x3, und MoS_2/$Ti_3C_2T_x$-gemischte Heterostrukturen, die mit einer Endschicht aus MoS_2, $Ti_3C_2T_x$ bzw. gemischten MoS_2/$Ti_3C_2T_x$-Nanoschichten ausgestattet sind. Wenn sie als Anoden für LIBs verwendet wurden, zeigten alle so hergestellten Heterostrukturen ein verbessertes elektrochemisches Verhalten im Vergleich zu einzelnen MoS_2- oder $Ti_3C_2T_x$-Elektroden. Insbesondere erreichte nur die (MoS_2/$Ti_3C_2T_x$)x3-Elektrode hohe und stabile Kapazitäten bei verschiedenen Raten (0,05-1,0 A g^{-1}), während sie noch viel mehr Zyklen für die Voraktivierung benötigt. Um das elektrochemische Verhalten weiter zu verbessern, wurde eine einwandige Kohlenstoffnanoröhren-Matrix (CNTs) eingebaut, um die (MoS_2/$Ti_3C_2T_x$/CNTs)x3-Heterostruktur zu erhalten. Sie liefert hohe reversible Kapazitäten von 891, 630, 578, 532 und 347 mAh g^{-1} bei Stromdichten von 0,05, 0,5, 1,0, 2,0 und 5,0 A g^{-1} und zeigt eine ausgezeichnete Kapazitätserhaltung von über 90 % über Tausende von Zyklen (ca. 1000-2000). Dies ist darauf zurückzuführen, dass die kontinuierlichen, großflächigen Schichten, die einen direkten Kontakt zwischen 2D-MoS_2 und $Ti_3C_2T_x$-Nanoschichten herstellen, die starke Volumenexpansion von MoS_2 während des Lithiierungs-/Delithiierungsprozesses besser abfedern können, insbesondere bei hohen Raten. Die CNT-Matrix, die als leitfähiger Zusatz für die Heterostruktur fungiert, erleichtert nicht nur den schnelleren reversiblen Transport von Elektronen und Ionen an den Grenzflächen zwischen benachbarten MoS_2/$Ti_3C_2T_x$-Nanoschichten, sondern verhindert auch die Aggregation der endständigen $Ti_3C_2T_x$-Schicht und ermöglicht so die Bildung von robusten Festkörper-Elektrolyt-Grenzflächen (SEI) während langfristiger Zyklen. Dies wird auch durch elektrochemische Impedanzspektroskopie (EIS) und Ex-situ-SEM bestätigt. Darüber hinaus liefert die (MoS_2/$Ti_3C_2T_x$/CNTs)x3-Heterostruktur vergleichbare spezifische Kapazitäten von 180 (0,1 C) und 158 mAh g^{-1} (1,0 C), wenn sie in einer Vollzelle mit der kommerziellen $LiNi_{0,6}Co_{0,2}Mn_{0,2}O_2$ (NCM622)-Kathode gekoppelt wird.

Obwohl LIBs bereits in großem Umfang für Energiespeicheranwendungen eingesetzt werden, müssen Bedenken hinsichtlich der Kosten und der

Verfügbarkeit von Lithiumreserven für groß angelegte Anwendungen unter Einbeziehung erneuerbarer Energien ausgeräumt werden. In diesem Zusammenhang haben Natrium-Ionen-Batterien (SIBs) aufgrund der drastisch niedrigen Kosten und der reichlich vorhandenen Natriumquellen zunehmende Aufmerksamkeit auf sich gezogen. Inspiriert von den oben genannten Studien zu 2D-MoS_2 und $Ti_3C_2T_x$-Elektroden sowie ihren verschiedenen 2D-MoS_2/$Ti_3C_2T_x$-Heterostrukturen mit und ohne CNTs, wurden diese, obwohl zunächst als Anoden für LIBs entwickelt, so direkt auch als Anoden für SIBs eingesetzt um festzustellen, ob die Kombination von $Ti_3C_2T_x$ und 2D MoS_2 zu einer verbesserten elektrochemischen Speicherung von Natrium führen kann. Zunächst wurde der Einfluss des Elektrolytzusatzes Fluorethylencarbonat (FEC) auf die Natriumspeicherung von 2D MoS_2- und $Ti_3C_2T_x$-Elektroden untersucht. Es wurde festgestellt, dass die Kapazität und die Zyklenstabilität beider Elektroden durch den FEC-Zusatz deutlich verbessert wurden, da er die Oberflächenpassivierungsschicht (mehr verschiedene organische Verbindungen, weniger anorganische Salze), einschließlich des SEI-Films, modifiziert. Als nächstes wurden drei Arten von MoS_2/$Ti_3C_2T_x$-Heterostrukturen in LIBs untersucht, nämlich MoS_2/$Ti_3C_2T_x$-gemischt, (MoS_2/$Ti_3C_2T_x$)x3- und (MoS_2/$Ti_3C_2T_x$/CNTs)x3-Heterostrukturen und als Anoden für SIBs in einem FEC-haltigen Elektrolyten verwendet. Ähnlich wie bei LIBs zeigt die gut definierte Stapelung der (MoS_2/$Ti_3C_2T_x$)x3-Heterostruktur eine verbesserte spezifische Kapazität und Zyklenstabilität, die der MoS_2/$Ti_3C_2T_x$-Gemischelektrode mit einer zufälligen Stapelung von MoS_2- und $Ti_3C_2T_x$-Nanoblättern deutlich überlegen ist. Schließlich wurde eine (MoS_2/$Ti_3C_2T_x$/CNTs)x3-Heterostruktur realisiert, um die Ratenfähigkeit der oben genannten (MoS_2/$Ti_3C_2T_x$)x3-Elektrode weiter zu verbessern. Überraschenderweise kann die (MoS_2/$Ti_3C_2T_x$/CNTs)x3-Heterostruktur nicht als Anode für SIBs verwendet werden, obwohl dies in LIBs sehr gut möglich war. Dies könnte daran liegen, dass der große Radius von Na^+ (1,02 Å) nicht in die CNTs oder die künstliche $Ti_3C_2T_x$/CNTs-Schichtstruktur interkaliert werden kann.

In dieser Arbeit konnte gezeigt werden, dass 2D MoS_2/$Ti_3C_2T_x$ Heterostrukturen attraktive Alternativen zu kommerziellen Anoden für LIBs und vielversprechende Anoden für SIBs sind. Wichtig ist, dass die hier entwickelten 2D-Heterostrukturen einen einfachen und effizienten Ansatz bieten, um die Probleme der geringen Leitfähigkeit und der Volumenexpansion anderer auf Metalloxiden/Sulfiden basierender Elektroden zu lösen.

1 Introduction

1.1 Background

Currently, human beings have to confront the ever-increasing fossil fuel shortage and energy crisis. The most promising strategy to address these serials of the conundrum is to develop advanced energy storage technologies that feature natural abundance, renewability, and sustainability. [1] Solar, wind, geothermal power, biomass energy, etc. are being used as power supplies thanks to their renewable and environmentally friendly properties. However, they are inherently intermittent and highly dependent on natural conditions such as weather, season, and geographical location. [2] To better use the renewable energy source, it is urgent to develop new electrochemical devices or techniques that can appropriately store energy from different sources. The ideal energy storage devices are supposed to be characterized by high efficiency, versatility, recyclable, large-scale, and low-cost. In this context, a secondary battery, also known as rechargeablility or storage battery, was proposed, which is a system of electrically connected electrochemical cells based on reversible electrochemical redox reactions. In the initial development stage, there are several battery devices that have been in use long enough to be considered mature technologies. For instance, lead-acid (Pb-H_2SO_4), nickel-cadmium (Ni-Cd), and nickel-metal hydride (NiMH) batteries are produced in different sizes (as the first generation of rechargeable batteries) for different applications. [3] Unfortunately, their application in large-scale energy storage is limited by low energy density, corrosion, unsatisfied rate capability, not sustainable and poor Coulombic efficiency (CE). To solve these issues, with the fast development of technology, the commercialized rechargeable lithium-ion batteries (LIBs) based on a lithium intercalation mechanism have been developed in 1991 by Sony Corp. and are considered to be of great importance as energy storage systems in modern society. [4] Up to date, LIBs have been widely used as the main power source for portable electronic devices such as laptops, various digital products, mobile phones, and stationary energy storage systems owing to their relatively high energy density and long life-span. [5-6] On the one hand, the LIBs market has been developing rather fast in the last three decades. In particular, LIBs were considered as a promising driving power for the next-generation hybrid electric vehicles (HEVs) and pure electric vehicles (EVs). [1, 7]

On the other hand, the blooming development of electronics and vehicles leads to an ever-increasing demand for LIBs, which thus results in booming consumption of Li sources. In addition, lithium resources are distributed unevenly on the Earth (mainly in South America), which finally triggers the

sharp rise of Li prices and destabilizes the supply chain in the world. Naturally, it is necessary to develop other rechargeable batteries based on cost-effective and rich resources as alternatives to LIBs. Sodium is widely distributed in crust and seawater and is the earth's fourth abundant element, which exhibits similar electrochemical properties to Li, since they belong to the same main group in the periodic table of elements. [8] As a matter of a fact, the research on sodium-ion batteries (SIBs) and LIBs was in parallel in the last century, but SIBs were nearly abandoned due to the advanced progress on the development and success of the commercial application of LIBs. [8] In recent years, SIBs have regained researchers' attention due to the rapid development of nanomaterials and characterization techniques and their natural abundance, which can meet the demands for large-scale energy storage systems (ESSs). [9] LIBs and SIBs are sharing similar battery components and electrical storage mechanisms except for their shuttling ion carriers. Compared to the LIBs system, sodium has a larger ionic radius (1.02 Å for Na^+ *versus* 0.76 Å for Li^+) and a reduction potential around 300 mV higher than lithium, [10-11] which could result in different physical properties of the ion storage materials and electrolytes system (e.g. salts and solvents). Therefore, more investigations are now needed for SIBs.

1.2 Aims and overview of the work

Tremendous efforts have been devoted to developing high-performance anode materials for LIBs and SIBs to achieve significantly improved capacity, high rate capability, and long cycling life. However, some inherent issues still need to be solved. For instance, high power density can only be achieved in batteries with rapid ion and electron transport, but the movement of ions in bulk electrodes is heavily restricted by the limited lattice spacing or interlayer spacing, which further leads to a sluggish charge-discharge process and rapid electrode failure due to the strain accumulation by ions intercalation. High energy density requires maximization of the charge storage capability, while most conventional bulk materials could only offer a limited number of active reaction sites for the redox reaction. In recent years, with the discovery of graphene in 2004, a growing number of two-dimensional (2D) materials such as transition metal dichalcogenides (TMDs), phosphorene, and transition metal carbides and nitrides (MXenes) have gained significant attention due to their multi-faceted advantageous properties: large specific surface area, high electrical and ionic conductivity, and mechanical strength. [12-16]

Up to date, many 2D materials have been reported as potential alternatives for energy storage. Nevertheless, according to the state-of-the-art literature, almost

all conventional 2D materials exhibit advantages and limitations when they are used as single component anode for LIBs and SIBs. [12, 17-18] For instance, 2D $Ti_3C_2T_x$ nanosheets, a typical MXenes-based material, shows high electrical conductivity, but demonstrates a moderate capacity (theoretical capacity of 320 mAh g^{-1}) due to the limited number of sites for charger storage on the surface. [19] [20] 2D MoS_2 exhibits high capacity (theoretical capacity of 670 mAh g^{-1}) thanks to the high redox activity in intercalation and conversion reactions, while the capacity value drops significantly at high cycling rates. [21] [22] To overcome these limitations, one potential way may be to use 2D van der Waals heterostructures, that is, stacking different individual conventional 2D materials in a well-defined heterostructure. Then it is possible to combine the advantages and eliminate the disadvantages of the single materials. [23-27]

Therefore, to research the 2D heterostructures for energy storage, 2D MoS_2 and $Ti_3C_2T_x$ nanosheets, as representatives of TMDs and MXenes materials, serve as building blocks in the current thesis. The synthesis, characterization, electrode design strategy, and investigation of them as anode materials for LIBs and SIBs were systematically explored.

Specifically, **chapter 2** introduces the manufacturing of the electrodes by spray-deposition with 2D MoS_2 and $Ti_3C_2T_x$ suspension, and the relevant *ex-situ* characterization techniques used in this thesis, such as SEM, TEM, XPS, and XRD. Afterwards, the basic electrochemical characterization techniques were introduced in detail, including electrochemical charge and discharge, cyclic voltammetry, and electrochemical impedance spectroscopy.

Chapter 3 presents few-layers 2D MoS_2 nanosheets that were synthesized by using a facile liquid-phase exfoliation (LPE) synthesis method. Thereafter, conductive additives-free thin-film electrodes were manufactured using a scalable layer-by-layer (LBL) spray-deposition technique. Compared to bulk MoS_2, the 2D MoS_2 electrode exhibits improved Li storage capacity, rate capacity due to the exfoliated nanosheets that have increased their interlayer distance and specific surface area. The reversible conversion reaction mechanism of the 2D MoS_2 electrode was unravelled by *ex-situ* Raman. Surprisingly, the 2D MoS_2 electrode shows a continuous capacity increase and stabilization after initial capacity fading at various high rates (0.75-3.0 C), and this so-called reactivated electrode can still deliver exceptional rate capability in the subsequent prolonged cycling. *Ex-situ* SEM was employed to track the structural and morphological change of the cycled electrode and electrode reaction kinetics and evolution of the SEI film were evaluated by electrochemical impedance spectroscopy (EIS).

What follows is a continuation from the last part, since the 2D MoS_2 electrode exhibited an unexpected lithiation activation at high rates due to the volume expansion. To address this, **chapter 4** is to determine if a 2D heterostructure of $Ti_3C_2T_x$ (MXene) and MoS_2, which is engineered by LBL spray deposition, can result in improved lithium storage performance regarding capacity and stability. To this end, firstly, three different types of 2D $MoS_2/Ti_3C_2T_x$ heterostructures were prepared, which are denoted as $(Ti_3C_2T_x/MoS_2)xn$ (n = 1, 2, 3, 4 and 8) and $(MoS_2/Ti_3C_2T_x)x3$, with the terminal layer of MoS_2 and $Ti_3C_2T_x$, respectively. And a $MoS_2/Ti_3C_2T_x$-mixed heterostructure, made by spraying a conventional mixture of MoS_2 and $Ti_3C_2T_x$ components, which was used as a comparison. All as-fabricated heterostructures exhibited improved performance for Li-ion storage with respect to the capacities and rate capabilities compared to the single material electrode. However, among them, only the $(MoS_2/Ti_3C_2T_x)x3$ electrode achieved high and stable capacities at various rates but required much more cycles for electrode activation. Next, to further improve the electrochemical performance, a single-wall carbon nanotubes matrix (CNTs) was incorporated to obtain the $(MoS_2/Ti_3C_2T_x/CNTs)x3$ heterostructure. The role of CNTs for the above heterostructure was investigated by *ex-situ* SEM and EIS. Finally, the electrochemical performance of the $(MoS_2/Ti_3C_2T_x/CNTs)x3$ heterostructure was also evaluated in lithium-ion full cells with the commercial $LiNi_{0.6}Co_{0.2}Mn_{0.2}O_2$ (NCM622) cathode material.

In **chapter 5,** inspired by the studies of 2D MoS_2 and $Ti_3C_2T_x$ electrodes as well as their several different 2D $MoS_2/Ti_3C_2T_x$ heterostructures with and without CNTs as anodes for LIBs in **chapters 3** and **4**, naturally, we applied them directly as anodes for SIBs to determine if the combination of $Ti_3C_2T_x$ and 2D MoS_2 can result in enhanced electrochemical performance for sodium storage. The improvement of capacity and cycling stability for 2D MoS_2 and $Ti_3C_2T_x$ electrodes in the electrolyte with fluoroethylene carbonate (FEC) additive was firstly verified. Based on this, the electrolyte with FEC additive was selected for further electrochemical experiments on the $(MoS_2/Ti_3C_2T_x)x3$, $MoS_2/Ti_3C_2T_x$-mixed, and $(MoS_2/Ti_3C_2T_x/CNTs)x3$ heterostructures. Finally, the electrochemical sodium storage performances of these heterostructures regarding charge/discharge capacities, rate capabilities, and cycling stabilities were systemically compared.

Chapter 6 summarizes the thesis and recommends a strategy for further studies.

1.3 Overview of Li- and Na-ions batteries

1.3.1 Components and working principles

In principle, a LIB system consists of a positive electrode (cathode) and a negative electrode (anode), which are separated by a porous membrane (separator) in an ion-conducting electrolyte (containing a dissociated lithium conducting salt). The separator is situated between the two electrodes and electrically isolates them from each other, as shown in **Figure 1.1**. Lithium ions are shuttled back and forth between the cathode and anode electrodes during charging and discharging (an electrochemical redox process within the active materials), involving a charge compensation mechanism. During the discharging process, electrons will be released when Li-ions are deintercalated from the anode (oxidation reaction) and transferred to the cathode side. This process is reversed in the charging process, on the contrary, lithium ions will be intercalated back into anode from the cathode by an externally imposed potential (reduction reaction). As a result, the so called rocking-chair mechanism is proposed based on this concept. Taking a battery of $LiCoO_2$ cathode and graphite anode as an example, the redox reaction can be described below: [28]

Discharge: cathode: $Li_{1-x}CoO_2 + xLi^+ + xe^- \rightleftharpoons LiCoO_2$ (**equation 1.1**)

anode: $CLi_x \rightleftharpoons C + xLi^+ + xe^-$ (**equation 1.2**)

Total reaction: $Li_{1-x}CoO_2 + CLi_x \rightleftharpoons LiCoO_2 + C$ (**equation 1.3**)

Charge: cathode: $LiCoO_2 \rightleftharpoons Li_{1-x}CoO_2 + xLi^+ + xe^-$ (**equation 1.4**)

anode: $C + xLi^+ + xe^- \rightleftharpoons CLi_x$ (**equation 1.5**)

Total reaction: $LiCoO_2 + C \rightleftharpoons Li_{1-x}CoO_2 + CLi_x$ (**equation 1.6**)

The energy density of rechargeable batteries is determined by the difference in Gibbs free energy between cathode and anode materials in the charged and discharged state: [29]

$\Delta G^0 = -nFE^0$ or $\Delta G = -nFE$ (**equation 1.7**)

Where G^0 is the standard Gibbs free energy, n is the number of electrons, F is the Faraday constant (96485.3 C mol^{-1} or 26.801 Ah mol^{-1}), E^0 is the standard battery potential (at 298 K and 1 bar), and E is the cell's potential under nonstandard condition. Therefore, developing high-performance LIBs is based on selecting appropriate electrode materials. In practice, LIBs can be produced in four kinds of shapes, including cylindrical, coin, prismatic, and pouch cells depending on the specific applications. In addition, a single cell can be used or

several cells are connected in series to a module, and a parallel connection is also possible according to the required capacity.

As for the components and working principles of SIBs, they are similar except that their ionic charge carriers are Na^+ ions and electrode materials (e.g. hard carbon for the anode) are different. [30] Therefore, the technology of sodium-ion battery can track and adopt most of the knowledge gained from the existing studies on LIBs, but a further breakthrough concerning the energy density highly relies on developing new types of electrode materials for cathode and anode, and even electrolyte systems.

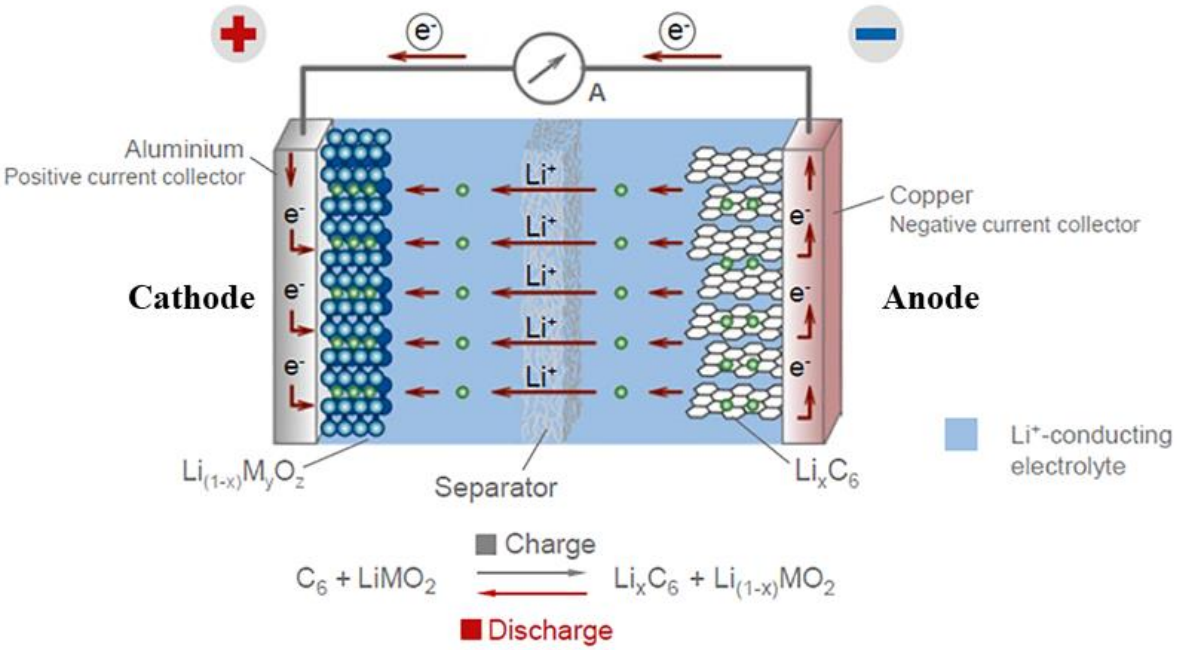

Figure 1.1 Schematic of a lithium-ion battery [31]

1.3.2 Basic definitions for LIBs and SIBs

1.3.2.1 Energy density and specific energy density

The energy density of a battery, about how much stored energy is available, is commonly expressed in two ways, in the form of gravimetric and volumetric energy density. The gravimetric and volumetric energy density is a measure of how much energy a battery contains in comparison to its mass and volume, respectively, and are typically expressed in Watt-hours/kilogram (Wh/kg) and Watt-hours/liter (Wh/L). Both of them are called specific energy density (by weight and volume). Specific energy is one of the many battery characteristics used chiefly to compare one type of battery system to another. A battery with a

higher specific energy density will be lighter than a similar capacity battery with a lower specific energy density. **Figure 1.2** presents the battery comparison chart illustrating that a battery with high volumetric and gravimetric specific energy densities shows smaller sizes and lighter weight cells.

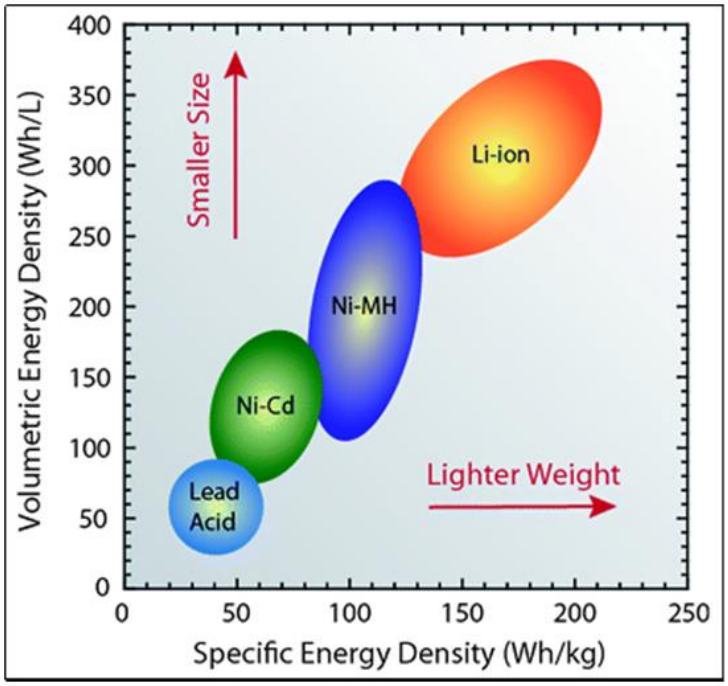

Figure 1.2 Battery specific energy densities by volume and weight [6]

1.3.2.2 Power density and specific power density

Power density of a battery is a measure of how quickly the energy can be delivered per unit volume, W L^{-1}. The specific power density is a measure of the amount of power that a cell can deliver per unit weight, W kg^{-1}. The specific power density of a battery is related to several dynamic factors such as conductivity of lithium ions and electrons within active materials and the motion of the ions rate at the electrode/electrolyte interface as well as in the electrolyte. Generally, reducing the energy barrier for Li-ion diffusion and shortening the transport pathway of the electrons/ions are commonly used strategies to improve the specific power density.

1.3.2.3 Theoretical capacity

The theoretical capacity of the electrode material, that is, the capacity provided by the assumption that all lithium ions in the material participate in the electrochemical reaction, which is directly translated into specific capacity and energy defines the potential of a new alternative. According to Faraday's law,

the theoretical capacity of an activated material can be calculated as the following equation:

$Q_{th} = nF/M_w$ As g^{-1} (**equation 1.8**)

Where n (in mole) is the number of charge carriers, F is the Faraday constant (96485.3 C mol^{-1}) and M_w is the molecular weight of the active material (g mol^{-1}), As g^{-1} is the unit of specific energy capacity, ampere-second per gram, which can be also expressed as mAh g^{-1} by 10^{-3} multiply by 3600 (1 h = 3600 s). For instance, for the cathode material $LiFePO_4$, the charge reaction can be presented as **equation 1.9**:

$LiFePO_4 \rightleftharpoons FePO_4 + 1Li^+ + 1e^-$ (**equation 1.9**)

In this case, n = 1 mole Li^+, M_w of $LiFePO_4$ is 157.7 g mol^{-1}, so $Q_{LiFePO4} = \frac{1 \times 96485.3\ \text{C}\ mol^{-1}}{157.7\ \text{g}\ mol^{-1}}$ = 611.83 As g^{-1} = 611.83/3600 Ah g^{-1} = 169.9 mAh g^{-1}.

1.3.2.4 Coulombic efficiency

The Coulombic efficiency (CE), is also known as faradaic efficiency, which is defined as the ratio (expressed as a percentage) of the ions that participate in the faradaic reactions to the total ions input into the electrode, can be presented in a mathematical equation:

$CE = Q_{out}/Q_{in}$ x 100%

Where Q_{out} is the output capacity and Q_{in} is the input capacity of a battery in the same cycle. For instance, for an anode, CE = charge capacity/discharge capacity (%), means the amount of charge flow during the charging process compared to the charge flow during the discharge process.

1.3.3 Anode materials for LIBs and SIBs

Up to date, tremendous efforts have been made to improve the electrochemical performance of LIBs and SIBs for different energy storage applications. Ideally, to reach a high specific capacity and excellent long-term cycling performance for secondary rechargeable batteries, the anode materials should have these characteristics:

I. The lithium or sodium ions can be inserted/extracted into/from anode materials at low redox potential. The closer to the potential of metallic lithium or sodium, the higher the output voltage of the battery will be;

II. A high number of Li^+ or Na^+ ions should be able to store and remove reversibly in the host structure of the anode, and should show little or no change during this process to ensure a stable cycling performance;

III. The anode should have an excellent electrochemical stability in the entire potential window to make sure the formation of a stable solid electrolyte interface (SEI), which thereby to reduce an increase of polarization during charge/discharge;

IV. In practical terms, the anode materials are low-cost, nontoxic, and environmentally friendly.

Based on these requirements, many materials such as carbon-based, and transition metal oxides (TMOs) have been designed and synthesized as anode matrix for LIBs and SIBs. Generally, anode materials can mainly be classified into three types according to the electrochemical reaction mechanism: intercalation/deintercalation materials, alloying/dealloying, and conversion materials, which will be discussed separately in the next section.

1.3.3.1 Intercalation type material

The reaction mechanism for intercalation type anode materials is based on the repetitive intercalation/deintercalation of lithium or sodium ions in the crystal lattice of the host structure, as shown in **Figure 1.3**. Normally, this type of material has a layered structure, mainly including carbonaceous- or titanium-based oxide materials. Graphite as a layered carbon-based material was first used as an anode electrode for commercial LIBs due to its good working potential, impressive electrical conductivity (~10^4 Scm^{-1}), and low-cost. So far, the reaction mechanism is also well-known as layered LiC_6 can be produced by intercalating Li-ions. However, the energy density and rate performance of graphite is not ideal due to its rather low theoretical capacity (372 mAh g^{-1}) and sluggish diffusion rate of lithium ions. In addition, the lithium dendrites and SEI can be easily formed resulting from the fact that the potential for lithium intercalation is almost similar to the plating potential of metallic lithium. [32] Moreover, sodium ions cannot be intercalated between the graphite layers to produce stable Na-C binary compounds, so that graphite cannot be used as anode material for SIBs. [33] Hard carbon was firstly used as anode for SIBs due to its special disordered structure, exhibiting a high reversible capacity of 300 mAh g^{-1}. [34] Later on, tremendous further works have been devoted to hard carbon derivatives such as heteroatom-doped carbon and biomass-based carbon materials.

Another typical intercalation anode material for LIBs and SIBs is layered titanium oxide, including TiO_2 and $Li_4Ti_5O_{12}$ (LTO). TiO_2 has various crystal structures such as anatase, rutile, brookite, and TiO_2 (B) (monoclinic *C2/*m). [35] Due to its unique properties, for instance, exceptional stability, cost-effectiveness, and natural abundance, TiO_2 has been considered as one of the most promising anode materials with the moderate insertion potential for Na^+ at around 0.6 V (*vs.* Na^+/Na) and high lithiation potential of 1.5 V (*vs.* Li^+/Li), which can provide excellent safety to the battery (e.g. eliminate the problem of lithium or sodium dendrite formation). [34, 36] $Li_4Ti_5O_{12}$ with spinel structure, is viewed as the most appropriate titanium-based oxide material for LIBs because it shows excellent Li-ions reversibility even at a higher operating potential of 1.55 V (*vs.* Li^+/Li). The spinel structure remains unchanged, and is well known as zero-strain material for lithium insertion that provides an extremely long cycle life. [37] Meanwhile, LTO has also been studied as a promising anode material for SIBs because it can be a host for Na^+ insertion based on a three-phase reaction. [33] However, LTO has been limited by poor electronic conductivity (~ 10^{-13} S cm^{-1}), low inherent theoretical capacities (~ 175-330 mAh g^{-1}), and undesirable gas release for large-scale electrochemical energy storage applications. [38]

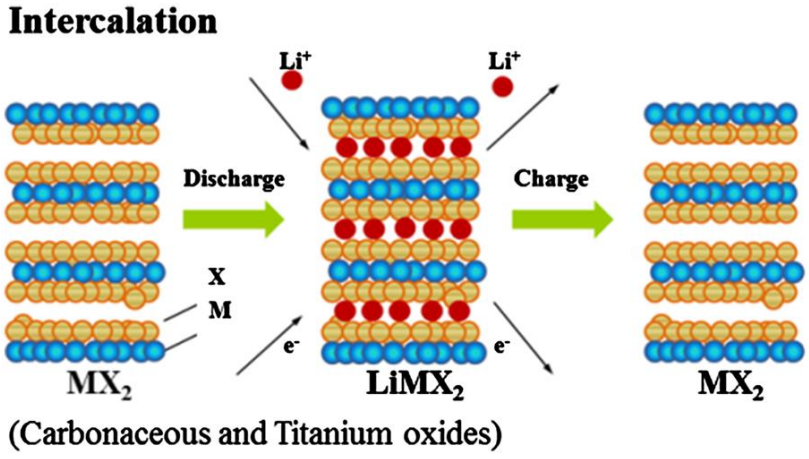

Figure 1.3 Schematic illustration of intercalative anode materials [36]

1.3.3.2 Alloying type material

At the very initial stage of developing LIBs, pure lithium metal was viewed as the best anode material since it has super high theoretical capacity (3860 mAh g^{-1}) and it does not carry any dead weight from the viewpoint of specific capacity. [7] However, the uncontrollable growth of lithium dendrite during cycling can cause an internal short circuit and further result in severe safety concerns. Similar to this metal electrode, alloyed anode materials were proposed, which

are primarily belonging to the groups 14 and 15. The alloying mechanism is illustrated in **Figure 1.4**, and can be expressed as **equation 1.10**:

$$xG^{+} + xe^{-} + M \rightleftharpoons G_xM \qquad \textbf{(equation 1.10)}$$

Where G is a guest ion (Li^+ and Na^+), M can be Si, Sn, Ge, P, Pb, and Bi. Alloying type anode materials have the potential to become the next generation anodes owing to their extremely high theoretical specific capacity (e.g. Si 4200 mAh g^{-1}). This is due to the atoms of any alloying materials theoretically holding 4.4 Li^+. [39] Nevertheless, the alloying reaction mechanism faces as the most challenging issue the volume expansion and fracture of an electrode during repetitive charge/discharge. The serious volume change in combination with the brittleness of the intermetallic compounds can lead to mechanical fracture in individual particles, which further results in a rapid capacity fading and destabilization of the SEI film. In addition, the larger volume expansion of active material could also lead to swelling of the whole electrode and threatens the safety of a battery system. [36, 40] To address these challenges, several strategies have been devoted, including reducing the particle size to nanoscale, synthesis of intermetallic compounds, and optimizing the electrolytes (solvents and salts), additives, and binder. [41]

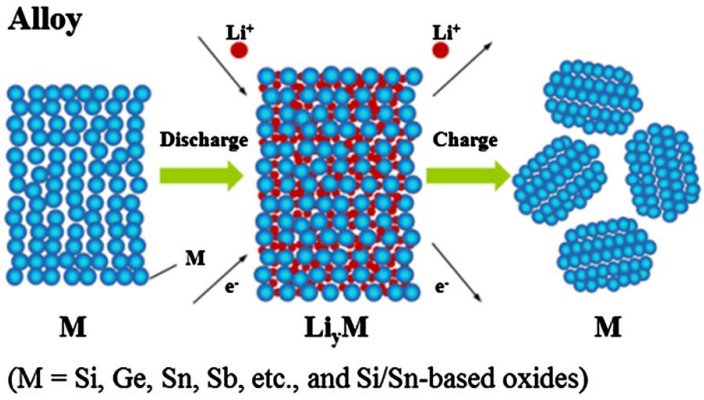

Figure 1.4 Schematic illustration of alloying anode materials [36]

1.3.3.3 Conversion type material

Conversion materials are attractive as anode materials for the next generation of LIBs and SIBs due to their high theoretical capacities (in a range of 500-1200 mAh g^{-1}) and abundant resources. There are basically four groups of them including transition metal oxides, [42] sulfides, [43-44] phosphides [45-46], and nitrogen compounds. [47] The electrochemical reaction mechanism of the conversion anode is presented in **Figure 1.5**, which can be described as follows:

$M_xN_y + zG^+ + ze^- \rightleftharpoons G_zN_y + xM$ **(equation 1.11)**

Where M = Fe, Co, Mn, Mo, Ni, and so on, N = O, P, S, and N, G is Li^+ or Na^+ ion. [37] Compared to intercalation and alloying materials, in which metal ions are reversibly inserted/deinserted into or from the host structure, conversion materials could accommodate metal ions through a conversion reaction that involves a chemical transformation of atomic species to produce a new compound. [40] Similar to alloying anodes, there is still a long way for conversion type anodes before they can be used as commercialized LIBs due to the issues of material pulverization, insufficient electronic conductivity, the morphology and volume change, and unstable SEI film as well as the significant voltage hysteresis (the difference between charge/discharge). [48] In addition, it is found that the practical capacity of conversion type anodes is lower than the theoretical one in SIBs, not LIBs, which is mainly due to the sluggish mobility of large Na^+ ions. [33] Up to date, tremendous efforts have been done to overcome the challenges of these conversion type materials, including designing them in nanostructured form, synthesis of porous structures and core-shell structures, and transition metal doping. [39, 49-51]

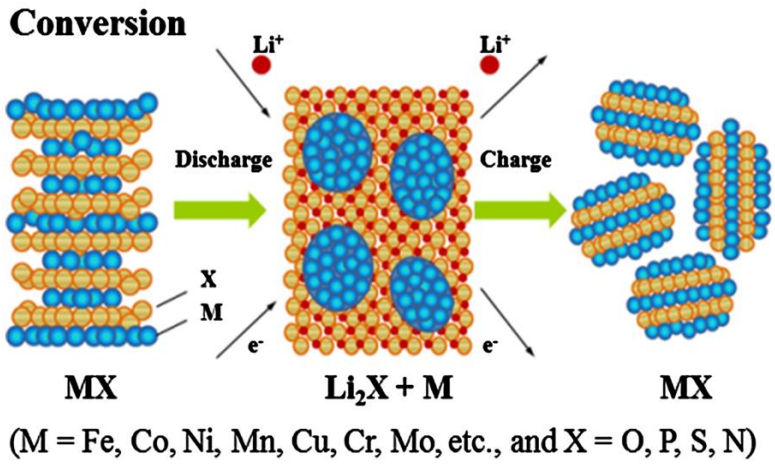

Figure 1.5 Schematic illustration of conversion anode materials [36]

2 Experimental Methods and Characterization

2.1 Spray deposition systems

Spray deposition is a process in which a stream of drops is atomized by compressed carrier gas, such as air and argon. This process is a well-developed and atomization process designed to produce high density and bulk shapes directly from the melted salt. The process consists of two basic steps: firstly, a molten metal stream is atomized using an inert gas such as argon or nitrogen, secondly, the spray thus produced is then collected onto a suitably designed substrate. [52-53] However, this technique has been limited over the past decades by clogging of the orifice. Therefore, a non-clogging spray system with repeatable performance is demanded. With the development of spray technologies, the ultrasonic coating technique has replaced conventional coating systems in a wide range of industrial and R&D applications and enabled spray processes that would otherwise be impossible. Compared to many other coating systems, ultrasonic spray nozzles are more precise, more controllable, and repeatable. The nozzles are inherently non-clogging, self-cleaning devices due to continuous ultrasonic vibrations and their relatively large orifice. The ultrasonic nozzles are ideal, for instance, when extremely low flow rates are needed. And they offer unique benefits when spraying particles in suspension, keeping particles evenly suspended during the entire spray process through the ultrasonic action of the nozzle itself. This results in a more uniform dispersion of functional particles in a thinner layer. Therefore, a spray coater equipped with ultrasonic nozzles opens up a broad range of new application possibilities. In this context, the ultrasonic spray deposition technique has been successfully applied to manufacture electrodes for lithium-ions batteries (LIBs). [54-57] In the current thesis, spray deposition was carried out using a Flexi-coat spray-deposition coater (*Sono-tek Corporation*, USA) equipped with three ultrasonic nozzles (48 kHz) and three syringes (25 ml, 0.01 to 5 ml min^{-1} flow rate range). Three pumps can drive three syringes at same time. The nozzles spray on a Teflon coated hot/vacuum plate (50 cm x 50 cm area, 4 vacuum zones, capable to reach temperatures up to 150 °C). The configuration of the ultrasonic spray coater for this thesis is shown in **Figure 2.1**. The ultrasonic nozzles are mounted on a three-axis coordinated motion system using servomotors that can be controlled manually (by a trackball) or by a provided programmable system. Most key functions of the equipment are controlled via the programmable system, including the control of the hot plate (vacuum zones), devices (nozzles, valves, and servomotors), spraying, and purging (in manual mode). Spray

deposition patterns can be pre-defined, executed, and automated using pre-created spray recipes.

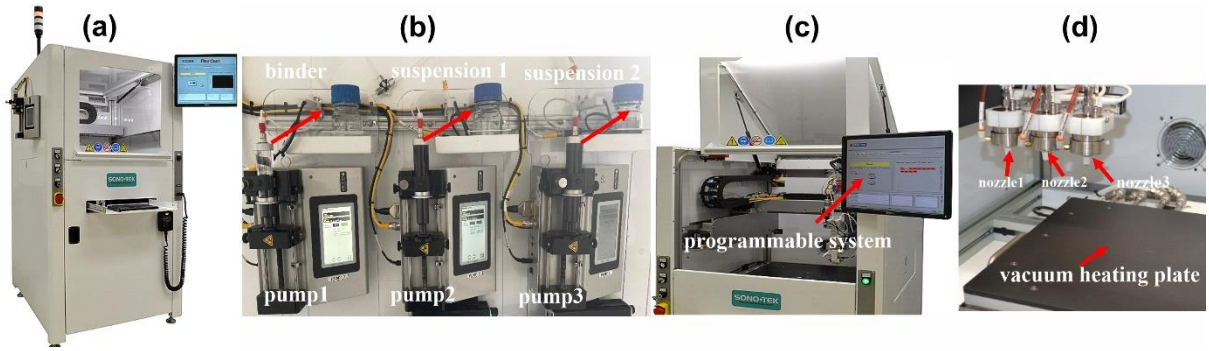

Figure 2.1 Configuration of ultrasonic spray coater for this thesis. (a) outside picture of the coater, (b) pumps system with syringes, (c) programmable system for creating spray recipes, (d) ultrasonic spray nozzles and heating plate with vacuum assistance.

2.2 Scanning electron microscopy

The scanning electron microscope (SEM) is one of the most versatile instruments available for the examination and analysis of microstructure and morphology and characterization of chemical composition. The image formation in the SEM depends on the acquisition of signals produced from the interaction between electron beam and specimen. [58] Normally, these interactions can be divided into two major categories; elastic interactions and inelastic interactions. The former results from the deflection of the incident electron by the specimen atoms, and the latter occurs through a variety of interactions between the incident electrons and the electrons and atoms of the sample, thereby transferring substantial energy from the primary electron beam to that atom. The amount of energy loss depends on whether the specimen electrons are excited singly or collectively and on the binding energy of the electron to the atom. As a result, the excitation of the electrons of the specimen during the ionization of the specimen atoms leads to the generation of secondary electrons (SE), which are conventionally defined as possessing energies of less than 50 eV and can be used to image with high-resolution the sample surface (< 1 nm). [58] The most widely used signal produced by the interaction of the primary electron beam with the sample is the SE emission signal. Another class of signals produced by the interaction of the primary electron beam with the samples are characteristic X-rays. The analysis of characteristic X-rays can be used as a technique to provide chemical elements information in the specimen and also map their distribution. [59] Moreover, in common SEM imaging, the samples must be electrically conductive to avoid an accumulation of electrostatic charge. Here, a brief working principle of SEM is introduced.

Figure 2.2 shows the column structure of a conventional SEM column. The main SEM components include the source of electrons, electromagnetic lenses, electron detector, sample chamber, and computer system to view the images. The electrons are firstly produced from an electron gun either by thermionic emission mode (tungsten or LaB_6) or field emission mode (cold-cathode type (tungsten single crystal) or thermally assisted Schottky cathode type (zirconium oxide), then accelerated down from the top of the column and passed through a combination of lenses to produce a focused beam of electrons which then strikes the surface of the sample. The sample is mounted on stage in the ultra-high vacuum chamber (the level of the vacuum will depend on the design of the microscope). The position of the electron beam on the sample is controlled by scanning coils located above the objective lens. These coils allow the beam to be scanned across the surface of the sample. This beam scanning enables information about a defined area on the specimen to be collected. Finally, in the electron-sample interaction, several signals are produced, which are then detected by appropriate detectors.

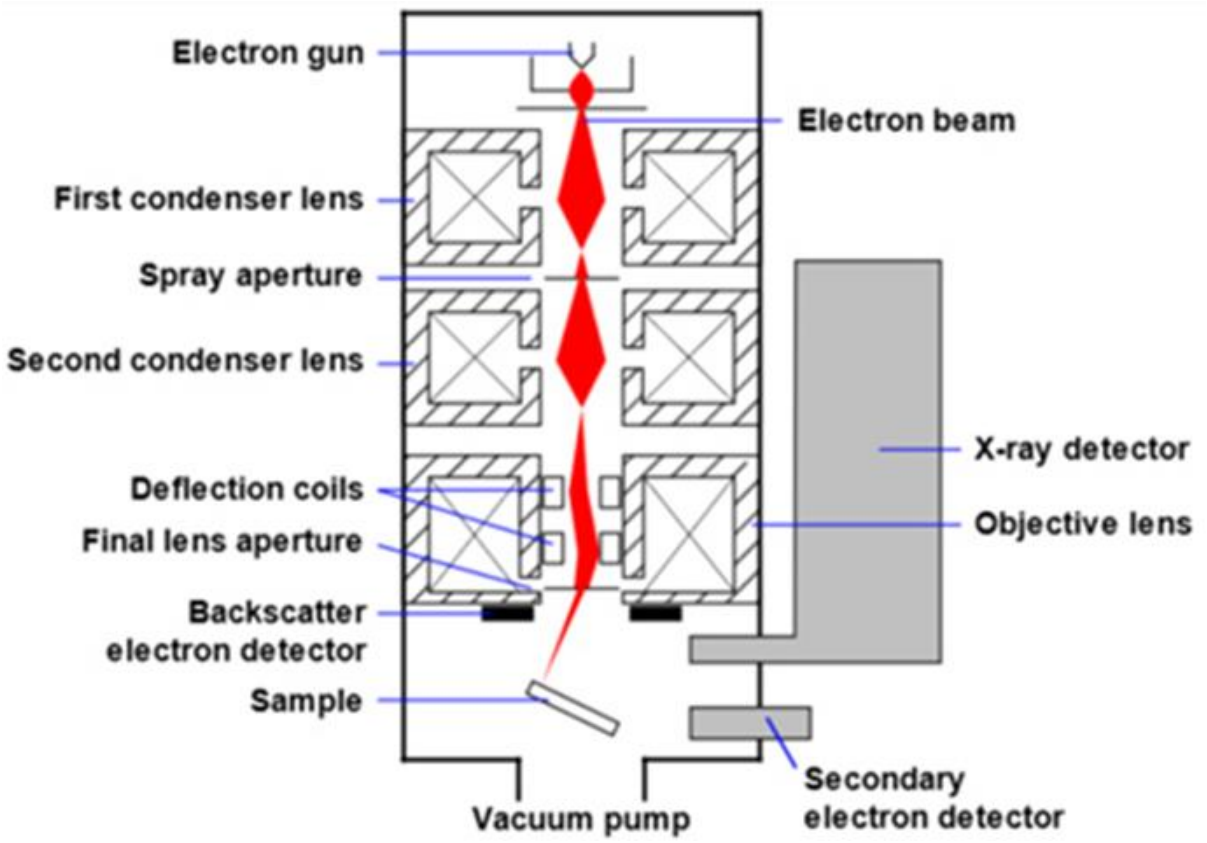

Figure 2.2 Schematic diagram of a scanning electron microscope
Open access https://www.nanoscience.com/techniques/scanning-electron-microscopy/

(The last date of access is May 29, 2022.)

2.3 Transmission electron microscopy

Transmission electron microscopy (TEM) is another powerful technique for imaging specimens. Electrons emitted from a thermionic or field-emission source are accelerated in the gun by a high voltage. The electron beam is formed with the assistance of condenser lenses, a condenser lens aperture, a condenser lens stigmator, and beam tilt and translating coils for alignment, and then it enters the objective lens and strikes the specimen in appropriate ways. After passing through the specimen, the electrons form an image through the action of the objective lens and an objective aperture in the back focal plane of the lens. [60] Finally, a highly magnified image can be obtained by tuning a series of intermediate units such as objective stigmator and projector lenses. Normally, several operating modes of TEM can be applied for imaging such as conventional imaging, scanning TEM imaging (STEM), and diffraction, here we only introduce two frequently-used basic modes: imaging and diffraction, as shown in **Figure 2.3**. In imaging mode, an objective aperture is inserted into a back focal plane of an objective lens, then the bright field and dark field images can be obtained if the central beam and diffracted beam are selected, respectively. While in diffraction mode, a selected area aperture is used to detect the observed specimen area, and the diffraction pattern can be acquired by changing the strength of the intermediate lens. Now, selected area electron diffraction (SAED) has been successfully used to determine crystal orientation, to measure lattice constants, or examine its defects.

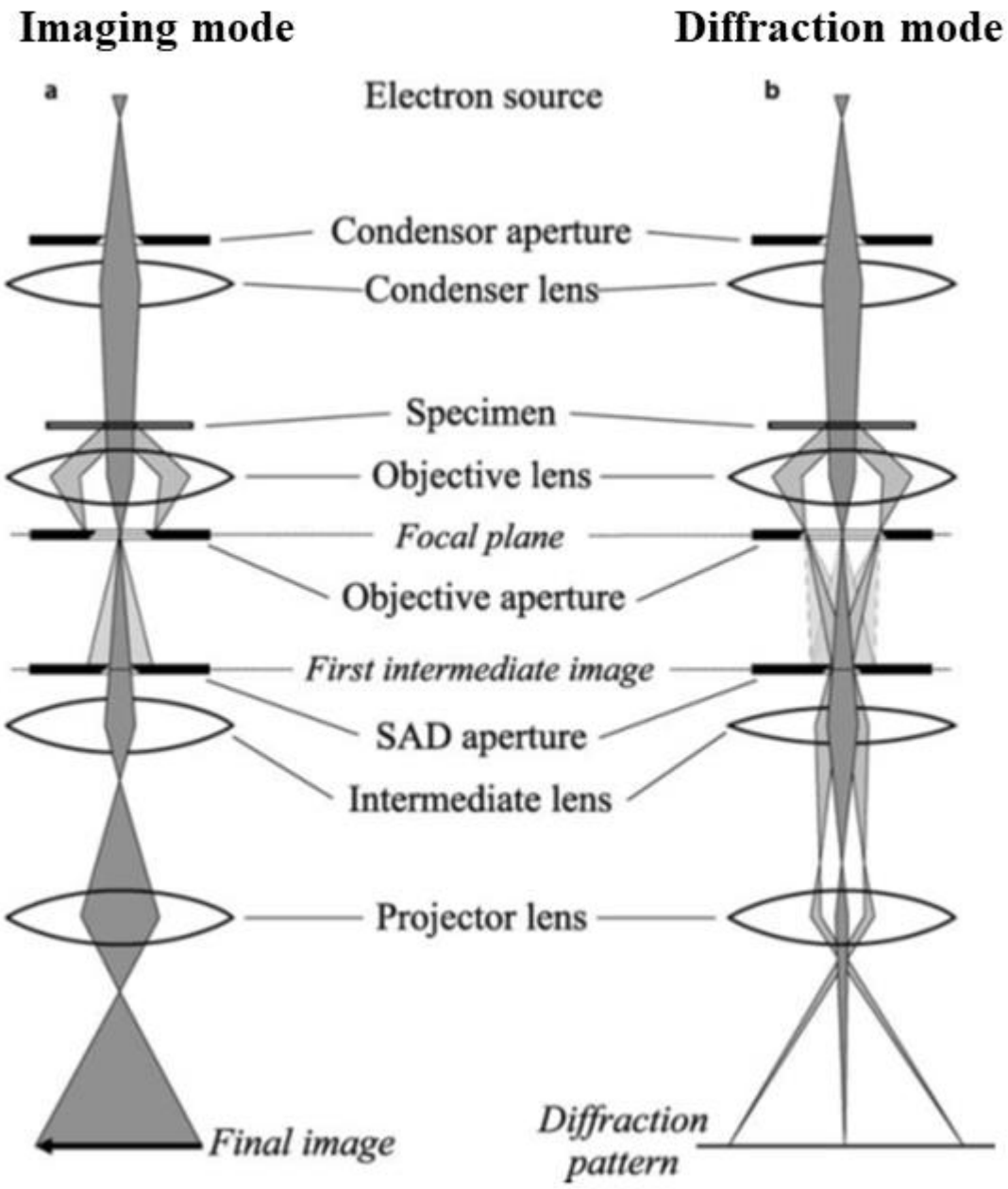

Figure 2.3 Schematic diagram of a transmission electron microscope [60]

2.4 X-ray powder diffraction

X-ray powder diffraction (XRD), as a non-destructive technique, has been widely utilized to attain precise information about the physicochemical attributes of materials such as amorphous/crystalline structures, crystalline lattice parameters, and crystallographic phase fractions. XRD is based on constructive interference of monochromatic X-rays in a crystalline sample. These X-rays are generated by a cathode ray tube, filtered to produce monochromatic radiation, collimated to concentrate, and directed toward the sample. The interaction between incident rays and sample will produce

constructive interference when conditions satisfy Bragg's Law ($n\lambda = 2d \sin\theta$), as shown in **Figure 2.4**, where d is the lattice spacing, θ is the diffraction angle, n is an integer and λ is wavelengths. The diffracted X-rays exhibit constructive interference when the distance between paths ABC and A'B'C' differs by an integer number of the wavelength (λ). This law relates the wavelength of X-rays to diffraction angle and the lattice spacing in a crystalline material. All possible diffraction directions of the lattices are supposed to be attained by scanning the sample through a range of 2θ angles. Modern X-ray diffractometers allow the samples to be measured in transmission, reflection, and Debye-Scherrer modes with the corresponding customized sample holder.

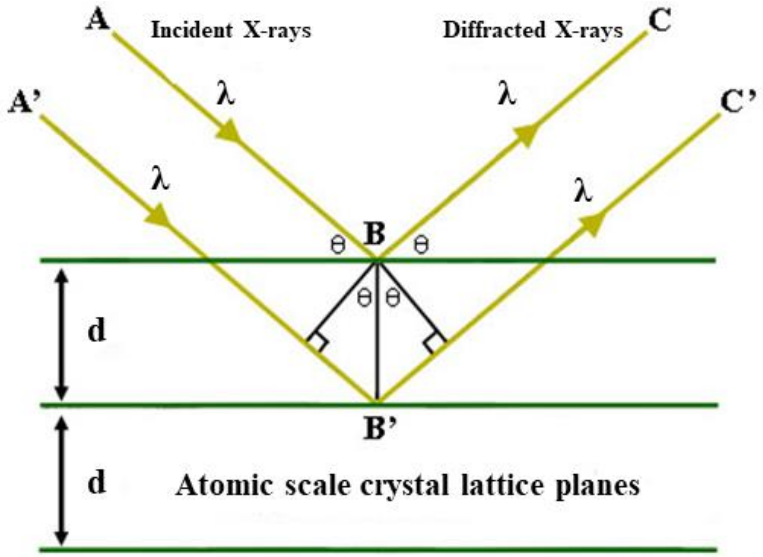

Figure 2.4 Schematic diagram of Bragg's Law reflection

2.5 X-ray photoelectron spectroscopy

X-ray photoelectron spectroscopy (XPS) is a non-destructive surface analytical technique, in which X-rays hit the surface of a material and the kinetic energy of the emitted electrons is measured. XPS is based on the photoelectric effect that is the electrons can be emitted from the surface of the specimen when irradiated with light. In a typical XPS measurement, the sample is irradiated by a beam of soft X-ray (energies lower than ~ 6 keV) with a constant frequency (fixed wavelength) and the kinetic energy of the emitted electrons is measured simultaneously. This process can be expressed mathematically in **equation 2.1**: $h\upsilon = BE + KE + \varphi$ (**equation 2.1**), where $h\upsilon$ is the energy of the exciting X-rays (h is Planck constant (6.62×10^{-34} J s) and υ (Hz) is the frequency of radiation), BE is the binding energy (BE) of the electron, KE is the kinetic energy (KE) of

the emitted electron, and φ is spectrometer work function (a constant value). [61] Normally, the oxidation state of an element is a general guide to determining BE, which is determined for photoelectron peaks. And the BE can be calculated by **equation 2.1**, where hυ and φ are known and KE can be measured in the XPS experiment. A schematic diagram of an XPS system is shown in **Figure 2.5**, which contains an X-ray source, sample holder, extraction lenses, analyzer, and detector housed in an ultra-high vacuum chamber. [62] The X-ray source of an XPS system can be various monochromatic elements such as Al (K_α) and Mg (K_α) or even a synchrotron light source. In theory, XPS can only analyze the elemental composition of a specimen surface around 0 ~ 10 nm in depth. Moreover, a deeper layer of the sample can be reached by using in-depth profiling with ion beam or cluster etching.

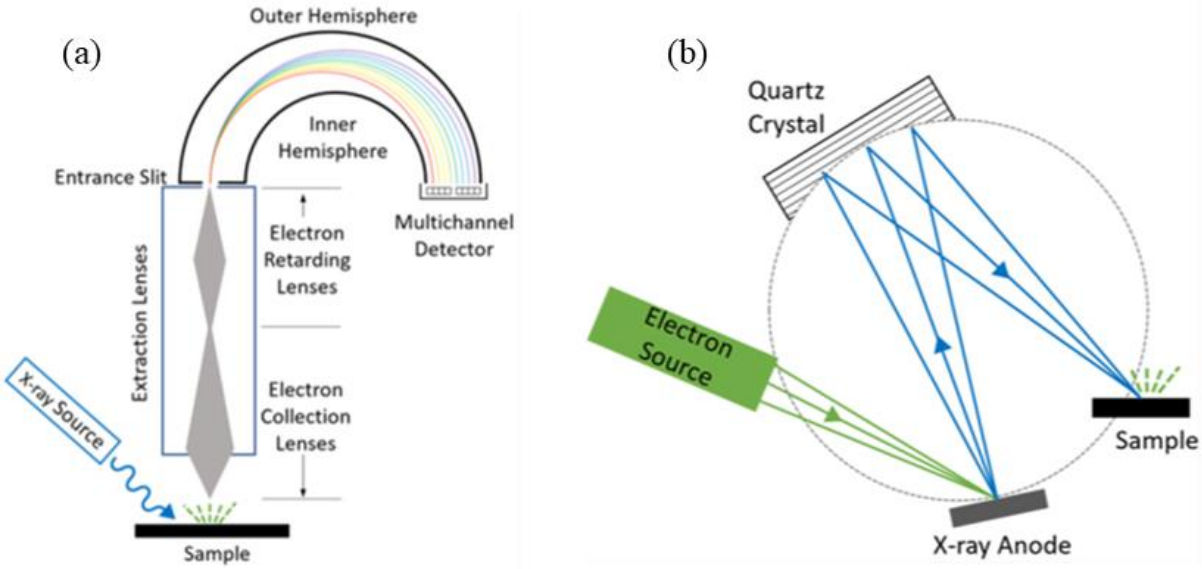

Figure 2.5 Schematic diagrams show the major components of an (a) XPS instrument and (b) monochromator. [62]

2.6 Raman spectroscopy

Raman spectroscopy is a form of molecular spectroscopy that involves the scattering of electromagnetic radiation by atoms or molecules, which has been developed as one of the non-destructive techniques to characterize the structure of various kinds of materials. It probes the vibrational, rotational, and other low-frequency modes of molecules, thereby providing a structural fingerprint for molecular identification. In a typical Raman measurement, when a laser beam with an energy and a frequency irradiates a substance, the reflected beam with the same frequency will be observed, namely, elastically scattered light, and

also some weak reflections of the light with slightly different frequencies, which are defined as inelastically scattered light. The Raman signal is observed by inelastically scattered light, which includes Stokes and Anti-Stokes scattering. The Raman Effect mainly depends on the electric dipole-electric dipole polarizability derivative of the chemical bonds. Consequently, the sample with neutral bonds (e.g. C-C and C=C) will show a strong Raman signal due to the significant changes in polarizability during a vibration, whereas the polar bonds only show a weak signal from the feeble effect on polarization

2.7 Theory of Brunauer-Emmett-Teller

The Brunauer-Emmett-Teller (BET) measurement is an effective method to characterize porous materials, measuring their specific surface area (SSA) and pore size distribution. The fundamental element of the BET theory is associated with the adsorption of a gas on the material's surface. The process of adsorption can be physical or chemical. Generally, the physical adsorption is related to van der Waals forces while chemical adsorption is a result of the chemical reaction between the solid and the adsorbate (gas). [63] Typically, N_2 gas is used for this purpose, and other gases, for instance, Ar or CO_2 can be also used. [64] The amount of the adsorbed gas on the adsorbent material can be correlated with its surface area. In BET theory, multilayer adsorption is assumed where all layers do not interact with each other, which is an ideal situation and highly close to the Langmuir theory. Based on this, the BET equation is defined as follows:

$$\frac{P/P_0}{\mathrm{n}(1-P/P_0)} = \frac{1}{n_m C} + \frac{(C-1)(P/P_0)}{n_m C} \qquad \textbf{(equation 2.2)}$$

where n is the specific amount of the adsorbed gas at the relative pressure P/P_0, n_m is the monolayer capacity of adsorbed gas, P and P_0 are the equilibrium and saturation pressure, respectively, and C is the BET constant which is exponentially related to the energy of monolayer adsorption. [63] **Figure 2.6** shows the six types of BET isotherms, type I isotherm is typical for microporous materials with different sizes; type II and type III correspond to materials that are nonporous or macroporous; type IV isotherm has two patterns which are common for mesoporous materials with different width of pores; the shape of type V isotherm is similar to the shape of type III at low P/P_0, which is attributed to the weak adsorbent-adsorbate interactions; type VI isotherm is common for multilayer adsorption of materials that have highly uniform nonporous surfaces. In many practical cases, materials can possess different

types of pores, thus showing isotherms as a combination of the above types. Furthermore, the BET specific area can be calculated from a BET plot $(P/P_0)/n(1- P/P_0)$ as a function of P/P_0.

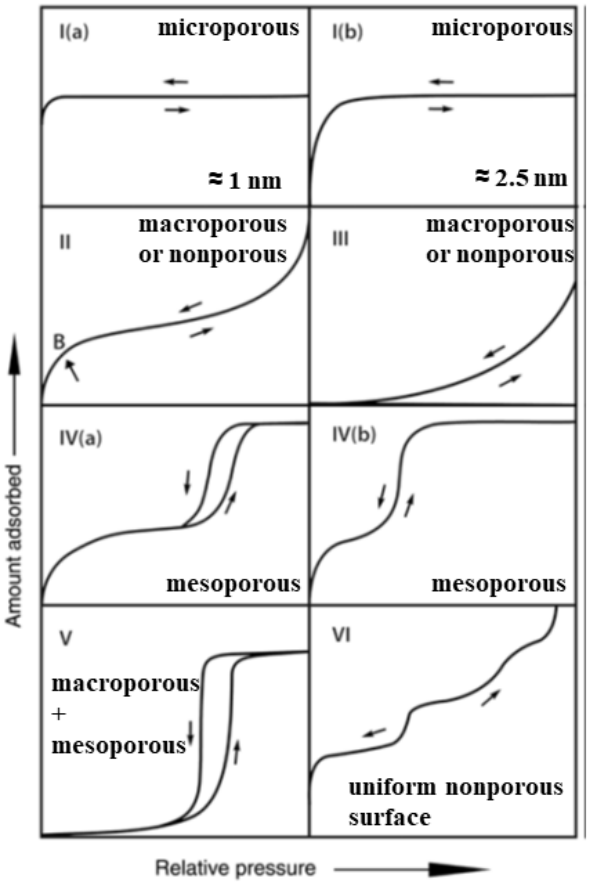

Figure 2.6 International Union of Pure and Applied Chemistry (IUPAC) classification of BET isotherms [65]

2.8 Cyclic voltammetry

Voltammetry is a technique for recording the electrical current flow of the working electrode by dynamically changing the potential. Cyclic voltammetry (CV) is a type of potentiodynamic electrochemical technique to investigate the initial electrochemical process of new systems and has been demonstrated to be a very useful tool to obtain information about fairly complicated electrode reactions. Compared to other measurements (e.g. linear sweep voltammetry (LSV)), CV is able to explore whether the chemical reaction of the reactants is reversible or irreversible and the potential at which an oxidation or reduction reaction occurs can be determined. In a typical CV experiment, the working electrode potential is ramped linearly versus time. The working electrode's potential can be ramped in the opposite direction to return to the initial potential after the set potential is reached. And these cycles of ramps in potential can be

repeated many times according to the measurement needs. As shown in **Figure 2.7**, the negative current curve is recorded when the applied potential decreases over sweep time, corresponding to a cathodic process or reduction reaction, while the positive current curve will be recorded when the potential increases that results from an anodic process (oxidation). In the CV measurements, the scan rate (υ) is the most important parameter. The voltage is swept from E1 to E2 and it represents the slope for a linear voltage change during the measurement. Therefore, additional information on the voltage, reversibility, and cyclability of redox reactions can be obtained by repeating several cycles. [66]

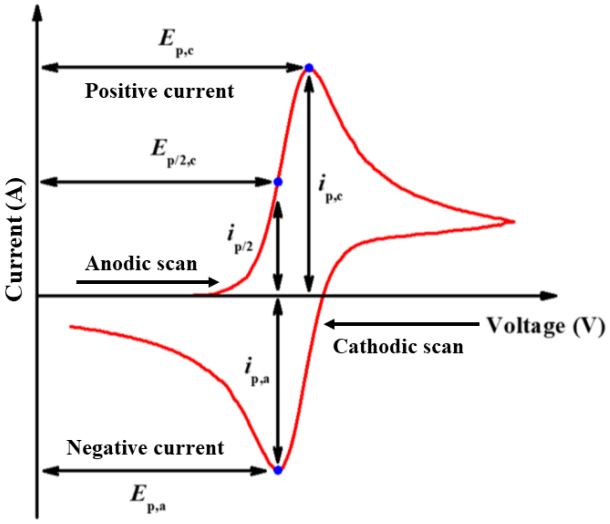

Figure 2.7 An example of reversible cyclic voltammetry [66]

2.9 Galvanostatic cycling with potential limitation

Normally, an assembled cell needs to be charged and discharged with a constant current or constant voltage. Currently, the constant current mode has been often applied for studying the electrochemical storage behavior of the electrode materials due to it helps eliminate imbalances of cells and batteries connected in series. Constant current charging includes single-rate and split-rate chargers, which can be applied according to the specific test requirements. In most lab cases, so-called Galvanostatic cycling with potential limitation (GCPL) is the most standard protocol for investigating the behavior of batteries being cycled, that is a battery is charged/discharged with a constant current density (e.g. mA g^{-1}) at a certain potential window, the current run direction will be changed once the potential reaches the upper or lower limitations. In this case, the electrochemical performance of a battery such as cyclic stability and rate capability can be determined at a given or continuously variable current density.

2.10 Electrochemical impedance spectroscopy

Electrochemical impedance spectroscopy (EIS) is a non-destructive technique to investigate the electrical and electrochemical properties of different systems or materials. Resistance (R) is the ratio of voltage or potential and current for a direct current (DC) system, while impedance Z is the ratio of that for an alternating current (AC) system. Impedance is the quotient of the voltage-time function V(t) and the resulting current-time function i(t), as expressed in **equation 2.3** :

$$Z = \frac{v(t)}{i(t)} = \frac{v_0 \sin(\omega t)}{i_0 \sin(\omega t + \theta)} \qquad \textbf{(equation 2.3)}$$

, where v_0 and i_0 are the maximum voltage and current signals, $\omega = 2\pi f$ is the angular frequency, and θ is the phase difference between the voltage and the current. [67] The impedance can be measured by introducing a signal of small AC of known frequency and small amplitude to a system, the signal of excitation can be either AC voltage or current, determining the amplitude and phase difference of the associated electrical potential that develops as a response. EIS gained a lot of attention for the investigation of LIBs in the last decade due to its capability to separate the influence of different processes, for instance, resistance contribution from the electron transfer process and double-layer capacitive process, and it is sensitive for investigating the interface between electrode and electrolyte. There are two ways to plot the EIS spectrum, namely the Bode plot and Nyquist plot, as shown in **Figure 2.8**. The Bode plot plots the logarithm of the absolute value of the impedance and phase shift *versus* log (frequency). The advantage of the Bode plot is that all information for frequency changes and phase angles is clearly visible. The Nyquist plot is consisting of imaginary impedance part (Y-axis) *versus* real part impedance (X-axis), which is quite popular in electrochemistry impedance due to its sensitivity to changes and some parameters of the most common circuits can be read directly. In these two plots, there is an overlap of different process responses that require careful analysis of the data. In this case, an equivalent electrical circuit is introduced to model the curve and each electrical element represents a part of the electrochemical system. The data fitting can be carried out with a suitable software and modelling the values for each circuit element (capacity (C), resistance (R), etc.), as shown in **Figure 2.8**, which brings the calculated spectrum as close as possible to the measured spectrum. In EIS experiment, several processes can occur simultaneously, thus the impedance contribution of a single element to the whole impedance needs to be identified. A variety of circuit elements are created, including resistors (electrolyte resistance, charge transfer resistance), capacitors (double layer capacity), constant phase element

(CPE), and Warburg impedance. The CPE is a non-intuitive circuit element that was discovered (or invented) while looking at the response of real systems. Since in real-world systems, the transfer functions obtained in EIS measurements do not follow strictly the theoretically expected patterns, instead they show definite distortions, typically in the form of depressed semicircles, which can be mathematically represented by the CPE. [68]

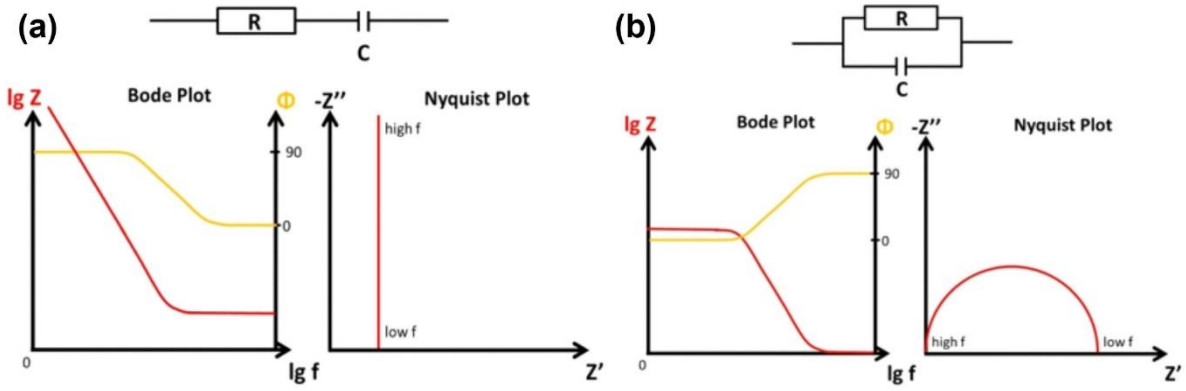

Figure 2.8 EIS of (a) a serial and (b) parallel resistor and capacitor in a schematic Bode and Nyquist plot, respectively.
Open access https://www.palmsens.com/knowledgebase-article/bode-and-nyquist-plot/

(The last date of access is May 29, 2022.)

3 Activation of 2D MoS_2 Electrodes Induced by High-rate Lithiation Processes

This chapter is partially based on the publication *Activation of 2D MoS_2 electrodes induced by high-rate lithiation processes*, submitted to *Journal of Energy Chemistry*.

3.1 Introduction

Transition metal dichalcogenides (TMDs) have attracted attention as promising anode materials. [69] TMDs are compounds with a generalized formula MX_2, where *M* is a metal atom from groups 4-10, i.e. M = Ti, V, Nb, Mo, W, and *X* is a chalcogenide atom *X* = S, Se, Te. [70] Each crystal layer of a TMD consists of hexagonally packed *M* atoms sandwiched in between two layers of *X* atoms. Interlayer *M-X* bonds are predominantly covalent, whereas crystal layers are held together by van der Waals forces. [70] Due to their layered structure, TMDs are excellent hosts for ion intercalation. Particularly, MoS_2 has been intensively investigated as an anode for LIBs. [69] In single-layered MoS_2 nanosheets, the Mo^{4+} and S^{2-} are arranged in S-Mo-S orientation, and 6 S atoms surround 1 Mo atom. MoS_2 generally exists in two structural phases: either trigonal prismatic (2H/3R) or octahedral (1T), which depends on the stacking sequence of the layers in MoS_2 with respect to the Mo coordination. [71] MoS_2 exists naturally as the 2H polymorph (a unit cell constituted by two layers where atoms have trigonal prismatic coordination). [72] Synthetically produced MoS_2 commonly shows a 3R structure, where it has a rhombohedral symmetry with three layers per unit cell, but is highly unstable. [73] The 1T MoS_2 polymorph (a unit cell constituted by one layer where atoms have octahedral coordination) is metastable and can be induced i.e. by Li-ion intercalation. [72] 2H MoS_2 is active in a 3-0.01 V *vs* Li^+/Li electrochemical window, where energy storage takes place via ion intercalation and conversion processes delivering a joint theoretical capacity of 669 mAh g^{-1}. [69] However, in some case, a higher capacity is realised, for instance, the capacity of nanoscale MoS_2 can reach to 1200-1300 mAh g^{-1}due to its nanostructures with high specific area. [69] This capacity is 3 times the capacity of graphite. Additional advantages of MoS_2 over other emergent anodes such as Si and Ge include a superior electrochemical performance at higher rates and structural stability to volume expansion. Due to its layered nature, MoS_2 can be cleaved into its constituent layers. Numerous synthesis methods have been developed to deliver nanostructured single to few-layers MoS_2. [74] Particularly, liquid-phase

exfoliation (LPE) is a rapid and scalable method that can deliver few-layers 2D nanomaterials, including high quality few-layers 2D MoS_2. [75] Nanostructured few-layers 2D MoS_2 brings in play additional energy storage mechanisms that take advantage of high surface areas including capacitive and pseudo-capacitive processes. [76] Spray-deposition, on the other hand, is an electrode manufacturing technology with enormous adaptability in terms of developing additive-free electrodes of controllable thickness. in the nanometre to the micrometre scale, large areas, in the m^2 scale, and controlled architecture, including a layer-by-layer (LBL) design. [77] Spray-deposition has been used to manufacture electrodes of a variety of nanostructured materials including various 2D nanomaterials. [57, 78-80] LPE and spray-deposition methods are highly compatible and together offer scope for scalability and high throughput of electrode manufacturing methods. Moreover, LBL architectures of 2D nanomaterials enable nanochannels in between 2D nanomaterials that shorten ion transport paths leading to a faster reaction kinetics and, thus, an enhanced power performance. [76, 81] Herein, 2D MoS_2 electrodes were produced, consisting of few layers 2H MoS_2 and with a LBL architecture, using a combination of LPE synthesis methods and spray-deposition.

Despite considerable advances in the field, the realisation of the promising potential of 2H-MoS_2 as a LIB anode is currently hindered by several performance issues, including unsatisfied cycling stability, and a lack of fundamental understanding of energy storage processes. To date, a full picture of the underlying energy storage mechanisms of MoS_2 anodes in the context of LIBs is not yet established. It is generally accepted that ion-intercalation and conversion processes take place during the first discharge (lithiation process). However, a ongoing debate is whether the conversion process is reversible upon the following charge, or, alternatively, if oxidation/reduction processes involving Li_2S/S take place. [69] The case is further complicated by secondary reactions linked to the formation of a solid electrolyte interface (SEI) occurring at 0.6 V, a potential at which the conversion process also occurs. [69] Moreover, irreversible surface-based processes, such as SEI formation are typically enhanced in nanostructured materials, as compared to their microsized counterparts.

Herein, energy storage mechanisms of 2D MoS_2 electrodes were investigated using a combination of electrochemical methods and *ex-situ* Raman spectroscopy. The reversibility of the conversion processes was confirmed where nanostructuring was found to play a key role. Remarkably, 2D MoS_2 electrodes showed an unusual energy storage performance that dynamically evolved over cycling. Capacity vs cycle curves went through a fall-increase-

fall-continuous increase trend. This intriguing behavior was investigated by a combination of electrochemical and microscopy methods. The study revealed that the underlying phenomena are physical activation processes induced by cycling and where the 2D nature of the pristine materials played a key role. The activation processes induced drastic electrode architecture changes and gave origin to a dynamic evolution of energy storage processes in place. Indeed, the energy storage processes of 2D MoS_2 electrodes dynamically evolved from pure ion intercalation and conversion processes to pseudo-capacitive and capacitive processes. Activation processes were current rate-dependent and took place only at high current rates above a given threshold. Importantly, activated electrodes held capacity retention of 71% (388 mAh g^{-1}) from the initial capacity and, unlike pristine electrodes, the capacity was stable for up to 1000 cycles. Their current rate performance was also superior to pristine electrodes. Therefore, the study have devised a methodology based on physical activation processes that can largely overcome problems of cycling stability of intercalation/conversion electrodes and that can be applied to improve the performance of other 2D nanomaterials-based electrodes. Moreover, this methodology could be further exploited to develop electrodes of even higher capacities by combining 2D nanomaterials of different chemistries.

3.2 Experimental methods

3.2.1 Materials

Molybdenum disulfide powder, (MoS_2, 99%, Sigma Aldrich), anhydrous 1-methyl-2-pyrrolidinone (NMP, >99%, Sigma Aldrich), 2-propanol (IPA, 99%, Sigma Aldrich), branched polyethyleneimine (PEI), (M.W. 70,000, 30% w/v, aqueous solution, Alfa Aesar), lithium sulphide powder (Li_2S, 99.8%, BASF) and S powder (S, 99.5%, BASF), sodium carboxymethyl cellulose sodium salt (NaCMC, M.W. ~9,000, Sigma Aldrich).

3.2.2 Equipment

Ultrasonication of suspensions was performed using an ultrasonication bath (*Elmasonic P120H*, 330 W effective power) and an ultrasonic probe processor (*Fisherbrand ultrasonic* Q500, 500 W). Suspensions were cooled down using a refrigerated circulation thermostat (*CORIO CD-600F, Julabo*, USA). Centrifugation was performed using a centrifuge (*Thermo Scientific Heraeus Multifuge X1R*) equipped with a TX-400 rotor (16.8 cm radius) and a

FIBERLite F15-8x 50cy rotor (10.4 cm radius). The concentration of suspensions was determined using a UV-Vis-IR spectrometer (*Cary 5000, Agilent Technologies*). The mass of the electrodes was measured using a microbalance (*Sartorius*, Germany) with a ± 0.0001 mg accuracy. Electrochemical measurements were performed in a VMP3 (*Bio-Logic*, France) potentiostat.

Spray-deposition was carried out using a Flexi-coat spray-deposition coater (Sono-tek Corporation, USA) equipped with two AccuMist ultrasonic nozzles (48 kHz), two ultrasonic syringes (25 ml, 0.01 to 5 ml min^{-1} flow rate range), each integrating an ECHO ultrasonic generator (3.5 W power) and an ultrasonic resonating plunger, a Teflon coated hot/vacuum plate (50 cm x 50 cm area, 4 vacuum zones, and capable to reach temperatures up to 150 °C). The ultrasonic nozzles are mounted on a three-axis coordinated motion system using servomotors that can be controlled manually (by a trackball) or by a provided software (*PathMaster*). Most key functions of the equipment are controlled via the software PathMaster, including the control of the hot plate (vacuum zones), devices (nozzles, valves, and servomotors), spraying, and purging (in manual mode). Spray deposition patterns can be pre-defined, executed, and automated using the PathMaster software.

3.2.3 Synthesis of 2D MoS_2

Few layers 2D MoS_2 was synthesized by established LPE methods [82-85] with key modifications. Typically, 1.0 g of MoS_2 was processed in 120 ml of anhydrous NMP, placed in a glass jacketed beaker (250 ml) (**Scheme 3.1a-b**). Ultrasonication was performed using an ultrasonic probe processor operated at 60% amplitude, using a pulse mode set for 6 s on and 2 s off, for 8 h. During sonication the mix was cooled down by continuously recirculating cold water (18°C) through the jacketed beaker. The water was recirculated using a refrigerated circulation thermostat. Subsequently, a series of centrifugation steps allowed for the separation and selection of few-layers 2H MoS_2 nanosheets, so-called liquid cascade centrifugation (LCC) method (**Scheme 3.1c**). The mix was centrifuged first at 2800 rpm (1475 g) obtaining supernatant 1, which was then centrifuged at 3800 rpm (2717 g) to obtain the supernatant 2. Subsequently, a solvent exchange of NMP for IPA was carried out using centrifugation - IPA was preferred over NMP due to its lower boiling point and non-toxicity, required for further processing using spray-deposition (**Scheme 3.1d**). The final product consisted of few-layers 2D MoS_2 in IPA of typically a 0.1-0.2 mg ml^{-1}

concentration. 2D MoS_2/IPA suspensions were then processed by spray-deposition (**Scheme 3.1e**).

3.2.4 Measurement of concentrations of suspensions

The concentration of suspensions was determined using UV-Vis spectroscopy. The method has been fully described in previous works. [79] In brief, the active material of a known volume of a suspension of 2D MoS_2 was collected by centrifuge-assisted separation, dried, and weighed up. The concentration was then determined by adding a given volume of IPA. A second volume of the very same suspension was diluted down to prepare aliquots of 0.01 to 0.1 mg ml^{-1} concentration. The absorption of these aliquots was measured using UV-Vis spectroscopy in a 200 to 1000 nm wavelength range (**Figure 3.1a**). This included the measurement of the solvent (IPA) as a blank. According to the Beer-Lambert law, $A/l = \alpha C$, where A is absorbance, l is the light path length (1 cm), α is the extinction coefficient and C is the dispersion concentration), a plot of A/l versus C is a line with slope α. Accordingly, A/l values, at a λ = 672 nm, were plotted versus concentration, and a linear fit led to the determination of the extinction coefficient as α = 10.58 cm^2 mg^{-1} (**Figure 3.1b**). The concentration of any suspension was then determined using the Beer-Lambert law and this extinction coefficient.

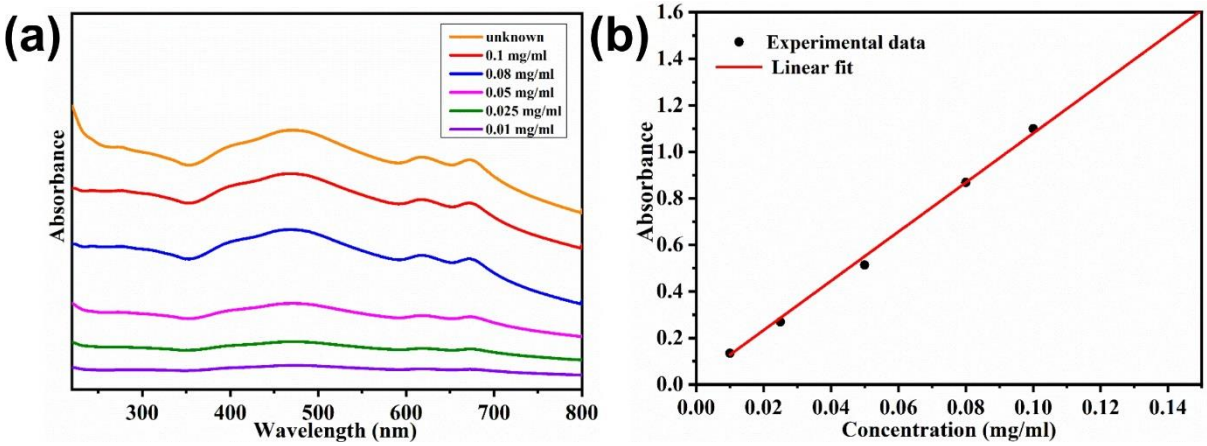

Figure 3.1 (a) UV-Vis spectra of a series of aliquot suspensions of 2D MoS_2 nanosheets in IPA, (b) UV-Vis absorbance *vs* given concentration of 2D MoS_2 curve by linear fitting with a slope of 10.579.

3.2.5 Electrode manufacture

2D MoS_2 electrodes were manufactured using a scalable spray deposition method (**Scheme 3.1e)**. In general, suspensions were syringe-pumped to the ultrasonic nozzles that produced a mist. The mist was deposited onto Cu foil

substrates (6 cm x 6 cm area, and thickness of 10 μm), which were set onto a hot/vacuum plate stage heated at 40 °C. The spray deposition process was automatically controlled using a user predefined program. Accordingly, a spray deposition area was defined by 3 coordinates. A spray deposition pattern was developed by continuously spray-depositing material over lines spaced by 2 mm. An aqueous suspension (A) consisted of PEI (0.05 mg ml^{-1}). A suspension (B) consisted of the active material 2H MoS_2 nanosheets/IPA. Suspensions A and B were spray-deposited in a LBL fashion. Subsequently, the film electrodes were dried in a Buchi-glass drying oven at 70 °C, in vacuum, and cut into 12 mm disks. The average mass load and thickness of the disc electrodes were ~ 0.3-0.5 mg cm^{-2} and ~ 3 μm, respectively. The PEI content of the electrode was around 2 wt. %. Electrodes comprised of commercially available microsized MoS_2 named in the text raw MoS_2 electrodes-were manufactured following conventional mixing methods. The MoS_2 powder was mixed with carbon black, and NaCMC (binder) in a weight ratio of 8:1:1. The mixture was dispersed in water (500 μl) and stirred overnight. Subsequently, the mixture was coated onto a Cu foil (thickness = 10 μm) using a coating bridge. The electrodes were dried at 80 °C in a vacuum oven for 12 h and cut into 12 mm disks. The average mass loading of the active material and thickness of the disc electrodes were 0.64 mg cm^{-2} and ~ 15 μm, respectively.

3.2.6 Materials characterization techniques

Scanning electron microscopy (SEM) was performed in a *Zeiss Supra 55* (Germany) microscope. Standard and high-resolution transmission electron microscopy (TEM and HRTEM) were performed using a *Themis-Z* (*FEI, USA*). Samples were prepared by dropping suspensions onto standard holey carbon copper grids. X-ray diffraction (XRD) was performed on an *STOE STADI P* diffractometer with Cu $K_{\alpha 1}$ radiation (λ = 1.54060 Å) in transmission mode and at room temperature. Samples were analyzed as a powder (raw MoS_2) or as a spray-deposited film (2D MoS_2) onto cellulose acetate (CA) and covered with another CA film. Raman spectroscopy was performed on a *LabRam Evolution HR800* (*Horiba Scientific*) using an excitation HeNe-laser (λ = 532 nm). Measurements were carried out using a backscattering geometry. The nominal excitation power at the sample was 39 mW, which was attenuated using a 1 % filter. The excitation light was focused and collected using an x100 objective lens, resulting in a spot size of ~5 μm. The scattered light was dispersed using a 600 grooves/mm grating resulting in a 1 cm^{-1} resolution. Samples were measured as a powder onto a Si wafer (raw MoS_2) or as dropped flakes onto a glass slide (2D MoS_2/IPA suspension). For measurements of pristine and charged/discharged electrodes, inside a glove box, the electrodes were carefully

taken out from coin cells, rinsed with DMC (x3 times), and dried at room temperature for 2 hours. Subsequently, the electrodes were sealed in between two pieces of film, Kapton at the bottom (current collector side) and a CA film at the top (active material side).

3.2.7 Electrochemical methods

Two-electrode cells were assembled using either 2D MoS_2 or raw MoS_2 as working electrode and Li foil as a counter electrode, both separated by a *Celgard* 2500 membrane, previously immersed in 70 µl of 1 M $LiPF_6$/ethylene carbonate/dimethyl carbonated (EC/DMC in a 1:1 V/V ratio). Assembly of cells was carried out in an Ar-filled glovebox (*MBraun*, Germany) with oxygen and water concentrations kept both below 0.1 ppm. Electrochemical tests were performed in a temperature-controlled environment at 25 °C.

Cyclic voltammetry (CV) and galvanostatic cycling with potential limitation (GCPL) were performed in a potential range of 3-0.01 V *vs.* Li^+/Li (here after, all potentials are with respect to Li^+/Li) at various scan rates and current densities, respectively. CV for *ex-situ* Raman measurements were performed from open circuit potential (OCP) down to the desired potential of lithiation or delithiation, the electrode was then left at rest for 3 h. Subsequently, the electrode was taken out from the coin cell and prepared for Raman measurements, as described in the Raman experimental section. The Coulombic efficiency (CE) was calculated as the ratio of charge capacity (ions output) to discharge capacity (ions input). [11]

Electrochemical impedance spectroscopy (EIS) was performed in three-electrode cells using 2D MoS_2 as a working electrode, a Li foil as a counter electrode, and a Li wire as a reference electrode. Measurements were performed applying an input alternate voltage V_{rms} = 5 mV and in a frequency range from 0.01 Hz to 500 kHz. All cells were discharged to 0.01 V first, then charged to 3.0 V, and then left at rest for 3 h before each EIS measurement. The EIS data were analyzed using the Relaxis (*rhd Instruments*, Germany) software.

3.3 Results and discussion

2D MoS_2 was synthesized using LPE methods, as described in detail in the experimental section (**Scheme 3.1**).

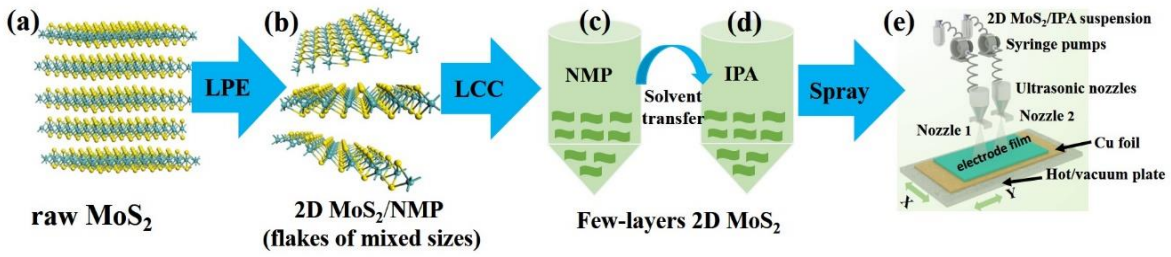

Scheme3.1 Synthesis and processing to produce 2D MoS_2. (a) Raw MoS_2 is processed by LPE methods to render (b) 2H MoS_2 of various flake sizes in an NMP suspension; (c) The 2D MoS_2 suspensions is purified by LCC into few layers 2D MoS_2; (d) few layers 2D MoS_2 in NMP is transferred into IPA; (e) 2D MoS_2/IPA suspensions are processed by spray-deposition to manufacture electrodes. Suspensions of active material are fed into ultrasonic nozzles via software-controlled ultrasonic pumps. The ultrasonic nozzles, moved in *x* and *y* directions by a software-controlled gantry, produce a mist that is deposited onto Cu substrates. The carrier liquid is evaporated by heat provided by a hot/vacuum plate.

The 2D MoS_2/IPA suspensions (**Figure 3.2a**) consisted of flakes of various shapes, e.g. elongated, triangular, and the flake lateral size ranged from 100-200 nm (**Figure 3.2b**). The high structural quality of the 2D MoS_2 flakes, free of defects on the basal planes was confirmed by high-resolution TEM (**Figure 3.3c**). Selected area electrode diffraction patterns (SAED) confirmed a hexagonal crystal structure typical of the 2H MoS_2 phase (**Figure 3.3d**). Bragg reflections, in agreement with the XRD analysis below, could be indexed with the hexagonal phase 2H MoS_2 ($P6_3/mmc$ (No. 194) space group, ICDD 00-002-1133).

The number of layers of the flakes was investigated by Raman. Previous studies have shown that shifts in the frequency of characteristic Raman modes of the 2H MoS_2 phase, E^1_{2g} and A_{1g}, are correlated to the number of flake layers. [86] The E^1_{2g} mode, due to in-plane S atom vibrations around Mo atoms in opposite directions, shifts to higher frequencies as the number of layers decreases from bulk to monolayer. [86] Whereas, the A_{1g} mode, due to out-of-plane vibrations of S atoms in opposite directions, shifts to lower frequencies as the number of flake layers decreases. [86] Raman studies of raw MoS_2 powder showed E^1_{2g} and A_{1g} modes at 383.5 and 408.4 cm^{-1}, respectively. Raman studies of various flakes of 2D MoS_2, directly dropped from a NMP suspension onto a glass slide, showed Raman shifts of e.g. E^1_{2g} and A_{1g} modes at 383.5 cm^{-1} and 406.6 cm^{-1}, respectively (**Figure 3.2e**). According to previous studies, this flake consisted of 4 layers. [86] At least 10 flakes were measured and the number of layers varied from 3 to 4. [87]

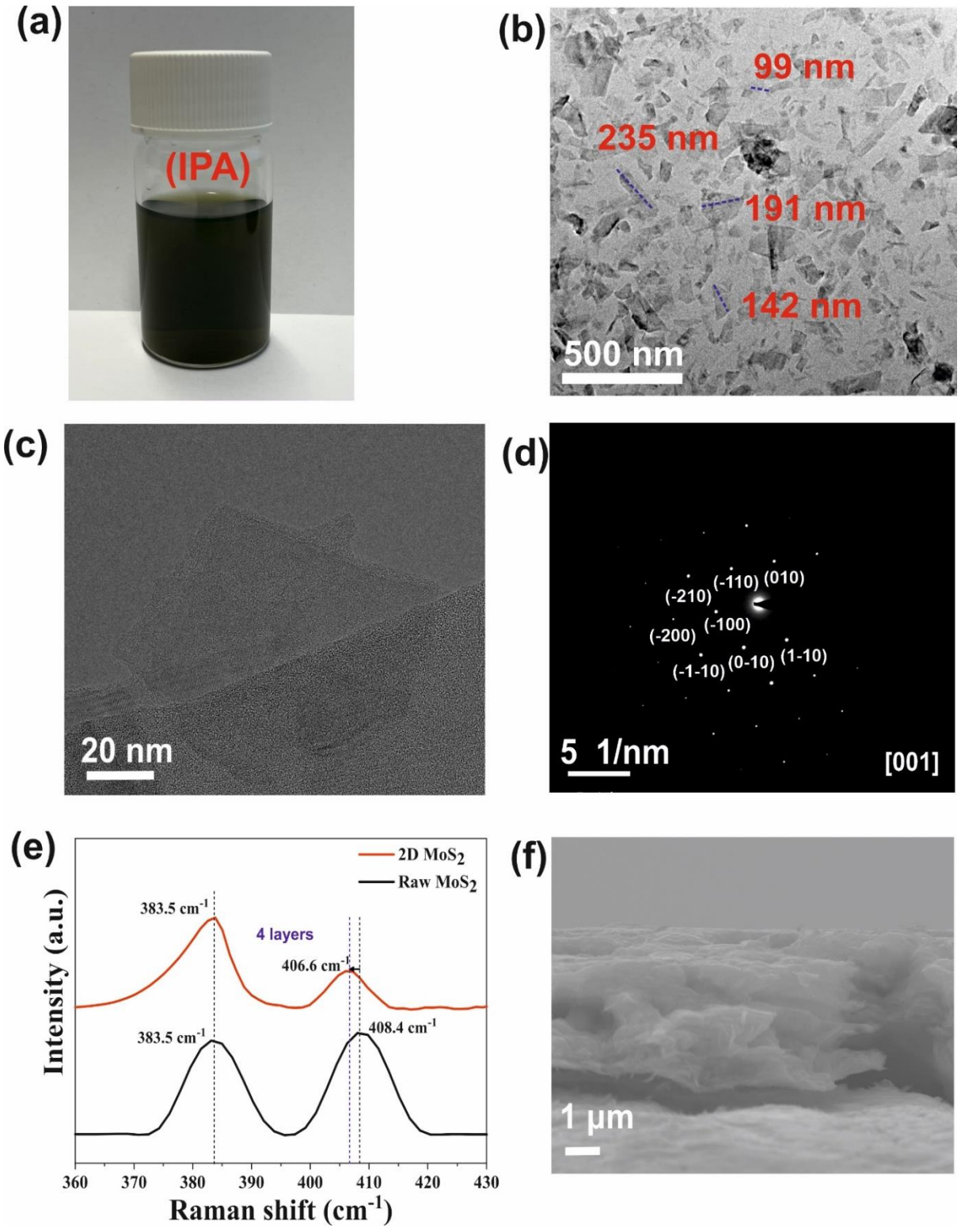

Figure 3.2 (a) Optical image of a 2D MoS_2/IPA suspension, (b) TEM image of 2D MoS_2 flakes, (c) HRTEM image of a few-layers 2D MoS_2 flake, (d) SAED pattern, (e) Raman spectra of raw MoS_2 powder and a 2D MoS_2 flake, (f) SEM image of a spray-deposited 2D MoS_2 film onto a Cu foil. The cross-section shows a LBL arrangement and a thickness of 2.5 µm.

Spray-deposited electrodes from 2D MoS_2/ IPA suspensions had a LBL stacking and thickness could be tuned from the nanometre to micrometre scale. Here, a film of 2.5 μm is shown (**Figure 3.2f**). At basal planes, a microporosity and mesoporosity, further discussed below, developed upon spray deposition. Raw MoS_2 powder, used as a precursor of the 2D MoS_2, consisted of flakes of 1-10 μm size (**Figure 3.9a**).

Rietveld refinement of the crystal structural parameters of the raw MoS_2 powder allowed the identification of the hexagonal structure of 2H MoS_2 ($P6_3/mmc$ space group, ICDD 00-002-1133), with $a = b = 3.1596$ Å, $c = 12.2962$ Å, and $R_{wp} = 9.9\%$ (**Figure 3.3a**).

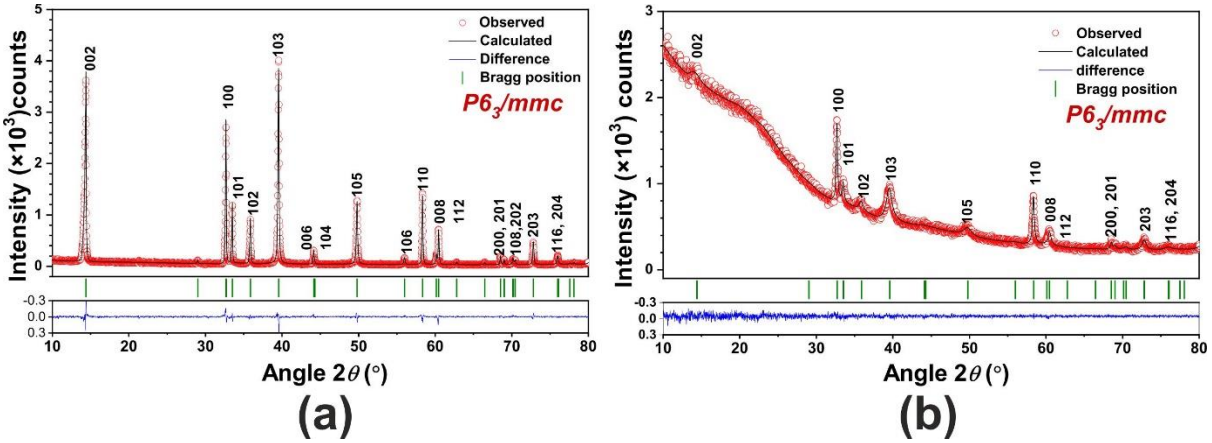

Figure 3.3 X-ray diffractograms and corresponding calculated curves from Rietveld refinements, based on data of (a) raw MoS_2 powder and (b) a spray-deposited 2D MoS_2 film onto cellulose acetate (CA).

Rietveld refinement of spray-deposited 2D MoS_2 films allowed the identification of the hexagonal structure of 2H MoS_2 ($P6_3/mmc$ space group, ICDD 00-002-1133), with a = $b = 3.1613$ Å and $c = 12.326$ Å, and $R_{wp} = 2.9\%$ (**Figure 3.3b**).

The diffractogram shows considerable diffuse intensities at scattering angles $2\theta < 30^{o}$. This is mainly due to a contribution of the CA substrate where the 2D MoS_2 film was spray-deposited (**Figure 3.3b**). However, there is a small contribution of non-Bragg *Debye* scattering at 2θ angles around the 002 reflection, which is known to be due to several factors including the finite size of crystallites, i.e. only a few stacking layers, [88] and to a contribution of rotationally disordered unstacked single-layers. [89] In the case of our sample, the former was more likely to play a role due to a successful exfoliation into a few layers of 2D MoS_2. Surely, a disordered stacking of the flakes was induced by spray deposition, thus, leading to a degree of diffuse scattering. However, the

presence of single-layered MoS_2 is not likely as per the presence of reflections 103 and 105 that describe a lattice of at least 2 stacked layers.

The broadening of most reflections was attributed to the few stacking layers of the successfully exfoliated 2D MoS_2, as described by the Debye-Scherrer equation. [88-89] No asymmetry or a drastic flattening of reflections was observed, which indicates the absence of translational or rotational defects. [88] Likewise, the 002 reflection shows no 2θ shift with respect to the bulk precursor, which indicates an unaltered interlayer distance. [88]

In summary, XRD, Raman, and microscopy studies confirmed the successful exfoliation of bulk MoS_2 into a few layers of 2D MoS_2 with good crystallinity and absence of defects.

3.3.1 Electrochemical mechanisms

The lithiation-delithiation mechanisms of MoS_2 have been a focus of interest since the 1980's and since then several points of controversy remain. Two main alternative electrochemical paths have been suggested.

During the first discharge, 2H MoS_2 lithiated according to **equation 3.1**, which occurs at ~ 1.1 V and involves a phase change from 2H to 1T polytype as shown in **equation 3.1**. [90-93] Then, a conversion reaction has been proposed to occur at ~0.4 - 0.6 V (**equation 3.2**), [94-95] which is accompanied by electrolyte decomposition. Subsequently, upon full charge, *Route 1* proposes the reversible oxidation back to MoS_2 (**equation 3.3**). It has also been proposed that a de-lithiation of non-reacted Li_xMoS_2 also occurs at ~1.7 V (**equation 3.3b**).

The alternative *Route 2* proposes lithiation (**equation 3.1**), followed by the irreversible conversion (**equation 3.2**) during discharge, then followed by oxidation of Li_2S to sulfur S_8, similar to processes occurring in sulfur batteries, [73, 96] (**equation 3.4**).

Route 1

Reduction

$$2H\ MoS_2 + xLi^+ + xe^- \rightleftharpoons 1T\ Li_xMoS_2 \quad (0< x<1, \sim 1.1\ V) \qquad \textbf{(equation 3.1)}$$

$$1T\ Li_xMoS_2 + (4 - x)Li^+ + (4 - x)e^- \rightleftharpoons Mo + 2Li_2S \quad (\sim 0.4 - 0.6\ V) \qquad \textbf{(equation 3.2)}$$

Oxidation

$Mo + 2Li_2S \rightleftharpoons 1T\ Li_xMoS_2 + (4 - x)Li^+ + (4 - x)e^-$ (**equation 3.3a**)

$1T\ Li_xMoS_2 \rightleftharpoons 2H\ MoS_2 + xLi^+ + xe^-$ (~1.7 V) (**equation 3.3b**)

$Mo + 2Li_2S \rightleftharpoons 2H\ MoS_2 + 4Li^+ + 4e^-$ (~2.4 V) (**equation 3**)

Route 2

Equations 3.1 and **3.2** followed by

Oxidation

$Li_2S \rightleftharpoons S + 2Li^+ + 2e^-$ (~2.4 V) (**equation 3.4**)

Here, energy storage mechanisms of the exfoliated 2D MoS_2 were investigated using electrochemical methods and *ex-situ* Raman. CVs were performed in a 3-0.01 V electrochemical window at a scan rate of 0.01 mV s^{-1}. During the first cycle, typical cathodic and anodic peaks were found in agreement with previous reports in the literature (**Figure 3.4a**).

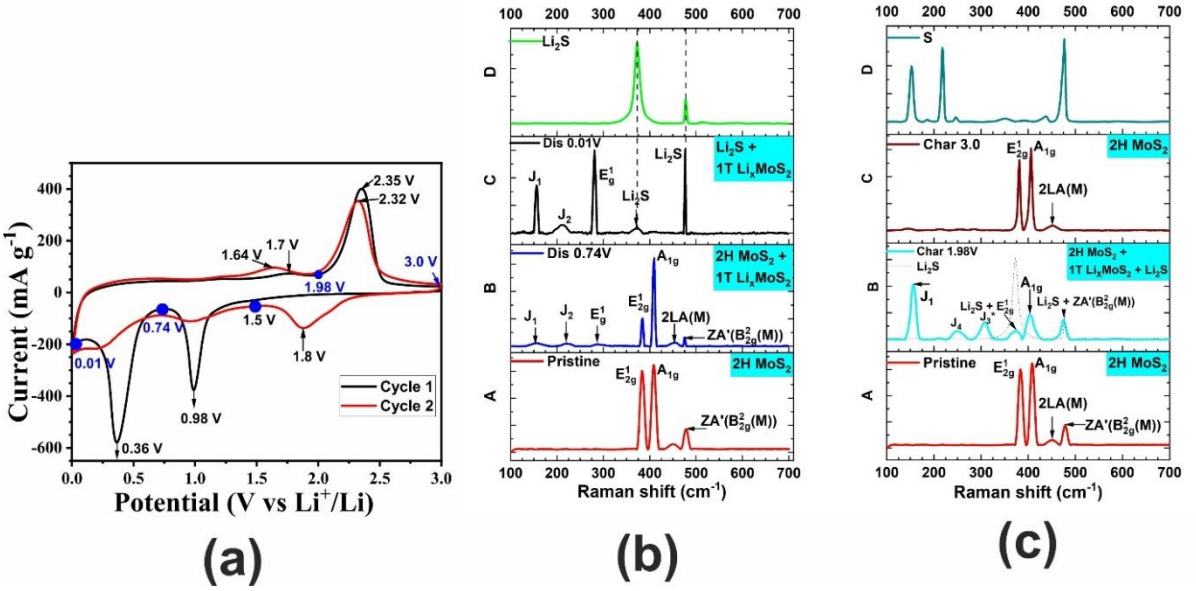

Figure 3.4 (a) CV of a 2D MoS_2 electrode at a scan rate of 0.1 mV s^{-1}. Potentials of current peaks are indicated in black font. Points of polarization are marked with a blue dot and/or blue font. *Ex-situ* Raman spectra at various potentials of polarization upon (b) discharge, and (c) charge of the first cycle. The spectra of the pristine electrode (without polarization) is shown in panels A for reference. In the same manner, Li_2S powder (panel D in (b)) and sulfur powder (panel (D) in (c)) were used as references.

Then, various electrodes were polarized running CVs from open circuit potentials down to key selected potentials (blue dots in **Figure 3.4a**): 0.74 V and 0.01 V during the first discharge (lithiation), and at 1.98 V and 3.0 V during the first charge (de-lithiation) after the first charge. Electrodes were held at

these potentials for 3 h and, as described in the experimental section, prepared for Raman studies. The pristine, 2D MoS_2 electrode films (**Figure 3.4b,** panel **A**), showed the typical A_{1g} (out-plane vibration) and E^1_{2g} (in-plane vibration) Raman modes of 2H MoS_2 at 408.6 cm^{-1} and 383.6 cm^{-1}, respectively. [97-98] In addition, the Raman mode at 450.7 cm^{-1} has been attributed to a combination of a second order longitudinal acoustic phonon 2LA(M) at the edge of the Brillouin zone and a first order optical phonon A_{2u} (Γ) [86, 99] The broadening observed in this mode is characteristic of nanosized materials due to phonon confinement. [99] The mode at 478.2 cm^{-1} has been discussed in the literature and assigned to a second order quasi-acoustic optical phonon ZA'(B^2_{2g}(M)). [97]

Upon lithiation down to 0.74 V (**Figure 3.4b,** panel **B**), all the Raman modes of the 2H MoS_2 phase were still present: 475.59 cm^{-1} (ZA'(B^2_{2g}(M))), 455.01 cm^{-1} (2LA(M)), 409.78 cm^{-1} (A^1_g), 384.19 cm^{-1} (E^1_{2g}). In addition, characteristic modes of the 1T-MoS_2 emerged: J_1 at 153.9 cm^{-1}, J_2 at 220.5 cm^{-1} and E^1_g at 288.3 cm^{-1} – corresponding to phonons at *M* points of the Brillouin zone, resulting from a Brillouin zone-folding mechanism when a $2a_0$ x a_0 super lattice of octahedrically coordinated and distorted MoS_2 single layers is formed. [100,101] Thus, this confirmed the lithiation process, ongoing at 0.98 V accompanied by a 2H MoS_2 to 1T Li_xMoS_2 phase transition (**equation 3.1**). However, this process was only partially proceeded, since a full conversion of the 2H to the 1T phase would have implied the absence of the E^1_{2g} mode. [100-102] This lithiation cathodic peak was comparatively broader and of a lower current in the raw MoS_2 electrode (**Figure 3.5a**), which indicated a more efficient lithiation in the nanosized 2D MoS_2 electrode.

Upon further discharge at 0.01 V (**Figure 3.4b,** panel **C**), two Raman modes at 476.1 cm^{-1} and 371.7 cm^{-1} were present. A reference Li_2S (**Figure 3.4b,** panel **D**), with Raman modes at 477.0 cm^{-1} and 371.7 cm^{-1}, confirmed that these modes corresponded to Li_2S. Therefore, this confirmed the occurrence of the conversion reaction at 0.36 V (**equation 3.2**). In addition, J_1 at 156.3 cm^{-1}, J_2 at 211.8 cm^{-1} and E^1_g at 281.1 cm^{-1} characteristic of the 1T MoS_2 phase were still present, which indicated a partial conversion reaction and the prevalence of unreacted 1T Li_xMoS_2.

Upon subsequent charge (after the first discharge) at 1.98 V (**Figure 3.4c,** panel **B**), the ZA'(B^2_{2g}(M)) and A_{1g} modes of the 2H MoS_2 phase reappeared at 474.2 cm^{-1} and 404.1 cm^{-1}, respectively. A broad band at ~ 372.2 cm^{-1} was attributed to Li_2S mainly (with a corresponding contribution at the band at 474.2 cm^{-1}), although it might involve contributions from the E^1_{2g} mode of the 2H MoS_2 phase at 384.2 cm^{-1}. Then, a significant structural change of the 1T

Li_xMoS_2 takes place as the modes J_2 and E^1_g modes disappeared, J_1 was present at 156.1 cm^{-1} and new ones emerged at 308.5 cm^{-1} and 249.0 cm^{-1}. The latter has been theoretically calculated (at 248 cm^{-1}) and corresponds to the frequency of a phonon at the *K* point of the Brillouin zone that becomes active as a result of the same zone-folding mechanism that gives origin to J_1 to J_3 modes of the 1T MoS_2 phase [100] (J_4 in **Figure 3.4c,** panel **B**). The former could be a displaced J_3 Raman mode (J_3* in **Figure 3.4c,** panel **B)**. The reason for this displacement could be linked to significant structural changes of the 1T MoS_2 phase. We can conclude that at the shoulder at 1.98 V, unreacted 1T Li_xMoS_2 was delithiated to give place to 2H MoS_2 (**equation 3.3b**). A fraction of the 1T Li_xMoS_2 underwent only a partial delithiation, thus, giving place to a partially delithiated phase 1T Li_yMoS_2, where $y < x$, that was structurally very different to 1T Li_xMoS_2. Hence, the very different Raman modes of such phase at 1.98 V as compared to the phase present at 0.74 V. At this low potential, it was unlikely that the conversion reaction (**equation 3.3a**) took place, thus Li_2S was still present in the electrode. In summary, these parallel electrochemical processes led to a mix of 2H MoS_2 +1T Li_yMoS_2 + Li_2S in the electrode. Notice that this current peak at 1.98 V was absent on the raw MoS_2 electrode (**Figure 3.5a**), which indicated that early delithiation processes are favored in nanosized MoS_2 electrodes.

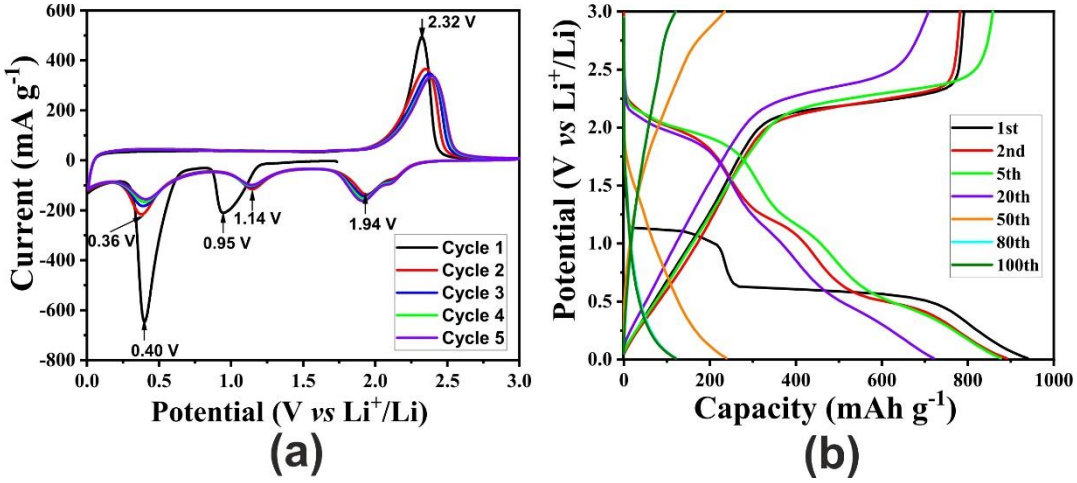

Figure 3.5 Electrochemical characterization of raw MoS_2 electrodes. (a) CV at a scan rate of 0.1 mV s^{-1}. Potentials of current peaks are indicated in black font, and (b) GCPL curves at a current rate of 0.05 A g^{-1} over several cycles.

Upon further charging at 3.0 V (**Figure 3.4c**, panel **C**), Raman modes of the 2H MoS_2 phase were dominant: 451.2 cm^{-1} (2LA(M)), 405.7 cm^{-1} (A_{1g}), 380.9 cm^{-1} (E^1_{2g}). Characteristic modes of the 1T MoS_2 lithiated phase were still present in a very minor fraction. No Raman modes of sulphur, also studied as reference (**Figure 3.4c**, panel **D**), were detected. Since Li_2S is not present either,

it is concluded that the reconversion back to 2H MoS_2 (**equation 3.3a)** took place. In summary, at 2.35 V, conversion (**equation 3.3a)** and a nearly full de-lithiation of 1T Li_xMoS_2/1T Li_yMoS_2 (**equation 3.3b**) confirmed the reversibility of the energy storage processes.

During the second cycle, the cathodic current peaks at 0.98 V and 0.36 V decreased drastically and a new one rose at 1.8 V; the anodic shoulder at 1.64 V shifted to 1.7 V; and the anodic peak at 2.35 V shifted to 2.32 V (**Figure 3.6a**). The electrochemical activity was also investigated by *ex-situ* Raman. Electrodes were polarized at 1.5 V and 0.01 V during discharge and at 1.98 V and 3.0 V during charge (**Figure 3.6a**). During discharge, at 1.5 V (**Figure 3.6b**, panel **B**), Raman modes of the 2H-MoS_2 and 1T Li_xMoS_2 were present, which indicated a partial lithiation process (**equation 3.1**). Upon discharge down to 0.01 V (**Figure 3.6b**, panel **C**), only Raman modes of Li_2S were found, indicating a full conversion process (**equation 3.2**). Upon charge up to 1.98 V (**Figure 3.6c**, panel **B**), Raman modes of the 1T Li_xMoS_2 and the 2H MoS_2 phase were present, which indicated the occurrence of the conversion (**equation 3.3a**) and delithiation process (**equation 3.3b**). Upon full charge to 3.0 V (**Figure 3.6c**, panel **C**), Raman modes of the 2H MoS_2 phase were present, indicating a full conversion process (**equation 3.3**).

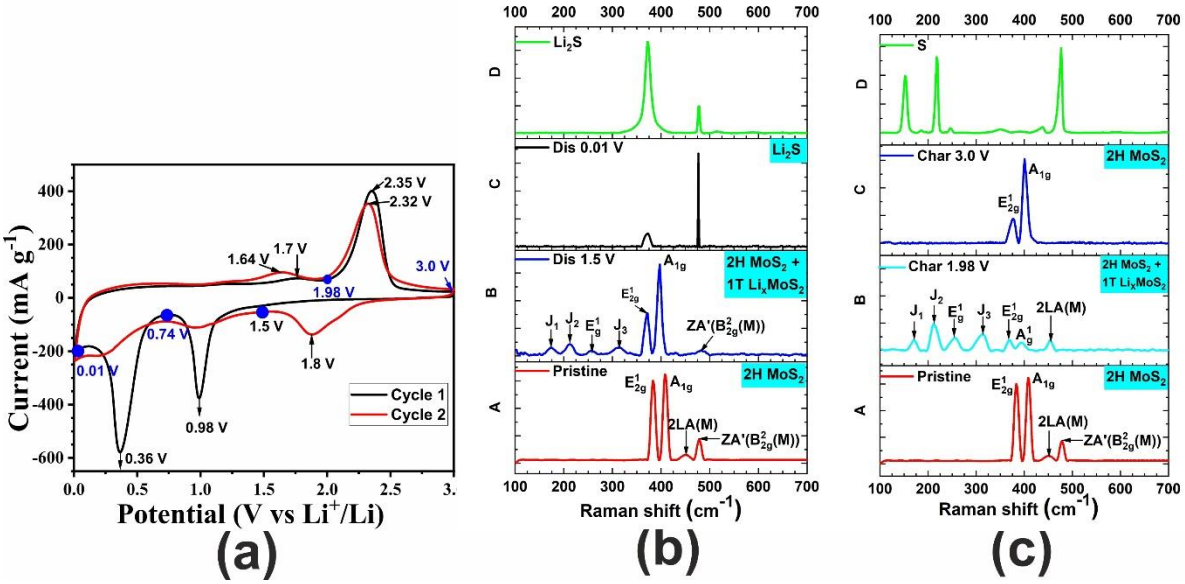

Figure 3.6 (a) CV of a 2D MoS_2 electrode at a scan rate of 0.1 mV s^{-1}. Potentials of current peaks are indicated in black font. Points of polarization are marked with a blue dot and/or blue font. *Ex-situ* Raman spectra at various potentials of polarization upon (b) discharge, and (c) charge of the second cycle. The spectra of the pristine electrode (without polarization) is shown in panels A for reference. In the same manner, Li_2S powder (panel D in (b)) and sulfur powder (panel (D) in (c)) were used as references.

In summary, Raman studies proved that intercalation and conversion energy storage processes are reversible in the 2D MoS_2 electrode. At intermediate potentials, mixed phases were found describing a partial completion of energy storage processes. At fully charged and discharged states, full completion of energy storage processes were achieved, especially during the second cycle. An increased reaction efficiency of the second cycle *vs* the first cycle can be attributed to electrode structural changes that opened up the structure for improved ion transport. This view was supported by cycling experiments described in the next sections. On the other hand, the capacity loss from cycle 1 to cycle 2, can then only be attributed to irreversible reactions related to SEI formation and other irreversible processes, also addressed in the next section.

The role of the nanostructure in the efficiency of energy storage mechanisms was evidenced by the contrast of CVs of the 2D MoS_2 electrodes *vs* the raw MoS_2 electrodes (**Figures 3.4a, 3.5a**). Supporting our views, previous reports on MoS_2 nanosheets have attributed an enhanced efficiency of the reversible conversion process (**equation 3.3**) to the large surface area of the nanosheets, where Mo nanoparticles can attach and readily react with Li_2S, while the open structure between nanosheets shortens mass transport paths. [103] In addition, Mo nanoparticles were reported to enhance electrical conductivity paths. [103]

In the next sections, the crucial role of electrode morphology and morphology changes undergone over cycling, on energy storage processes were further confirmed.

3.3.2 Cycling behavior

Next, the cycling stability and CE of 2D MoS_2 and raw MoS_2 electrodes were investigated using GCPL experiments at a current density of 0.05 A g^{-1}.

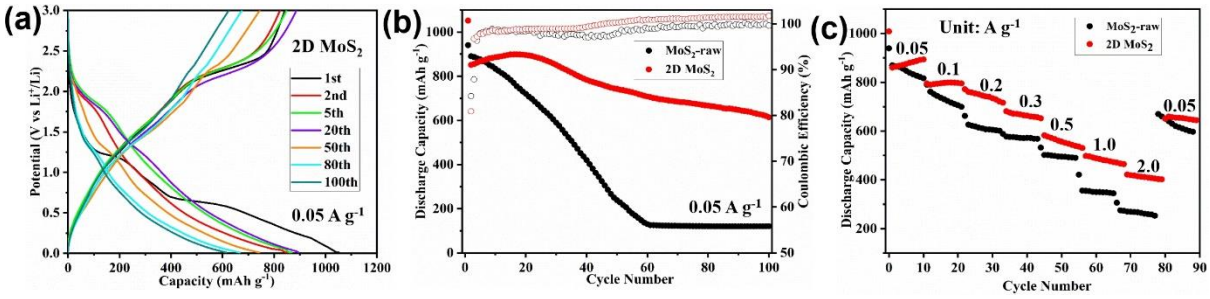

Figure 3.7 Electrochemical characterization of 2D MoS_2 and raw MoS_2 electrodes. (a) GCPL curves at 0.05 A g^{-1} of 2D MoS_2 electrodes, (b) discharge capacity (solid markers) and Coulombic efficiency (empty markers) *vs* cycle number of 2D MoS_2 and raw MoS_2 electrodes at 0.05 A g^{-1}, (c) current rate performance curves of 2D MoS_2 and raw MoS_2 electrodes measured in a range of 0.05 to 2.0 A g^{-1} current rates.

The discharge capacity decreased from the first to the second cycle in both electrodes (**Figures 3.7a** and **3.5b**). This was attributed mainly to secondary reactions related to the formation of the SEI. [104] However, a second process might have also played a role, especially in the nanostructured 2D MoS_2 electrode. According to previous studies, an additional gel-like film develops on top of the SEI in conversion-type electrodes. [105-106] This film is believed to be composed of organic compounds resulting from electrolyte decomposition at reductive low potentials. The formation of this polymeric-like film is thought to be catalyzed by metal particles resulting from conversion processes [105-106] as it is the case here with the presence of Mo particles, resulting from the conversion process (**equation 3.2**). There are previous work reporting that this polymeric-like film favors pseudo-capacitive processes that contribute to an extra capacity at low potentials. [105] However, as explained by this work, this film inevitably dissolves at high potentials above 2.0 V. [105] Thus, in the case of 2D MoS_2 electrodes a formation of such a film may have occurred upon discharge contributing to an extra capacity via electrolyte decomposition and pseudo-capacitive processes. Upon charge, dissolution of the film prevented a reversible capacity contribution upon the following discharge.

In the subsequent cycles, there were contrasting differences in the cycling behavior of the 2D MoS_2 *vs* the raw MoS_2 electrode (**Figure 3.7b**). Whereas the raw MoS_2 electrode shows a continuous steep capacity fall, the 2D MoS_2 electrode shows first a capacity increase, from cycles 2-17, followed by a more steadily decreasing capacity (**Figure 3.7b**). At cycles 2-5, the capacity of the raw MoS_2 electrode was higher (890.3-876.5 mAh g^{-1}) than the capacity of the 2D MoS_2 electrode (851.5-867.7 mAh g^{-1}). In subsequent cycles, the capacity of the 2D MoS_2 electrode was always higher than the capacity of the raw MoS_2 electrode. Morphological studies explained these trends, as described in the next section.

Equally, both electrodes show a very different evolution of CE upon cycling (**Figure 3.7b**). Initially both electrodes show a low CE of 84.6 % and 77.8 % for the raw MoS_2 and the 2D MoS_2 electrodes, respectively. The lower CE of the 2D MoS_2 electrode was attributed to the higher irreversible capacity originating from SEI formation of an electrode of much higher surface area than the microsized raw MoS_2 electrode. [104] Upon charge, and due to the irreversible formation of the SEI, Li-ions experience a higher diffusion resistance undermining the achieved charge capacity, and thus typically decreasing the CE. This effect is enhanced for nanostructured electrodes. [104] Upon further cycling,

the CE of the 2D MoS_2 electrode then increased rapidly to 98 % at cycle 5, reached 100 % at cycle 46, then continuously increased to reach 101.6 % at cycle 100. The origin of a small extra charge capacity is not clear at the moment, but most likely was related to surface-based oxidation processes developed upon cycling. This view is compatible with the occurrence of activation processes, described in the next section. In contrast, the raw MoS_2 electrode reached a value of 98.2% at cycle 5 and remained under 100 % during all cycling.

In addition, the 2D MoS_2 electrode showed a superior rate performance as compared to the raw MoS_2 electrode in a current range of 0.05 A g^{-1} to 2.0 A g^{-1} (**Figure 3.7c**).

3.3.3 Morphology

The correlation of the observed cycling behavior of both electrodes and the electrode morphology was investigated by *ex-situ* SEM. Spray deposition rendered pristine 2D MoS_2 electrode films where the nanosheets formed ring-like structures of 4-15 μm diameter (**Figure 3.8a**). The size and shape of such structures was determined by the droplet size of the spray mist. Inside those ring-like structures, the nanosheets arranged in a porous structure (inset of **Figure 3.8a**). Nitrogen adsorption isotherms measurements (**Figure 3.9a**) and the application of the Brunauer-Emmett-Teller (BET) method revealed a specific surface area (SSA) of 97.96 $m^2 g^{-1}$. Barrett-Joyner-Halenda (BJH) pore size analysis (**Figure 3.9b**) confirmed an average pore size of 8.68 nm, confirming a mesoporous structure of the 2D MoS_2 electrodes. In contrast, the raw MoS_2 electrode consisted of loosely packed MoS_2 flakes of 1-10 μm size (**Figure 3.10a**), with a SSA of only 35.65 $m^2 g^{-1}$ and a BJH average pore size of 5.03 nm. (**Figure 3.9**)

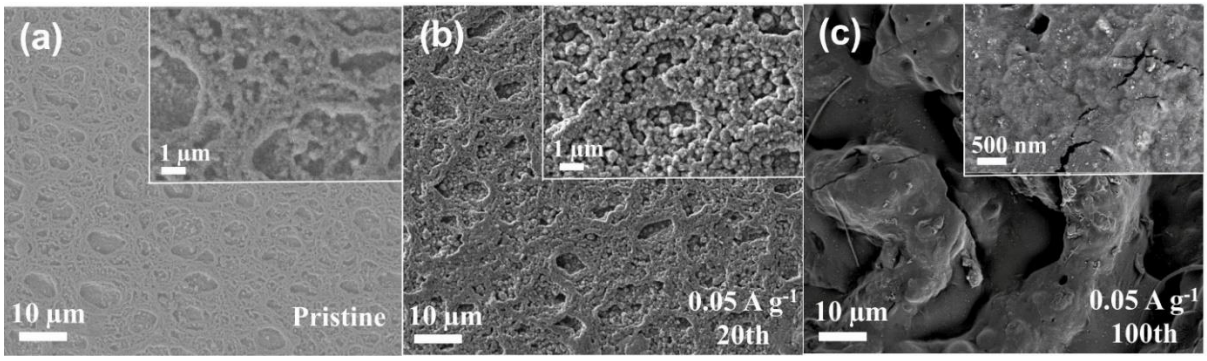

Figure 3.8 SEM images of (a) the pristine 2D MoS_2 electrode, (b) after 20th cycle and (c) after100th cycle at current density of 0.05 A g^{-1}, respectively. High magnification of each SEM images are shown as insets.

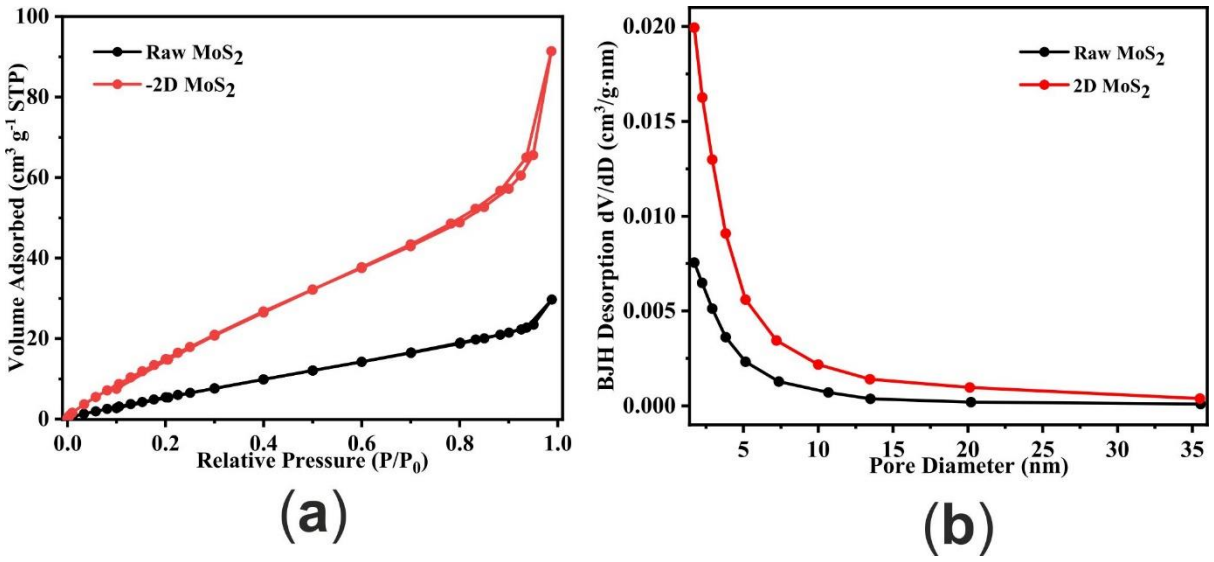

Figure 3.9 (a) Nitrogen adsorption isotherms and (b) pore size distribution curves of raw MoS_2 and 2D MoS_2 powder, respectively. Measurement of two samples has been introduced in the characterization section in the main text.

Therefore, the larger pores and higher SSA of the 2D MoS_2 explained its larger capacity, as compared to the raw MoS_2 electrode, at cycle 1. However, the higher SSA also led to a larger irreversibility linked to an enhanced SEI formation. [104] During cycles 2-17, the capacity rise of the 2D MoS_2 electrode can be explained in terms of a further opening of its porous structure upon cycling, which facilitated electrolyte infiltration and further exposure of active material to the electrolyte for a deeper lithiation. [107-109] This is a well-known phenomenon in 2D nanomaterials named activation. A prior cycling is necessary to "activate" or open, the normally restacked structure, allowing for an increasing access of electrolyte ions to the surface of active materials. [110-111] It is likely that these phenomena took place at the nanoscale and involved deep sites in the electrode as drastic changes were not obvious on the top-most layer at cycle 20 (**Figure 3.8b**). The need for an activation period of the 2D MoS_2 electrode to deliver its true accessible capacity explains the slightly lower capacity as compared to the raw MoS_2 electrode during the first 2-5 cycles.

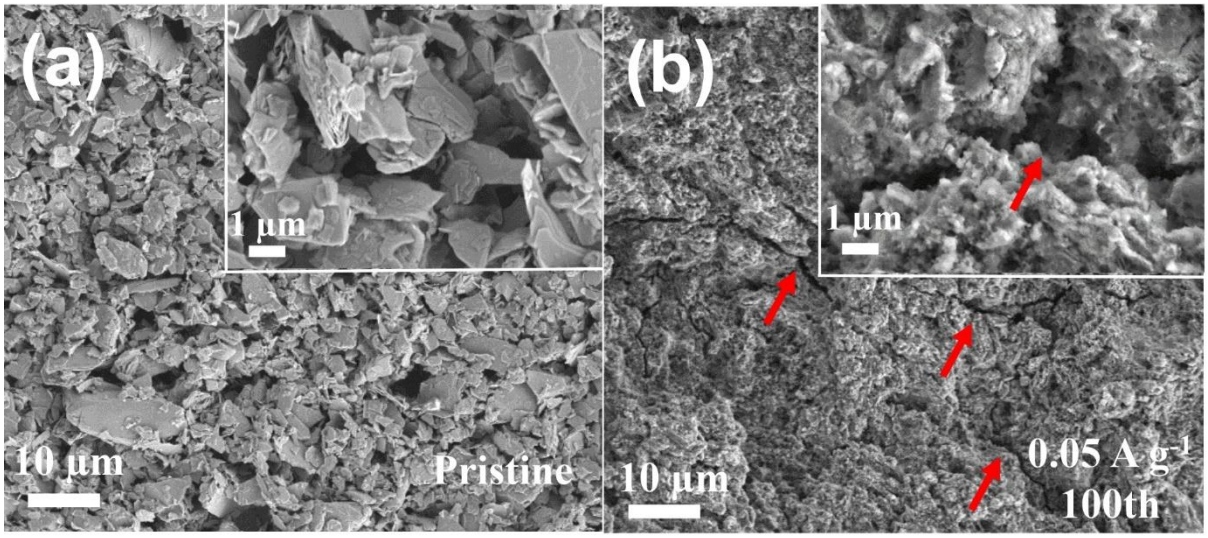

Figure 3.10 SEM images of (a) raw MoS_2 pristine electrode and (b) after cycling using GCPL at 0.05 A g^{-1} and after cycle 100. High magnification images are shown as insets. The cracks after cycling in (b) are marked by some arrows.

Upon further cycling, up to cycle 100, the 2D MoS_2 electrode showed a compact texture with slight mechanical degradation. (**Figure 3.8c**) In contrast, in the raw MoS_2 electrode, cracks were evident after 100 cycles (**Figure 3.10b**). This is known to, eventually, lead to full pulverization and failure of microsized electrodes. [103] Thus, the more stable mechanical structure of the 2D MoS_2 electrode allows for a better capacity stability as compared to the microsized raw MoS_2 electrode.

Lastly, the enhanced rate performance of the 2D MoS_2 electrode can be attributed to shorter ion transport paths in between nanosheets, aided by suitable electrolyte reservoirs at the mesopores of the electrode. It has been previously reported that "slit-shaped" ion channels in between 2D nanosheets will reduce the energetic barrier for lithium-ion intercalation and favor a fast ion diffusion. [112-114]

3.3.4 Cycling at higher rates

The interesting cycling behavior of the 2D MoS_2 electrodes was investigated further at higher cycling rates. GCPL experiments were performed at 0.5, 1.0, 1.5, and 2.0 A g^{-1} (**Figure 3.11**).

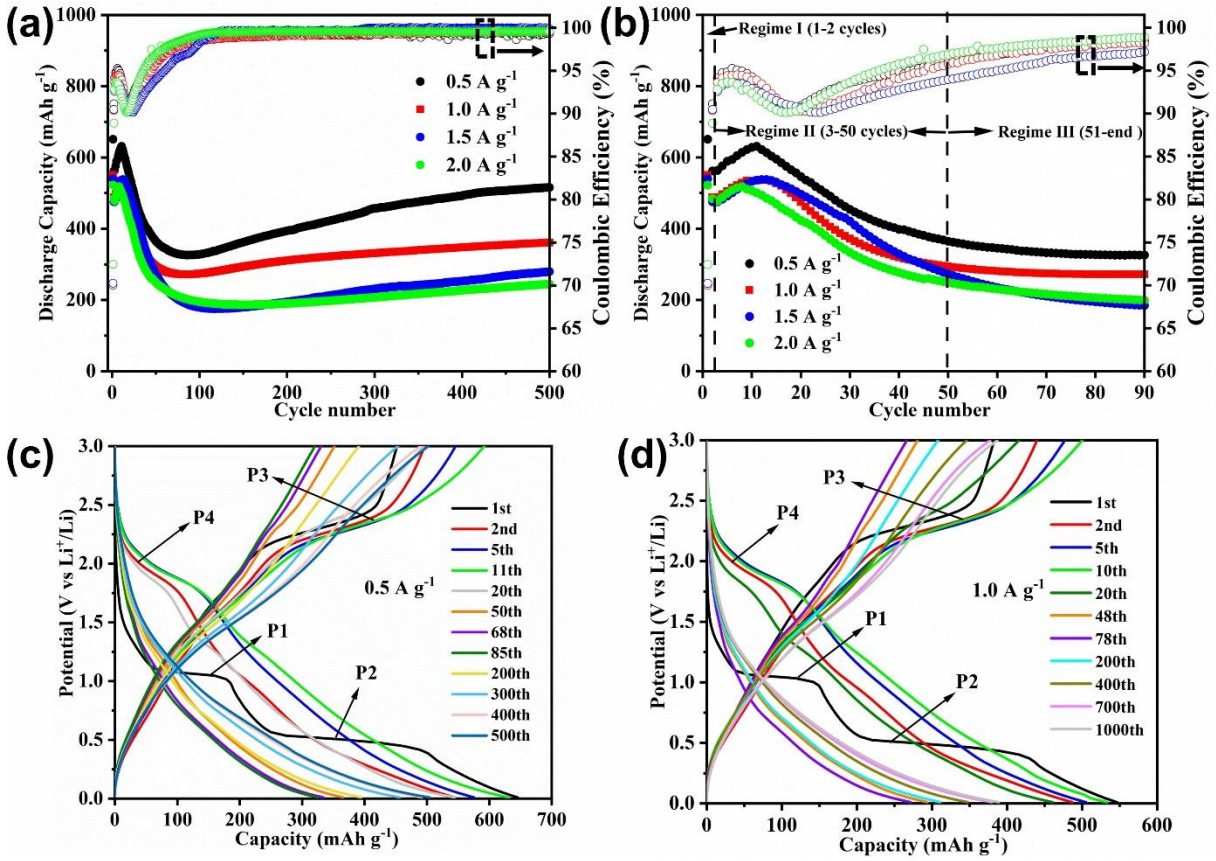

Figure 3.11 Electrochemical performance of 2D MoS_2 electrodes. (a) Discharge capacity *vs* cycles curves and (b) corresponding insets during the first 80 cycles of 2D MoS_2 electrodes cycled at 0.5, 1.0, 1.5 and 2.0 A g^{-1} current rates, (c) corresponding GCPL curves 0.5 A g^{-1} and (d) 1.0 A g^{-1} current rates.

The 2D MoS_2 electrode cycled at 0.5 A g^{-1} (**Figure 3.11a** and **b**) showed a similar initial capacity fall followed by a rising trend, when cycled at 0.05 A g^{-1} (**Figure 3.7b**). The discharge capacity dropped from 651 mAh g^{-1} at cycle 1 to 562 mAh g^{-1} at cycle 2. Subsequently, the capacity increased up to a peak capacity of 631 mAh g^{-1} at cycle 11. This rising trend was explained in terms of the same activation process described for the experiment at 0.05 A g^{-1}. Subsequently, the maximum of capacity was followed by a fall that reached a minimum of 325 mAh g^{-1} at cycle 85 (**Figure 3.11a**). Remarkably, and unlike the experiment at the cycling rate at 0.05 A g^{-1} (**Figure 3.11b**), this trend was followed by a continuously raising capacity trend until the end of the 500 cycles test (**Figure 3.11a**).

From cycles 1 to 2, the CE increased from 70% to 91% (**Figure 3.11b**). This was expected as per the transition of a highly irreversible regime at cycle 1 to a more stable regime from cycle 2 onwards. During the period of increasing capacity, at cycles 3-11, the CE stabilized around 94-95%. During the following capacity drop period, at cycles 12-18, the CE decreased from 93.8 % to 90.6 %. These reversibility variations can be explained in terms of processes involving

the SEI. During the first cycles, it is expected that the SEI first grows steadily enhancing a diffusion control of the delithiation processes. [104, 115] After the growing period, the SEI can undergo dynamic changes of formation/decomposition, [104, 115] which in this case, were very likely enhanced by the structural changes undergone by the electrode. [116] From cycles 19 until the end of test, the CE increased first constantly up to 98 % at cycle 85, describing an increasingly reversible capacity fall, and then stabilized for the rest of the test at 98-99%, describing reversible processes during the rising trend of the capacity, the reason for this will be provided in the EIS section.

Analysis of the charge-discharge curves at 0.5 A g^{-1} (**Figure 3.11c**) revealed further information about the ongoing electrochemical processes. The discharge curve at cycle 1 showed the *plateau 1,* describing lithiation processes at ~ 1.0 V, and the *plateau 2* corresponding to the conversion process at ~0.4 V. The corresponding charge curve showed a *plateau 3*, corresponding to the reconversion process at ~2.3 V. At the discharge curve 2, the *plateaus 1* and 2 vanished and a new and sluggish one, *plateau 4*, emerged at 1.94 V. At the charge curve 2, the *plateau 3* at 2.3 V was still present. This curve shape was maintained until cycle 50. Then, featureless curves remained from cycle 50 onwards. In summary, the electrochemical behavior can be divided into three regimes (**Figure 3.11b**):

Regime I, dominated by battery processes. At cycle 1-2, battery processes described by **equations 3.1** to **3.3** were involved.

Regime II, dominated by a combination of battery and pseudo-capacitive processes. From cycle 3-50, the plateaus 3 and 4 vanished progressively, and a sluggish shape was dominant for the rest of the GCPL curves. MoS_2 is known to transform from a battery charge storage behavior to an extrinsic pseudo-capacitance behavior as the particle size decreases from bulk microscale to the nanoscale. [117-119] This is the case for this regime, where battery processes were still in play at plateaus 3 and 4, while pseudo-capacitive processes arise due to structural changes induced over cycling (as described below). Indeed, CV studies (below) confirmed that at cycle 3, energy storage processes had a contribution of faradaic and capacitive processes (**Figure 3.18**).

Regime III, dominated by capacitive processes. From cycle 51 until the end of the test, the featureless charge-discharge curves describe purely capacitive processes with a degree of polarization. Morphological changes (as described below) led to an enhancement of capacitive processes that most likely involved not only pseudo-capacitive but also double layer capacitive processes as the surface of active material increased.

The following conclusions could be drawn:

(1) Since the same type of electrochemical activity, regime I, prevailed during the rising capacity stage (cycles 3-11), it follows that the rise of capacity could not be attributed to a new electrochemical process but rather to physical changes, here proposed as an activation mechanism.

(2) At cycles 12-18, where the CE decreased while the discharge capacity dropped, the same electrochemical processes dominated. This supports the hypothesis that the observed irreversibility is correlated to physical changes of the electrode and/or changes at the surface of active materials involving SEI formation/decomposition. This view was further supported by the fact that these fluctuating trends of CE at early cycling were observed only at the high current rates of 0.5, 1.0, 1.5 and 2.0 A g^{-1} (**Figure 3.11b**) where surface, rather than bulk, based processes contributed largely to storage but not at the comparatively slower current rate of 0.05 A g^{-1} (**Figure 3.7b**), where bulk processes were more likely to dominate and where the CE increased steadily.

(3) The fall of capacity from cycles 12 to 85 involves two regimes, II and III, with not observed change in the falling trend of capacity around cycle 51 (cycle of transition between regimes). This smooth transition indicated that at regime II the pseudo-capacitive mechanisms dominated increasingly over cycling, while double layer capacitive contributions may have emerged. However, at cycle 85, the drastic transition to a rising capacity occurred and was dominated by purely capacitive processes. Here, current work proposes that this transition is induced by a second activation process involving further morphological changes of a considerably restructured electrode where surface-based storage processes dominated. This was indeed supported by further microscopy studies (see **Figure 3.12**).

Similar trends in capacity and CE were observed for the tests at 1.0, 1.5 and 2.0 A g^{-1} (**Figure 3.11a**). A similar shape evolution was observed for the charge-discharge curves at 1.0 A g^{-1} (**Figure 3.11d**). At this rate, the cycles of maximum and minimum capacity were cycles 10, and 78, respectively. The capacity, then, continued increasing until cycle 1000. The electrochemical regimes, as defined previously were, regime I (cycles 1-2), regime II (cycles 3-48) dominated by a combination of battery and pseudo-capacitive process and regime III (cycles 49-1000) dominated by capacitive processes.

3.3.5 Further microscopy studies

Microscopy studies of the MoS_2 electrode cycled at 1.0 A g^{-1} were performed at the key cycles 10, 100, 500 and 1000 (**Figure 3.12**). At cycle 10, the end of the initial rise of capacity and within regime II, the electrode showed a nanostructure and opened meso-porosity (**Figure 3.12a** and **b**) very similar to that of the pristine electrode (**Figure 3.8a**). Therefore, it is likely that the first activation process at early cycling involved only opening of nanoscale porosity without major microstructural changes. At cycle 100, still around the minimum of capacity at cycle 78 and within regime III, a major microstructural change was observed **(Figure 3.12c** and **d**); ball-like structures of a diameter of 1-3 μm were formed and organized in a larger porous microstructure with pore sizes ranging from 1-2 μm. Therefore, the fall of capacity can be explained by an evolution of the electrode structure going from an open mesoporosity and even nanostructure at cycle 10 to a microporous structure where the microsized aggregates decreased the surface area but probably allowed a deeper infiltration of electrolyte in the bulk of electrode eventually leading to a rise of capacity. [120-121] Then, during the capacity rise, at cycle 500, the architecture of the electrode again changed drastically (**Figure 3.12e** and **f**). The porosity was closed, the ball-like microsized structures collapsed to form a compact structure comprised of MoS_2 nanosheets that stood vertically. At cycle 1000, the electrode continued to be compact, few pores in the microscale were opened, and the MoS_2 nanosheets were transformed into tiny, needle-like structures (**Figure 3.12g** and **h**).

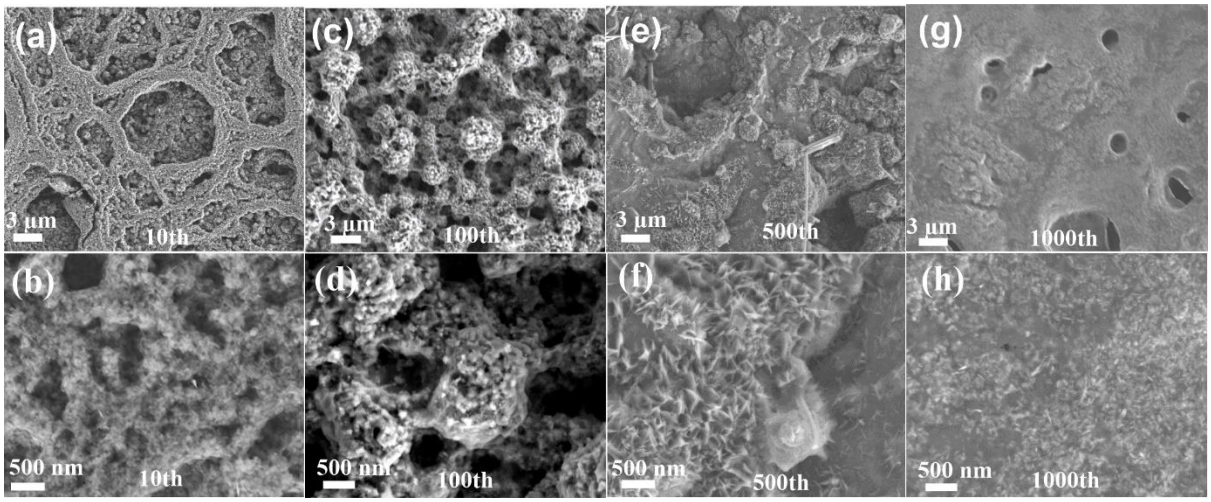

Figure 3.12 SEM images of 2D MoS_2 electrodes after cycling at a current rate of 1.0 A g^{-1}. (a), (b) at cycle 10, (c), (d) at cycle 100, (e), (f) at cycle 500, and (g), (h) at cycle 1000.

This work concludes that the rise of capacity of the electrode cycled at 1 A g^{-1}, from cycles 79 to 1000, regime III, was induced by a second activation process,

consisting of a continuously evolving major electrode restructurating. In this second activation process cycling strains led to a collapse of the microstructure emerging at cycle 100 into a compact electrode comprised of even smaller nanosheets than the pristine 2D MoS_2. Energy storage took place, then, via capacitive processes facilitated by a nanostructured electrode with a large surface area exposed to the electrolyte, infiltrated during the prior capacity fall stage. In this new structure, a rapid ion transport was facilitated across short nano-channels between the vertically aligned tiny nanosheets. [110-111] A very similar restructuration was observed for the electrode cycled at the other current rates. For instance, a very similar compact morphology was found in the 2D MoS_2 electrodes cycled at 0.5 A g^{-1} at cycle 500 (**Figure 3.13**).

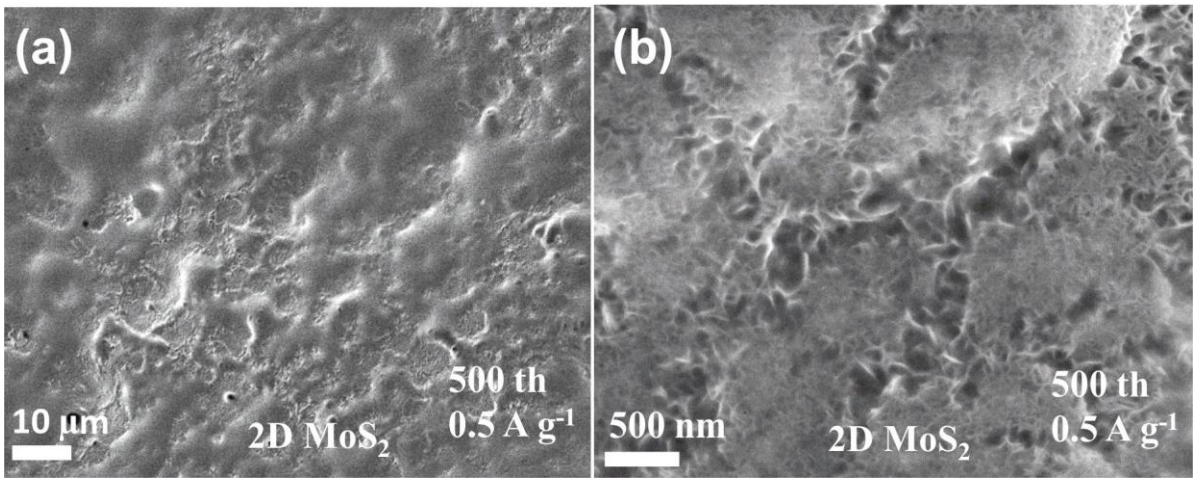

Figure 3.13 (a), (b) SEM images of a 2D MoS_2 electrode previously cycled using GCPL at a current density of 0.5 A g^{-1} and after cycle 500.

It is worth noticing that the capacitive regime III (cycles 49-1000) was dominant in electrodes of very different structures (**Figure 3.12c-h**). This implied that in this regime, physical and surface-based, rather than bulk and new chemical processes dominate the energy storage mechanisms and that the structural changes had a major impact on the capacity achieved. Note that the raw MoS_2 electrode had a totally different cycling behavior at 0.5 and 1.0 A g^{-1} (**Figure 3.14a** and **b**). Unlike the 2D MoS_2 electrodes, the bulk electrodes simply failed as early as 200 cycles and cracks on cycled electrodes were evident (**Figure 3.15**).

3.3.6 Energy storage processes of raw MoS_2 electrodes

Unlike the 2D MoS_2 electrodes, the electrodes comprised of raw MoS_2 (microsized), had a very poor cycling stability failing as early as 200 cycles

(**Figure 3.14a** and **b)**. These electrodes did not even show a capacity rise. The GCPL curves also showed clear plateaus, typical for battery behavior (**Figure 3.14c** and **d)**.

Microscopy studies revealed the occurrence of cracks and the emergence of amorphous structures at the end of cycling tests (**Figure 3.15**). This confirmed what is known about bulk electrodes: failure occurs due to volume expansion over cycling, which eventually leads to pulverization.

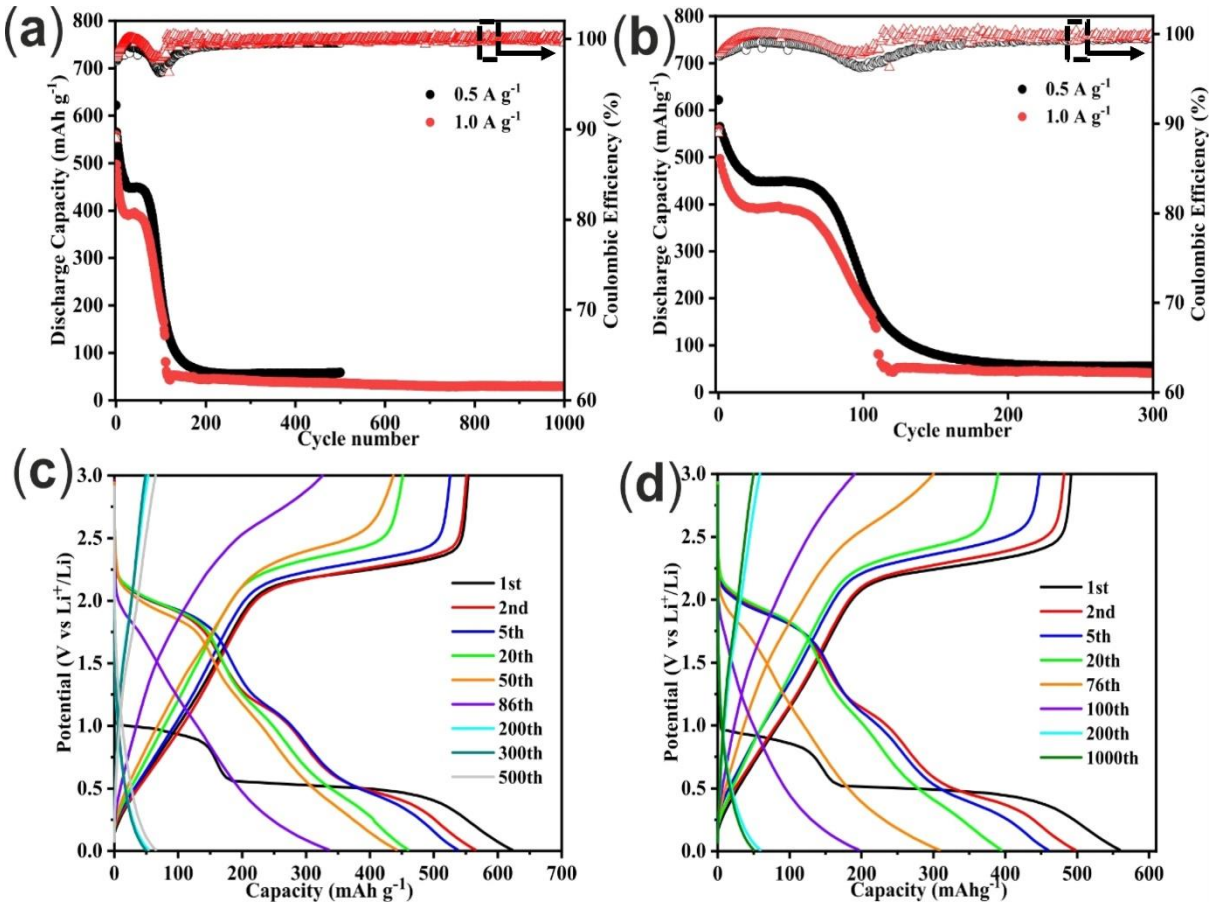

Figure 3.14 Electrochemical performance of raw MoS_2 electrodes at high rates. (a) Discharge capacity (left axis) and Coulombic Efficiency (right axis) *vs* cycles curves at 0.5 and 1.0 A g^{-1} current rates, and (b) zoom into the first 300 cycles, (c) corresponding GCPL curves at 0.5 A g^{-1} and (d) 1 A g^{-1} current rates.

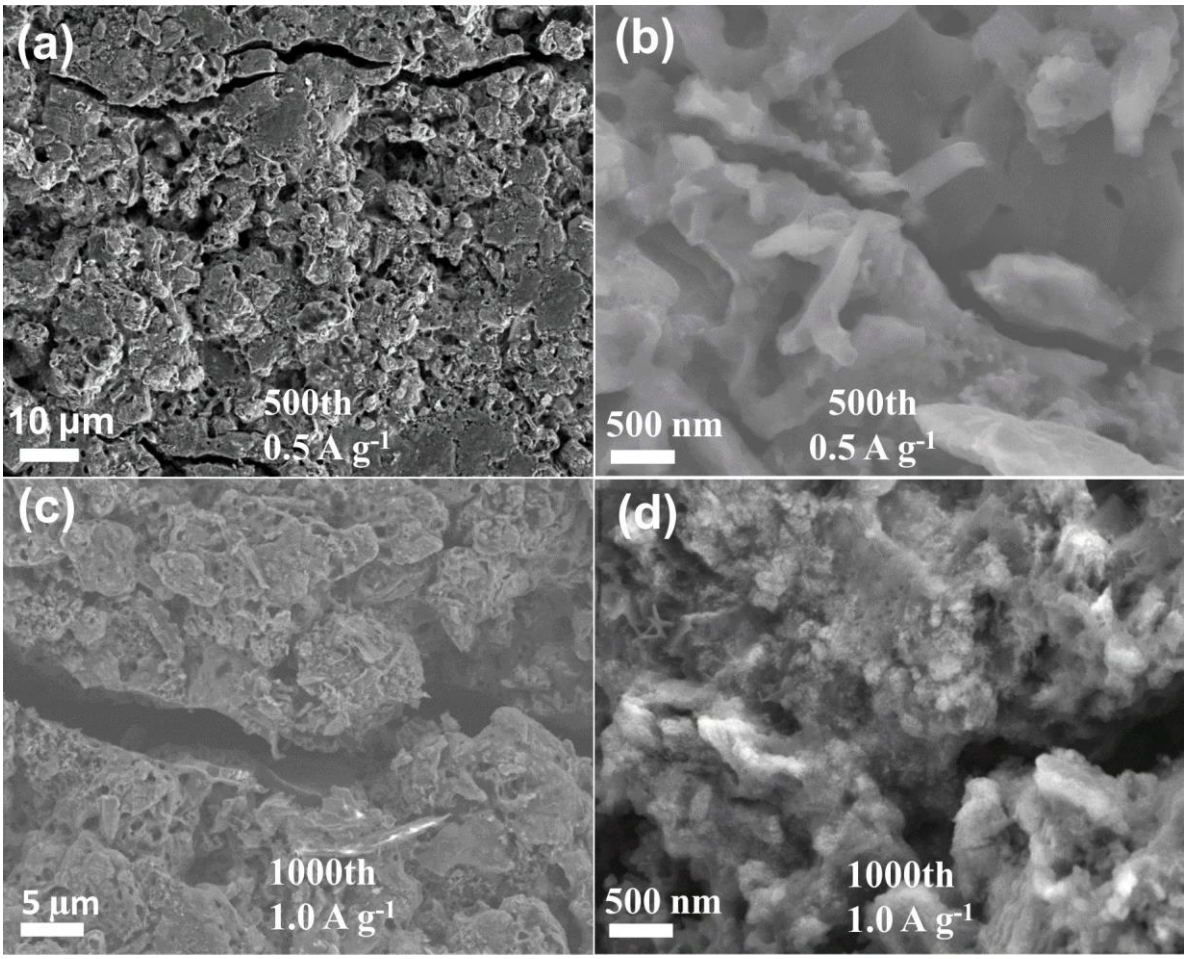

Figure 3.15 SEM images of cycled raw MoS_2 electrodes: (a), (b) at a current rate of 0.5 A g^{-1} and after cycle 500, and (c), (d) at a current rate of 1.0 A g^{-1} and after cycle 1000.

3.3.7 Rate performance of 2D MoS_2 after cycling at high rates

Next, the rate performance of the 2D MoS_2 electrodes after long-term cycling (pre-cycled electrodes) was investigated. First, the capacities of the pre-cycled electrodes (**Figure 3.16**) were lower than in the fresh electrode (**Figure 3.7b**). For instance, for the pre-cycled electrode at 0.5 A g^{-1}, the discharge capacity at 0.05 A g^{-1} was 698 mAh g^{-1} (cycle 502) (**Figure 3.16a**), lower than the capacity of a fresh electrode 851.4 mAh g^{-1} (cycle 2) (**Figure 3.7c**). This is expected after pre-cycling, which rendered a totally restructured electrode that stored charge mainly by capacitive processes. Although, at the pre-cycling stage, the electrode followed a continuously rising capacity trend, it did not reach the initial values (cycle 1) (**Figure 3.11a**).

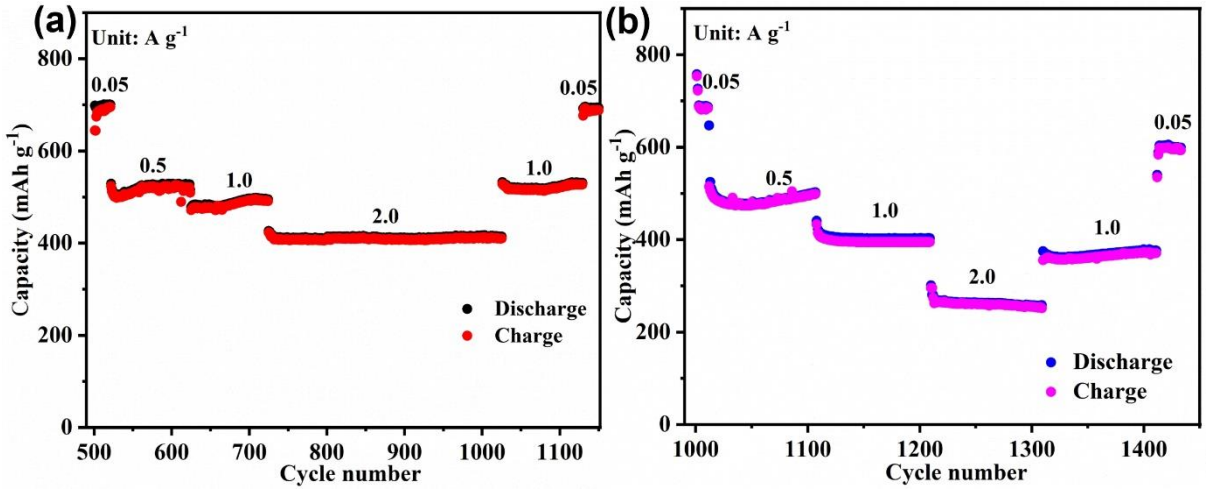

Figure 3.16 Rate performance evaluation of 2D MoS_2 electrodes after long-term cycling tests. (a) Capacity *vs* cycles curves at various current rates after the 500 cycles test at 0.5 A g^{-1}. (b) Capacity *vs* cycles curves at various rates after the 1000 cycles test at 1.0 A g^{-1}.

Second, remarkably, the capacities of a pre-cycled electrode (**Figure 3.16**) were more stable than a fresh electrode (**Figure 3.7c**). Moreover, the capacities at most scan rates followed a similar trend than for the long-term cycling (**Figure 3.11a** and **b**), i.e. a fall-rise trend followed by a steady trend. e.g. at 0.5, 1.0 and 2.0 A g^{-1} (**Figure 3.16a** and **b**).

Finally, at the end of the rate test, the structural morphology of the two pre-cycled electrodes was also evaluated by *ex-situ* SEM, highly similar flower-like nanostructures with various aggregation of nanoparticles but no cracks were observed in both of electrodes (**Figure 3.17**), demonstrating that the reactivated electrodes exhibit a remarkable structural stability.

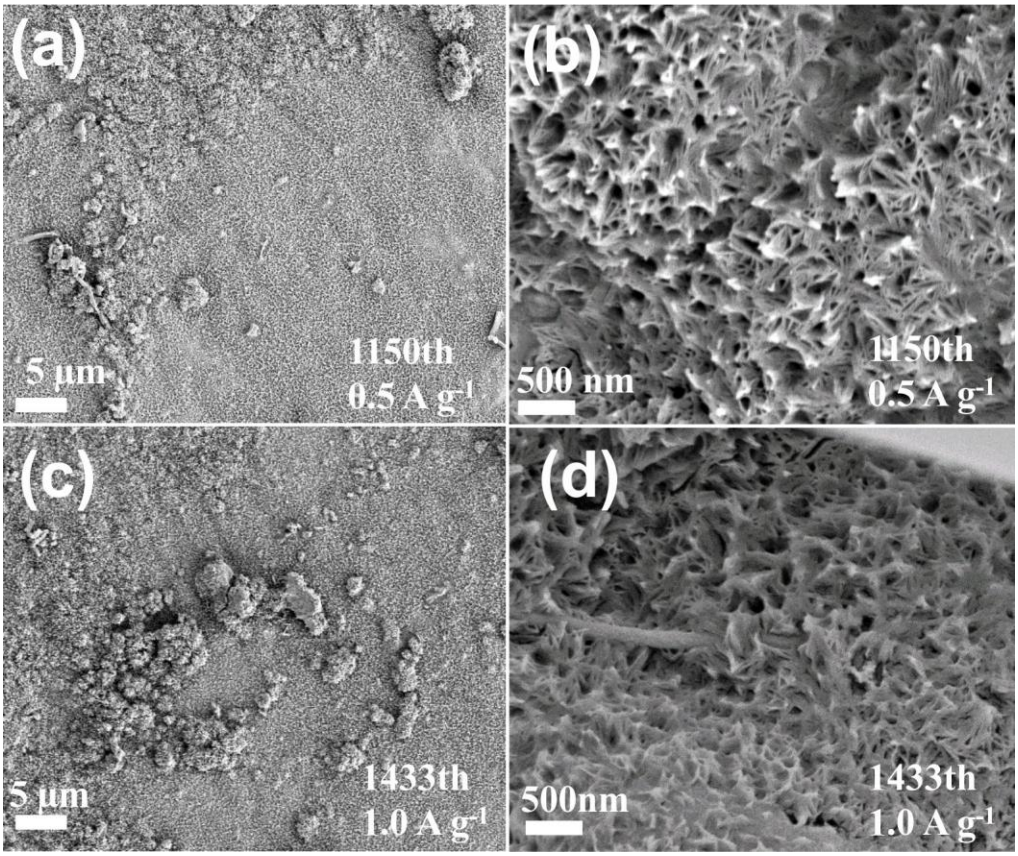

Figure 3.17 (a), (b) SEM images of a 2D MoS_2 electrode that was first cycled over 500 cycles at 0.5 A g^{-1}, and then cycled at several current rates, (c), (d) SEM images of a 2D MoS_2 electrode that was first cycled over 1,000 cycles at 1.0 A g^{-1}, and then cycled at several current rates. The cycle number at which the electrode was imaged is indicated in the text, where cycle 1 corresponds to the starting point of the pre-cycling test.

Therefore, a main conclusion of this work is that the activation mechanisms undergone by 2D MoS_2 electrodes can indeed be used as a suitable methodology to obtain electrodes that, although with less capacity than a fresh electrode, they will have a greatly enhanced cycling stability via induced capacitive processes. Future work should focus on fine tuning the precycling current rates to obtain an optimized balance between capacities and cycling stability.

Next, the nature of the charge storage of the 2D MoS_2 electrodes was investigated by evaluating their kinetics during the first cycles. Established methods state the dependence of CV current on scan rate as $I_i\ (V_i) = k_i v_j^b$ (**equation 3.6**), where $I_i\ (V_i)$ is the current at a defined potential $Vi_1 ... Vi_n$, k_i is a constant, v_j is the scan rate considered in a range $j_1 ... j_n$, and b is a constant that defines the nature of the energy storage in place, i.e. b =1 describes capacitive processes and b = 0.5 describes diffusion-controlled processes. [118, 122]

CVs of 2D MoS_2 electrodes were performed at a 0.1 to 2.0 mV s^{-1} scan rate range (**Figure 3.18a)**. CVs were analyzed at cycle 3, corresponding to regime II, established by GCPL studies, where pseudo-capacitive processes were found. Here this information is confirmed and quantified. The CVs showed cathodic peaks at c_1 =1.88 V and c_2 = 1.04 V, and anodic peaks a_1 = 2.31 V and a_2 = 1.64 V (**Figure 3.18a)**. The evolution of the current with scan rates was evaluated for the main anodic and cathodic peak (c_1, a_1). The obtained *b* values were b = 0.72 for c_1 and b = 0.78 for a_1, describing a mix of faradaic and capacitive processes at these particular potentials.

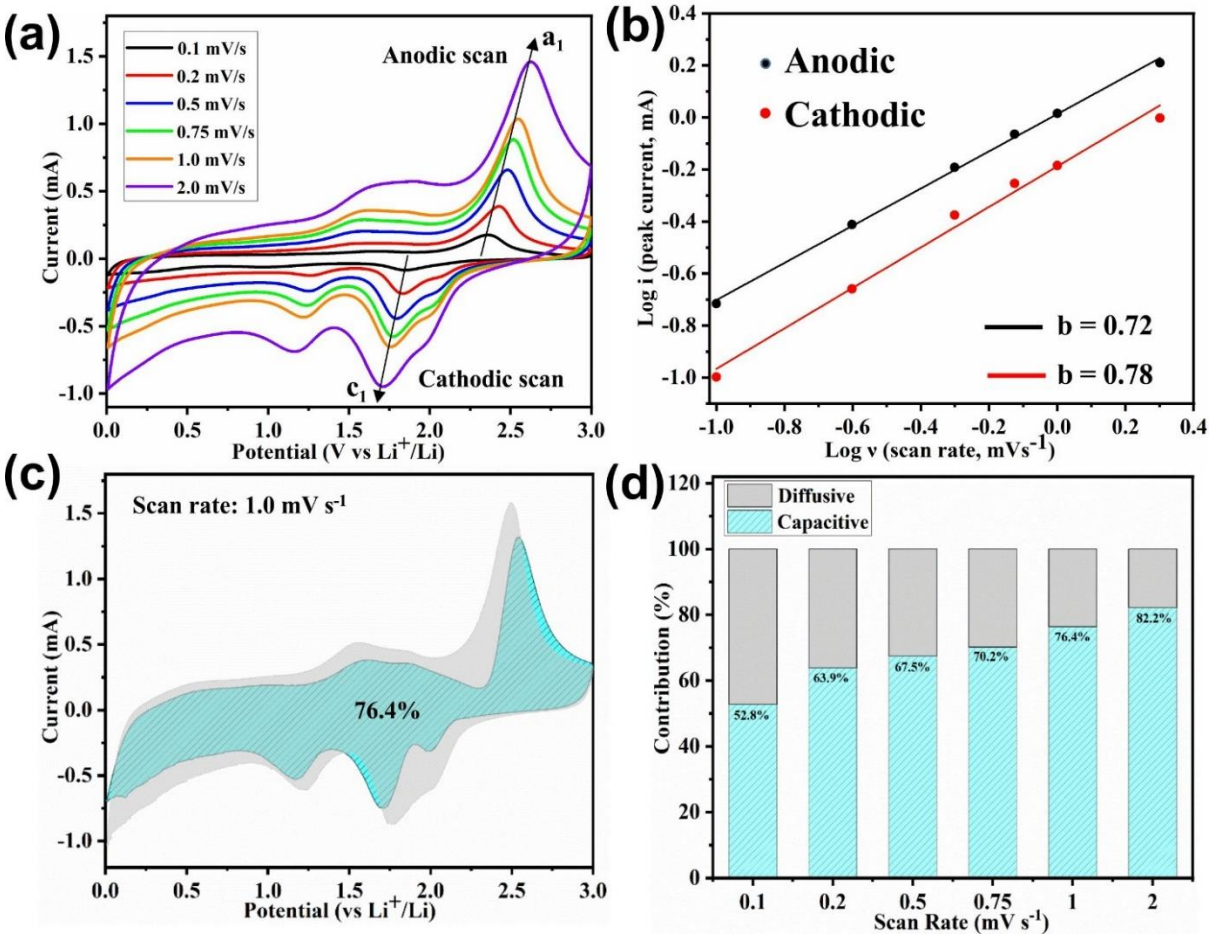

Figure 3.18 Evaluation of the kinetic behavior of 2D MoS_2 electrodes. (a) CVs at scan rates of 0.1 mV s^{-1} to 2 mV s^{-1}, (b) log (I_i (V_i)) *vs* log (v_i) curve at c_1 and a_1 current peaks, (c) CV at 1.0 mVs^{-1} where the capacitive and diffusive contributions to energy storage have been depicted, (d) bar graph describing the percentage contributions to capacitive and diffusion-controlled energy storage at each considered scan rate.

The contributions of each process to energy storage over the entire CV were calculated according to $I_i(V_i) = k_{1i}v_j + k_{2i}v_j^{1/2}$ (**equation 3.7**), where variables are defined as in **equation 3.6** and the first and second terms account for the capacitive and diffusion-controlled processes, respectively. [118, 123] A

rearrangement of **equation 3.7** as $I_i\ (V_i)/v_j^{1/2} = k_{1i}v_j^{1/2} + k_{2i}$ (**equation 3.8**) allows to calculate k_1 and k_2 when plotting $I_i\ (V_i)/v_j^{1/2}$ *vs* $v_j^{1/2}$. Applying this methodology, capacitive and diffusion-controlled contributions to energy storage were calculated over the entire CVs using $\Delta V = 0.2$ V voltage steps. First, it is confirmand that, indeed, at the start of regime I (at CV scan cycle 3), energy storage processes have contributions from faradaic (battery) processes and capacitive processes. Second, at the slowest current rate of 0.1 mV s^{-1}, the capacitive contribution was 52.8 %. This increased as the scan rate increased (**Figure 3.18d**). A graphical illustration of the contribution of such energy storage processes at 1.0 mV $^{-1}$ is given in **Figure 3.18c**. Notice that: 0.1 mV s^{-1} ≈ 0.09 A g^{-1}, 0.5 mV s^{-1} ≈ 0.5 A g^{-1} and 1.0 mV s^{-1} ≈ 1.0 A g^{-1}, thus this CV analysis can be compared to the previous GCPL studies.

3.3.8 Electrochemical impedance spectroscopy

The evolution of the electrical properties at the electrode-electrolyte interface upon cycling was investigated by EIS. The electrodes were fully discharged (0.01 V) and then fully charged (3.0 V), left at rest for 3 hours and EIS measurement was then recorded. This analysis was done at 0.05 A g^{-1} and 1.0 A g^{-1} current rates and at specific cycles.

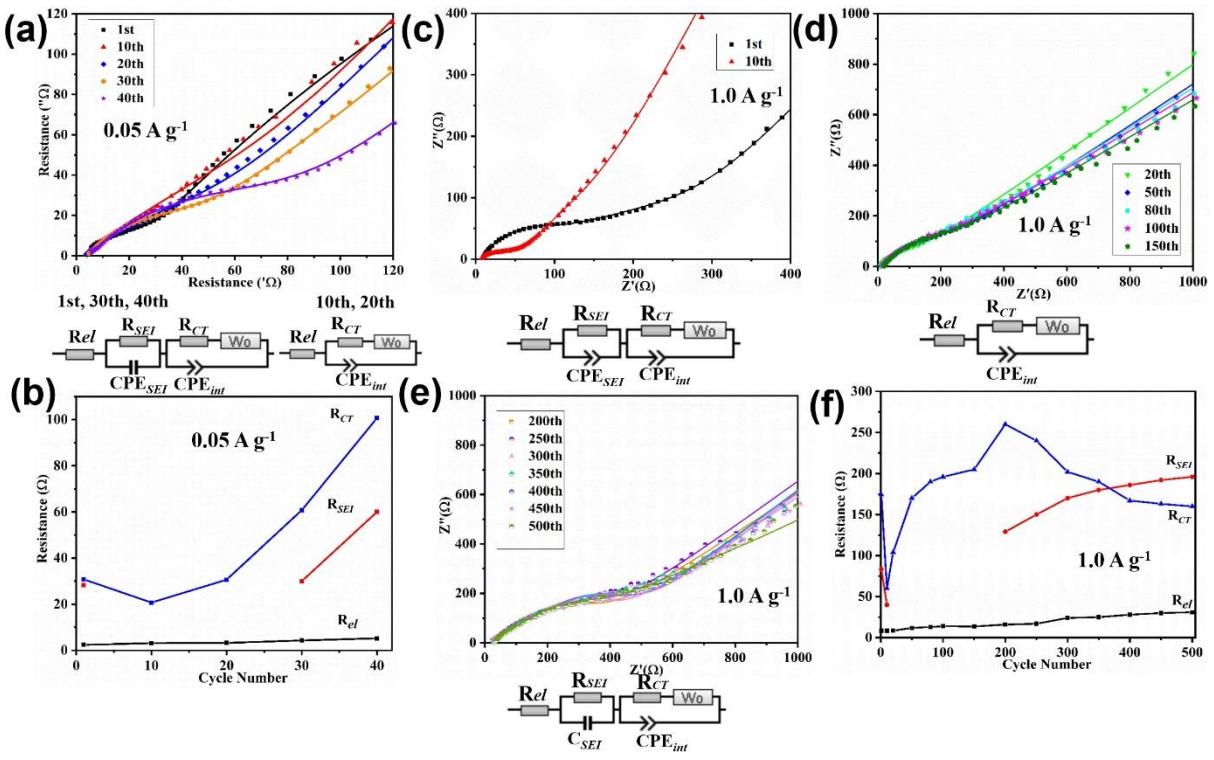

Figure 3.19 EIS data of 2D MoS_2 electrodes at the charge potential of 3.0 V *vs.* Li^+/Li at specific cycles of a GCPL cycling experiment. (a) Nyquist plots for EIS obtained at a GCPL experiment at 0.05 A g^{-1} and corresponding EEC used for data modelling, (b) corresponding

R*el*, R_{CT} and R_{SEI} *vs* cycles curves (c), (d) and (e) Nyquist plots for EIS obtained at a GCPL experiment at 1.0 A g^{-1} and corresponding EEC used for data modelling, (f) corresponding R*el*, R_{CT} and R_{SEI} *vs* cycles curves.

The EIS data at 0.05 A g^{-1} was modelled using the electrical equivalent circuit (EEC): $R_{el}(R_{SEI})(CPE_{SEI})$ $(R_{CT}Wo)(CPE_{int})$ and $R_{el}(R_{CT}Wo)(CPE_{int})$ (**Figure 3.19a**). [124-125] Here, R_{el} is the sum of the resistance of the electrolyte, separator and internal resistance of the cell, corresponding to the high-frequency region. A parallel circuit $(R_{SEI})(CPE_{SEI})$ modelled the physics of the SEI, where R_{SEI} and CPE_{SEI} are the SEI resistance and capacitance, respectively, corresponding to the middle-high-frequency region. The capacitance was modelled using a constant phase element (CPE) accounting for a frequency dispersed capacitance. [126-127] A second parallel circuit $(R_{CT}Wo)(CPE_{int})$ modelled the charge storage activity at the electrode-electrolyte interface, corresponding to the middle-low-frequency region, where R_{CT} is the charge transfer resistance, CPE_{int} is the capacitance at the interface and *Wo* is an open circuit terminus Warburg element accounting for diffusion processes. [128] The corresponding Nyquist plots are shown in **Figure 3.19a**. The R_{el} was slightly increased from 2.4 Ω (1st cycle) to 5.2 Ω at 40th cycle due to the growth of internal contact resistance (**Figure 3.19b**). Surprisingly, the R_{SEI} shows an initial value of 28.3 Ω while cannot be detected between cycles 10 and 20, (**Figure 3.19b**), which is most likely caused by the decomposition or breaking of the SEI film. After that, R_{SEI} was rapidly increasing from 30 to 60 Ω at cycle of 30 and 40, respectively, demonstrating the regeneration of the SEI film. The R_{CT} firstly dropped from an initial value of 30.8 to 20.7 Ω at cycle of 10, which is in a good agreement with the continuous capacity increase of MoS_2 in the first 17 cycles due to the pre-activation (**Figure 3.7b**). As expected, R_{CT} again continuously increased from 30 (20th cycle) to 100 Ω till the 40th cycle (**Figure 3.19b**), which indicated an increasingly sluggish electrochemical reaction kinetics developed upon cycling, which is expected from the considerable restructuration that the electrode underwent, as revealed by the morphology analysis (**Figure 3.7**), and that was accompanied by a slow capacity fall (**Figure 3.6b**).

The EIS data at 1.0 A g^{-1} was modelled by different EECs at specific cycles (**Figure 3.19c-e**). The definition of the circuit elements has been introduced before. The sum of R_{el} was increased from 8.4 (cycle 1) to 30 Ω at cycle of 500, which is ascribed to the growth of the cell's internal contact resistance upon cycling. As shown in **Figure 3.19c**, two semi-circles correlated to R_{SEI} and R_{CT} in the high- and middle-frequency region, with values of 83 and 174 Ω, obtained in the first cycle, which are then significantly reduced to 40 and 60 Ω

at the10th cycle due to the pre-activation process of the electrode, which is well consistent with the capacity increase in the first ten cycles (see **Figure 3.11b**). Interestingly, the mentioned two semicircles were merged to a single one between cycles 20 and 150, indicating that the electrochemical processes of the electrode at the electrode/electrolyte interface have dramatically changed. The resistance contribution from the SEI (R_{SEI}) film cannot be extracted by the EIS measurement due to a large fraction of the SEI that was broken or decomposed in the delithiation process, which is supposed to be caused by the drastic volume expansion of the MoS_2 electrode during repeated Li-ions insertion/extraction. Meanwhile, R_{CT} rapidly increased from 104 (cycle 20) to 205 Ω up to cycle 150, which is in a good agreement with the serious capacity degradation that results from the structural changes. (**Figures 3.11a** and **3.12c**). Impressively, the depressed two semicircles appeared again from cycle 200, with R_{SEI} and R_{CT} values of 129 and 250 Ω, respectively, indicating that the new SEI layer was reformed during the initial stage of the capacity rise. Subsequently, the R_{SEI} steadily increased and tends to be stabilized at 190 Ω at cycle 500, demonstrating that a stable SEI was obtained upon cycling. However, R_{CT} gradually declined from 260 to 163 Ω during the cycling, which should be linked to a structurally more stable electrode, with remarkably improved charge transfer at the nano channels between vertically aligned nanosheets (see **Figure 3.12e-f**).

3.4 Conclusion

In summary, we have demonstrated the liquid-phase exfoliation (LPE) of commercial MoS_2-raw materials to give mono- or few-layer 2D MoS_2 nanosheets, which were further deposited onto Cu foil through layer-by-layer spray deposition technique. Due to shortened lithium-ion diffusion paths and enhanced accessible contact area for electrolyte and ions because of the porosity, the conductive additive-free thin film electrode (labelled as 2D MoS_2) exhibits higher capacity and rate capability than that of bulk MoS_2. The conversion reaction reversibility of the 2D MoS_2 electrode was further confirmed by *ex-situ* Raman. More importantly, the reason behind the capacity decay and further on continued increase, that stabilized at high-rate cycling was comprehensively explored by *ex-situ* SEM and EIS analysis. We discovered that the structure and morphology of the 2D MoS_2 electrode is reconstructed and/or reactivated by the volume change at high-rate cycling. Simultaneously, the nanoscale diffusion length of the activated electrode facilitates mass and charge transports that benefit from the self-optimized static SEI layer during long-term cycling, which allow the electrodes to deliver exceptionally stable rate capability and extended

lifespan. This work provides a strategy to manufacture electrodes from suspensions in a scalable way and a reference for the mechanism investigation of MoS_2 nanosheets-based materials.

4 Engineering 2D $MoS_2/Ti_3C_2T_x$/CNTs Heterostructures as Anodes for Superior Lithium Storage

This chapter is partially based on the publication on *Engineering 2D $MoS_2/Ti_3C_2T_x$/CNTs Heterostructures via Layer-by-Layer Spray deposition as Highly Stable Anode for Lithium-ion Batteries*, in final stage of preparation.

4.1 Introduction

As demonstrated in **chapter 3**, despite 2D MoS_2 has shown a promising potential for the application in LIBs, it is still limited by poor capacity retention and unexpected activation process at high rates, which can be attributed to the unsatisfactory electrical conductivity and volume expansion of the electrodes. In this context, to further improve the electrochemical performances of the 2D MoS_2 electrodes, one promising solution may be mixing them with additives that possess excellent conductivity and mechanical strength. In 2011, a new family of 2D materials, transition metal carbides and nitrides, called MXene, has been discovered by Yury and co-workers. [12, 15, 129] MXene can be produced from their ternary carbide or nitride precursors (MAX phase), by selective etching of the A (group 4, 5 and 6 element) layer in hydrofluoric (HF) or HF-containing etchants. [130-131] The formula of MXenes is $M_{n+1}X_nT_x$, where M is the early transition metal, X is carbon and/or nitrogen, n = 1, 2, or 3, and T_x represent the surface terminations functional group such as -OH, -O and -F. [132] In particular, MXenes are promising candidates for lithium-ion storage due their attractive features such as excellent mechanical flexibility and low Li^+ diffusion barriers (easy lithium-ions transport) [133] as well as superior conductivity. [134] Nevertheless, like other conventional 2D materials (for example, graphene, TMDs and TMOs), MXenes also have certain limitations in energy storage such as moderate capacity (theoretical capacity is 320 mAh g^{-1} for LIBs) [20, 133] and aggregation of 2D nanosheets during cycling.

To overcome these limitations, 2D van der Waals heterostructures were proposed, [26, 135] which are assembled by stacking different 2D materials in hetero-layered architectures. [17] In this case, individual 2D materials can be constructed into heterostructured electrodes with different 2D building blocks. By building the 2D heterostructures, it is possible to combine the advantages and eliminate the disadvantages of the individual 2D materials. To engineer the 2D heterostructures, many techniques have been performed such as vacuum

deposition, [136] dipping or spinning, [17] and in-situ wet chemistry synthesis, [137] which are highly efficient for electronic applications, but not practical for creating battery electrodes due to the problematic scalability. Recently, the layer-by-layer (LBL) spray deposition technique has been widely recognized as an efficient, low-cost, and scalable approach to prepare 2D film electrodes. [54-56] In addition, LBL spray deposition allows for precise control of film electrode thickness and the assembled layer sequence. As mentioned in **chapter 3**, an easy solution processing of 2D MoS_2 and MXenes has been established, which is perfectly convenient for creating heterostructured electrodes through the spraying deposition technique.

Herein, the goal of the current work is to determine if a 2D heterostructure of $Ti_3C_2T_x$ (MXene) and MoS_2, which is engineered by LBL spray deposition, can result in improved lithium storage performance regarding capacity and stability. To this end, firstly, three different types of 2D $MoS_2/Ti_3C_2T_x$ heterostructures were prepared (**Scheme 4.1**), which are denoted as $(Ti_3C_2T_x/MoS_2)xn$ (n = 1, 2, 3, 4 and 8) and $(MoS_2/Ti_3C_2T_x)x3$ and are featured with a terminal layer of MoS_2 and $Ti_3C_2T_x$ nanosheets, respectively. As a comparison, $MoS_2/Ti_3C_2T_x$-mixed heterostructure was made by spraying a conventional mix of MoS_2 and $Ti_3C_2T_x$ suspensions. Compared to the single 2D MoS_2 electrode, both $(Ti_3C_2T_x/MoS_2)xn$ (n = 3 and 8) and $MoS_2/Ti_3C_2T_x$-mixed heterostructures still have shown capacity degradation during long-term cycling, especially at high rates (e. g. 0.5 and 1.0 A g^{-1}). However, the $(MoS_2/Ti_3C_2T_x)x3$ heterostructure does not exhibit capacity decline at various rates, but long-term activation cycles were required to achieve high and stable capacities. Next, to further improve the electrode activity of $(MoS_2/Ti_3C_2T_x)x3$, single-wall carbon nanotubes (CNTs) were incorporated to obtain the $(MoS_2/Ti_3C_2T_x/CNTs)x3$ heterostructure. Meanwhile, in the same way, the $MoS_2/Ti_3C_2T_x$/CNTs-mixed heterostructure was prepared and evaluated as a reference. The electrochemical results demonstrated that the $(MoS_2/Ti_3C_2T_x/CNTs)x3$ heterostructure with continuous large-area layers of the face-to-face contacts between 2D MoS_2 and $Ti_3C_2T_x$ nanosheets can better buffer the severe volume expansion of MoS_2, particularly at high current densities. Moreover, this rationally engineered heterostructure with an order stacking of MoS_2/CNTs and $Ti_3C_2T_x$/CNTs layers can maximize the lithium storage capability of each constituent component due to synergistic effects, which is also highly superior to the conventional heterostructure mixing with a random restacking. The CNTs acting as conductive additive for the heterostructure, not only facilitate faster reversible transport of electrons and ions at the interface between adjacent nanosheets but also prevent the terminal $Ti_3C_2T_x$ layer from aggregation during

lithiation/delithiation, which is further confirmed by electrochemical impedance spectroscopy (EIS) and *ex-situ* SEM, respectively. Finally, the electrochemical performance of the ($MoS_2/Ti_3C_2T_x$/CNTs)x3 heterostructure was evaluated in lithium-ion full cells with the commercial $LiNi_{0.6}Co_{0.2}Mn_{0.2}O_2$ (NCM622) cathode material.

4.2 Experimental section

4.2.1 Materials

Molybdenum disulfide powder, (MoS_2, 99%, Sigma Aldrich), 1-methyl-2-pyrrolidinone (NMP, >99%, Sigma Aldrich), 2-propanol (IPA, 99%, Sigma Aldrich), lithium fluoride, (LiF, ≥99.98%, Sigma Aldrich), hydrochloric acid (HCl, 37% wet. in H_2O, Sigma Aldrich), polyethyleneimine (PEI), branched (M.W. 70,000, 30% w/v, aqueous solution), carbon nanotubes (single-walled, carboxylic acid functionalized), $LiNi_{0.6}Co_{0.2}Mn_{0.2}O_2$ (NCM622) cathode (60%Ni, 20%Co, 20%Mn) was obtained from BASF SE (Ludwigshafen, Germany), (polyvinylidene difluoride) PVdF binder (Solefs130, Sigma Aldrich), carbon black (Super C65, Alfa Aesar).

All chemicals were used as received without further purification.

4.2.2 Synthesis of Ti_3AlC_2 (MAX phase)

Ti_3AlC_2 MAX phase was provided by Dr. Christopher Shuck, Drexel University, U.S.A.

4.2.3 Synthesis and delamination of 2D $Ti_3C_2T_x$ nanosheets

$Ti_3C_2T_x$ was synthesized by using Minimally Intensive Layer Delamination (MILD) method through selective etching of the aluminum layer from Ti_3AlC_2 by a so-called in-situ HF etchant solution, which can be found elsewhere in detail. [12, 131, 138] Typically, 1.0 g LiF powder was added to 20 ml of 6 M HCl in a PTFE bottle (100 ml) under magnetic stirring for 10 min. 1.0 g Ti_3AlC_2 powder was added slowly to the above solution for 5 min at room temperature. Subsequently, the mixture was transferred into an oil bath with a temperature of 35 °C and continued stirring for 24 h at 450 rpm. The mixture was washed with deionized water by centrifugation in a 150 ml conical centrifuge tube, after which the supernatant was disposed, of at 3500 rpm 3 or 4 times for 5 min per cycle until the supernatant with a pH of ≥ 6 was obtained. At this stage, adding

DI H_2O to the sediment and then hand-shaking it strongly for 10 ~ 15 min results in delamination of the nano-flakes. The mixture was subjected to further centrifugation at the same condition, then a dark-green supernatant was obtained and transferred into a new tube to centrifuge at 3500 rpm for 30 min. The concentration of $Ti_3C_2T_x$ MXene is around 0.2 ~ 0.3 mg ml^{-1}, which was detected by UV-vis.

4.2.4 Synthesis of exfoliated 2D MoS_2 nanosheets

MoS_2 nanosheets were prepared by LPE, which has been described in **chapter 3**. In the end, a processible colloidal solution with a concentration of 0.1 ~ 0.2 mg ml^{-1} was obtained (detected by UV-vis).

4.2.5 Fabrication of SWCNTs suspension

SWCNTs suspension was prepared by the same tip sonication conditions from the exfoliation of MoS_2 raw material. Typically, 5.0 mg SWCNTs were dispersed into the 100 ml mixture solution of H_2O and IPA (50:50 in volume), and subsequently, ultra-sonicated for 1 h. The mixture of SWCNTs was centrifuged at 2500 rpm for 1 h to get rid of undispersed nanotubes such as impurities. Finally, a concentration of around 0.05 mg ml^{-1} SWCNTs was obtained by pipetting approximately 98% supernatant from the above mixture.

4.2.6 Concentration determination of delaminated $Ti_3C_2T_x$ nanosheets and exfoliated MoS_2 nanosheets

The measurement of exfoliated MoS_2 nanosheets concentration has been introduced in **chapter 3**. Here, similar to the case of MoS_2, concentration of $Ti_3C_2T_x$ suspension was measured by UV-Vis spectrometer. Firstly, measuring the absorbance for a series of given concentrations (from 0.05 to 0.5 mg ml^{-1}) $Ti_3C_2T_x$ suspension; secondly, collecting the absorbance data at the wavelength of 780 nm; finally, the linear correlation equation between absorbance value and concentration was obtained by fitting these data points (y-axis is absorbance and standard concentration as the x-axis). Once the correlation line is established, the unknown concentration of the $Ti_3C_2T_x$ suspension can be determined by the above-plotted graph, as shown in **Figure 4.1a** and **b**.

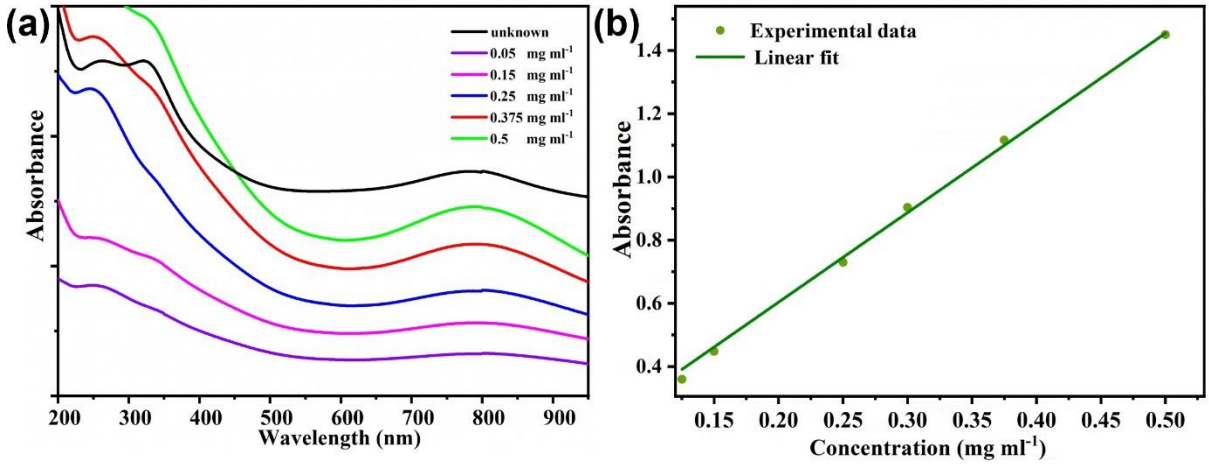

Figure 4.1 UV-vis spectra of (a) $Ti_3C_2T_x$ suspension and corresponding linear fitting of (b) $Ti_3C_2T_x$ (at 780 nm) with a slope of 2.84.

4.2.7 Layer-by-layer spray deposition assembly of 2D MoS_2 and $Ti_3C_2T_x$ electrodes

The two pure exfoliated MoS_2 and delaminated $Ti_3C_2T_x$ electrodes were made by a scalable automatic spray machine equipped with two suspension atomization nozzles and a heated vacuum stage-chuck (Sono-tek, coater 300, USA). Here, the manufacturing of MoS_2 electrodes by spray deposition is introduced in brief. As for the case of $Ti_3C_2T_x$, one just need to change the feeding suspension from MoS_2 to $Ti_3C_2T_x$ and adjust the flow rate of the nozzle to 0.1 ml min^{-1}. Typically, two types of suspensions were prepared through the whole spray process: (1) an aqueous solution of PEI (binder) with a known concentration of 0.1 mg ml^{-1}; and (2) exfoliated MoS_2 nanosheets in IPA (activated materials) with a given concentration. First, according to the concentration of binder and MoS_2, as well as the fixed moving speed of nozzles with flow rates of 0.2 (for MoS_2) and 0.1 (for PEI) ml min^{-1} by counting spray time (in minutes), all of the electrodes in this work were sprayed with a mass ratio of 5:95 (PEI:MoS_2). Secondly, the above two suspensions were pumped into separate nozzles, atomized into fined droplets within the nozzles (equipped with sonication generator), and then were sprayed into a column by compressed Ar, and consecutively sprayed onto Cu foil, clamped on a heated vacuum chuck with keeping a temperature of 40 °C through the whole spraying process. The distance between spray nozzles and chuck was kept at 40 mm and a dwell time of 5 seconds was applied in consecutive cycles. In this case, any solvent droplets were immediately evaporated on the Cu foil surface from the shaping gas stream (here: Ar gas). Thirdly, to produce the electrode, two cycles of PEI were sprayed onto the Cu foil first to interface with the coming MoS_2 nanosheets (50 cycles) afterwards. The moving speed of the nozzles is 30 mm

min^{-1} (**Scheme 4.1**). This alternative spray operation was repeated until all of the pre-calculated suspension of MoS_2 nanosheets was consumed. Finally, a thin film of the MoS_2 electrode with a thickness of ~ 3 μm was obtained. The as-sprayed electrode was then subjected to dry in a vacuum oven at 70 °C overnight in preparation for electrochemical measurement.

4.2.8 Layer-by-layer spray deposition assembly of three different types of 2D $Ti_3C_2T_x/MoS_2$ heterostructures

To investigate the effect of 2D heterostructures on lithium storage, three different types of heterostructured electrodes were prepared:

I) $Ti_3C_2T_x/MoS_2$-mixed and $Ti_3C_2T_x/MoS_2$/CNTs-mixed

A conventional mixture of MoS_2 and $Ti_3C_2T_x$ suspension was blended in a mass ratio of 1:1 as a feeding solution to spray with PEI binder. The same alternative spray protocol was adapted from the spray process of MoS_2 except for changing the flow rate of a nozzle to 0.15 ml min^{-1}. The as-sprayed electrode is labeled as $Ti_3C_2T_x/MoS_2$-mixed. In the case of $Ti_3C_2T_x$ and MoS_2 mixed with SWCNTs (nanotubes were used as the conductive additives), 10% SWCNTs suspension was mixed with the $Ti_3C_2T_x$ and MoS_2 supernatants separately, then the same LBL spray recipes were applied to prepare the $Ti_3C_2T_x/MoS_2$/SWCNTs heterostructures, which labeled as $Ti_3C_2T_x/MoS_2$/CNTs-mixed.

II) $(Ti_3C_2T_x/MoS_2)xn$ (n = 1, 2, 3, 4 and 8)

Compared to a straightforward blend of the suspension of $Ti_3C_2T_x$ and MoS_2 to randomly restack mixed nanosheets, a consecutive alternatively spray can restack these two types of nanosheets in a well-ordered way to create the heterointerfaces with continuous large-area layers of 2D MoS_2 and $Ti_3C_2T_x$ nanosheets. To this end, the creation of several bilayers of MoS_2 and $Ti_3C_2T_x$ were performed by so-called alternative spraying. Firstly, 2 cycles of PEI were sprayed onto a Cu foil at a defined area, and then 100 cycles of $Ti_3C_2T_x$ were sprayed (at a flow rate of 0.1 ml min^{-1}) on top of the PEI layer with a flow rate of 0.1 ml min^{-1}. Secondly, 50 cycles of MoS_2 were sprayed (at a flow rate of 0.2 ml min^{-1}) on top of the $Ti_3C_2T_x$ layer after spraying 2 cycles of PEI in between. The same mass ratio of binder (PEI) to activated materials (MoS_2 and $Ti_3C_2T_x$) was kept at 5:95, but the weight ratio of $Ti_3C_2T_x$ to MoS_2 is 1:1. Note that the full coverage of 100 and 50 spray cycles for $Ti_3C_2T_x$ and MoS_2, respectively, was confirmed by SEM. At this stage, one bilayer of $Ti_3C_2T_x/MoS_2$ was obtained, which was labelled as the $(Ti_3C_2T_x/MoS_2)x1$ heterostructure. By analogy, the $(Ti_3C_2T_x/MoS_2)x3$ heterostructure was made by repeating 3 times the above spray process. In addition, to optimize the electrochemical

performance of the $Ti_3C_2T_x/MoS_2$ heterostructured electrode, the $(Ti_3C_2T_x/MoS_2)xn$ electrodes (n= 1, 2, 4, and 8) were prepared under the same spray conditions. Here, it is important to point out that the $(Ti_3C_2T_x/MoS_2)xn$ electrodes are featured with the end termination layers of MoS_2, which means that the top surface of these electrodes consists of 2D MoS_2 nanosheets.

III $(MoS_2/Ti_3C_2T_x)x3$ and $(MoS_2/Ti_3C_2T_x/CNTs)x3$

For the sake of exploring how the top surface of the electrodes (termination layer is $Ti_3C_2T_x$ or MoS_2 nanosheets) affect the electrochemical performances, a $(MoS_2/Ti_3C_2T_x)x3$ heterostructure electrode was fabricated with the same parameters as for $(Ti_3C_2T_x/MoS_2)x3$. The only change was to spray 50 cycles of MoS_2 firstly onto the Cu foil with 2 cycles of PEI layer, and then 100 cycles of $Ti_3C_2T_x$ were sprayed on top of that afterward, to build a $MoS_2/Ti_3C_2T_x$ bilayer. $(MoS_2/Ti_3C_2T_x)x3$ heterostructures electrode with the termination layer of $Ti_3C_2T_x$ was produced by repetitive spraying three times of the $MoS_2/Ti_3C_2T_x$ bilayer. In addition, in the case of the heterostructures with SWCNTs, which was prepared by mixing SWCNTs suspension with MoS_2 and $Ti_3C_2T_x$ solution, respectively, and then the same spray recipes of $MoS_2/Ti_3C_2T_x$ bilayer were performed to manufacture a new bilayer of MoS_2-SWCNT/$Ti_3C_2T_x$-SWCNT. It is worth noting that the weight fraction of SWCNTs is 10% of the sum mass of MoS_2 and $Ti_3C_2T_x$ nanosheets. In the same way, the (MoS_2-SWCNTs/$Ti_3C_2T_x$-SWCNTs)x3 heterostructures electrode was obtained by repeating spraying this bilayer three times, which is labeled as $(MoS_2/Ti_3C_2T_x/CNTs)x3$. All of the electrodes were sprayed at the mass ratio of 5:95 (PEI:$MoS_2/Ti_3C_2T_x$/CNTs).

4.2.9 Material characterization

SEM was performed in a *Zeiss Supra 55* (Germany), XRD was performed on a *STOE STADI P* diffractometer with Cu $K_{\alpha 1}$ radiation (λ=1.54060 Å) in transmission mode at room temperature. TEM imaging was performed on A Themis-Z transmission electron microscopy (*TEM, FEI Tecnai F20*, U.S.A). XPS investigation was performed in a K-Alpha spectrometer (*ThermoFisher Scientific*, East Grinstead, UK) using a micro-focused, monochromated Al K_α X-ray source (400 µm spot size).

4.2.10 Electrochemical measurements

CR-2025 coin cells were assembled by using exfoliated 2D MoS_2 nanosheets, delaminated $Ti_3C_2T_x$ flakes, and their different heterostructures as the working electrode. All electrodes were punched into a disk with a diameter of 12 mm. The average mass loading of the activated material (MoS_2 and $Ti_3C_2T_x$) is around 0.3-0.5 mg cm^{-2} except for the special case of $(Ti_3C_2T_x/MoS_2)x8$

electrode with an activated mass loading of 0.8 mg cm^{-2}. Furthermore, the NCM cathodes used in the full cells consisted of 80 wt% NCM622 as active material, 10 wt% Super C65, and 10 wt% PVdF as a binder. The NCM-based slurry was prepared by a mixer centrifuge at 2500 rpm for 5 min, afterward cast on the Al foil utilizing a lab coating bridge (wet active film with a thickness of 60 μm). The casted electrode was firstly dried in an oven at 80 °C for 6h and then further dried in a vacuum oven at 120 °C overnight. Finally, the electrode is punched to a disk (ø = 12 mm) with a mass loading of active material about 1.3 – 1.8 mg cm^{-2}. The overall mass for all electrodes was measured by a microbalance (*Sartorius*, Germany) with 0.0001 mg accuracy. 1 M $LiPF_6$ in ethylene carbonate/dimethyl carbonated (EC/DMC, 1:1, V/V) was used as an electrolyte. *Celgard* 2500 separator soaked in electrolyte with 70 μl and Li metal foil served as the counter electrode. The cells were assembled in an Ar-filled glovebox with the O_2 and H_2O levels below 0.1 ppm (*MBraun*, Germany), and then placed into a big oven with a temperature of 25 °C (*Binder*, Germany) for the electrochemical measurements.

Cyclic voltammetry (CV), galvanostatic cycling with potential limitation (GCPL), and electrochemical impedance spectra (EIS) were performed on a multichannel potentiostat. CV and GCPL were recorded in the voltage range of 0.01-3.0 V *vs.* Li^+/Li at various scan rates and current densities, respectively. EIS measurements were conducted with frequencies ranging from 0.01 Hz to 500 kHz at defined GCPL cycles. An input voltage with an amplitude of 5 mV was employed and all the cells rested for 3 hours before each recording of the impedance data. The impedance data were further analyzed by using the software Relaxis (*rhd* Instruments, Germany).

4.3 Results and Discussion

4.3.1 Structural and morphological characterization of delaminated $Ti_3C_2T_x$ and exfoliated MoS_2 nanosheets

First, $Ti_3C_2T_x$ and MoS_2 nanosheets were produced by selectively etching the metal bonds (Al-Ti) with in-situ HF (HCl + LiF) and then sonicating MoS_2-bulk materials in NMP solvent, [139-140] respectively, as illustrated in **Scheme 4.1**. Then the quality of both nano-flakes was evaluated by electron microscopy techniques. The SEM image (**Figure 4.2a**) shows a typical bulk structure of Ti_3AlC_2, which can be completely delaminated into well-shaped and clean surface 2D nano-flakes with a uniform size of around 500 nm in diameter (**Figure 4.2b**). A higher resolution (HR) TEM image is presented in **Figure 4.2c**, showing that a few-layer of $Ti_3C_2T_x$ nanosheets with well-defined edges and hole-free planes were obtained. The hexagonal arrangement of atoms of the

$Ti_3C_2T_x$ nanosheets was confirmed by the selected area electron diffraction (SAED) pattern (**Figure 4.2d**). These images show that high-quality few-layer $Ti_3C_2T_x$ flakes without defects are obtained after delaminating Ti_3AlC_2 crystals. In the case of MoS_2, **Figure 4.2e** shows a chunk-like structure of the pristine MoS_2 raw materials before exfoliation. The electron-transparent exfoliated-MoS_2 nanosheets with well-defined, edges and basal planes are presented in **Figure 4.2f** and **g**, demonstrating that a few-layer exfoliated MoS_2 nanosheets is of high quality. This is further confirmed by the SAED patterns (**Figure 4.2h**) in which a hexagonal lattice symmetry is observed in the exfoliated MoS_2 nanosheets with a highly-crystalline structure, which indicates that the crystal structure of hexagonal MoS_2 bulk was well-retained.

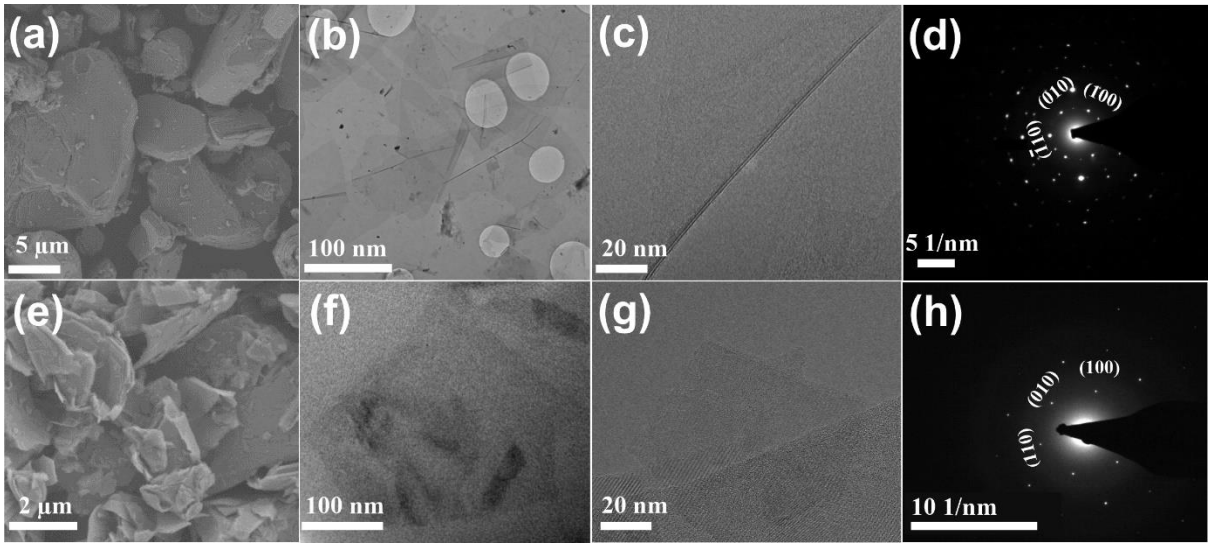

Figure 4.2 (a) SEM image of Ti_3AlC_2 MAX phase, (b) and (c) are TEM images of delaminated $Ti_3C_2T_x$ nanosheets with different magnifications, and (d) SAED pattern of (c) $Ti_3C_2T_x$ nanosheets; (e) the SEM image of MoS_2-bulk materials, (f) and (g) are TEM images of exfoliated MoS_2 nanosheets, and (h) SAED pattern of (g) MoS_2 nanosheets.

Next, the delaminated $Ti_3C_2T_x$ (in H_2O) and exfoliated MoS_2 (in IPA) nanosheets suspension or $Ti_3C_2T_x$ mixed with MoS_2 supernatant were served as feeding materials to produce electrodes with different types of heterostructures through layer-by-layer spray deposition, which is elaborated in **Scheme 4.1**. The detailed preparation process of the electrodes can be found in the section **4.2.8**.

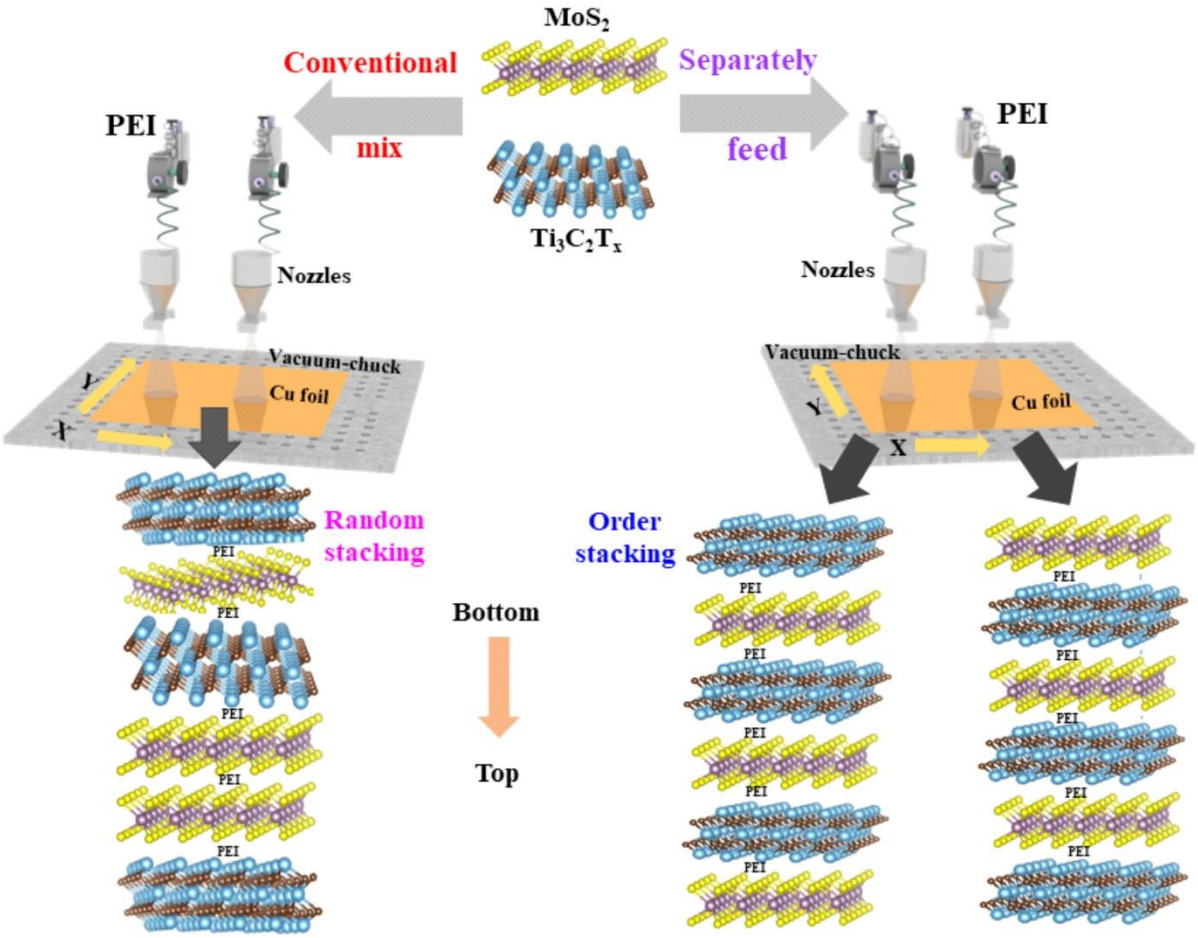

Scheme 4.1 Schematic diagram for the preparation of $Ti_3C_2T_x$ and MoS_2 nanosheets, and engineering of different types of $MoS_2/Ti_3C_2T_x$ heterostructures with MoS_2 and $Ti_3C_2T_x$ nanosheets through layer-by-layer spray deposition.

4.3.2 XRD characterization of MoS_2-bulk, Ti_3AlC_2-bulk, and sprayed electrodes with corresponding 2D nanosheets

Crystal structure of raw MoS_2 and Ti_3AlC_2 as well as sprayed heterostructures with their respective nanosheets (exfoliated MoS_2 and delaminated $Ti_3C_2T_x$) were evaluated by XRD and analyzed by Rietveld refinement with the *FullProf* software package. XRD patterns of raw MoS_2 powder and 2D MoS_2 electrode are presented in **Figure 3.3a** and **b**, respectively. The description of that has been introduced in detail in **chapter 3**.

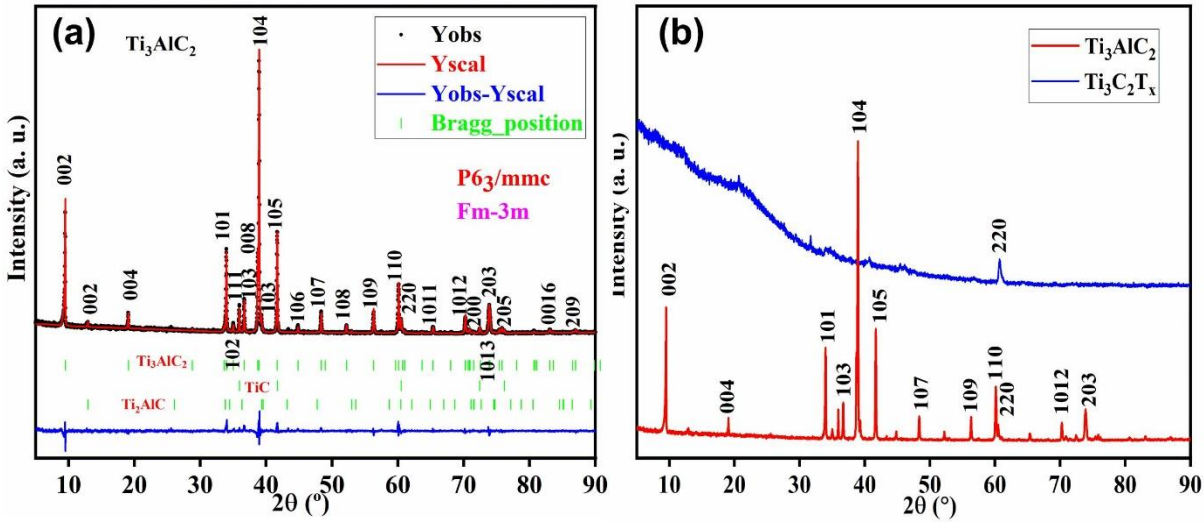

Figure 4.3 (a) the XRD pattern and Rietveld refinement data of Ti_3AlC_2-bulk powder, and (b) XRD pattern of the sprayed $Ti_3C_2T_x$ nanosheets on a cellulose acetate film in comparison to Ti_3AlC_2.

In the case of the Ti_3AlC_2 MAX phase, the raw material shows quite sharp peaks with high intensity, suggesting good crystallization (see **Figure 4.3a**). The XRD pattern of Ti_3AlC_2 was fitted well by the Rietveld refinement method. The phase composition of the raw material can be fitted into three phases, which are Ti_3AlC_2 (95%), TiC (4.3%), and Ti_2AlC (0.7%), respectively, the impurity phases (TiC and Ti_2AlC) might be caused by the synthesis process of Ti_3AlC_2. The reflections of Ti_3AlC_2 and Ti_2AlC are assigned to the hexagonal structure space group $P6_3/mmc$ (No. 194). The corresponding parameters of the TiC indicated the cubic structure which belongs to the space group Fm-3m (No. 225). The lattice parameters of the main phase (Ti_3AlC_2) are calculated to be a = b = 3.071(1) Å, c = 18.56(1) Å, which are in good agreement with a previous report. [141] The characteristic reflection of the raw Ti_3AlC_2 MAX phase at (2θ = 39.2°) almost vanished after spray-restacking of delaminated $Ti_3C_2T_x$ nanosheets, leaving only one 220 reflection at 60.7°, indicating successful etching of the Al layer from Ti_3AlC_2 into layered $Ti_3C_2T_x$ structures. [132] Moreover, the full delamination of the etched $Ti_3C_2T_x$ was also confirmed by the disappearance of 00*l* peaks in the restacked $Ti_3C_2T_x$ nanosheets. [142]

4.3.3 XPS studies of MoS_2, $Ti_3C_2T_x$, $MoS_2/Ti_3C_2T_x$/CNTs-mixed and $(MoS_2/Ti_3C_2T_x/CNTs)x3$ heterostructures

The formation and chemical components of two representative heterostructures, $(MoS_2/Ti_3C_2T_x/CNTs)x3$ (order stacking) and $MoS_2/Ti_3C_2T_x$/CNTs-mixed (random stacking), were investigated using X-ray photoelectron spectroscopy

(XPS). Pristine 2D MoS_2 and $Ti_3C_2T_x$ electrodes were also analyzed and used as references. These three electrodes exhibit clearly an intensive Mo 3d doublet with Mo $3d_{5/2}$ at 229.7 eV and corresponding S 2p doublet with S $2p_{3/2}$ at 162.6 eV, respectively, (green area), as shown in **Figure 4.4a-b**. Note that the pristine MoS_2 and $MoS_2/Ti_3C_2T_x$/CNTs-mixed heterostructure have no deconvoluted peaks attributable to MoO_x and S (VI), but they are clearly visible in the Mo 3d (at 232.5 eV) and S 2p (at 168.5 eV) XPS spectras of the $(MoS_2/Ti_3C_2T_x/CNTs)x3$ heterostructure. This result suggests that the $(MoS_2/Ti_3C_2T_x/CNTs)x3$ heterostructure with order stacking cannot protect MoS_2 layers from oxidation as good as pristine MoS_2 and $MoS_2/Ti_3C_2T_x$/CNTs-mixed heterostructure. The Ti 2p spectrum of above two heterostructures (**Figure 4.4c**) shows the doublet with Ti $2p_{3/2}$ at 455.3 eV for TiC (Ti-C), as well as several other doublets arising from oxidized and fluorinated species such as O-Ti-C (456.0 eV), F-Ti-C (457.0 eV), and oxy-fluorinated moieties with Ti $2p_{3/2}$ at 460.0 eV. [143] [144] There are pronounced peaks at 458.8 eV attributed to TiO_2 (pink area) in the pristine $Ti_3C_2T_x$, $MoS_2/Ti_3C_2T_x$/CNTs-mixed, and $(MoS_2/Ti_3C_2T_x/CNTs)x3$ heterostructures, a fact verifies the oxidation of Ti_3C_2 after spraying. Also, here the well-defined $(MoS_2/Ti_3C_2T_x/CNTs)x3$ heterostructure is more oxidized than the $MoS_2/Ti_3C_2T_x$/CNTs-mixed heterostructure with random stacking of MoS_2 and $Ti_3C_2T_x$ nanosheets, which is consistent with the oxidation of Mo and S atoms (**Figure 4.4a-b**). Finally, the C 1s spectrum of three electrodes is presented in **Figure 4.4d**, which shows a peak at 281.8 eV for TiC (orange area) and two peaks corresponding to carbon species of C-H/C-C (285 eV) and C-O (286.3 eV). Furthermore, the presence of the C-C sp^2 hybrid orbital (284.3 eV, grey area) in the C 1s XPS spectrum of $(MoS_2/Ti_3C_2T_x/CNTs)x3$ and $MoS_2/Ti_3C_2T_x$/CNTs-mixed heterostructures is fully evident (**Figure 4.4d**), a peak originating from the CNTs. Therefore, the presence of MoS_2, Ti_3C_2, and CNTs is confirmed in the aforementioned two heterostructures, demonstrating that the 2D MoS_2, $Ti_3C_2T_x$ nanosheets, and CNTs were successfully engineered.

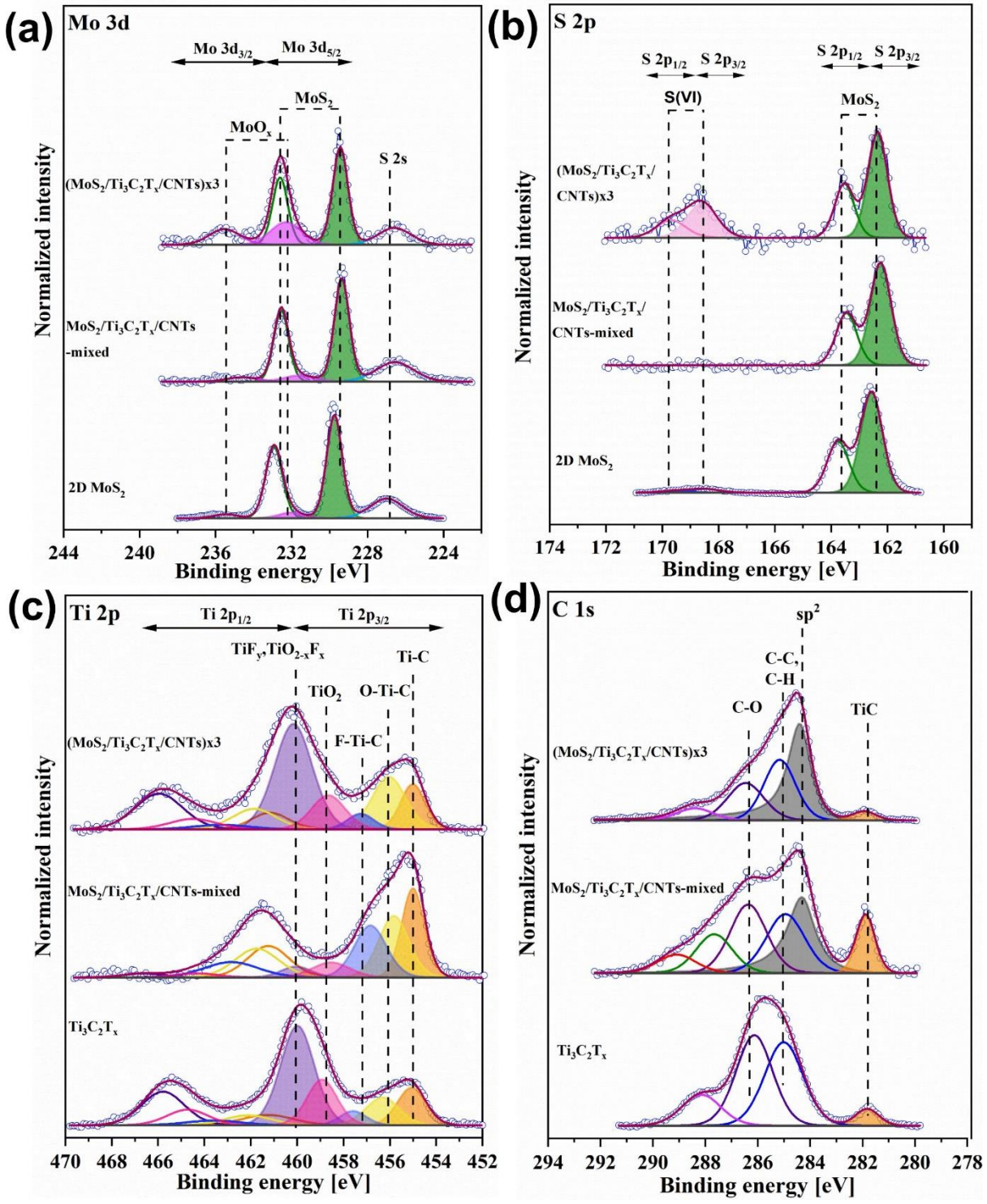

Figure 4.4 (a) Mo 3d, (b) S 2p, (c) Ti 2p and (d) C 1s XPS spectra of the $MoS_2/Ti_3C_2T_x$/CNTs-mixed, $(MoS_2/Ti_3C_2T_x/CNTs)x3$ heterostructures, pristine 2D MoS_2 and $Ti_3C_2T_x$ electrodes

4.3.4 Electrochemical Characterization

4.3.4.1 Electrochemical performance of $Ti_3C_2T_x$ and MoS_2 electrodes

Herein, firstly, the lithium storage behavior of the sprayed $Ti_3C_2T_x$ and 2D MoS_2 electrodes were elucidated by cyclic voltammetry (CV) and galvanostatic cycling with potential limitation (GCPL) measurements.

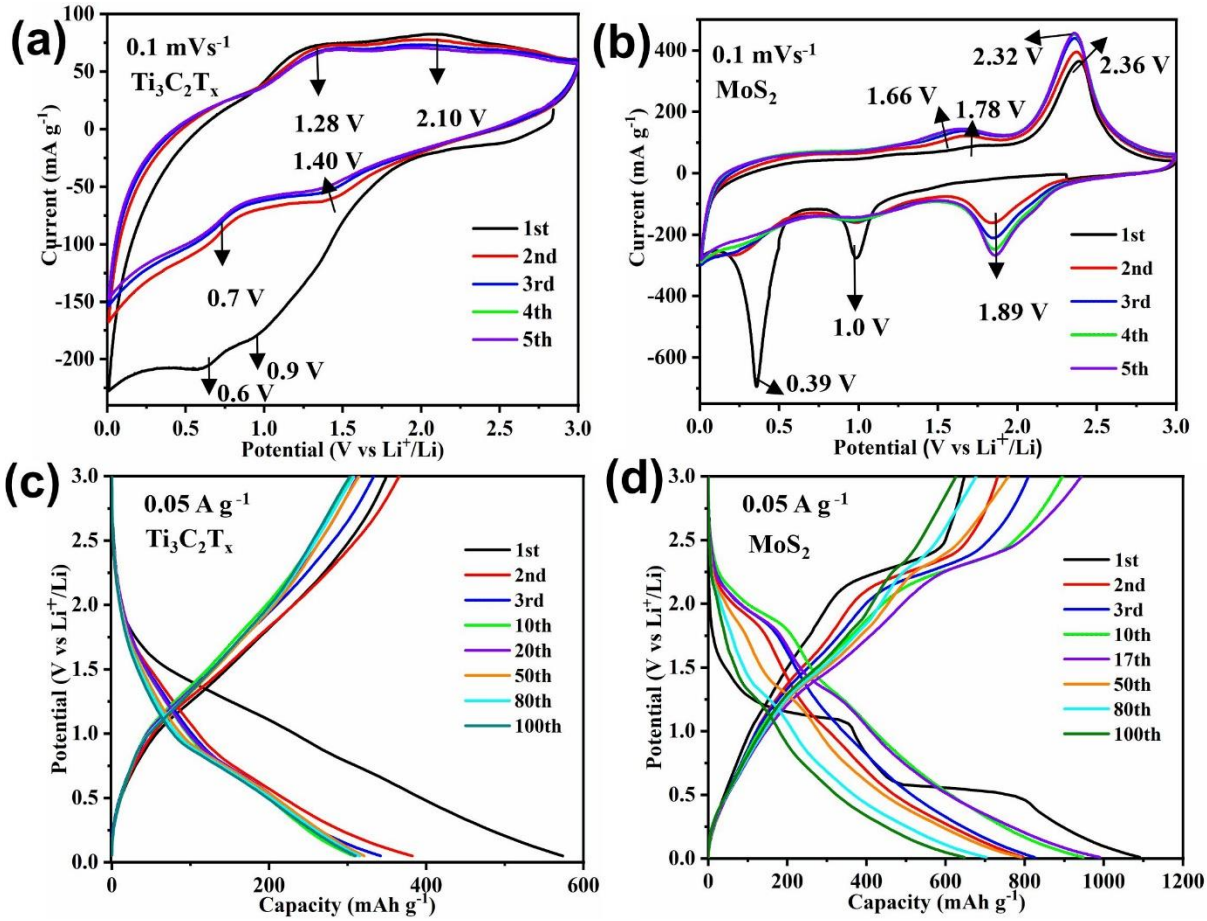

Figure 4.5 Electrochemical measurements of the sprayed $Ti_3C_2T_x$ and 2D MoS_2 electrodes (a) and (c) are the CVs at a sweep rate of 0.1 mV s^{-1} and voltage profile of sprayed $Ti_3C_2T_x$ electrode at a current of 0.05 A g^{-1}, respectively; (b) and (d) are the CV at a sweep rate of 0.1 mV s^{-1} and voltage profile of sprayed MoS_2 electrode at a current of 0.05 A g^{-1}, respectively.

Figure 4.5a shows the first five CV plots of $Ti_3C_2T_x$ electrode at a scan rate of 0.1 mV s^{-1} within a potential window between 0.01 and 0.3 V. The distorted rectangular-like CV curves of the $Ti_3C_2T_x$-sprayed is quite similar to previous reports. [137, 145-146] Two broad reduction peaks around 0.90 and 0.60 V can be observed in the first discharge process (lithiation), which were related to the lithium-ion intercalation between interlayers [147] and the formation of a solid electrolyte interphase (SEI) in the working electrode, respectively. [19] There are two weak peaks at 1.28 and 2.10 V in the subsequent charge process, which are attributed to the de-intercalation of Li-ion from the $Ti_3C_2T_x$ interlayers. It is worth noticing that the peak at 1.28 V was mostly unchanged and the peak at 2.10 V exhibited a slight decrease in subsequent anodic scans. There are two

new peaks at 1.40 and 0.7 V appearing from the second to fifth cathodic sweeps, which should correspond to the lithium-ion intercalation into the cycled $Ti_3C_2T_x$ interlayer spacing. [134, 137] The highly overlapped rectangular-shaped CV curves demonstrated that the Li-ion intercalation/de-intercalation into/from the $Ti_3C_2T_x$ electrode is highly reversible, which was further confirmed by the reversible charge capacity of 314 mAh g^{-1} after 50 cycles, as shown in the voltage profile (**Figure 4.5c**). Sprayed $Ti_3C_2T_x$ nanosheets deliver a specific capacity of 537 mAh g^{-1} with a current density of 0.05 A g^{-1} in the first discharge process. And a charge capacity of 365 mAh g^{-1} was obtained with an initial coulombic efficiency (ICE) of 59%, a large irreversible capacity loss was ascribed to the formation of the solid electrolyte interfaces (SEI) layer because of the restacked-layered electrode with porous morphology (see **Figure 4.6a** and **b**). In addition, the low ICE might have also resulted from some irreversible reactions between Li-ions and hydroxyl/fluorine-containing species on the surfaces of $Ti_3C_2T_x$ layers. [20, 134] On the whole, the sluggish-shaped potential profiles demonstrate that the $Ti_3C_2T_x$ electrode exhibits a typical pseudo-capacitive behavior, although Li^+ insertion/extraction occurs upon cycling. [148] Moreover, a relatively stable electrochemical performance of the $Ti_3C_2T_x$ electrode was observed, for instance, the electrode delivers a discharge capacity of 301 mAh g^{-1} at the 10th cycle, which even continuously increased to 323 mAh g^{-1} with a coulombic efficiency of 99 % at the end of 100 cycles. This result has also been observed in previous $Ti_3C_2T_x$ works and has been attributed to the exposure of additional electrochemically active sites upon cycling. [134, 136, 149] The morphological structure of cycled electrodes was investigated by *ex-situ* SEM, as shown in **Figure 4.6c**, as expected, no cracked or slit-like structure was obtained on the electrode surface, indicating that the sprayed $Ti_3C_2T_x$ electrode possesses a robust mechanical strength.

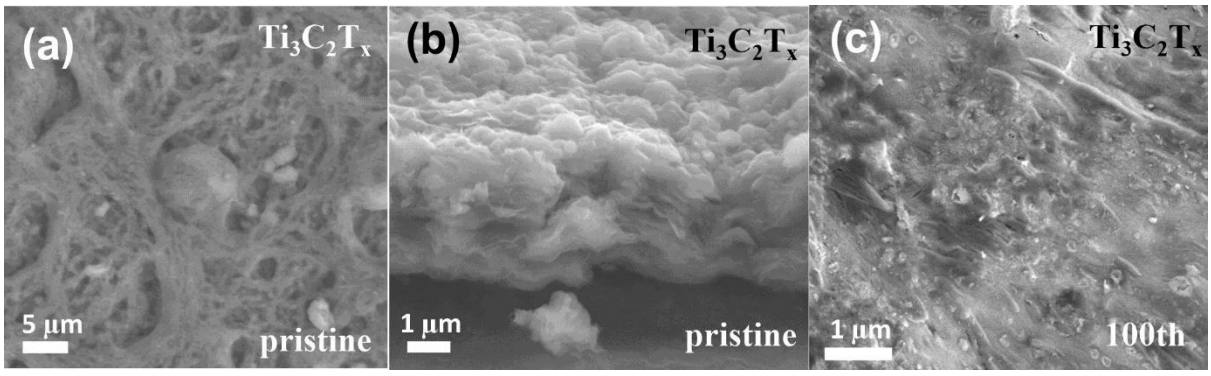

Figure 4.6 SEM images of (a) and (b) are the top view and cross-section for pristine sprayed $Ti_3C_2T_x$ electrode, respectively. (c) The top view of sprayed $Ti_3C_2T_x$ electrode after 100 cycles at a current density of 0.05 A g^{-1}.

Figure 4.5b shows the CV curves (from 1st to 5th cycle) of the sprayed MoS_2 nanosheets at a scan rate of 0.1 mV s^{-1}. Two pronounced peaks can be observed at 1.0 and 0.39 V, respectively, during the first lithiation process. The reduction peak at 1.0 V can be assigned to the Li-ion insertion into the interlayer of the sprayed MoS_2 electrode, which has undergone a phase transformation from the 2H to 1T structure, to form 1T Li_xMoS_2 ($0< x <1$), see **equation 4.1** *i.e.*, from the original trigonal prismatic or hexagonal structure (2H) to octahedral (1T) Mo coordination. [150-152] As shown in the following equations:

$$2H\ MoS_2 + xLi^+ + xe^- \rightleftharpoons 1T\ Li_xMoS_2 \quad (0< x<1, \sim 1.1\ V) \qquad \textbf{(equation 4.1)}$$

$$1T\ Li_xMoS_2 + (4 - x)Li^+ + (4 - x)e^- \rightleftharpoons Mo + 2Li_2S \quad (\sim 0.4 - 0.6\ V) \qquad \textbf{(equation 4.2)}$$

$$Mo + 2Li_2S \rightleftharpoons 2H\ MoS_2 + 4Li^+ + 4e^- \quad (\sim 2.4\ V) \qquad \textbf{(equation 4.3)}$$

As the discharge further proceeds deeply, the second strong peak at 0.39 V appears, which can be ascribed to the reduction of Li_xMoS_2 to produce the Mo atoms with Li_2S (by known conversion reaction, **equation 4.2**) and the decomposition of electrolyte to form the SEI layer. [73] These two reduction peaks at 1.0 and 0.39 V are corresponding to the voltage plateau at 1.0 and 0.5 V in the potential profile in the first lithiation process, respectively, which are in good agreement with previous reports. [153-154] In the subsequent charge process (delithiation), a weak oxidation peak at 1.78 V and a pronounced oxidation peak at 2.36 V were observed. In general, it is widely accepted that the first oxidation peak is attributed to the partial or stepwise oxidation of Mo and Li_2S to produce 1T Li_xMoS_2 ($0< x <1$). [155] Following the results of previous reports, [90, 156-157] the secondary oxidation peak can be assigned to the reformation 2H MoS_2 but with highly decreased crystallinity or amorphous structure, as shown in **equation 4.3**. In addition, the reversibility mechanism of the 2D MoS_2 electrodes has been investigated separately in **chapter 3**. The current work still argue this reversible mechanism. The two pronounced reduction peaks in the first lithiation curve disappeared in subsequent cathodic scans (from the 2nd to the 5th cycle), instead of appearing as a new peak at ca. 1.89 V, which is generally attributed to the phase transformation of the produced 2H MoS_2 to 1T Li_xMoS_2 again. [90, 94, 156] This significant difference of the CV curves between the first and subsequent lithiation process implies that the 2D MoS_2 undergoes an irreversible phase transition during the first discharge and cannot recover to the original structure at the end of charging back (at a cut-off potential of 3.0 V). In the next four anodic scan cycles, two pronounced oxidation peaks at 1.78 and 2.36 V (in the initial delithiation process) are shifting lightly to lower potential at 1.66 and

2.32 V, respectively. With increasing cycle numbers, the current increased due to a further opening of its mesoporous structure during cycling, which facilitates electrolyte infiltration and further exposure of active material to the electrolyte, resulting in improved lithiation. [158, 92]. This could be further confirmed by the reversible capacity of the 2D MoS_2 electrode that continually increased in the first 17 cycles, as shown in **Figure 4.5d**. The 2D MoS_2 electrode exhibits a specific capacity of ca. 1090 mAh g^{-1} at a current density of 0.05 A g^{-1} in the first lithiation process (**Figure 4.5d**). Two pronounced voltage plateaus can be observed at 1.1 and 0.55 V in the first discharge curve, which are corresponding to the first two reduction CV peaks at 1.0 and 0.39 V, respectively. The slight difference between secondary voltage plateau and current peak position might be related to the kinetic properties of the electrode. [154] In the subsequent delithiation process, a slope-like potential plateau at ca. 2.3 V was obtained, which is corresponding to the first oxidation peak at 2.36 V in the CV curve. Note that a charge capacity of 676 mAh g^{-1} was achieved with an ICE of 62%. The relatively low ICE was most likely ascribed to the formation of the SEI layer onto the electrode surface with porous morphology (see **Figure 4.7a**). A short plateau at 1.90 V can be found in the discharge voltage profile from the 2nd to 20th cycle, which is in good agreement with the reduction peak observed at 1.89 V in the correspondent CV curve. The charge voltage profile of that can be divided into one sloped region in the potential range of 1.5-2.0 V and one plateau at 2.25 V, which are assigned to the oxidation peaks at 1.66 and 2.32 V in the CV plots, respectively. Note that the length of all these short plateaus in discharge and charge voltage profiles were reduced and almost disappeared after cycle 80, which might be a result from the decreased nano-crystallinity and size of the spray-stacked MoS_2 nanosheets due to the repetitive Li-ions intercalated into the electrode. [156, 159] Interestingly, the reversible capacity of discharge and charge was increasing from 731.8 to 990 mAh g^{-1} at the 2nd and 20th cycle, respectively, which was mainly due to the sprayed MoS_2 nanosheets with a porous structure (**Figure 4.7a**) that leads to constantly increasing the accessible contact area between the electrolyte and activated material, thereby increasing the reactivity of the material. [160-161] After that, the specific capacities of the 2D MoS_2 electrode were continuously fading to 647 mAh g^{-1} at cycle 100, which is caused by the lithiation-induced stress accumulation, volume expansion, and pulverization of the MoS_2-based electrode. [10, 73, 152, 162] Given this, the cycled MoS_2 electrode after cycle 100 was further investigated by *ex*-situ SEM, a cracked structure was observed, as shown in **Figure 4.7c**, which explained why the capacity declined during long-term cycling. It is worth noticing that the CE of the MoS_2 approached over 100% and it remained around ~100.1% between cycles 55 and 100. According to previous studies, a thick gel-

like film, also known as "electrolyte-derived surface layer" (EDS), results from electrolyte decomposition at low potential regions and covers the SEI layer, which may contribute an extra capacity during delithiation due to the decomposition of the EDS. [105-106, 162]

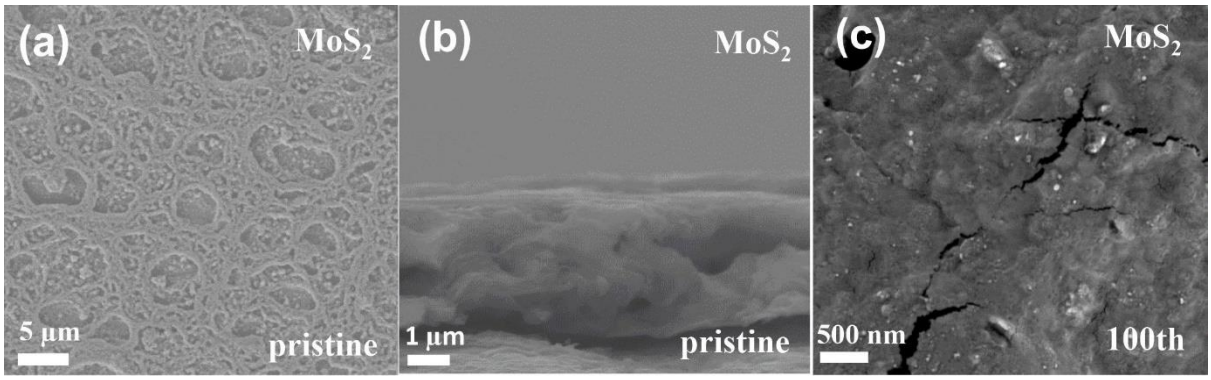

Figure 4.7 SEM images of (a) and (b) are the top view and cross-section for pristine sprayed MoS_2 electrode, respectively. (c) The top view of 2D MoS_2 electrode after 100 cycles at a current density of 0.05 A g^{-1}.

4.3.4.2 Electrochemical performance of $(Ti_3C_2T_x/MoS_2)$xn heterostructure

2D MoS_2 electrodes have shown relatively high capacities, but undergo poor capacity retention due to severe volume expansion and insufficient conductivity (2H MoS_2 is a semi-conductive phase). [90] Compared with MoS_2, sprayed $Ti_3C_2T_x$ electrodes exhibited only moderate charge/discharge capacities due to the pseudo-capacitive mechanism [147, 163] but excellent cycling stability, which benefits from its superior conductivity and mechanical strength. [129] Based on these, it is possible to combine the advantages and eliminate the disadvantages of both individual components via engineering heterostructures made by stacking 2D MoS_2 and $Ti_3C_2T_x$ nanosheets. First of all, we start with building the heterostructures $(Ti_3C_2T_x/MoS_2)$xn (n=1, 2, 3, 4, and 8). $Ti_3C_2T_x/MoS_2$ is a bilayer that is terminated with MoS_2 nano-flakes. The preparation process of this heterostructured electrode has been introduced in detail in the experimental section. Firstly, for comparison, the cycling performance of the pure MoS_2 and $Ti_3C_2T_x$ is presented in **Figure 4.8a**. The discharge capacity of the 2D MoS_2 was continuously increasing from 812 (cycle 2) to 1002 mAh g^{-1} (cycle 17), the capacity rise can be explained in terms of a further opening of its mesoporous structure upon cycling, which facilitates electrolyte infiltration and further exposure of active sites to the electrolyte resulting in an enhanced lithiation. However, the capacity then gradually declined to 647 mAh g^{-1} due to the volume expansion of 2D MoS_2 after 100 cycles. On the contrary, the sprayed $Ti_3C_2T_x$ electrode showed a stable cycling performance during 100 cycles. Next,

the cycling performance of various bilayer $Ti_3C_2T_x/MoS_2$ electrodes was systematically evaluated, as shown in **Figure 4.8b**.

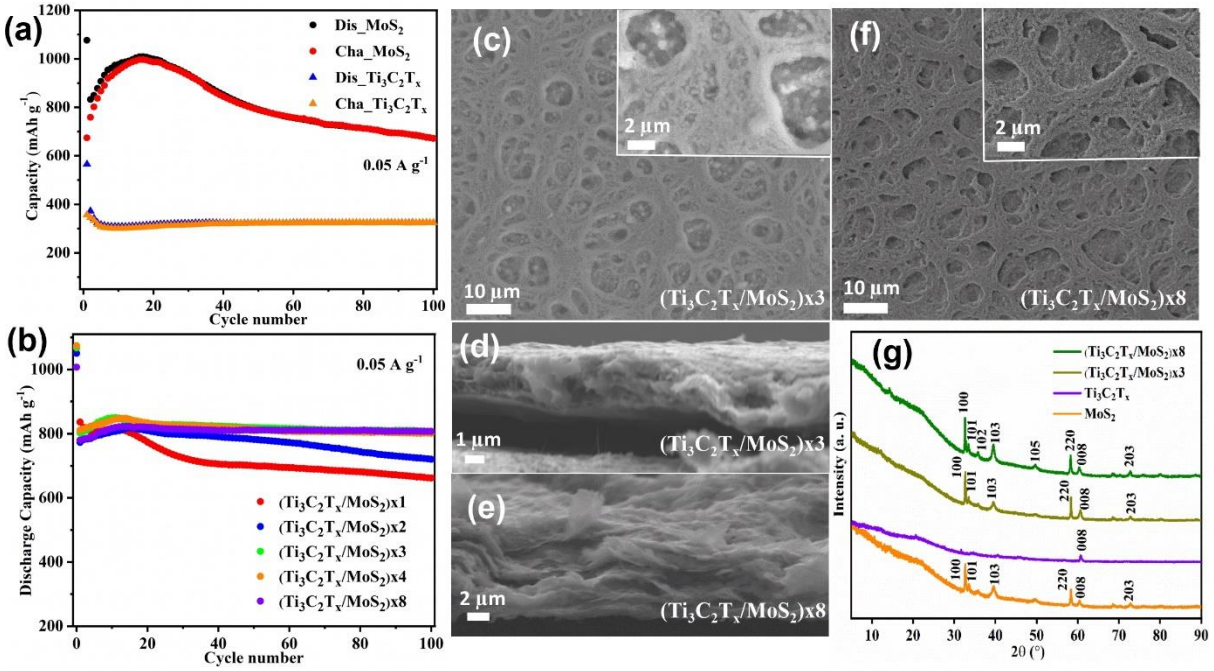

Figure 4.8 (a) cycling performance of the sprayed $Ti_3C_2T_x$ and MoS_2 electrodes at a current density of 0.05 A g^{-1}, (b) cycling performance of $(Ti_3C_2T_x/MoS_2)$xn (n=1, 2, 3, 4 and 8) heterostructure electrode at a current density of 0.05 A g^{-1}, (c) and (f) are the top-view of $(Ti_3C_2T_x/MoS_2)$x3 and $(Ti_3C_2T_x/MoS_2)$x8 heterostructures (insets with higher magnification), respectively; (d) and (e) are the cross-section view of $(Ti_3C_2T_x/MoS_2)$x3 and $(Ti_3C_2T_x/MoS_2)$x8 heterostructures, respectively; (g) the comparison XRD patterns of MoS_2, $Ti_3C_2T_x$, $(Ti_3C_2T_x/MoS_2)$x3 and $(Ti_3C_2T_x/MoS_2)$x8 electrodes after spraying onto a CA foil.

Interestingly, compared to the pure sprayed MoS_2, $(Ti_3C_2T_x/MoS_2)$x1 electrode exhibited a highly similar tendency in terms of the discharge capacity, but with distinctly improved cycling stability. The discharge capacity of the electrode reached the maximum 814 mAh g^{-1} at cycle 14, dropped to 711 mAh g^{-1} at cycle 29, and continuously degraded to 663 mAh g^{-1} at the end of the cycling test, which mainly results from the volume expansion of MoS_2 composites. [73, 152, 164]As expected, the cycling performance of the heterostructures was further promoted by engineering $(Ti_3C_2T_x/MoS_2)$x2 electrode. The discharge capacity of the electrode firstly increased from 782 (cycle 2) to 817 mAh g^{-1} (cycle 16), which then gradually declined to 720 mAh g^{-1} at cycle 100. Inspired by these results, $(Ti_3C_2T_x/MoS_2)$x3 and $(Ti_3C_2T_x/MoS_2)$x4 were fabricated and the stability of (dis)charging was evaluated as well at the same conditions. Both two heterostructured electrodes have shown extremely similar cycling performance and delivered the highest discharge capacity of 845 mAh g^{-1} around cycle 13, however, which declined quickly to 822 mAh g^{-1} nearby cycle 30, finally, the

capacity was stepwise shrinking to 801 mAh g^{-1} at cycle 100, with a capacity retention rate of 97% (from cycle 30 to 100). Apparently, the cycling stability of the above electrodes has been improved significantly by increasing the number of $Ti_3C_2T_x/MoS_2$ bilayers, to a certain extent. Nevertheless, all four types of heterostructured electrodes still suffer a rapid capacity degradation between cycles 10 and 40, which is supposed to result from the repetitive volume expansion/contraction of the MoS_2 components during cycling. To better suppress the capacity degradation of MoS_2, a heterostructure of $(Ti_3C_2T_x/MoS_2)x8$ was engineered and the cyclic performance was evaluated subsequently, as shown in **Figure 4.8b** (purple line). Discharge capacity increased from 780 (cycle 2) to 822 mAh g^{-1} (cycle 16), which slightly decays to 815 mAh g^{-1} at cycle 32 and tends to be stabilized at a capacity of 807 mAh g^{-1} until the end of cycling measurement (the discharge capacity retention rate is 98% from cycle 16). This result demonstrated that the cyclic stability of the heterostructures can be improved by rationally engineering the number of $Ti_3C_2T_x/MoS_2$ bilayers. To further investigate how the $Ti_3C_2T_x/MoS_2$ heterostructures with the different number of bilayers effects the lithium storage performance, $(Ti_3C_2T_x/MoS_2)x3$ and $(Ti_3C_2T_x/MoS_2)x8$ heterostructures were selected as a case study. Structural morphologies of both heterostructures were characterized by *ex-situ* SEM. The SEM images of $(Ti_3C_2T_x/MoS_2)x3$ and $(Ti_3C_2T_x/MoS_2)x8$ electrodes are shown in **Figure 4.8c** and **f**, respectively, and highlights their 3D porous network properties, which were formed due to the restacking of 2D MoS_2 nano-flakes with random orientation during layer-by-layer spray-deposition. Cross-sectional SEM images show the alternating layers of $Ti_3C_2T_x$ and MoS_2 with a good layer alignment and compact stacking in the $(Ti_3C_2T_x/MoS_2)x3$ and $(Ti_3C_2T_x/MoS_2)x8$ heterostructured electrodes (**Figure 4.8d** and **e**). XRD measurement was performed to further confirm the formation of the $Ti_3C_2T_x/MoS_2$ heterostructures. **Figure 4.8g** presented the XRD patterns of the sprayed $(Ti_3C_2T_x/MoS_2)x3$ and $(Ti_3C_2T_x/MoS_2)x8$ heterostructures, which both combined all of the characteristic peaks from the sprayed MoS_2 and $Ti_3C_2T_x$ films, indicating that the nano-crystalline structures of MoS_2 and $Ti_3C_2T_x$ nanosheets were kept during this spray-restacking environment.

Next, the lithium storage behavior of the $(Ti_3C_2T_x/MoS_2)x3$ and $(Ti_3C_2T_x/MoS_2)x8$ heterostructures was further elucidated by cyclic voltammetry (CV) and galvanostatic cycling with potential limitation (GCPL) measurements. As we can see from **Figure 4.9a**, the CV plot of $(Ti_3C_2T_x/MoS_2)x3$ heterostructures regarding peak position and shape is highly similar to that of MoS_2 (**Figure 4.5b**), therefore, the current work agrees that both electrodes follow the same mechanism of lithium storage. **Figure 4.9a**

shows the first five CV plots at a scan rate of 0.1 mV s^{-1} within a voltage window of 0.01–3.0 V. Two sharp peaks can be observed in the first cathodic scan, being two reduction peaks at 1.03 and 0.42 V, which are corresponding to the lithium-ion intercalated into the 2H MoS_2 component to form 1T Li_xMoS_2 ($0< x <1$) and the subsequent reduction reaction of Li_xMoS_2 into Mo atom and Li_2S. [154, 156] One weak peak at 1.78 V and a relatively broad oxidation peak at 2.38 V were obtained in the subsequent anodic scan, which can be ascribed to the probable partial oxidation of metallic Mo atoms and Li_2S to form Li_xMoS_2 ($0< x <1$) and the regeneration of 2H MoS_2 due to the continuous delithiation of Li_xMoS_2 at the end of charging process, respectively. [73, 152] In the next cathodic and anodic scan, one reduction peak at 1.84 V was corresponding to the reduction of 2H MoS_2 due to the Li-ions intercalation of 2H MoS_2 (produced in the first charge process) and two anodic peaks at 1.64 and 2.32 V, which are assigned to the oxidation reaction of Mo and Li_2S. It is worth noting that there is also a slight increase and shift regarding peak intensity and position in these two peaks compared to the initial anodic scan, which shows the same electrochemical behavior of pure MoS_2. Hence, the increased current densities and shift of peak potential might be caused by the activation of the MoS_2 electrode, which thereby enhanced the lithium storage ability. These results were further confirmed by the voltage profile of $(Ti_3C_2T_x/MoS_2)x3$ heterostructure, as shown in **Figure 4.9b**. As expected, the discharge capacities of the electrode continuously increased from 741 (cycle 2) to reach the maximum value of 840 (cycle 13) mAh g^{-1}. Two plateaus around 1.0 and 0.5 V were observed in the first discharge curve (lithiation process), which are ascribed to the phase transition (**equation 4.1**) and the conversion reaction of the lithiated Li_xMoS_2 (**equation 4.2**), and both of which are in good agreement with the current peaks at 1.03 and 0.42 V in the initial cathodic CV curve (**Figure 4.9a**), respectively. There is a sluggish plateau of around 2.3 V obtained in the subsequent charge curve (delithiation process), which belongs to the reformation of 2H MoS_2 at the end of charging and is consistent with the oxidation peak at 2.38 V in the first anodic scan as well (**equation 4.3**). From the secondary cycle, there is a short sluggish plateau at ca.1.9 V in the discharge curve, which almost disappeared at cycle 80 without a distinct capacity loss (**Figure 4.9b**). Quite similar behavior of the potential plateau at 2.3 V was also obtained in the charge profiles, the length of the plateau shrunk from cycles 1 to 50 while it tends to be stabilized at a certain value between cycles 50 and 100, indicating that the electrochemical process transited from battery-like (intercalation dominant) to a capacitive process. Moreover, the discharge capacity of $(Ti_3C_2T_x/MoS_2)x3$ heterostructure only slightly declined from 816 (cycle 50) to 804 mAh g^{-1} (cycle 100). However, this significantly improved

capacity retention upon cycling was not observed in the case of the pure sprayed MoS_2 electrode, demonstrating fairly high electrochemical stability of the $Ti_3C_2T_x/MoS_2$ heterostructures.

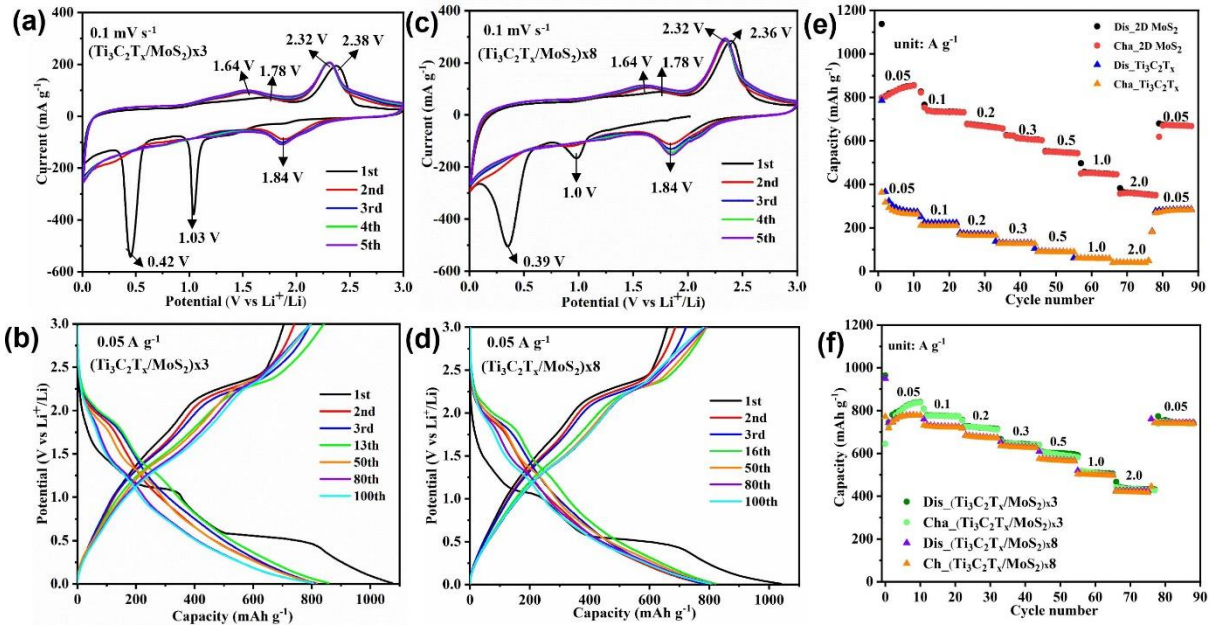

Figure 4.9 Electrochemical measurements of the $(Ti_3C_2T_x/MoS_2)x3$ and $(Ti_3C_2T_x/MoS_2)x8$ heterostructures (a) and (c) are the CV at a sweep rate of 0.1 mV s^{-1} and voltage profile of sprayed $(Ti_3C_2T_x/MoS_2)x3$ electrode at a current of 0.05 A g^{-1}, respectively; (b) and (d) are the CV at a sweep rate of 0.1 mV s^{-1} and voltage profile of $(Ti_3C_2T_x/MoS_2)x8$ electrode at a current of 0.05 A g^{-1}, respectively; (e) the rate performances of sprayed $Ti_3C_2T_x$ and 2D MoS_2 electrodes, (f) the rate performances of $(Ti_3C_2T_x/MoS_2)x3$ and $(Ti_3C_2T_x/MoS_2)x8$ heterostructures.

As for the CV and discharge/charge curves of $(Ti_3C_2T_x/MoS_2)x8$ heterostructure, as shown in **Figure 4.9c** and **d**, respectively, they are nearly identical to those of the $(Ti_3C_2T_x/MoS_2)x3$ heterostructure. To further evaluate the morphology changes of the $(Ti_3C_2T_x/MoS_2)x3$ and $(Ti_3C_2T_x/MoS_2)x8$ heterostructure after cycling, *ex*-situ SEM characterization was carried out, as shown in **Figure 4.10**. As expected, unlike in the pure MoS_2 electrode, there are no cracked-slit structures observed in both cycled heterostructures, indicating that the volume expansion of the MoS_2 component can be effectively buffered by the Ti_3C_2/MoS_2 heterostructure.

Rate performance of the $(Ti_3C_2T_x/MoS_2)x3$ and $(Ti_3C_2T_x/MoS_2)x8$ heterostructures were also compared and are shown in **Figure 4.9f**. $(Ti_3C_2T_x/MoS_2)x3$ electrodes cycled at various current densities of 0.05, 0.1, 0.2, 0.3, 0.5, 1.0, and 2.0 A g^{-1}, exhibit capacities as high as 838, 775, 716, 640, 596, 505, and 431 mAh g^{-1}, respectively, which are slightly higher than those of 2D

MoS_2 electrode (see **Figure 4.9e**). Note that when the current density relaxed to 0.05 A g^{-1}, the capacities of both heterostructures do not return to 838 mAh g^{-1} but stabilizes around 743 mAh g^{-1}, which are still higher than that of a single MoS_2 electrode with a capacity of 670 mAh g^{-1} in the last ten cycles. It should be emphasized that the stability of the rate capabilities for $Ti_3C_2T_x$ is much better than the MoS_2, which is supposed to be favored by the excellent mechanical strength of $Ti_3C_2T_x$ nanosheets. [134, 145, 165] When compared to the $(Ti_3C_2T_x/MoS_2)x3$ heterostructure, the $(Ti_3C_2T_x/MoS_2)x8$ heterostructure exhibits a very similar rate performance, especially when cycled at high rates (from 0.5 to 2.0 A g^{-1}).

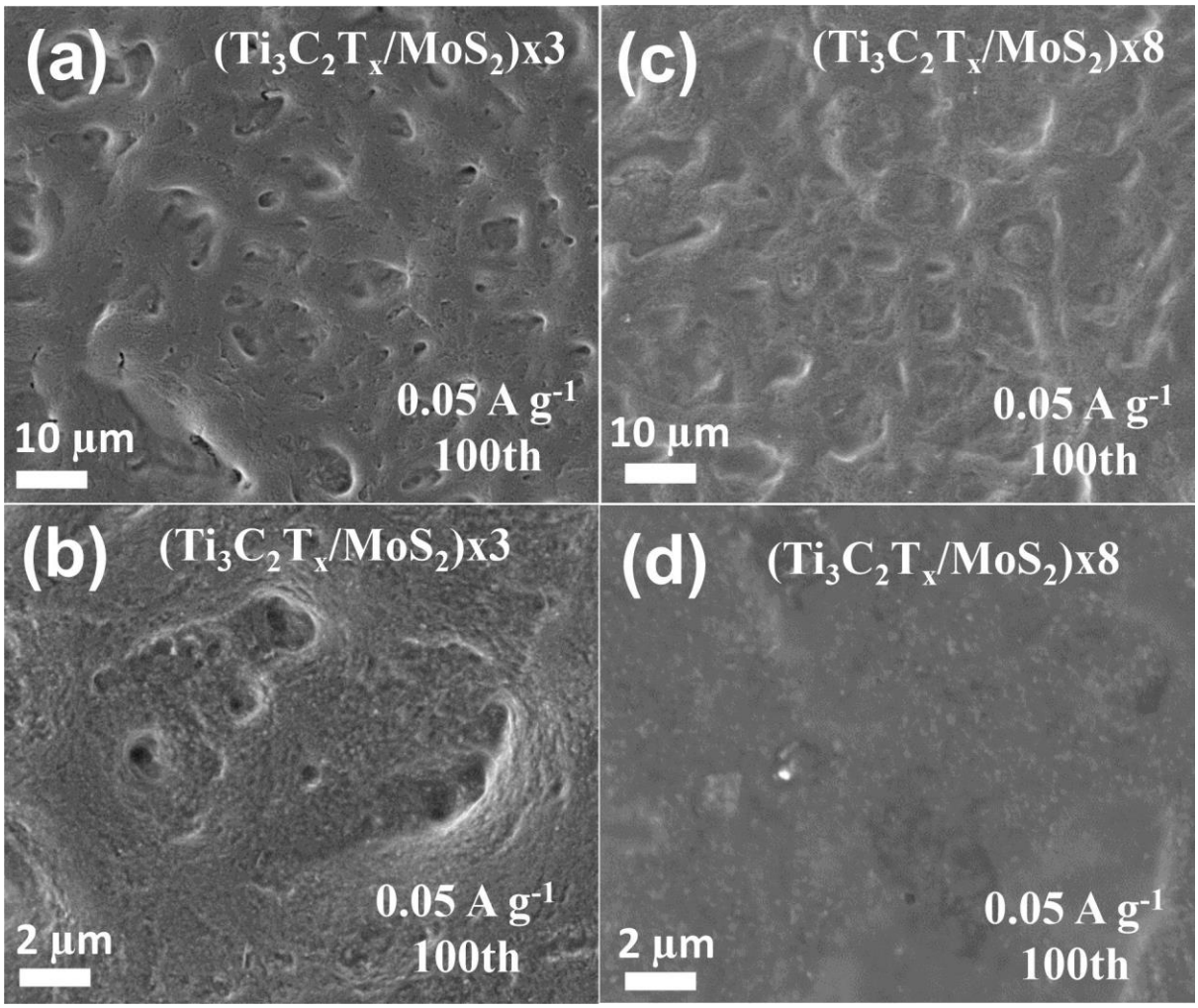

Figure 4.10 SEM images of cycled $Ti_3C_2T_x/MoS_2$ heterostructures; (a) and (b) are the top view of $(Ti_3C_2T_x/MoS_2)x3$ electrode after 100 cycles at a current density of 0.05 A g^{-1}; (c) and (d) are the top view of $(Ti_3C_2T_x/MoS_2)x8$ electrode after 100 cycles at a current density of 0.05 A g^{-1}.

Hence, the cycling stability of the $(Ti_3C_2T_x/MoS_2)x3$ and $(Ti_3C_2T_x/MoS_2)x8$ heterostructures was evaluated by cycle tests at high current densities of 0.5 and

1.0 A g^{-1}, as shown in **Figure 4.11**. To investigate performance of the $Ti_3C_2T_x/MoS_2$ heterostructures, the cycle behavior of the MoS_2 and $Ti_3C_2T_x$ nanosheets was also tested and used as a comparison (**Figure 4.11**). Sprayed $Ti_3C_2T_x$ nanosheets showed an ultra-robust cycling performance at low capacity when cycled at a current density of 0.5 A g^{-1}, its capacity steadily increased from 122 (cycle 11) to 155 mAh g^{-1} after 500 cycles (with a stable coulombic efficiency of 99.97%). Note that the exactly same capacity evolution of $Ti_3C_2T_x$ was also observed when cycled at the current density of 1.0 A g^{-1}, capacity rising has been reported in previous literature, which is attributed to the exposure of an increasing number of electrochemically active sites upon cycling. [136, 149]

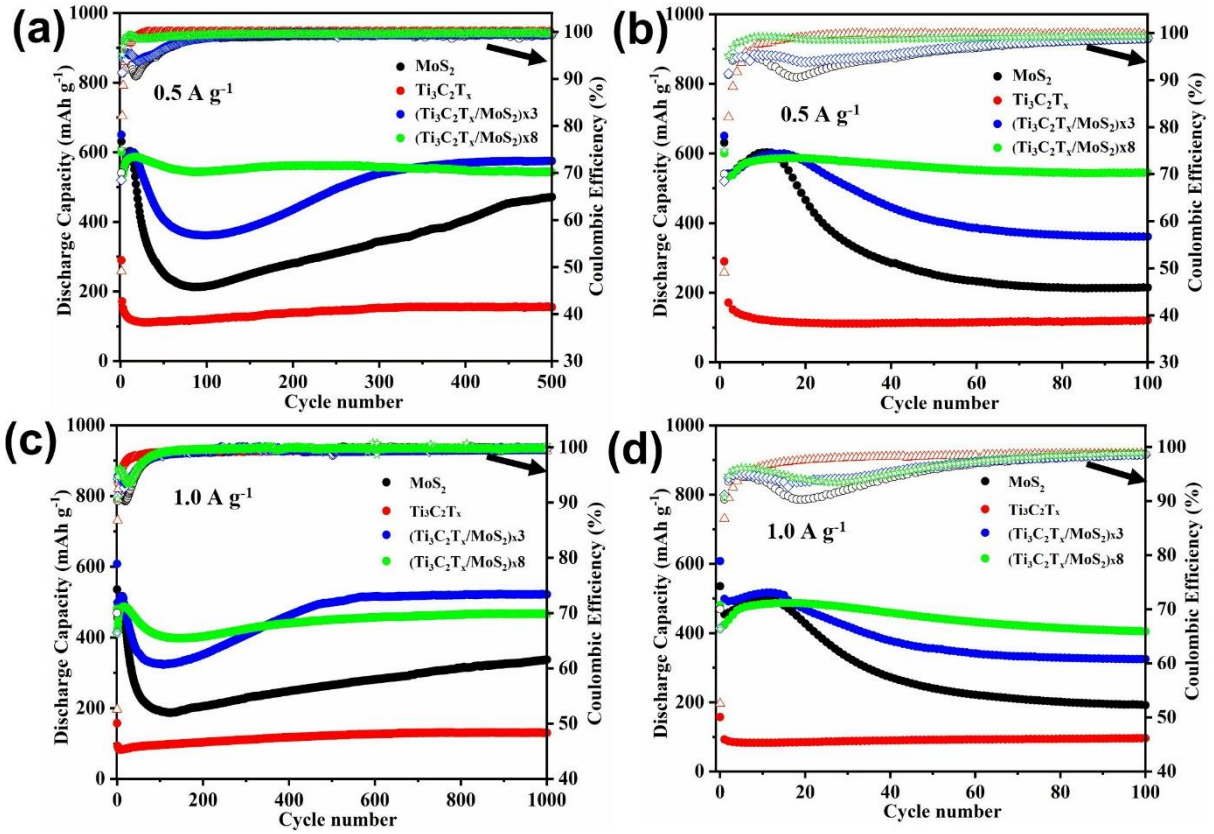

Figure 4.11 (a) and (b) are the long-term cycling of MoS_2, $Ti_3C_2T_x$, $(Ti_3C_2T_x/MoS_2)x3$ and $(Ti_3C_2T_x/MoS_2)x8$ heterostructures at 0.5 A g^{-1} for 500 and 100 cycles, respectively; (c) and (d) are the long-term cycling of MoS_2, $Ti_3C_2T_x$, $(Ti_3C_2T_x/MoS_2)x3$ and $(Ti_3C_2T_x/MoS_2)x8$ heterostructures at 1.0 A g^{-1} for 1000 and 100 cycles, respectively.

The MoS_2 electrode exhibits a quite different capacity evolution at a current density of 0.5 A g^{-1} when compared with $Ti_3C_2T_x$, which continuously increased from 541 mAh g^{-1} (cycle 2) to reach the peak capacity of 602 mAh g^{-1} (cycle 10) and then rapidly degraded to a minimum of 213 mAh g^{-1} (cycle 89), with a low capacity retention rate of 35%, followed by a progressive growth that stabilizes

around 470 mAh g^{-1} at cycle 500 (**Figure 4.11a** and **b**). Corresponding coulombic efficiency (CE) showed some fluctuations in the first 20 cycles, it first increased from 70.03% (cycle1) to 90.14% (cycle 2), then tends to fluctuate around 94.5% (between cycles 3 and 11), then decreased to 90.58% (cycle 18), followed by a gradual increase till cycle 178 and finally stabilized at 99.4% (**Figure 4.11a** and **b**). Note that similar trends in discharge capacity and CE were observed when MoS_2 was cycled at a current rate of 1.0 A g^{-1} (**Figure 4.11c** and **d**). The explanation for this high-rate induces the activation of 2D MoS_2 has been introduced in **chapter3**.

Volume expansion of the MoS_2 component is expected to be buffered by rational design $Ti_3C_2T_x/MoS_2$ heterostructure, consequently, the long-term cycling performance of the $(Ti_3C_2T_x/MoS_2)$x3 electrode was evaluated at current densities of 0.5 A g^{-1} for 500 cycles, as shown in **Figure 4.11a** and **b** (blue line), which delivers an initial discharge capacity of 650 mAh g^{-1} with an ICE of 68.50%. The lithiation capacity then increased from 541 mAh g^{-1} (cycle 2) to reach the maximum value of 599 mAh g^{-1} (cycle 14), and then continuously decreased to 360 mAh g^{-1} (cycle 98). The capacity reduction is much lower than that of pure MoS_2 electrode from cycle 14 to 98. The capacity rapidly grows to 540 mAh g^{-1} (cycle 303) afterwards, and then increased slowly and stabilized around 575 mAh g^{-1} eventually. Compared to MoS_2 alone electrode, the CE fluctuations of the $(Ti_3C_2T_x/MoS_2)$x3 electrode were suppressed by the heterostructures. The life-span of $(Ti_3C_2T_x/MoS_2)$x8 heterostructure was evaluated at 0.5 A g^{-1} as well, which delivers a relatively lower initial lithiation capacity of 600 mAh g^{-1} but with higher ICE of 75%. The capacity rised from 534 (cycle 2) to 587 mAh g^{-1} (cycle 18), which slightly declined to 543 mAh g^{-1} (cycle 86) with a capacity retention rate of 82.5%, and a more stable CE evolution was obtained when compared with $(Ti_3C_2T_x/MoS_2)$x3 heterostructure. Obviously, the capacity degradation of the $Ti_3C_2T_x/MoS_2$ heterostructures was suppressed by increasing the number of $Ti_3C_2T_x/MoS_2$ bilayers. As expected, $(Ti_3C_2T_x/MoS_2)$x3 and $(Ti_3C_2T_x/MoS_2)$x8 heterostructures have shown a similar tendency in terms of discharge capacity and CE evolution when cycled at 1.0 A g^{-1}. Both two $Ti_3C_2T_x/MoS_2$ heterostructures exhibited higher capacities and better cyclic stability when compared to pure MoS_2 or $Ti_3C_2T_x$ electrodes, demonstrating the synergistic effects of the high-conductive $Ti_3C_2T_x$ flakes with outstanding mechanical strength combined with high-capacity MoS_2 nanosheets. *Ex-situ* SEM was used to examine the morphology of the cycled $(Ti_3C_2T_x/MoS_2)$x3 and $(Ti_3C_2T_x/MoS_2)$x8 heterostructures (cycled at 1.0 A g^{-1}), as shown in **Figure 4.12c-f**. There are no mechanical failures such as cracks or slit-like structures

observed, instead bean-like structures appear with rich-porosity in both of above-cycled electrodes, which is supposed to be related to the high-rate lithiation induced reactivation of 2D MoS_2 nanosheets according to **chapter 3**. However, it is worth pointing out, that even though the capacity recession of $Ti_3C_2T_x/MoS_2$ was suppressed by the heterostructure, in particular at high current rates (e.g. 0.5 and 1.0 A g^{-1}), the intrinsic volume expansion of the MoS_2 component was still not fully buffered.

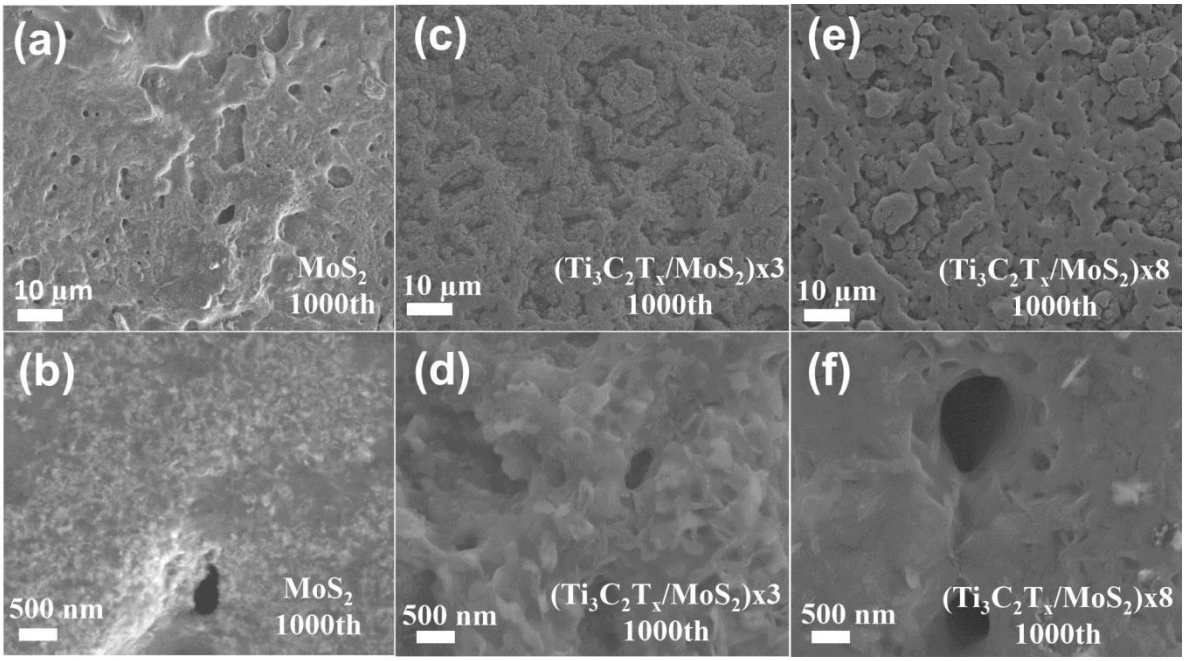

Figure 4.12 SEM images of cycled MoS_2 and $Ti_3C_2T_x/MoS_2$ heterostructures (a) and (b) are the top view of the MoS_2 electrode after 1000 cycles at a current density of 1.0 A g^{-1}; (c) and (d) are the top view of $(Ti_3C_2T_x/MoS_2)x3$ electrode after 1000 cycles at a current density of 1.0 A g^{-1}, (e) and (f) are the top view of $(Ti_3C_2T_x/MoS_2)x8$ electrode after 1000 cycles at a current density of 1.0 A g^{-1}.

4.3.4.3 Morphology and electrochemical performance of $Ti_3C_2T_x/MoS_2$-mixed heterostructure

For comparison, a $MoS_2/Ti_3C_2T_x$-mixed heterostructure was fabricated by the same spray method but with conventionally mixing suspensions of 2D MoS_2 and $Ti_3C_2T_x$ nanosheets (see **Scheme 4.1**).

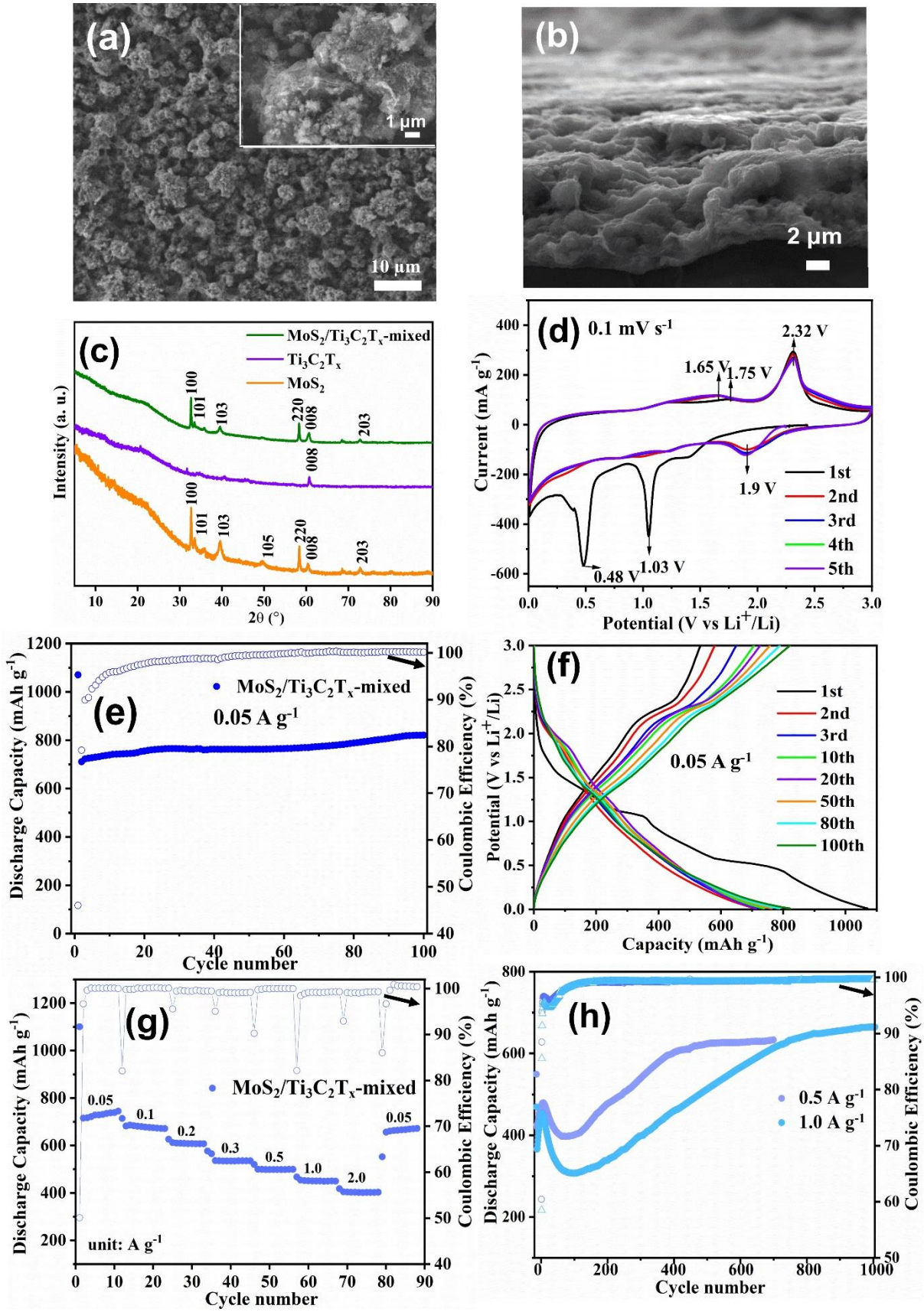

Figure 4.13 (a) and (b) are SEM images of the top-view and cross-sectional view of $MoS_2/Ti_3C_2T_x$-mixed heterostructure, respectively; (c) the comparison XRD patterns of MoS_2, $Ti_3C_2T_x$, $MoS_2/Ti_3C_2T_x$-mixed heterostructure by spraying onto a cellulose acetate foil; (d)

the CV of $MoS_2/Ti_3C_2T_x$-mixed heterostructures at a sweep rate of 0.1 mV s^{-1}; (e) and (f) are the cycling performance and voltage profile of $MoS_2/Ti_3C_2T_x$-mixed heterostructure at a current of 0.05 A g^{-1}, respectively; (g) the rate performance of $MoS_2/Ti_3C_2T_x$-mixed heterostructure at various current densities; (h) the long-term cycling performance of $MoS_2/Ti_3C_2T_x$-mixed heterostructure at the current densities of 0.5 and 1.0 A g^{-1}.

A Sphere-like structure with rich-porosity was obtained in the $MoS_2/Ti_3C_2T_x$-mixed electrode, as shown in **Figure 4.13a**, which is significantly more aggregated compared with that of the $(Ti_3C_2T_x/MoS_2)$x3 and $(Ti_3C_2T_x/MoS_2)$x8 heterostructures (compare **Figure 4.8c** and **f**). A good alignment and compact restacking in the $MoS_2/Ti_3C_2T_x$-mixed thin film with a thickness of ~ 3 μm was confirmed by the cross-sectional SEM image (**Figure 4.13b**). XRD characteristic peaks of both 2D $Ti_3C_2T_x$ and MoS_2 were observed in the as-sprayed film, implying the successful formation of $MoS_2/Ti_3C_2T_x$-mixed heterostructure. The electrochemical performance of $MoS_2/Ti_3C_2T_x$-mixed heterostructure in the anode of a LIB was investigated by CV and GCPL. **Figure 4.13d** shows the initial five scans of $MoS_2/Ti_3C_2T_x$-mixed heterostructure, which displays characteristics similar to the pure MoS_2 electrode (see **Figure 4.5b**). Two reduction peaks, located at 1.03 and 0.48 V, are observed in the first cathodic scan (lithiation process), which are assigned to the phase transition of 2H MoS_2 to 1T Li_xMoS_2 and conversion reaction of Mo atoms and Li_2S with Li^+ ions, respectively. [103, 153] They are corresponding to the first two lithiation plateaus around 1.0 and 0.5 V in the voltage profile of the electrode, as shown in **Figure 4.13f**. In the subsequent anodic scan (delithiation process), a broad peak at 1.75 V and a distinct oxidation peak at 2.32 V were obtained. They are ascribed to the partial oxidation of Mo and Li_2S to produce 1T Li_xMoS_2 and further delithiation to regenerate 2H MoS_2, respectively. [73, 152] The anodic peak at 2.32 V is corresponding to the plateau around 2.30 V in the delithiation profile (**Figure 4.13f**). From the second to the fifth anodic scan, the peak at 1.75 V shifts to 1.65 V, most likely due to the reactivation process of the electrode, while the position of the peak at 2.32 V did not move, which is quite different from that of MoS_2 alone (**Figure 4.5b**). In the rest of the cathodic sweeps (second to fifth cycles), one new broad peak around 1.90 V appears, corresponding to the lithiation of regenerated 2H MoS_2 to 1T Li_xMoS_2. On the one hand, the cathodic peaks at 1.90 V overlap each other from second cycle onward, underlining the excellent reversibility of $MoS_2/Ti_3C_2T_x$-mixed heterostructure. Current intensities, on the other hand, increased over cycling, indicating capacity increases, which was further verified by the electrode's cycling performance, as shown in **Figure 4.13e.** $MoS_2/Ti_3C_2T_x$-mixed heterostructures deliver an initial lithiation capacity of 1146 mAh g^{-1} with an

ICE of 46% at a current density of 0.05 A g^{-1}. The irreversible capacity loss during the first cycle is commonly attributed to the formation of the SEI layer and other irreversible side reactions between Li^+ and surface functional groups (e.g. –OH, O^{2-}) on $Ti_3C_2T_x$ nanosheets. [19-20, 136, 149] The discharge capacity of the as-prepared heterostructure steadily increased from 761 (cycle 2) to 781 mAh g^{-1} (cycle 30), followed by a stabilization around 783 mAh g^{-1} till cycle 69 and finally a gradual increase to 810 mAh g^{-1} at the end of cycling. Accordingly, the CE of the electrode firstly increased rapidly from 79% (cycle 2) to 98% (cycle 22), then increased continuously and tended to stabilize at around 99.5% between cycles 43 and 61. After that, the CE approached over 100% at cycle 72 and was kept around 100.2% till cycle 100, which is similar to the case of pure MoS_2 electrode and has been explained in the previous part. Interestingly, compared to pure MoS_2 and $(Ti_3C_2T_x/MoS_2)$xn heterostructures (see **Figure 4.5a** and **b**), the $MoS_2/Ti_3C_2T_x$-mixed heterostructure exhibits lower capacity but without capacity degradation upon cycling, which might be ascribed to the numerous heterointerfaces that were formed on the scale of the individual flakes and thus improved the cyclic stability. On the other hand, these excessive heterointerfaces may lead to a sluggish pre-activation process. As a result, longer cycles were required to achieve the high capacities compared to the MoS_2 and $(Ti_3C_2T_x/MoS_2)$xn electrodes cycled at low current density of 0.05 A g^{-1}. Morphology changes of cycled $MoS_2/Ti_3C_2T_x$-mixed heterostructure were investigated by *ex-situ* SEM, as shown in **Figure 4.14a** and **b**.

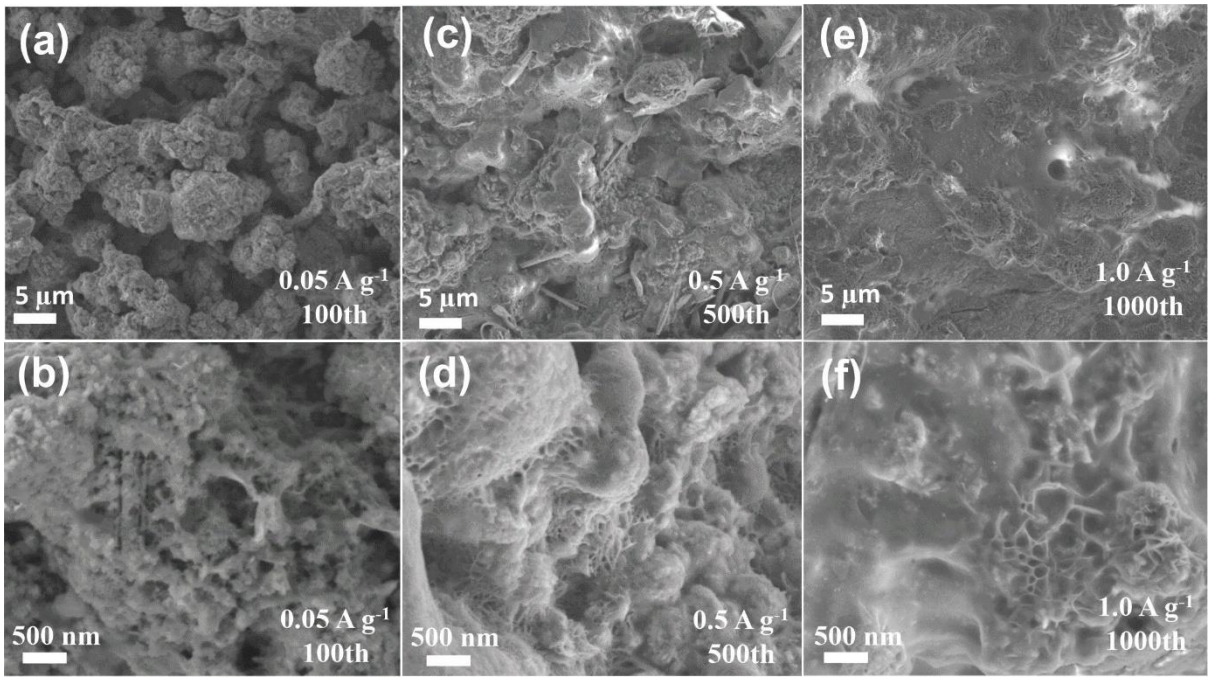

Figure 4.14 SEM images of cycled $MoS_2/Ti_3C_2T_x$-mixed heterostructure, (a) and (b) are the top view of $MoS_2/Ti_3C_2T_x$-mixed heterostructures after 100 cycles at a current density of 0.05 A g^{-1}; (c) and (d) are the top view of $MoS_2/Ti_3C_2T_x$-mixed heterostructure after 500 cycles at

a current density of 0.5 A g^{-1}, (e) and (f) are the top view of $MoS_2/Ti_3C_2T_x$-mixed heterostructure after 850 cycles at a current density of 1.0 A g^{-1}.

Comparing the SEM images of a pristine electrode (**Figure 4.13a**), the original sphere-like particles with rich porosity structure remained. There is no cracked structure, which can explain that the capacity did not drop during cycling. The rate performance of the $MoS_2/Ti_3C_2T_x$-mixed heterostructure and corresponding CE evolution were evaluated at various current densities from 0.05 to 2.0 A g^{-1}, as shown in **Figure 4.13g**. A reversible capacity of 716 mAh g^{-1} was achieved at a current rate of 0.05 A g^{-1} and kept increasing during several initial cycles. After that, reversible capacity changes were observed as increasing charge-discharge current density, which exhibits discharge capacities of 680, 608, 533, 505, 455, and 400 mAh g^{-1} at current densities of 0.1, 0.2, 0.3, 0.5, 1.0, and 2.0 A g^{-1}, respectively. Compared to the pure MoS_2 electrode, the mixed MoS_2 and $Ti_3C_2T_x$ heterostructure showed much better stability at all rates, particularly at a high rate (e.g. from 0.5 to 2.0 A g^{-1}). This can be due to the excellent mechanical strength of $Ti_3C_2T_x$. The electrochemical stability of $MoS_2/Ti_3C_2T_x$-mixed heterostructure was further investigated by cycling at higher current rates (here, 0.5 and 1.0 A g^{-1}), as shown in **Figure 4.13h**. The initial discharge capacity was 549 mAh g^{-1} with an ICE of 60%; the second lithiation capacity was 425 mAh g^{-1} after which the capacity increased to 479 mAh g^{-1} with a CE of 96% at cycle 21; then decreased quickly to 396 mAh g^{-1} at cycle 88 (capacity retention rate is 82.6%), which comes from volume expansion of the MoS_2 component; followed by a steady rise to 626 mAh g^{-1} till cycle 535 and finally stabilized around 633 mAh g^{-1} at 700th cycle afterwards. At 1.0 A g^{-1}, the $MoS_2/Ti_3C_2T_x$-mixed electrode displayed a very similar cycling profile in terms of discharge capacity and CE as the 0.5 A g^{-1} electrode. The slight differences are that it showed lower capacity retention (from the maximum capacity of 453 mAh g^{-1} at the 17th cycle to the minimum that of 306 mAh g^{-1} at cycle 110, here capacity retention is 67.6%) and took much more cycles to achieve high and stable capacities. Morphological and structural changes of the $MoS_2/Ti_3C_2T_x$-mixed electrode after cycling at the current rates of 0.5 and 1.0 A g^{-1} were investigated by *ex-situ* SEM. Instead of showing cracks in both cycled electrodes, pristine sphere-like structures were found to be compact and moss-like structures with a wrapped surface, as shown in **Figure 4.14c-f**, which can enlarge the contact area between the activated materials and electrolyte, thus enhancing the electrochemical reaction due to easier transportation of electrons and Li^+ ions. Compared to MoS_2 alone electrode, it is worth noticing that cyclic stability (at 0.05 A g^{-1}) and rate capability of the electrode were improved by as-prepared $MoS_2/Ti_3C_2T_x$-mixed heterostructure, but the high-rate lithiation-

induced reactivation of the electrode due to the significant volume expansion of MoS_2 nanosheets was still observed.

4.3.4.4 Morphology and electrochemical performance of $(MoS_2/Ti_3C_2T_x)x3$ heterostructure

To assess how the vertically stacked architecture and interface impact electrochemical performance, $(MoS_2/Ti_3C_2T_x)x3$ heterostructure with terminal $Ti_3C_2T_x$ layer was prepared, and the electrochemical properties compared against previous $(MoS_2/Ti_3C_2T_x)x3$ heterostructure produced with the same spray receipt.

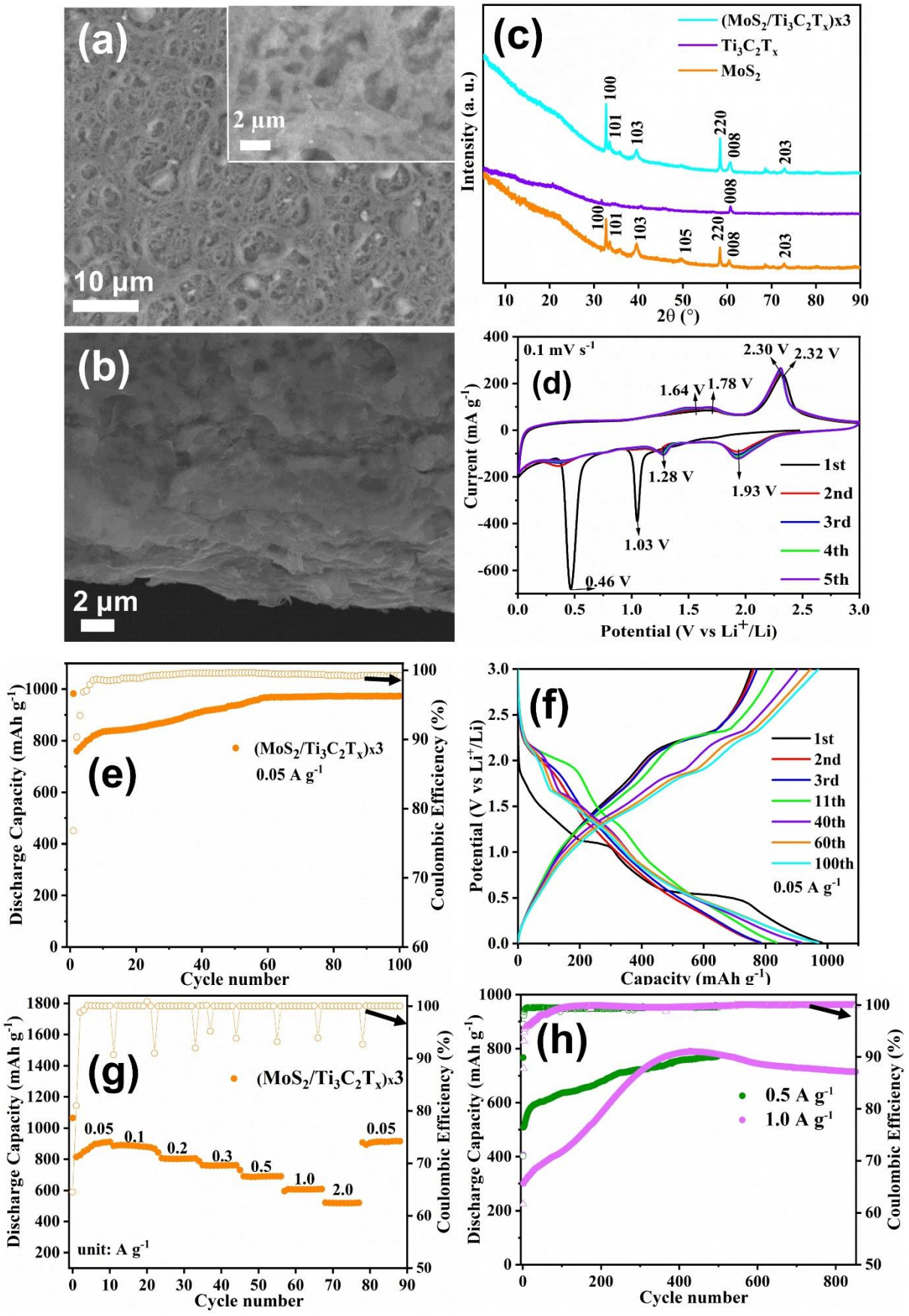

Figure 4.15 (a) and (b) are SEM images of the top-view and cross-sectional view of $(MoS_2/Ti_3C_2T_x)x3$ heterostructure, respectively; (c) the comparison XRD patterns of MoS_2,

$Ti_3C_2T_x$ and $(MoS_2/Ti_3C_2T_x)x3$ heterostructure by spraying onto a cellulose acetate foil; (d) the CV of $(MoS_2/Ti_3C_2T_x)x3$ heterostructure at a sweep rate of 0.1 mV s^{-1}; (e) and (f) are the cycling performance and voltage profile of $(MoS_2/Ti_3C_2T_x)x3$ heterostructure at a current density of 0.05 A g^{-1}, respectively; (g) the rate performance of $(MoS_2/Ti_3C_2T_x)x3$ heterostructure at various current densities; (h) the long-term cycling performance of $(MoS_2/Ti_3C_2T_x)x3$ heterostructure at the current densities of 0.5 and 1.0 A g^{-1}.

A representative SEM image of the $(MoS_2/Ti_3C_2T_x)x3$ electrode is shown in **Figure 4.15a**, and a porous network structure was observed for the heterostructure. The layered structure of MoS_2 and $Ti_3C_2T_x$ was successfully built with an in total thickness of around 3-4 μm, which is confirmed by the cross-sectional SEM image (see **Figure 4.15b**). XRD peaks of both MoS_2 and $Ti_3C_2T_x$ layers were observed in the hybrid heterostructure, as shown in **Figure 4.15c**, indicating a good alignment and compact stacking of 2D nanosheets. The first five CV scans of the electrode are shown in **Figure 4.15d,** two subsequent reduction peaks were observed in the initial cathodic scan, with the first one at 1.03 V and the second at 0.46 V, which are corresponding to the insertion of Li^+ ions into pristine 2H MoS_2 to produce 1T Li_xMoS_2 and subsequent conversion reaction of Mo and Li_2S from Li_xMoS_2 afterwards, respectively. These two reduction peaks are further confirmed by appearing of the plateaus at 1.0 and 0.5 V in the initial lithiation curve, as shown in the voltage profile **Figure 4.15f**. One weak oxidation peak around 1.78 V and a sharp anodic peak at 2.32 V were observed in the first anodic scan, which is assigned to reduction of 1T Li_xMoS_2 and regeneration of 2H MoS_2, respectively. The peak at 2.32 V is corresponding to the pronounced plateau at ca. 2.26 V in the first charge curve shown in **Figure 4.15f** (black line). And they are slightly shifted to a lower potential of 1.64 and 2.30 V in several subsequent anodic sweeps. These results are consistent with the pure MoS_2 electrode (**Figure 4.5b**). A reduction peak at 1.93 V and one small peak at 1.28 V were obtained in the rest of the cathodic scans (from second to fifth cycles). They are ascribed to the reduction reaction of reformed 2H MoS_2 and a possible deeper lithiation of pristine 2H MoS_2 layer [154] (the incompletely intercalated MoS_2 from previous cycles), respectively. The sluggish-like plateaus at ca. 2.0 V corresponds well to the reduction peaks at 1.93V in the discharge curves (**Figure 4.15f**).

Cycling profile of $(MoS_2/Ti_3C_2T_x)x3$ heterostructure at a current density of 0.05 A g^{-1} is shown in **Figure 4.15e**, which delivers an initial discharge capacity of 982.5 mAh g^{-1} with an ICE of 76%. Similar to the case of pure MoS_2 electrode, the lithiation capacity promptly increased from 760 (cycle 2) to 836 mAh g^{-1} (cycle 11), which is a well-known electrochemical behavior in 2D nano-materials named pre-activation, most likely due to the restacked structure

allowing for an increasing access of electrolyte ions to the surface of 2D nanosheets. [112-114, 166] The growth of discharge capacity can be further confirmed by enhancing the length of the plateau ca. 2.0 V, as shown in **Figure 4.15f** (from cycle 2 to 11). After that, the capacity gradually increased to 967 mAh g^{-1} at the 60th cycle and finally stabilized around 971 mAh g^{-1} with a CE of 99.5% till the end of cycling. In short, a long pre-cycle (around 60 cycles) needs to be done for the $(MoS_2/Ti_3C_2T_x)x3$ heterostructure to achieve a high and stable capacity. Meanwhile, the length of voltage plateaus at 2.0 and 2.3 V shrunk between cycles 11 and 100, but did not disappear completely (see **Figure 4.15f**), which is quite different from the pure MoS_2, $(Ti_3C_2T_x/MoS_2)x3$, and $(Ti_3C_2T_x/MoS_2)x8$ heterostructures **(Figures 4.5d, 4.9b** and **d,** and **4.13f**). Structural and morphology changes of cycled $(MoS_2/Ti_3C_2T_x)x3$ electrode (cycling at 0.05, 0.5, and 1.0 A g^{-1}) were unravelled by *ex-situ* SEM and presented in **Figure 4.16a** and **b**.

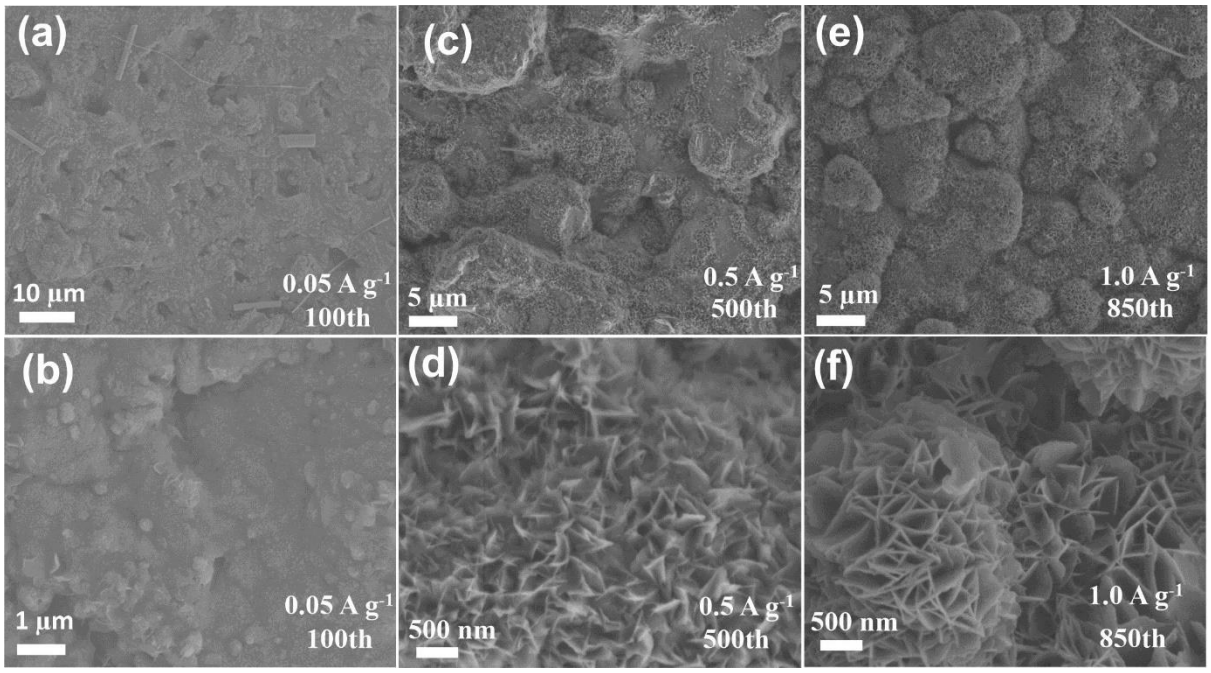

Figure 4.16 SEM images of cycled $(MoS_2/Ti_3C_2T_x)x3$ heterostructures, (a) and (b) are the top view of $(MoS_2/Ti_3C_2T_x)x3$ electrode after 100 cycles at a current density of 0.05 A g^{-1}; (c) and (d) are the top view of $(MoS_2/Ti_3C_2T_x)x3$ electrode after 500 cycles at a current density of 0.5 A g^{-1}, (e) and (f) are the top view of $(MoS_2/Ti_3C_2T_x)x3$ electrode after 850 cycles at a current density of 1.0 A g^{-1}.

Compared to the pristine one, the porous network (**Figure 4.15a**) was transferred into a more compact structure with a sags-crests-like surface. Moreover, there are no cracks and obvious aggregations of $Ti_3C_2T_x$ nanosheets observed in the cycled electrode, which is the most probable reason for the remained stable capacity upon cycling. The rate capability of $(MoS_2/Ti_3C_2T_x)x3$

heterostructure was evaluated by cycling at a current density range from 0.05 to 2.0 A g^{-1}. The discharge capacity and corresponding CE evolution versus cycles are shown in **Figure 4.15g**. A reversible capacity of 813 mAh g^{-1} (cycle 2) was achieved at 0.05 A g^{-1} and kept increasing to 907 mAh g^{-1} during the first ten cycles, then stabilized around 885 mAh g^{-1} between cycles 11 and 20 with a current density of 0.1 A g^{-1}. After pre-cycling at 0.05 and 0.1 A g^{-1}, the $(MoS_2/Ti_3C_2T_x)x3$ heterostructure exhibited stable capacities of 803, 760, 686, 605, and 518 mAh g^{-1} at various current densities of 0.2, 0.3, 0.5, 1.0, and 2.0 A g^{-1}, respectively. In addition, the lithiation capacity quickly returns to 911 mAh g^{-1} when the current density relaxed to 0.05 A g^{-1}, close to value shown in cycle 10, demonstrating fairly excellent rate capability and stability of the $(MoS_2/Ti_3C_2T_x)x3$ heterostructure. As a result, the cyclability of the $(MoS_2/Ti_3C_2T_x)x3$ electrode was further tested at the current densities of 0.5 A g^{-1}, as shown in **Figure 4.15h**. The initial discharge capacity of 766 mAh g^{-1} with an ICE of 71% was achieved at 0.5 A g^{-1}, then it rapidly rose from 508 (cycle 2) to 586 mAh g^{-1} with the CE increased to 99.4% (cycle 24); followed by a continuous increase with slower growth rate to 773 mAh g^{-1} (CE = 99.6%) till the end of cycling. Note that the eventual capacity upon cycling is even higher than the above initial value, which might be ascribed to the structural morphology changes of the cycled electrode. Therefore, the morphology of cycled $(MoS_2/Ti_3C_2T_x)x3$ heterostructure was checked by *ex-situ* SEM and presented in **Figure 4.16c** and **d**, which shows an aggregation of large clusters composed of petaloid-like nanosheets vertically crowded together. This could be the reason for the capacity increase due to the improved electrolyte accessibility into the nanoscale electrode with increased specific surface area.

Finally, the electrode was also tested at a higher current density (1.0 A g^{-1}) to evaluate the stability of the $(MoS_2/Ti_3C_2T_x)x3$ heterostructure, which is presented in **Figure 4.15h** (light red line). An initial discharge capacity of 406 mAh g^{-1} with an ICE of 61.7% was achieved, then the capacity climbed rapidly from 300 (cycle 2) to 791 mAh g^{-1} (cycle 427), accompanied by the CE gradually increasing from 87% to 99.1%, respectively; followed by a steady capacity decay to 718 mAh g^{-1} at end of cycling (850th cycle) with a CE of 99.9%. Finally, the morphology change of the cycled $(MoS_2/Ti_3C_2T_x)x3$ heterostructure was characterized by *ex-situ* SEM, as shown in **Figure 4.16e** and **f**. As we can see from that, $Ti_3C_2T_x$ flakes tend to be agglomerated and form a bulk particle that is composed of countless nano-flower-like nanosheets, which can enlarge the contact area between the active material and electrolyte, thus enhancing the high efficiency of the electrochemical activity, which could be the reason for the capacity rise. [167] On the other hand, this opening of the

structure of the electrode continuously facilitates electrolyte infiltration upon cycling, which can lead to the irreversible loss of electrolyte (e.g. new SEI formation) thus resulting in a reduction of the amount of cyclable lithium available for transport between electrodes, which should be accountable for the capacity decay after the cycle of 427. [115, 168-169] In a comparison of the $(MoS_2/Ti_3C_2T_x)x3$ heterostructure to the pure MoS_2, $(Ti_3C_2T_x/MoS_2)x3$ and $MoS_2/Ti_3C_2T_x$-mixed heterostructures, $(MoS_2/Ti_3C_2T_x)x3$ heterostructure does not show a capacity degradation at the current densities of 0.5 and 1.0 A g^{-1} in the first 100 cycles, demonstrating that the $(MoS_2/Ti_3C_2T_x)x3$ heterostructure with the terminal layer of $Ti_3C_2T_x$ helps to accommodate the volume changes during the cycling. Nevertheless, it is worth noticing that a long-cycle was required to activate the $(MoS_2/Ti_3C_2T_x)x3$ heterostructure at the current densities of 0.05, 0.5, and 1.0 A g^{-1}, thus the reaction kinetics of the electrode need to be further improved by enhancing the transportation of ions and electrons between electrodes.

4.3.4.5 Morphology and electrochemical performance of $(MoS_2/Ti_3C_2T_x/CNTs)x3$ heterostructure

As reported in the last section, the results highlight two main problems with the $(MoS_2/Ti_3C_2T_x)x3$ heterostructure as anode materials for LIBs. First is the electronic conductivity of the vertically stacked 2D structures, especially along the *c* direction because of the semi-conductive MoS_2 layer. The second problem is associated with the significant self-aggregation of $Ti_3C_2T_x$ nanosheets in the terminal layer of the $(MoS_2/Ti_3C_2T_x)x3$ heterostructure. To this end, $(MoS_2/Ti_3C_2T_x/CNTs)x3$ heterostructure was obtained by mixing carbon nanotubes (CNTs) with $(MoS_2/Ti_3C_2T_x)x3$ heterostructure, the preparation of the electrode has been introduced in detail in the experimental part. A top-view of the SEM image of a typical $(MoS_2/Ti_3C_2T_x/CNTs)x3$ electrode is presented in **Figure 4.17a**, indicating that the CNTs are uniformly entangled with $Ti_3C_2T_x$ nanosheets to form porous networks. Moreover, a cross-sectional SEM image (**Figure 4.17b**) shows a good alignment and compact stacking in the layered $MoS_2/Ti_3C_2T_x$ heterostructure with the CNTs interlinked networks.

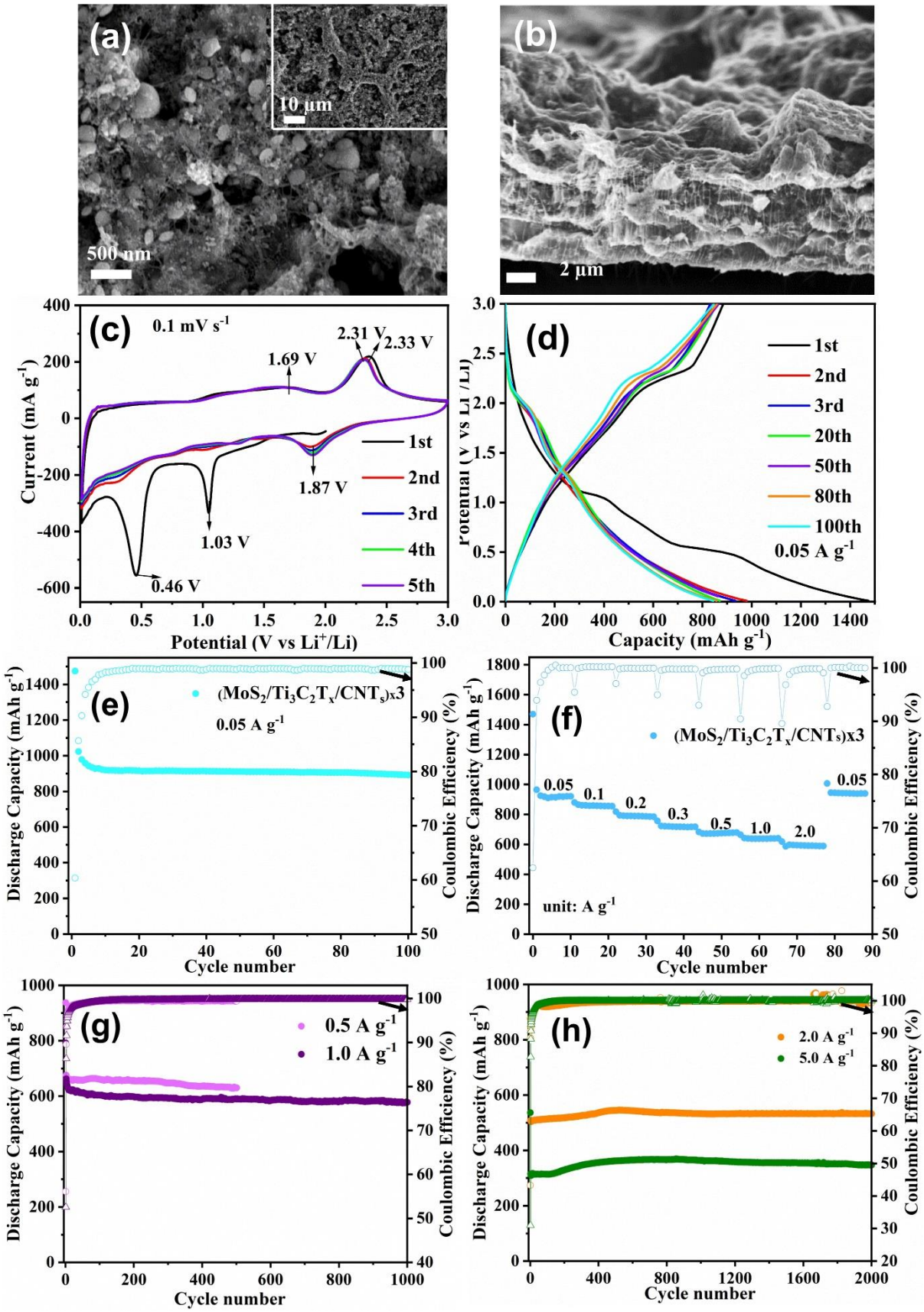

Figure 4.17 (a) and (b) are SEM images of the top and cross-sectional view of the $(MoS_2/Ti_3C_2T_x/CNTs)x3$ heterostructure, respectively; (c) CV of $(MoS_2/Ti_3C_2T_x/CNTs)x3$ heterostructure at 0.1 mV s^{-1}; (d) and (e) are the cycling performance and voltage profile of

($MoS_2/Ti_3C_2T_x$/CNTs)x3 heterostructure at 0.05 A g^{-1}, respectively; (f) the rate performance of ($MoS_2/Ti_3C_2T_x$/CNTs)x3 heterostructure at various current densities; (g) and (h) the long-term cycling performance of ($MoS_2/Ti_3C_2T_x$/CNTs)x3 heterostructure at 0.5, 1.0 and 2.0, 5.0 A g^{-1}, respectively.

Figure 4.17c displays the typical CV curves of the ($MoS_2/Ti_3C_2T_x$/CNTs)x3 heterostructure for the first five cycles with a scan rate of 0.1 mV s^{-1}. Highly similar to the CV of the MoS_2 alone electrode (**Figure 4.5b**), two peaks are occurring at 1.03 and 0.46 V in the first discharge process (lithiation), which are correlated to the intercalation of 2H MoS_2 by lithium ions to form 1T Li_xMoS_2 and the conversion reaction of that to produce Mo atoms and Li_2S, respectively. These two cathodic peaks are well corresponding to the discharge plateaus around 1.0 and 0.5 V in the voltage profiles, respectively, as shown in **Figure 4.17d** (black line). A broad anodic peak centered at 1.69 V and one pronounced oxidation peak located at 2.33 V were observed in the subsequent anodic scan (delithiation process), which can be ascribed to the regeneration of 1T Li_xMoS_2 and 2H MoS_2, respectively. [154, 156] The anodic peak at 2.33 V is correlated to the charge plateau around 2.3 V in the voltage curves (**Figure 4.17d**). All following cycles featured one cathodic peak at 1.87 V and two anodic peaks at 1.69 and 2.31 V, indicating excellent stability of ($MoS_2/Ti_3C_2T_x$/CNTs)x3 heterostructure. The electrode delivers an initial galvanostatic discharge/charge capacity of 1474/929 mAh g^{-1}, respectively, with an ICE of about 63%. Distinctly, the first lithiation capacity of the current electrode is higher than any of the others in this work, which could be caused by the addition of the CNTs, thus enhancing the electrochemical reactivity of ($MoS_2/Ti_3C_2T_x$/CNTs)x3 heterostructure and additional capacity contribution from CNTs. [170-171] The significant capacity loss in the subsequent charge process can be ascribed to the decomposition of electrolyte to form SEI and possibly an irreversible reaction between Li ions and the surface functional groups on the $Ti_3C_2T_x$ flakes. [133, 149, 170] After that, the discharge capacity rapidly fell from 1023 (cycle 2) to 918 mAh g^{-1} (cycle 10) and was accompanied by the CE increasing from 85% to 98%. The capacity loss in the initial 10 cycles is mainly attributed to the side reactions that have been mentioned before. [172] As expected, at the end of side reactions, the electrode becomes stable and exhibits a reversible capacity of 891 mAh g^{-1} (capacity retention of 97% from cycle 10) with a CE of about 99% till the 100th cycle. Impressively, the charge/discharge plateaus around 2.3 and 2.0 V have remained but with reduced plateau length upon cycling. In the same way, the cycling profile of ($MoS_2/Ti_3C_2T_x$/CNTs)x3 heterostructure at a current density of 0.05 A g^{-1} is shown in **Figure 4.17e**. The curve of discharge capacity can coincide well with superior stable CE evolution after around the 10th cycle,

demonstrating fairly high stability of the ($MoS_2/Ti_3C_2T_x$/CNTs)x3 heterostructure, which could be further confirmed by the *ex-situ* SEM characterization of the cycled electrode at end of testing, as displayed in **Figure 4.18a** and **b**. One can see that the pristine porous network transforms into a compact structure with consists of numerous tiny ball-like particles but without any cracks, which further supports the excellent structural stability of the ($MoS_2/Ti_3C_2T_x$/CNTs)x3 heterostructure.

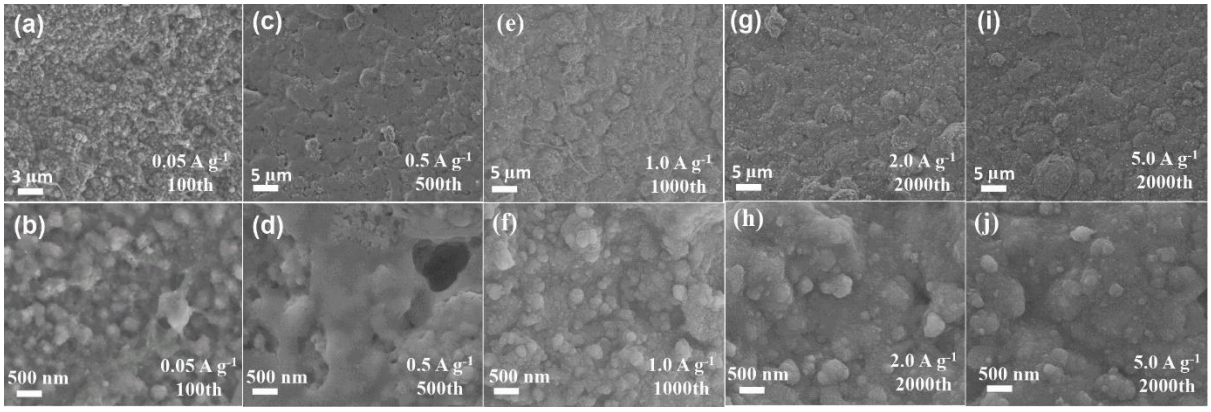

Figure 4.18 SEM images of cycled ($MoS_2/Ti_3C_2T_x$/CNTs)x3 heterostructures, (a) and (b) are the images for 100 cycles at 0.05 A g^{-1}; (c) and (d) are the images for 500 cycles at 0.5 A g^{-1}, (e) and (f) are the images for 1000 cycles at 1.0 A g^{-1}, (g) and (h) are the images for 2000 cycles at 2.0 A g^{-1}, (i) and (j) are the images for 2000 cycles at 5.0 A g^{-1}.

Rate performance of ($MoS_2/Ti_3C_2T_x$/CNTs)x3 heterostructure was investigated at various current densities ranging from 0.05 to 2.0 A g^{-1}, as shown in **Figure 4.17**. ($MoS_2/Ti_3C_2T_x$/CNTs)x3 electrode exhibits reversible specific capacities of 919, 860, 790, 719, 675, 639, and 592 mAh g^{-1}, respectively, from 0.05 to 0.1, 0.2, 0.3, 0.5, 1.0, and 2.0 A g^{-1}. When cycling at different rates for 80 cycles, the reversible capacity can attain 939 mAh g^{-1} immediately after the current density returns to 0.05 A g^{-1}. The discharge capacity and CE evolution of ($MoS_2/Ti_3C_2T_x$/CNTs)x3 heterostructure at 0.5 and 1.0 A g^{-1} for 500 and 1000 cycles, respectively, are noted in **Figure 4.17g**. For the initial ten cycles, the quick capacity loss is due to the SEI formation and side reactions at both current densities in the discharge/charge process. The stable capacity of 630 (0.5 A g^{-1}, at 500th cycle) and 578 mAh g^{-1} (1.0 A g^{-1}, at 1000th cycle) were acquired, with capacity retentions of 93% and 88%, respectively, and both CEs are close to 100%. The morphology of cycled electrodes at above current rates was checked by *ex-situ* SEM and presented in **Figure 4.18c-f**, there is no visible fracture observed instead it shows a close-knit surface. Furthermore, the ultra-long cycling profile of ($MoS_2/Ti_3C_2T_x$/CNTs)x3 heterostructure was evaluated at higher current rates of 2.0 and 5.0 A g^{-1} for 2000 cycles, as shown in **Figure**

4.17h. The discharge capacity of both electrodes was slightly reduced in around the first five cycles, then continuously increased and tended to stabilize at around a cycle of 400, which most likely can be ascribed to the extremely slow electrode activation process. The reversible capacity can keep up at 532 and 347 mAh g^{-1} for 2.0 and 5.0 A g^{-1} after 2000 cycles, respectively, with a stable CE of 99.8%. Finally, the structure changes of the cycled electrodes were also investigated by *ex-situ* SEM as shown in **Figure 4.18g-j**. Still, there is no significant mechanical failure or serious aggregation of $Ti_3C_2T_x$ nanosheets noticed on the terminal layer. These results demonstrate that the engineered ($MoS_2/Ti_3C_2T_x$/CNTs)x3 heterostructure can obviously enhance the stability and capability of the MoS_2-based electrode during the super long cycling process.

To further understand the excellent rate performance of the ($MoS_2/Ti_3C_2T_x$/CNTs)x3 heterostructure as anode for LIBs, a kinetic analysis was performed by the CV measurements at a rate current range from 0.1 to 2.0 mV s^{-1}. CV curves of ($MoS_2/Ti_3C_2T_x$/CNTs)x3 electrode are shown in **Figure 4.19a**, and exhibited high similarity indicating good reversibility of the heterostructure. The anodic/cathodic peaks at 2.31 and 1.87 V (marked with peak 1 and peak 2), respectively, represent the de-intercalation/intercalation behavior of lithium in the MoS_2 component. Normally, diffusive-process (e.g. intercalation, conversion, and alloying process) and (pseudo)capacitive-controlled charge storage contribute to the total lithium storage. [118, 173] The capacitive contribution can be elucidated qualitatively by applying varying CV scans.[174] According to the previous reports of Dunn and co-workers, the relationship between measured peak current (i) and scan rate (v) can be described as follows: $i = av^b$ (**equation 4.4**), where a and b are adjustable parameters. The value of b can be obtained from the slope of plotting log (i) versus log (v) as shown in **Figure 4.19b**. A b value of 0.5 or 1.0 demonstrates an ideal diffusion-controlled (battery-like) process or capacitance-dominated behavior, respectively. The calculated values of b for the ($MoS_2/Ti_3C_2T_x$/CNTs)x3 heterostructure are 0.79 and 0.90, respectively, corresponding to the anodic and cathodic current peaks, indicating that the charge storage is dominated by capacitive process. [175] Furthermore, based on the above concepts, the current response i(v) at a fixed potential can be divided into surface capacitive effects (k_1v) and diffusion-controlled insertion processes ($k_2v^{1/2}$), the capacitive contribution can be quantitatively calculated by the following equation: $i(v) = k_1v + k_2v^{1/2}$ (**equation 4.5**), where v is scan rate, k_1 and k_2 are constants. The equation can be rearranged to $i(v)/v^{1/2} = k_1v^{1/2} + k_2$ (**equation 4.6**) due to analytical purposes. Thus, the k_1 value at a given potential

can be determined as the slope of the curves by plotting $i(v)/v^{1/2}$ *vs* $v^{1/2}$, and k_2 is corresponding to the intercept. For instance, **Figure 4.19c** exhibits that ca. 68% of the total capacity is resulting from capacitive effects at a scan rate of 0.1 mV s^{-1}. Clearly, as we can see from **Figure 4.19d**, the capacitive contribution continuously increases with the rising of scan rates, reaching values as high as 79% at 2.0 mV s^{-1} from 45% at 0.1 mV s^{-1}. The diffusion-controlled (battery-like) process is limited due to the ultra-fast electronic transfer at high rates. [172] Such high contributions from capacitive effects probably originate from the porous structure (large surface area) that are entangled with CNTs, thereby enhancing the excellent rate capability. [161, 176]

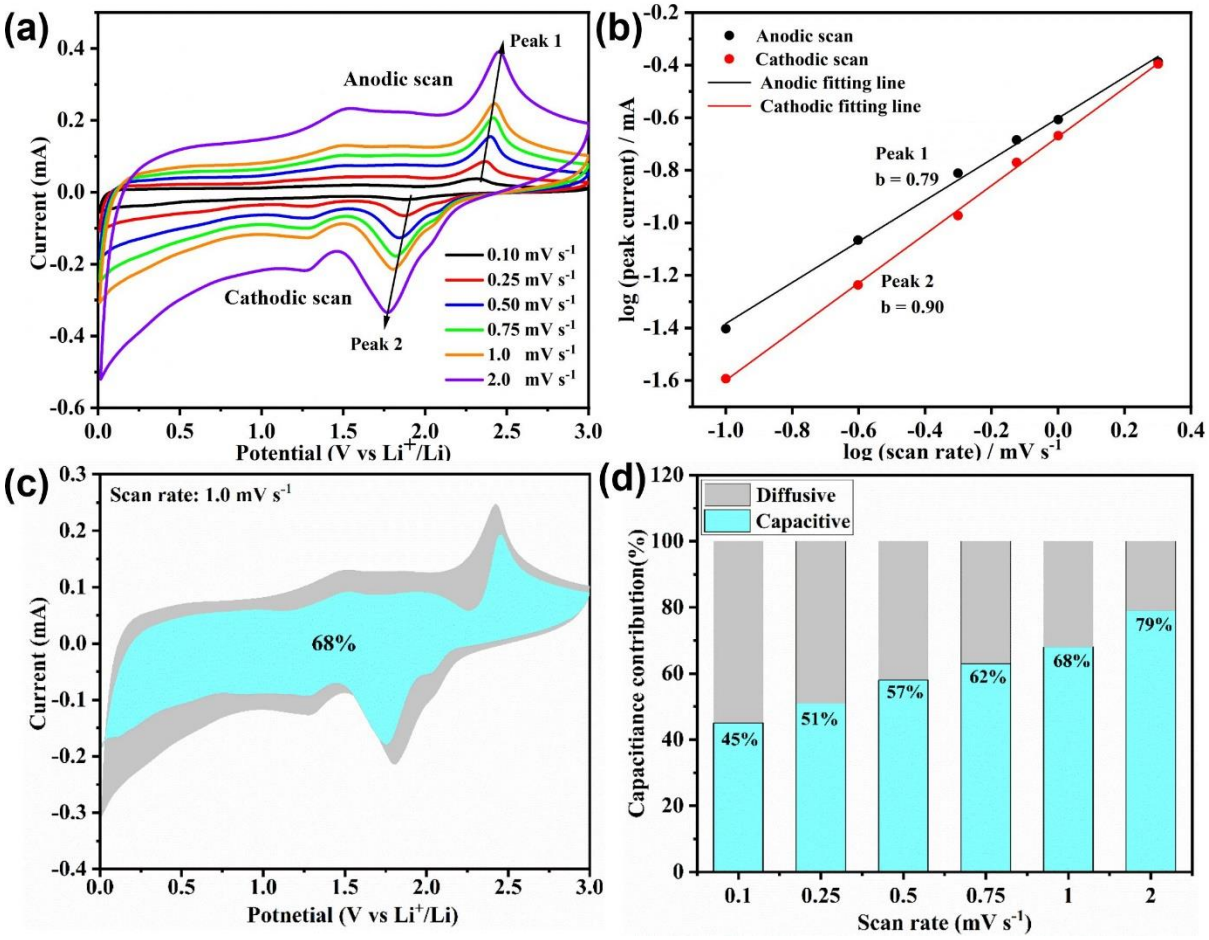

Figure 4.19 Evaluation of the kinetic behavior of $(MoS_2/Ti_3C_2T_x/CNTs)x3$ electrode. (a) CVs at scan rates of 0.1 mV s^{-1} to 2.0 mV s^{-1}, (b) log (i) *vs* log (v) curve at marked anodic and cathodic current peaks, (c) CV at 1.0 mVs^{-1} where the capacitive and diffusive contribution to energy storage has been depicted, (d) bar graph describing the percentage contributions to capacitive and diffusion-controlled energy storage at each considered scan rate.

4.3.4.6 Morphology and electrochemical performance of $MoS_2/Ti_3C_2T_x$/CNTs-mixed heterostructure

CNTs significantly improved the electrochemical performance of ($MoS_2/Ti_3C_2T_x$/CNTs)x3 heterostructure, especially in terms of cyclic stability and rate capability. Therefore, in the same way, $MoS_2/Ti_3C_2T_x$/CNTs-mixed heterostructure was also prepared and tested as a reference, and key electrochemical features (e.g. CV and GCPL cycling) were evaluated as well. Structural morphology of the electrode was nicely revealed by *ex-situ* SEM as shown in **Figure 4.20a**, demonstrating that some aggregations of MoS_2 and $Ti_3C_2T_x$ nanosheets form porous structures. A cross-sectional SEM image (**Figure 4.20b**) confirms that a compact stacking in the hybrid film that is interwoven with CNT networks was obtained. Compared to the pure MoS_2 and other $MoS_2/Ti_3C_2T_x$ heterostructures, **Figure 4.20c** displays high similarity to CV curves for $MoS_2/Ti_3C_2T_x$/CNTs-mixed heterostructure, regarding peak potential and intensities, here we do not introduce them in detail. Next, the cycling performance of the heterostructure was evaluated at a current density of 0.05 A g^{-1}, as presented in **Figure 4.20d**. The $MoS_2/Ti_3C_2T_x$/CNTs-mixed heterostructure delivered a high initial discharge capacity of 1092 mAh g^{-1} with an ICE of 65%, then continuously increased from 759 (cycle 2) to 907 mAh g^{-1} (cycle 100), which is consistent with the cycling profile of $MoS_2/Ti_3C_2T_x$-mixed heterostructure without CNTs (a reference to **Figure 4.13e**). The reasons for increasing capacity during cycling have been mentioned in the previous part. Morphology of the cycled electrode was characterized by *ex-situ* SEM, as shown in **Figure 4.21a-b**. As we can see from that, the porous structure remained even though with slightly agglomerated MoS_2 and $Ti_3C_2T_x$ nanosheets, but there are no cracks or slit-like surfaces observed, which further explains why the $MoS_2/Ti_3C_2T_x$/CNTs-mixed heterostructure showed no capacity degradation.

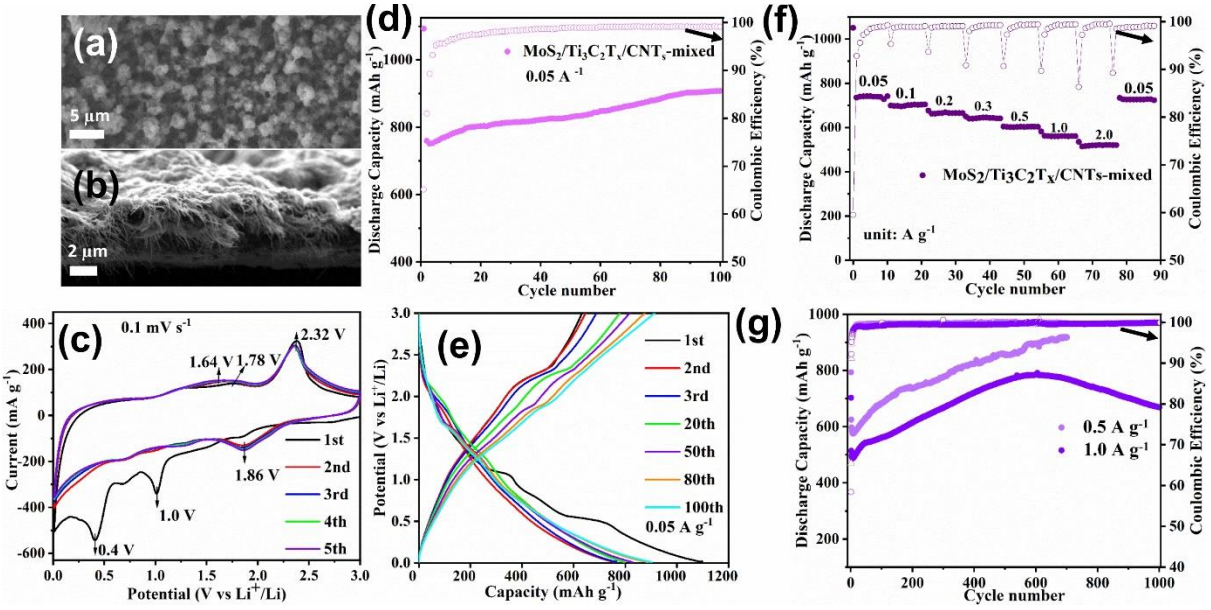

Figure 4.20 (a) and (b) are SEM images of the top and cross-sectional view of $MoS_2/Ti_3C_2T_x$/CNTs-mixed heterostructure, respectively; (c) the CV of $MoS_2/Ti_3C_2T_x$/CNTs-mixed heterostructure at a sweep rate of 0.1 mV s^{-1}; (d) and (e) are the cycling performance and voltage profile of $MoS_2/Ti_3C_2T_x$/CNTs-mixed heterostructure at 0.05 A g^{-1}, respectively; (f) the rate performance of $MoS_2/Ti_3C_2T_x$/CNTs-mixed heterostructure at various currents from 0.05 to 2.0 A g^{-1}; (g) the long-term cycling performance of $MoS_2/Ti_3C_2T_x$/CNTs-mixed heterostructure at 0.5 and 1.0 A g^{-1}, respectively.

The voltage profile of the $MoS_2/Ti_3C_2T_x$/CNTs-mixed heterostructure is shown in **Figure 4.20e**. Again, obvious initial discharge/charge voltage plateaus at 1.0, 0.5, and 2.3 V were observed for the 1st cycle, which is in good agreement with the redox peaks at 1.0, 0.4, and 2.32 V, respectively, in the CV curves (**Figure 4.20a**). The changes in voltage plateaus after 100 cycles are similar to that of the $MoS_2/Ti_3C_2T_x$-mixed heterostructure (see **Figure 4.13f**). Rate capabilities of $MoS_2/Ti_3C_2T_x$/CNTs-mixed heterostructure with corresponding CE values *vs* cycle number under a current range from 0.05 to 2.0 A g^{-1} are shown in **Figure 4.20f**. The reversible and stable capacity of the electrode is 739, 701, 665, 641, 602, 560, and 520 mAh g^{-1} at 0.05, 0.1, 0.2, 0.3, 0.5, 1.0 and 2.0 A g^{-1}, respectively, with the CE around 99% during 80 cycles (apart from the initial several cycles). Obviously, the reversible capacity can return to 728 mAh g^{-1} when the current is reduced to 0.05 A g^{-1}, which is significantly different from that of $MoS_2/Ti_3C_2T_x$-mixed heterostructure (**Figure 4.13g**). Therefore, the construction of the $MoS_2/Ti_3C_2T_x$-mixed heterostructure with CNTs can markedly enhance the stability during cycling at varying currents, which might be ascribed to the enhanced conductivity and mechanical strength of the electrode because of the entangled CNTs with MoS_2 and $Ti_3C_2T_x$ nanosheets.

The long-term cycling performance of the $MoS_2/Ti_3C_2T_x$/CNTs-mixed heterostructure at the current densities of 0.5 and 1.0 A g^{-1} is shown in **Figure 4.20g**. The electrode delivers a capacity of 793 mAh g^{-1} with a CE of 65% for the first discharge capacity at 0.5 A g^{-1}, then rapidly decayed from 624 (cycle 2) to 575 mAh g^{-1} (cycle 9) accompanied by an increasing CE from 91% to 98.6%, respectively. Afterwards, a steady capacity growth was observed and reached the maximum value of 917.8 mAh g^{-1} at end of cycling (700th cycle), while the CE remained at ca. 99.5% during the cycling, indicating that good reversibility and a stable mixed heterostructure. The structural morphology of the cycled $MoS_2/Ti_3C_2T_x$/CNTs electrode was investigated by *ex-situ* SEM and presented in **Figure 4.21c** and **d**. Some clusters of MoS_2 and $Ti_3C_2T_x$ nanosheets preferred to agglomerate and form a large bulk due to the strain accommodation during Li-ion insertion/extraction. Note that these bulks are composed of nanoparticles and are equally interconnected with porous CNTs networks, and thus suppress

the formation of cracks upon cycling, which enhanced the structure stability of the electrode. However, the nanosheets aggregation is not beneficial for realizing fast reaction kinetics. This might be the reason that extra-long cycles were required to activate the electrode to reach a high and stable capacity.

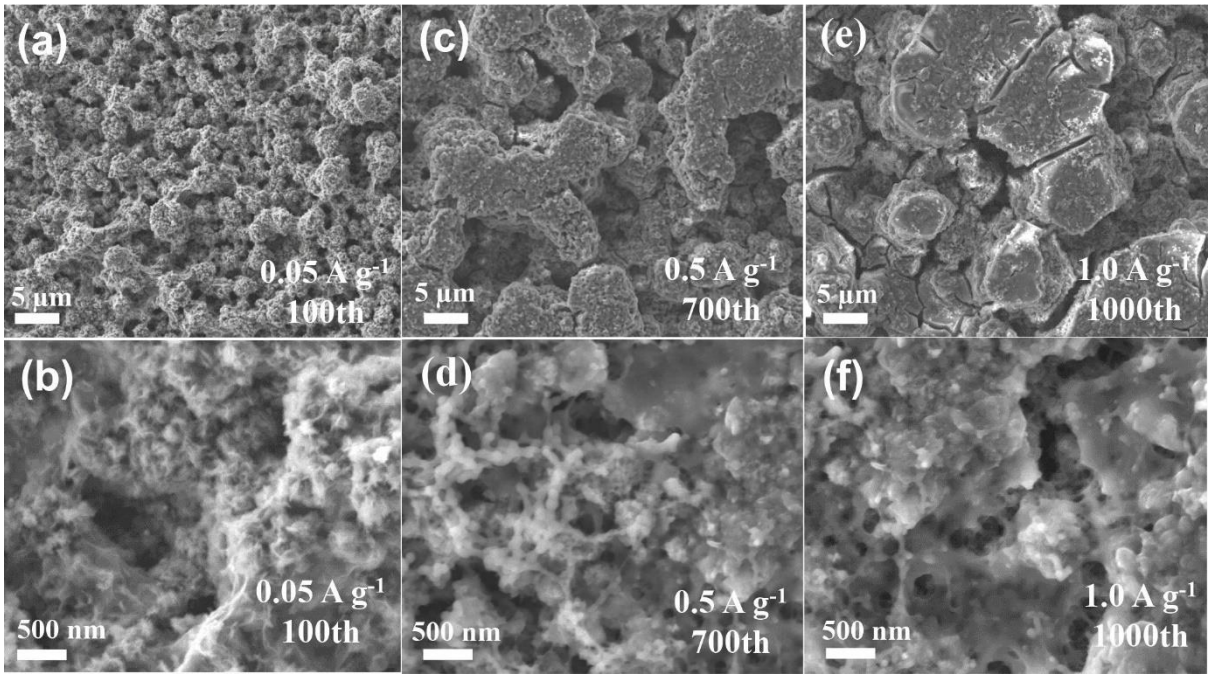

Figure 4.21 SEM images of cycled $MoS_2/Ti_3C_2T_x$/CNTs-mixed heterostructures, (a) and (b) are the top view of $MoS_2/Ti_3C_2T_x$/CNTs-mixed electrode after 100 cycles at a current density of 0.05 A g^{-1}; (c) and (d) are the top view of $MoS_2/Ti_3C_2T_x$/CNTs-mixed electrode after 500 cycles at a current density of 0.5 A g^{-1}, (e) and (f) are the top view of $MoS_2/Ti_3C_2T_x$-mixed electrode after 1000 cycles at a current density of 1.0 A g^{-1}.

Additionally, the long-term cycling stability under a higher current of 1.0 A g^{-1} was also evaluated. Interestingly, a high similarity regarding discharge capacity and CE evolution was obtained for the first round of 600 cycles (see **Figure 4.20g**). That is, the electrode exhibited an initial lithiation capacity of 702 mAh g^{-1} with a low ICE of 58%; followed by a capacity fading from 513 (cycle 2) to 488 mAh g^{-1} at cycle 9; subsequently, it constantly climbed to a peak capacity as high as 790 mAh g^{-1} till 605th cycle, whereas eventually the capacity degraded to 669 mAh g^{-1} for the last 400 cycles. *Ex-situ* SEM was performed to investigate the morphology of the cycled electrode. **Figure 4.21e** and **f** show that the large cluster agglomerates are similar to the ones at 0.5 A g^{-1}, which are isolated by countless slit-like cracks, thus resulting in the capacity decrease of the $MoS_2/Ti_3C_2T_x$/CNTs-mixed heterostructure for the later 400 cycles. In summary, compared to the $MoS_2/Ti_3C_2T_x$-mixed electrode, the rate performance and cyclic stability of the $MoS_2/Ti_3C_2T_x$/CNTs-mixed (at 0.5 and 1.0 A g^{-1}) were dramatically improved by introducing the CNT matrix into the structure.

Hence, the role of CNTs in the electrochemical behavior of MoS_2 and $Ti_3C_2T_x$ will be investigated later.

4.3.4.7 Role of CNTs

First of all, the electrochemical behavior of pure CNTs in the anodes of LIBs was evaluated by CV and galvanostatic charge/discharge. The related results are presented in **Figure 4.22**. **Figure 4.22a** displays some weak and one pronounced reduction peaks at 1.55 and 0.68 V in the first cathodic scan, respectively, which are assigned to a combination of several reduction processes (e.g. metal particle-assisted reduction of solvents) and the formation of SEI. [87, 177] A rather broad peak at 2.55 V was observed in the subsequent anodic scan, which is not clear for the moment. In the rest of CV scans, CNTs showed a typical pseudo-capacitive behavior (without well-defined redox couple peaks), which is consistent with the voltage profile of the pure CNTs, as shown in **Figure 4.22b**. **Figure 4.22c** shows that CNTs deliver an initial discharge/charge capacity of 807 and 412 mAh g^{-1}, respectively, with an ICE of 51%. Therefore, the capacity contribution of CNTs to the $(MoS_2/Ti_3C_2T_x/CNTs)x3$ is considerable. However, the discharge capacity gradually declined from 453 (2nd cycle) to 330 mAh g^{-1} at the 100th cycle, with a low capacity retention of 72.8%, demonstrating poor cycling stability of the CNT electrode.

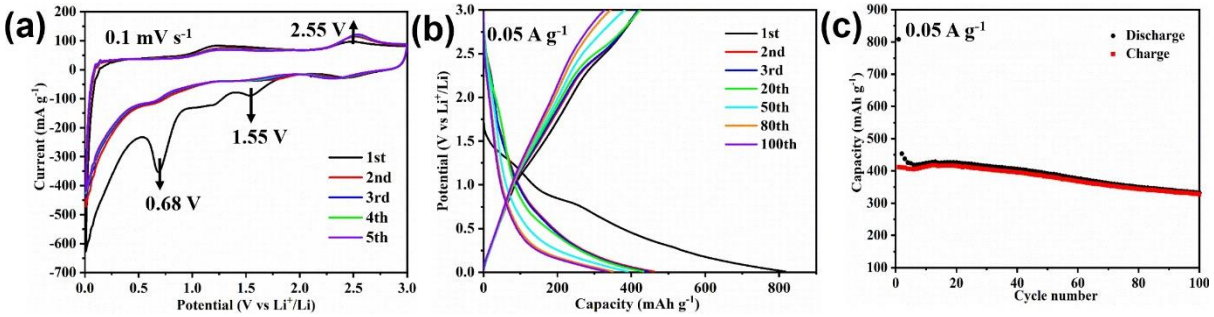

Figure 4.22 (a) CV of pure CNTs electrode at a sweep rate of 0.1 mV s^{-1}; (b) voltage profile of pure CNTs at of 0.05 A g^{-1}; (c) corresponding cycling profile of pure CNTs at 0.05 A g^{-1}.

Next, the electrochemical performance of the $Ti_3C_2T_x$/CNTs and MoS_2/CNTs composites were intensively investigated, as shown in **Figure 4.23**. One can see from **Figure 4.23a** and **b**, much fewer cycles were required for $Ti_3C_2T_x$/CNTs electrode to achieve stable capacities of 335 mAh g^{-1} (cycle 10) compared to the pure $Ti_3C_2T_x$ one at 0.05 A g^{-1}. A similar phenomenon was also observed for cycling at the high current densities of 0.5 and 1.0 A g^{-1}. As a result, the addition of CNTs resulted in a better activation process due to the enhanced

reaction kinetics (improved electrical conductivity). This could be further confirmed by the significantly improved rate performance of the $Ti_3C_2T_x$/CNTs electrode (see **Figure 4.23c**). In addition, the morphology changes of cycled $Ti_3C_2T_x$/CNTs at 0.05 and 0.5 A g^{-1} were studied by *ex-situ* SEM, related results are presented in **Figure 4.24a-b** and **c-d**, respectively. The pristine porous structure was transformed into a compact structure that interlinked with CNT networks. The CNTs helped to prevent the agglomeration of $Ti_3C_2T_x$ nanosheets and the formation of the cracks, which can explain why the stable capacity remained upon cycling.

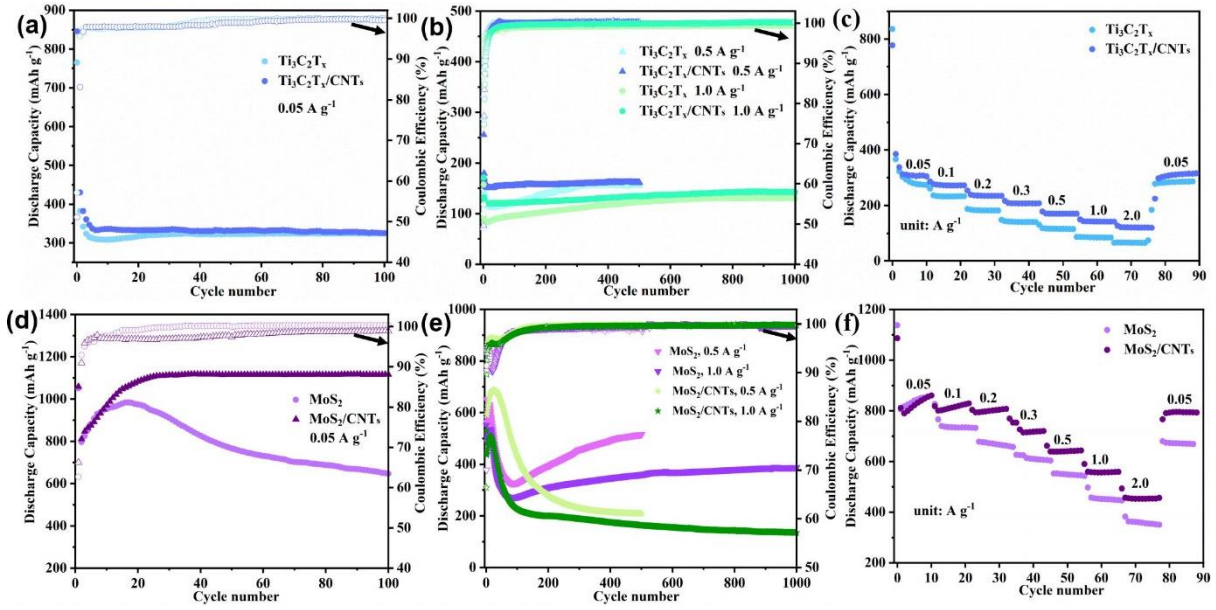

Figure 4.23 Comparison electrochemical performance of $Ti_3C_2T_x$ and $Ti_3C_2T_x$/CNTs, MoS_2, and MoS_2/CNTs. (a) cyclic performance of $Ti_3C_2T_x$ and $Ti_3C_2T_x$/CNTs at a current density of 0.05 A g^{-1}; (b) cyclic performance of $Ti_3C_2T_x$ and $Ti_3C_2T_x$/CNTs at the current density of 0.5 and 1.0 A g^{-1}; (c) rate performance of $Ti_3C_2T_x$ and $Ti_3C_2T_x$/CNTs at various current densities; (d) cyclic performance of MoS_2 and MoS_2/CNTs at the current densities of 0.05 A g^{-1}; (e) cyclic performance of MoS_2 and MoS_2/CNTs at the current densities of 0.5 and 1.0 A g^{-1}; (f) rate performance of MoS_2 and MoS_2/CNTs at various current densities.

Finally, the same electrochemical test was applied to the MoS_2/CNTs electrode. **Figure 4.23d** shows that the lithiation capacity of MoS_2/CNTs continuously increased from 810 (cycle 2) to 1102 mAh g^{-1} at cycle 23, followed by stabilization around 1115 mAh g^{-1} between cycles 48 and 100. Similar to the case of pure MoS_2, the activation process of the MoS_2/CNTs electrode is supposed to be the reason for capacity increase in the first 23 cycles, which has been explained in detail before. Meanwhile, the CE was steadily growing from 66.3% (cycle 1) to 98.4% at cycle 54 and tends to remain at ca. 99% till the end of cycling, which is quite different from the case of pure MoS_2 electrode (CE

was above 100% after cycle 55), demonstrating that excellent cyclic stability of MoS_2 was enabled by introducing CNT networks. **Figure 4.24e** and **f** presented the structural morphology of the cycled MoS_2/CNTs electrode, confirming that some bulk particles were generated due to the aggregation of MoS_2 nanosheets. However, it is worth pointing out that these bulks are composed of ball-like nanoparticles with entangled CNT networks.

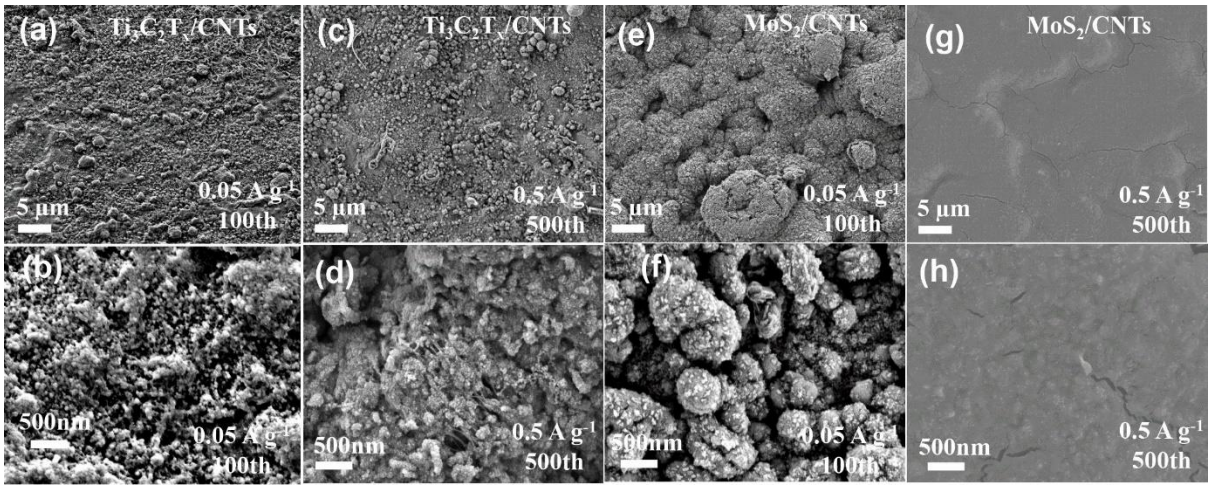

Figure 4.24 SEM images of cycled $Ti_3C_2T_x$/CNTs and MoS_2/CNTs electrodes, (a) and (b) are the top view of $Ti_3C_2T_x$/CNTs electrode after 100 cycles at a current density of 0.05 A g^{-1}; (c) and (d) are the top view of $Ti_3C_2T_x$/CNTs electrode after 500 cycles at a current density of 0.5 A g^{-1}, (e) and (f) are the top view of MoS_2/CNTs electrode after 100 cycles at a current density of 0.05 A g^{-1}, (g) and (h) are the top view of MoS_2/CNTs electrode after 500 cycles at a current density of 0.5 A g^{-1}.

This result highlights that the mechanical stability of the electrode can be enhanced by mixing with CNTs, thereby buffering the volume expansion of the MoS_2 flakes at a low current rate. To further investigate the cyclic stability of MoS_2/CNTs composite, cycling at high current rates of 0.5 and 1.0 A g^{-1} was carried out. Both electrodes exhibited similar behavior concerning the tendency of discharge capacity and CE evolution, as shown in **Figure 4.23e**. Taking the cycling at 0.5 A g^{-1} as an example, MoS_2/CNTs delivers an initial lithiation capacity of 754 mAh g^{-1} and an ICE of 66%, then it straightly increased from 590 (cycle 2) to 688 mAh g^{-1} at cycle 25, the corresponding CE increased from 91.6% to 97%. Like the case of pure MoS_2 electrode, the capacity rapidly declined to 261 at cycle 225, which is commonly ascribed to the volume expansion of MoS_2 nanosheets. Surprisingly, the MoS_2/CNT composites did not show a capacity increase like the pure MoS_2 electrode (**Figure 4.23e**), instead it degraded to 209 mAh g^{-1} till the end of cycling (500th cycle). Obvious cracks and pulverization of nanosheets were observed in the cycled MoS_2/CNTs electrode, as presented in **Figure 4.24g** and **h**, which accounts for the worse

electrochemical efficiency. This result highlights that CNT networks cannot effectively buffer the volume expansion/constriction of MoS_2 at a high rate, instead of suppressing the activation process of the MoS_2 electrode. The reason for that is not entirely clear. Additionally, the rate performance of the MoS_2/CNT electrode was evaluated as well, it exhibited dramatically improved rate capability and stability at various current rates when compared to MoS_2 alone electrode, as shown in **Figure 4.23f**, which can be related to the enhanced electrical and mechanical properties of the MoS_2/CNT matrix. [22]

4.3.4.8 Electrochemical impedance spectroscopy

As demonstrated in the previous part, among the different $MoS_2/Ti_3C_2T_x$ heterostructures, the $(MoS_2/Ti_3C_2T_x/CNTs)x3$ heterostructure exhibited superior lithium storage performance in cycling stability and rate capability. Herein, electrochemical impedance spectroscopy (EIS) was applied to further examine the reaction kinetics of the Li^+ insertion/extraction process upon cycling for the $(MoS_2/Ti_3C_2T_x/CNTs)x3$ heterostructure. In comparison, the kinetics of pure MoS_2 and $Ti_3C_2T_x$ electrodes were investigated as well. **Figure 4.25a** displays the Nyquist plots of pure MoS_2 obtained at a lithiation potential of 0.1 V (discharge process) for 40 cycles with a current density of 0.05 A g^{-1}, which was modeled using the electrical equivalent circuit (EEC): $R_{el}(R_{SEI})(C_{SEI})(R_{CT}Wo)(CPE_{int})$. The R_{el} is the sum of the resistance of the electrolyte, separator, and internal resistance of the cell, corresponding to the high-frequency region. R_{SEI} and C_{SEI} represented the SEI resistance and double-layer capacitance, respectively, corresponding to the first semicircle in the middle-high-frequency region (200k ~ 100 Hz). A second parallel circuit $(R_{CT}Wo)(CPE_{int})$ modeled the charge transfer process at the interface between electrode and electrolyte, where R_{CT} is the charge transfer resistance and Wo is an open circuit terminus Warburg element accounting for diffusion processes. [128] The CPE_{int} is the capacitance at the interface, where a constant phase element (CPE) is accounting for a frequency dispersed capacitance. [126-127] The R_{el} for the MoS_2 electrode at a lithiation potential of 0.1 V was 3.3 Ω and stayed almost unchanged upon cycling, as shown in **Figure 4.25b**. However, the R_{SEI} increased from 5 (cycle 1) to 25 Ω (cycle 40), which is supposed to be a result of the continuous growth of the SEI film., A R_{CT} value of 9.8 Ω at cycle 1 was obtained, then decreased to 3.0 Ω at cycle 10 and rapidly increased to 29.7 Ω till 40th cycle (**Figure 4.25b**), which is consistent with the capacity growth of the MoS_2 electrode in the first 10 cycles and the capacity degradation afterwards (a reference to **Figure 4.8a**). As demonstrated before, the increase of capacity is

correlated with a further opening of the electrode structure upon cycling, facilitating electrolyte infiltration and further exposure of active material to the electrolyte for a deeper lithiation, [107-109] which could be also accounting for the decline of R_{CT}. The subsequent capacity degradation was caused by the severe volume expansion of MoS_2, which thereby hamper fast and stable charge transfer processes. To better evaluate the impedance evolution of SEI for the MoS_2 electrode during the delithiation (charge process), the impedance was recorded at the polarized potential of 1.84 and 3.0 V, which takes place before and after the oxidation of Mo and Li_2S (at 2.34 V), respectively. **Figure 4.25c** shows the impedance changes of the MoS_2 electrode in delithiation at a potential of 1.84 V for the initial 40 cycles. The electrolyte resistance R_{el} remained around 3.5 Ω over cycling, indicating the cell assembly was quite stable (**Figure 4.25d**). The calculated values of R_{SEI} and R_{CT} are 4.5 and 6.1 Ω for the initial cycle, respectively, which is rather close to that of the lithiation condition. However, the R_{SEI} and R_{CT} increased from 8.8 and 5.0 Ω (cycle 10) to 61 and 100 Ω (cycle 40), respectively, which is similar to the lithiation process but with significantly higher values. In comparison to the lithiation condition, these results indicate that the SEI film did not decompose and instead shows less ionic conductivity during the delithiation process. As expected, a highly similar impedance evolution for the MoS_2 electrode was observed at a delithiation potential of 3.0 V, as presented in **Figure 4.27a**. Here, the analysis of that will not be discussed in detail.

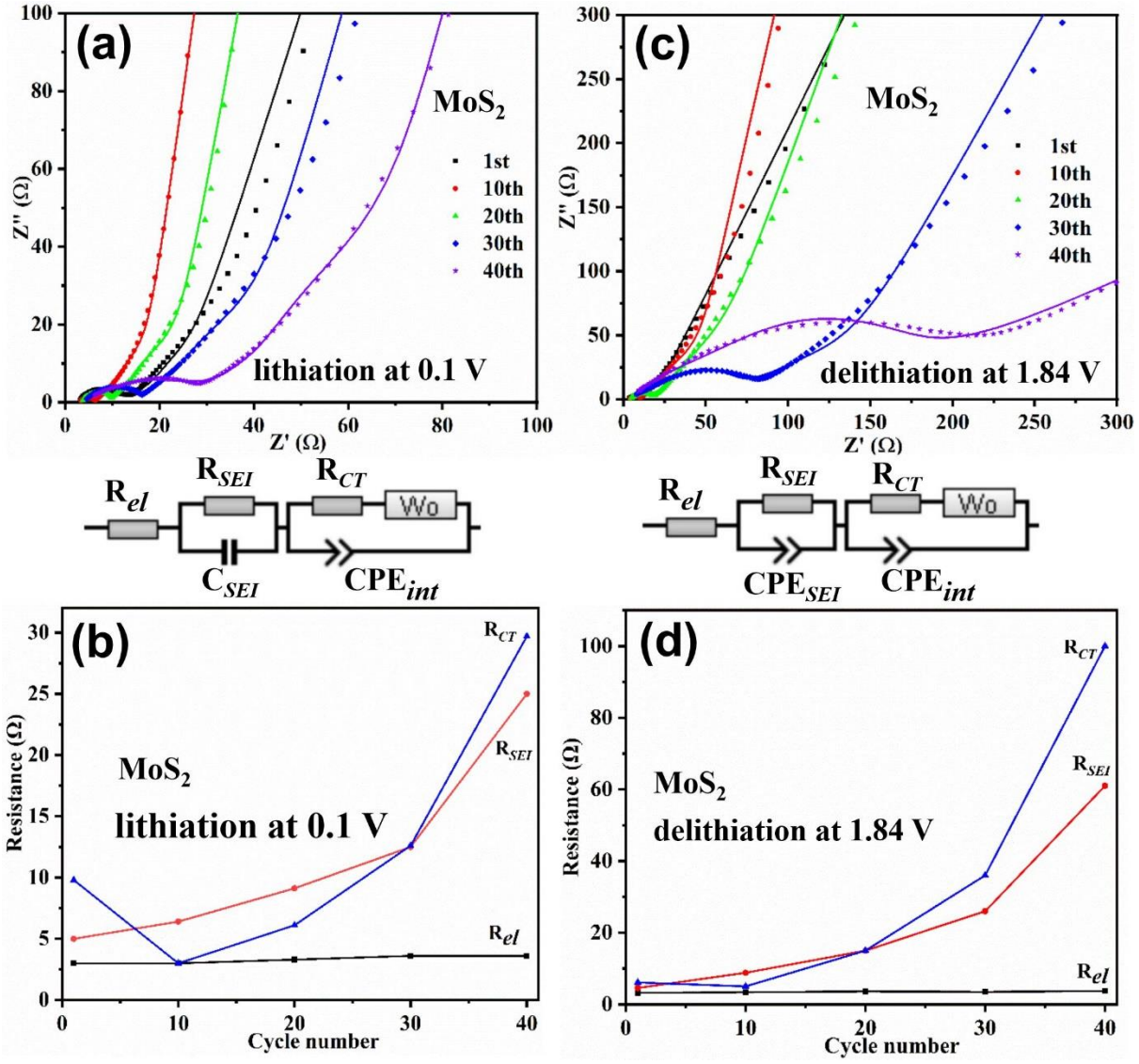

Figure 4.25 EIS data of pure MoS_2 electrodes at lithiation and delithiation states with specific cycles of a GCPL cycling experiment (point: raw data, line: fitted data). (a) Nyquist plots of pure MoS_2 obtained at lithiation state (discharge process) with a current density of 0.05 A g^{-1} and corresponding EEC used for data modeling, (b) corresponding evolution of R*el*, $R_{CT,}$ and R_{SEI} *vs* cycles curves, (c) Nyquist plots of pure MoS_2 obtained at delithiation state (charge process) with a current density of 0.05 A g^{-1} and corresponding EEC used for data modeling, (d) corresponding evolution of R*el*, $R_{CT,}$ and R_{SEI} *vs* cycles curves.

Figure 4.26a shows the impedance changes for the $Ti_3C_2T_x$ electrode at a lithiation voltage of 0.1 V at specific cycles and were fitted by using the same EEC $R_{el}(R_{SEI})(C_{SEI})$ $(R_{CT}Wo)(CPE_{int})$ from the MoS_2 electrode in lithiation condition. The evolution of the fitted resistances is shown in **Figure 4.26b**, the R_{el} shows an initial value of 4.3 Ω and exhibited almost no variation over cycling, and indicating that the change of the assembled cell resistance is negligible. Similarly, the R_{SEI} slightly increased from 42 (cycle 1) to 44.3 Ω at

cycle 40, which demonstrates that the formed SEI in the lithiation process is highly stable during the long-term cycling. Nevertheless, the R_{CT} presents a fluctuating tendency upon cycling, it increased from 37 (1st cycle) to 45 Ω at cycle 10, followed by a drop to 32 Ω at the 20th cycle, and tends to stabilize at this value till cycle 40. The increase of R_{CT} in the first ten cycles can be ascribed to the side reactions, after that, the resistance degradation might be attributed to the exposure of a large number of electrochemically active sites with cycling which facilitates a fast charge transfer. [136, 149] These results are in good agreement with the capacity evolution *vs* cycle (see **Figure 4.8a**). Note that the value of the R_{SEI} and R_{CT} resistances for the $Ti_3C_2T_x$ electrode in lithiation conditions is higher than that of MoS_2 electrode, which could result from the much thicker SEI film and partial oxidation of $Ti_3C_2T_x$ nanosheets during the spray deposition.

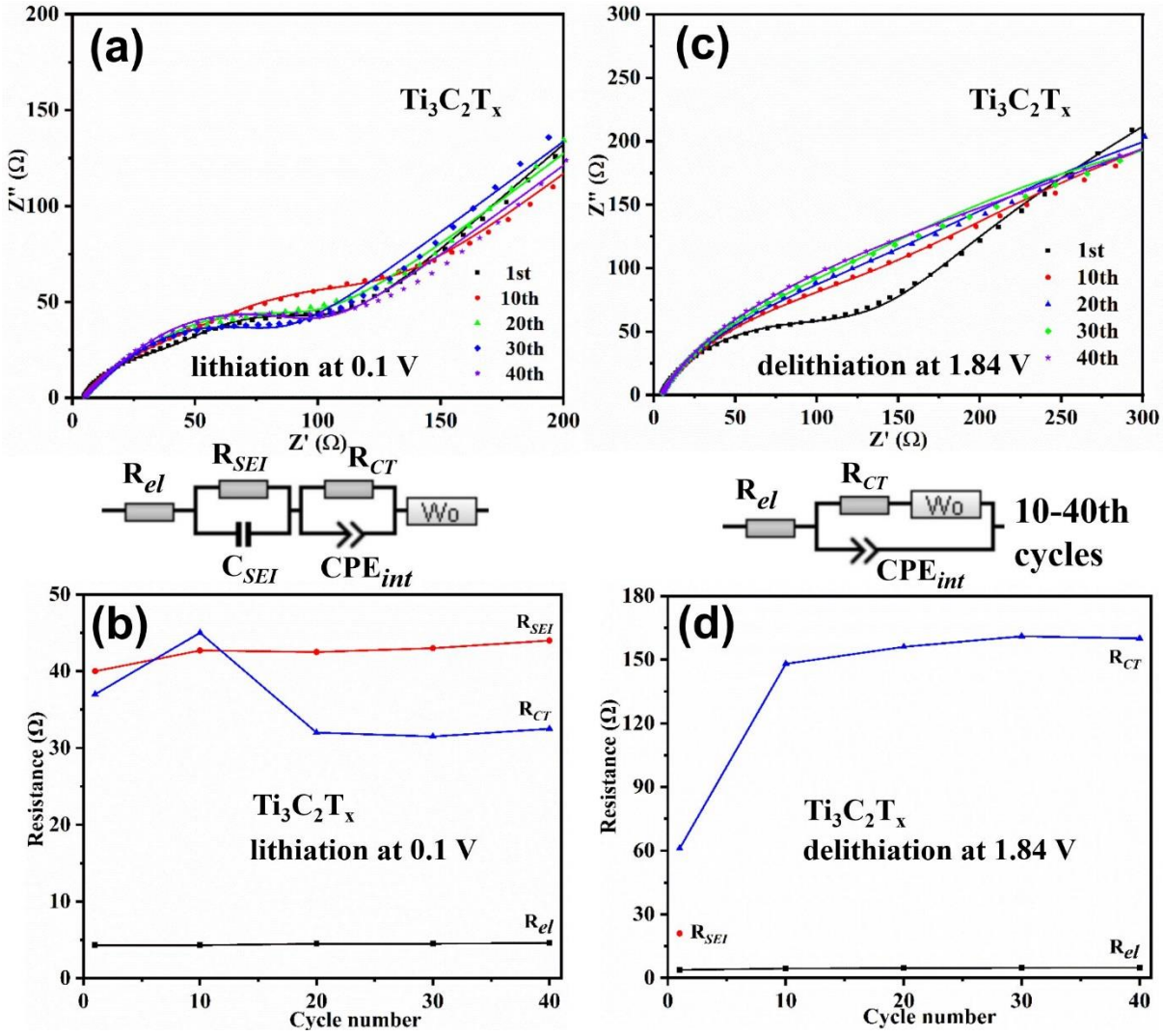

Figure 4.26 EIS data of pure $Ti_3C_2T_x$ electrodes at lithiation and delithiation states with specific cycles of a GCPL cycling experiment (point: raw data, line: fitted data). (a) Nyquist plots of pure $Ti_3C_2T_x$ obtained at delithiation state (discharge process) with a current density

of 0.05 A g^{-1} and corresponding EEC used for data modeling, (b) corresponding evolution of R*el*, $R_{CT,}$ and R_{SEI} *vs* cycles curves, (c) Nyquist plots of pure MoS_2 obtained at delithiation state (charge process) with a current density of 0.05 A g^{-1} and corresponding EEC used for data modeling, (d) corresponding evolution of R*el*, $R_{CT,}$ and R_{SEI} *vs* cycles curves.

In comparison, the Nyquist plots of the $Ti_3C_2T_x$ in the delithiation process (at 1.84 V) during 40 cycles were also recorded and analyzed, as shown in **Figure 4.26c**. The curve obtained at the first cycle with two depressed semicircles is remarkably different from the rest of the cycles but similar to the curves of lithiation condition. Therefore, the resistances data of the 1st cycle in the delithiation can be well fitted by using the same EEC of the lithiation process, and another EEC: R_{el} (R_{CT}W*o*)(CPE$_{int}$) was applied to analyze the cycles 10 to 40. The trend of the fitted resistance values *vs* cycles is presented in **Figure 4.26d**. As expected, the value of R_{el} remained around 4.3 Ω upon cycling. As we can see from **Figure 4.26c**, the two semicircles obtained at the 1st cycle, corresponding to the SEI and charge transfer process in the high and mid-frequency region (200k ~ 100 Hz), merged into one semicircle with an inclined line, which thereby makes it impossible to extract the resistance contribution from SEI (R_{SEI}) by EIS from 10 to 40 cycles, therefore only an initial value of 21 Ω is shown. The disappearance of the SEI semicircle was most probably caused by the continuous decomposition of SEI film in the delithiation process, which could be further confirmed by the semicircle vanishing for all of the cycles at a fully charged state (at delithiation potential of 3.0 V), as shown in **Figure 4.27b**. The R_{CT} rapidly increased from 60 (cycle 1) to 148 Ω (cycle 10) and then slightly reached 160 Ω till cycle 40, which is a little different from the lithiation situation. Therefore, compared to the lithiation condition, the above-mentioned exposure of the new active sites with cycling most likely does not have a similar influence on the delithiation process.

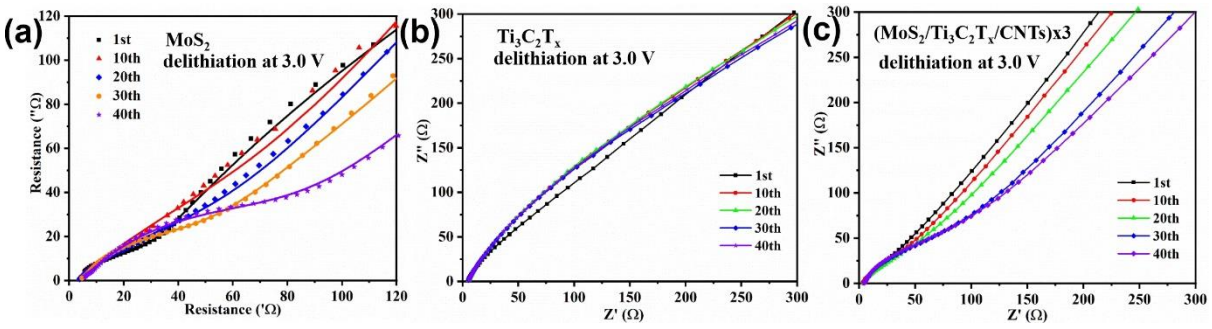

Figure 4.27 Nyquist plots of the MoS_2, $Ti_3C_2T_x$, and ($MoS_2/Ti_3C_2T_x$/CNTs)x3 electrodes at different cycles in delithiation state with a current density of 0.05 A g^{-1}.

Next, the same methodology was applied to analyze the impedance data of the ($MoS_2/Ti_3C_2T_x$/CNTs)x3 heterostructure. **Figure 4.28a** displays the impedance evolution over cycling for the ($MoS_2/Ti_3C_2T_x$/CNTs)x3 electrode at a lithiation potential of 0.1 V, which was fitted by the EEC: $R_{el}(R_{SEI})(C_{SEI})$ $(R_{CT}Wo)(CPE_{int})$. The calculated values of R_{el}, $R_{SEI,}$ and R_{CT} at specific cycles are shown in **Figure 4.28b**. Therefore, one can see that the electrolyte resistance R_{el} slightly increased from 3.5 (1st cycle) to 4.5 Ω at cycle 40, which could be caused by the change of the electrode contact resistance (e.g. pulverization process of activated materials) upon cycling. [178] Obviously, the fitted values of R_{SEI} and R_{CT} exhibited a similar increasing tendency with cycling. The R_{SEI} was gently increasing from an initial value of 3.0 to 5.8 Ω at the 20th cycle, followed by rapidly growing to 9.7 Ω (cycle 30) and tends to stabilize at this value till cycle 40. The slow increase of R_{SEI} in the first 20 lithiation cycles can be assigned to the steady growth of SEI and the sharp increase of that in the following cycles 20 to 30 is most likely resulting from the volume expansion of the MoS_2 layers inside the ($MoS_2/Ti_3C_2T_x$/CNTs)x3 heterostructure, which leads to producing additional surface area. This can be further confirmed by the slight increase of the R_{SEI} curve of pure MoS_2 that was observed from cycles 20 to 30 in lithiation conditions (**Figure 4.28b**) while the pure $Ti_3C_2T_x$ electrode exhibited quite stable R_{SEI} resistances over cycling (**Figure 4.28f**). Meanwhile, the R_{CT} increased from 7.2 (cycle 1) to 9.5 Ω at cycle 20 due to side reactions (as mentioned before), and then rose to 15.5 Ω at cycle 30 and reached 17 Ω till the 40th cycle. Likewise, the reason for the increase of R_{CT} is supposed to result from the volume expansion of the MoS_2 layer as well.

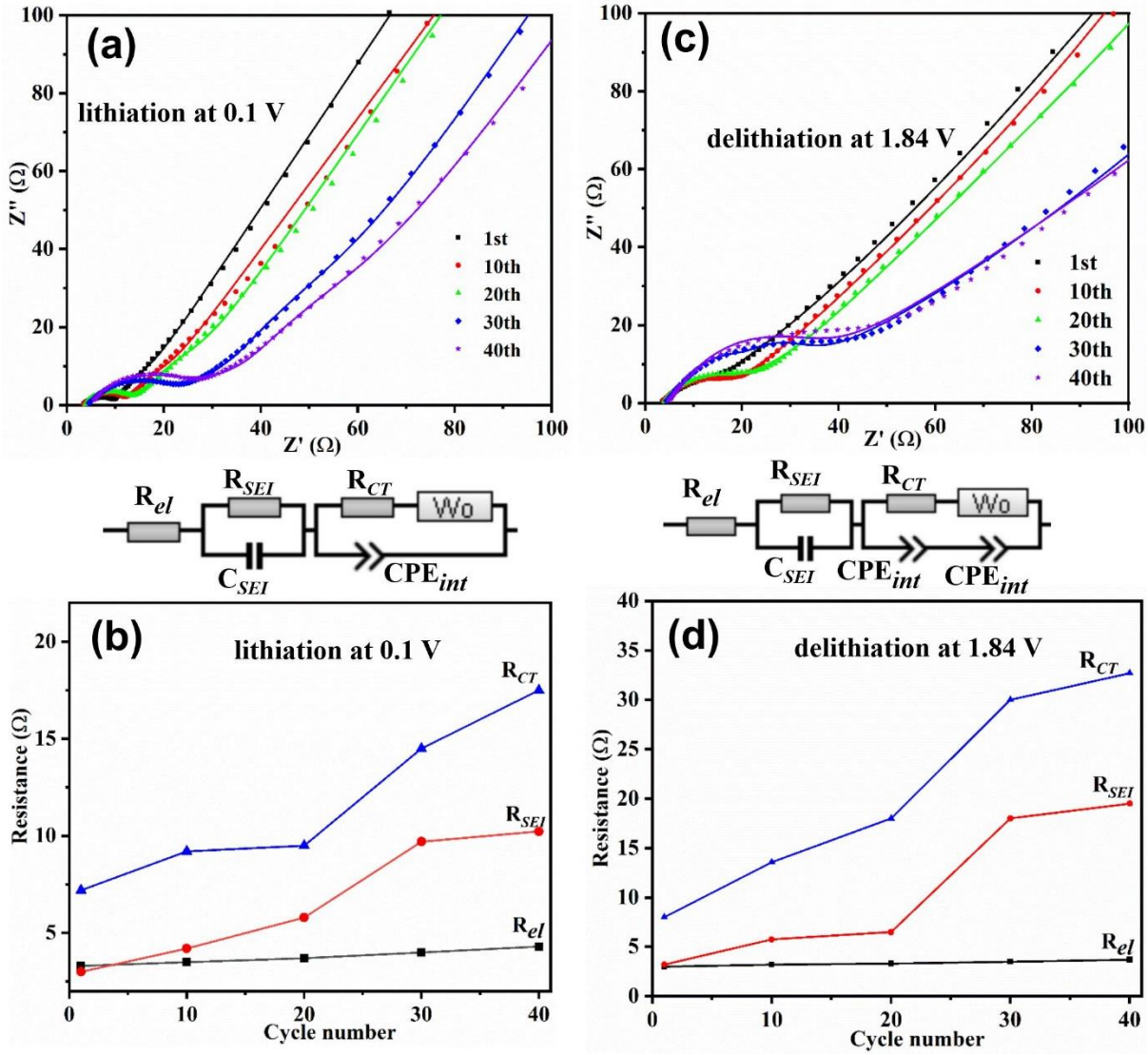

Figure 4.28 EIS data of $(MoS_2/Ti_3C_2T_x/CNTs)x3$ electrode at lithiation and delithiation condition with specific cycles of a GCPL cycling experiment (point: raw data, line: fitted data). (a) Nyquist plots of $(MoS_2/Ti_3C_2T_x/CNTs)x3$ obtained at lithiation state (discharge process) with a current density of 0.05 A g^{-1} and corresponding EEC used for data modelling, (b) corresponding evolution of R*el*, $R_{CT,}$ and R_{SEI} *vs* cycles curves, (c) Nyquist plots of $(MoS_2/Ti_3C_2T_x/CNTs)x3$ obtained at delithiation state (charge process) with a current density of 0.05 A g^{-1} and corresponding EEC used for data modelling, (d) corresponding evolution of R*el*, $R_{CT,}$ and R_{SEI} *vs* cycles curves.

Subsequently, the impedance evolution of the $(MoS_2/Ti_3C_2T_x/CNTs)x3$ heterostructure at the delithiation potential of 1.84 V was recorded and fitted by the EEC: $R_{el}(R_{SEI})(C_{SEI})$ $(R_{CT}Wo)(CPE_{int}CPE_{int})$, as presented in **Figure 4.28c**. **Figure 4.28d** shows the changes in the calculated resistances for R_{el}, $R_{SEI,}$ and R_{CT} *vs* cycles. The R_{el} was continuously growing from 3.8 (cycle 1) to 4.9 Ω at cycle 40, which reflects the slight increase in the internal resistance of the cell. The calculated R_{SEI} and R_{CT} with the values of 3.2 and 8.0 Ω were obtained for

the first cycle, then both of them increased with varying degrees to 19 and 32 Ω at cycle 40 afterward. Compared to the lithiation condition, highly similar value changes of R_{SEI} and R_{CT} with cycling were observed in the delithiation process. In addition, R_{SEI} and R_{CT} have shown slightly higher values for the delithiation process, which demonstrated that the SEI film did not decompose and becomes less conductive after repeated discharge/charge cycles. Finally, the Nyquist plots with cycling for the ($MoS_2/Ti_3C_2T_x$/CNTs)x3 heterostructure at full charge (with delithiation potential of 3.0 V) was also collected and used as a reference, as presented in **Figure 4.27c**. The two semicircles corresponding to the R_{SEI} and R_{CT} evolved into one depressed arc-like circle spontaneously, indicating that the SEI formed in the lithiation process was further completely decomposed at the fully charged state, which is the same as in the case of pure $Ti_3C_2T_x$ electrode at delithiation voltage of 3.0 V (see **Figure 4.27b**). This is thanks to the ($MoS_2/Ti_3C_2T_x$/CNTs)x3 heterostructure with a terminal layer of $Ti_3C_2T_x$/CNTs, which hence exhibited similar impedance behavior. It is worth noting that even a variation of R_{SEI} and R_{CT} was observed in the lithiation and delithiation process, but remains at a quite low level when compared to the pure MoS_2 and $Ti_3C_2T_x$ electrodes (**Figure 4.28b** and **f**). From the above results, it is reasonable to conclude that the ($MoS_2/Ti_3C_2T_x$/CNTs)x3 heterostructure possess excellent integrity of the electrode, thus preventing the loss of contact between the MoS_2 and $Ti_3C_2T_x$ nanosheets or CNT matrix, meanwhile, leading to a stable formation of SEI film due to well-buffered volume expansion, and eventually exhibiting superior reaction kinetics.

4.3.4.9 Electrochemical performance of the Li-ion full cell

Finally, to evaluate the potential for the practical application of the $MoS_2/Ti_3C_2T_x$ heterostructures in LIBs, a Li-ion full cell was assembled by coupling the ($MoS_2/Ti_3C_2T_x$/CNTs)x3 heterostructure anode (among several heterostructures, it exhibited the best electrochemical performance) with the $LiNi_{0.6}Co_{0.2}Mn_{0.2}O_2$ (NCM622) cathode. Firstly, the NCM622 half cell (Li foil used as a counter electrode) was tested as a comparison, as shown in **Figure 4.29** and **b**, which delivered an initial discharge capacity of 190 mAh g^{-1} with an ICE of 93%, which is in good agreement with previous reports. [179-180]. The initial capacity loss can be ascribed to slow lithium kinetics at high lithium contents. In other words, after the first delithiation (charge process), the kinetics of the NCM-based cathodes degraded during lithium back-intercalation (discharge process), meaning that a part of the Li-ions could not be re-inserted into the cathodes. [181] **Figure 4.29b** shows that the NCM622 cathode exhibited

excellent cycling properties over 100 cycles, with a high capacity of 188 (10th cycle) and 165 mAh g^{-1} (100th cycle) at 0.1C and 1.0 C, respectively. Next, however, to obtain good performance in the Li-ion full cell, a pre-lithiation operation is recommended or necessary for $(MoS_2/Ti_3C_2T_x/CNTs)x3$ heterostructure anode. [182-183] The $(MoS_2/Ti_3C_2T_x/CNTs)x3$ anode was galvanostatically activated in a half cell configuration for six cycles (final delithiation to 2.6 V), before being assembled in the full cell. The $(MoS_2/Ti_3C_2T_x/CNTs)x3$//NCM622 shows an initial specific discharge capacity of 188 mAh g^{-1} (for NCM622) in a wide operating voltage window from 0.3 to 4.0 V, with a CE of 94.5%. The voltage profile mostly overlaps in the following cycles (2nd-10th cycles), demonstrating good reversibility. The full cell delivered excellent cycling performance with a discharge capacity of 186 (10th cycle) and 155.8 mAh g^{-1} (100th cycle) at 0.1 C and 1.0 C, respectively, and especially a high capacity retention of 96.7% was obtained after hundreds of cycles (**Figure 4.29c** and **d**). **Figure 4.29e** and **f** depict the rate capability of the full cell, with discharge capacities of 188, 177, 165, 158, and 144 mAh g^{-1} (*vs.* NCM622) at 0.1, 0.2, 0.5, 1.0, and 1.5 C, respectively, which did not show significant capacity differences as the current rate increases. The only distinct capacity drops occurred at 2.0 C, the capacity of full cell decreased to 118 mAh g^{-1}, which might be resulting from the inherent unstable cycling property of the pure NCM622 cathode at high rates. [184-185] Finally, however, the cell exhibits good cycling stability at 1.0 C after rate tests, with a capacity of 150 mAh g^{-1} at the 80th cycle, corresponding to the 98.3% capacity retention with respect to cycle 31.

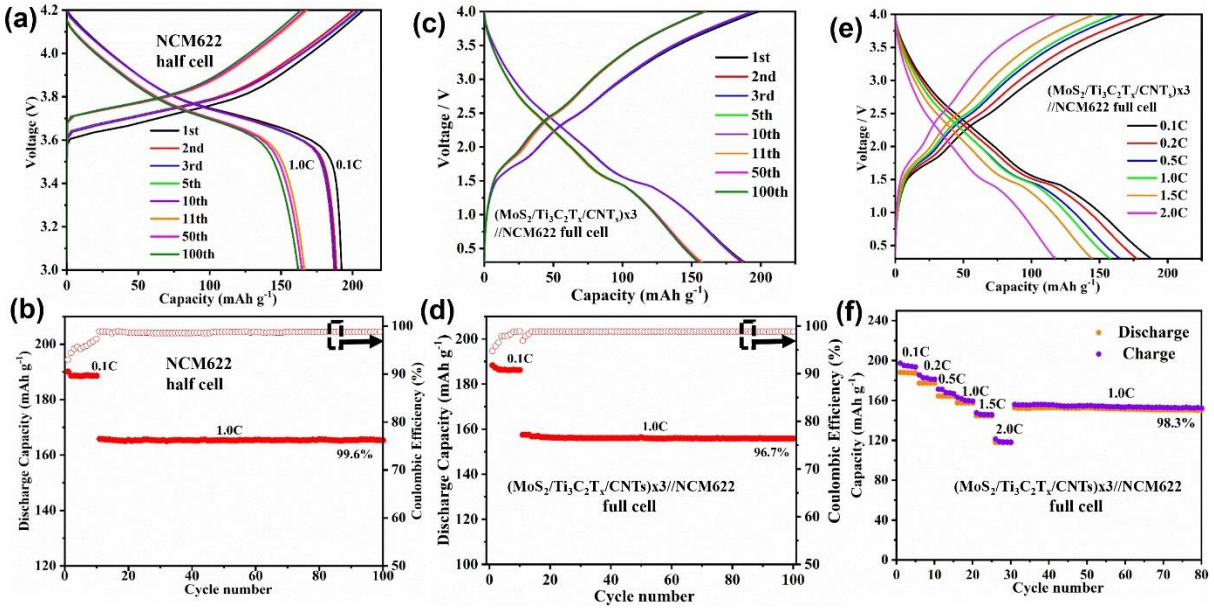

Figure 4.29 (a) voltage profiles of selected cycles at 0.1C (first to tenth cycles) and 1.0C (following 90 cycles) of the NCM622 electrode in a half cell configuration; (b) the

corresponding charge/discharge profiles and coulombic efficiency of the half-cell during cycling at 0.1C and 1.0C; (c) voltage profiles of selected cycles at 0.1C (first to tenth cycles) and 1.0C (following 90 cycles) of the ($MoS_2/Ti_3C_2T_x$/CNTs)x3//NCM622 full cell; (d) the corresponding charge/discharge specific capacity and coulombic efficiency of the full cell during cycling at 0.1C and 1.0C; (e) voltage profile of the ($MoS_2/Ti_3C_2T_x$/CNTs)x3//NCM622 full cell at selected rates current (0.1-2.0C); (f) the corresponding rate capability of the full cell at different rates (from 0.1 to 2.0C) for 80 cycles in total. The values of specific capacity for the full cell are referred to the active materials of the cathode NCM622; 1.0C = 200 mA g^{-1}.

4.4 Conclusions

In summary, three different types of 2D $MoS_2/Ti_3C_2T_x$ heterostructures were successfully engineered via LBL spray deposition, which are denoted as ($Ti_3C_2T_x/MoS_2$)xn (n = 1, 2, 3, 4 and 8) and ($MoS_2/Ti_3C_2T_x$)x3, featured with the terminal layer of either MoS_2 and $Ti_3C_2T_x$ nanosheets, respectively, and $MoS_2/Ti_3C_2T_x$-mixed heterostructure, made by spraying a conventional mix of MoS_2 and $Ti_3C_2T_x$ suspension. All the well-defined stacked structures of the heterostructures were further confirmed by SEM and XRD. The resulting 2D $MoS_2/Ti_3C_2T_x$ heterostructures sufficiently integrate the merits of two individual building blocks. Therefore, when used directly as anodes for LIBs, all as-prepared heterostructures exhibit enhanced electrochemical performance in terms of capacity and cycling stability compared with single MoS_2 or $Ti_3C_2T_x$ nanosheets. We systematically investigated how the terminal layers (with MoS_2 or $Ti_3C_2T_x$ nanosheets) of the heterostructures affect the electrochemical performances, demonstrating that the denoted as ($MoS_2/Ti_3C_2T_x$)x3 heterostructure with a terminal layer of $Ti_3C_2T_x$ can better buffer the volume expansion of MoS_2 component, especially at high rates, but much more cycles of activation process are required to achieve a high capacity and stability. As a result, carbon nanotubes (CNTs) were incorporated into ($MoS_2/Ti_3C_2T_x$)x3 electrode to obtain ($MoS_2/Ti_3C_2T_x$/CNTs)x3 heterostructure. It exhibits a superior reversible capacity of 578 mAh g^{-1} (after 1000 cycles) at 1.0 A g^{-1}, and 532, 347 mAh g^{-1} at the 2000th cycle at 2.0 and 5.0 A g^{-1}, respectively. The addition of CNTs not only improves electron and ion transport but also acts as a substrate to prevent the aggregation of the terminal $Ti_3C_2T_x$ layers, thus rendering the formation of a robust SEI layer, which was further confirmed by *ex-situ* SEM and EIS. The excellent lithium storage performance in half/full cell measurements confirms the ($MoS_2/Ti_3C_2T_x$/CNTs)x3 heterostructure may be ranked as a promising anode material for next-generation LIBs. Finally, the 2D heterostructures reported in this work may offer a facile and high-efficient

strategy for addressing the low conductivity and volume expansion limitations of other TMDs-based materials.

5 Electrochemical Performance Investigation of 2D $MoS_2/Ti_3C_2T_x$ Heterostructures as Anodes for Sodium-ion Batteries

5.1 Introduction

Recently, sodium-ions batteries (SIBs) have attracted extensive attention again and are viewed as a promising alternative to LIBs due to the low-cost, natural abundance, and competitive energy density. LIBs and SIBs share a similar mechanism with the Li^+/Na^+ repetitive insertion/deinsertion between anode and cathode materials. [186] Therefore, the knowledge arising from the extensive research of the LIBs is suitable for the SIBs systems such as the routine of exploring designing advanced anode and cathode materials. [187] However, there are some intrinsic differences between these systems, for instance, the most well-known graphite anode matching well LIBs are not applicable for SIBs due to the larger atomic radius of Na^+ ions, which leads to the Na^+ hardly forming staged intercalation compounds with graphite. [188] Moreover, the larger Na^+ radius could result in a relatively sluggish reaction kinetics of Na^+ and more serious volume expansion of anode materials during the continuous sodiation/desodiation process. [8, 189] Therefore, the development and design of novel anode materials for SIBs which could accommodate larger Na^+ to reach high capacity and excellent rate capability are highly expected.

Inspired by the studies of 2D MoS_2 and $Ti_3C_2T_x$ electrodes as well as their 2D $MoS_2/Ti_3C_2T_x$ heterostructures as anodes for LIBs in **chapters 3** and **4**, they were tested directly as anodes for SIBs to determine if the combination of $Ti_3C_2T_x$ MXene, which have metallic conductivity and excellent mechanical strength but only a moderate capacity, and MoS_2 with high capacity but poor cycling stability, can result in enhanced electrochemical sodium storage. In addition, according to previous publications, fluoroethylene carbonate (FEC) has been proposed as an effective electrolyte additive in SIBs, which can significantly enhance the stability and mechanical flexibility of the as-formed SEI film. [190-192] As a consequence, the influence of fluoroethylene carbonate (FEC) electrolyte additive on the electrochemical performance of the pure MoS_2 and $Ti_3C_2T_x$ was firstly evaluated. Then, three different types of 2D $MoS_2/Ti_3C_2T_x$ heterostructures were prepared by the same spray deposition method of **chapter 4**, denoted as $MoS_2/Ti_3C_2T_x$-mixed, $(MoS_2/Ti_3C_2T_x)$x3, and $(MoS_2/Ti_3C_2T_x/CNTs)$x3, and evaluated in FEC-containing electrolyte as

anodes for sodium-ion storage. Finally, their charge/discharge behavior, specific capacities, cycling stabilities, and rate capabilities were systemically compared.

5.2 Experimental methods

5.2.1 Materials

Molybdenum disulfide powder, (MoS_2, 99%, Sigma Aldrich), 1-methyl-2-pyrrolidinone (NMP, >99%, Sigma Aldrich), 2-propanol (IPA, 99%, Sigma Aldrich), lithium fluoride, (LiF, ≥99.98%, Sigma Aldrich), hydrochloric acid (HCl, 37% wet. in H_2O, Sigma Aldrich), polyethyleneimine (PEI), branched (M.W. 70,000, 30% w/v, aqueous solution), carbon nanotubes (single-walled, carboxylic acid functionalized), Sodium perchlorate ($NaClO_4$, 98%, Sigma Aldrich), Fluoroethylene carbonate (FEC, 99%, Sigma Aldrich), Whatman Grade GF/D Glass Microfiber Filters (Pore Size: 2.7 µm Diameter: 5.5cm; thickness: 675 µm).

5.2.2 Manufacture of electrodes

All electrodes were fabricated by the same method as in **chapter 4**

5.2.3 Materials characterization

The morphology and structure of all samples and electrodes were already investigated in **chapter 4.**

5.2.4 Electrochemical methods

Two-electrode cells were assembled in a CR2032-type coin-cell using either 2D MoS_2, $Ti_3C_2T_x$, and various $MoS_2/Ti_3C_2T_x$ heterostructures as working electrodes and Na foil as a counter electrode, both separated by Whatman GFD membrane, previously immersed in 150 µl of 1 M $NaClO_4$/ethylene carbonate/propylene carbonate (EC/PC in a mass ratio of 1:1) without and with 5 wt% fluoroethylene carbonate (FEC) additive. Assembly of cells was carried out in an Ar-filled glovebox (*MBraun*, Germany) with oxygen and water concentrations kept both below 0.1 ppm. Electrochemical tests were performed in a temperature-controlled environment at 25 °C.

Cyclic voltammetry (CV) and galvanostatic cycling with potential limitation (GCPL) were performed in a potential range of 3-0.01 V *vs.* Na^+/Na at various scan rates and current densities, respectively.

5.3 Results and Discussion

5.3.1 Influence of FEC electrolyte additive on the electrochemical performance of 2D MoS_2 electrode

Since FEC has been proposed as an effective electrolyte additive for enhancing the stability of SEI film and cycling lifespan that is frequently used in SIBs, the influence of FEC on the electrochemical performance of 2D MoS_2 electrodes was investigated by CV and GCPL, as shown in **Figure 5.1a-d**. For the 2D MoS_2 electrode featured with FEC-free, two pronounced reduction peaks at 0.89 and 0.68 V *vs* Na^+/Na during the first cathodic scan (**Figure 5.1a**) are observed, which are assigned to the intercalation of Na^+ into layered 2H MoS_2 to form 1T Na_xMoS_2 and the subsequent conversion reaction of 1T Na_xMoS_2 with Na^+ to produce Na_2S and Mo atoms, respectively. [193-195] In general, the proposed discharge storage mechanism for MoS_2 can be described as a two-step reaction: [196]

Step I: $MoS_2 + xNa^+ + xe^- \rightleftharpoons Na_xMoS_2$ $(0< x <1)$ (**equation 5.1**)

Step II: $Na_xMoS_2 + (4-x)Na^+ + (4-x)e^- \rightleftharpoons 2Na_2S + Mo$ (**equation 5.2**)

One sharp reduction peak at 0.08 V appeared in the cathodic scan down to 0.01V, which is commonly ascribed to the formation of SEI since it disappeared in the rest of the cathodic scans (2nd-5th cycle). [195] These three peaks are in good agreement with the discharge plateaus around 0.9, 0.7, and 0.1 V. (**Figure 5.1b**) In the subsequent first anodic scan, three relatively weak oxidation peaks at 1.32, 1.81, and 2.61 V were observed, which are related to the stepwise oxidation of 1T Na_xMoS_2 and regeneration of 2H MoS_2 with distorted crystal structure due to micro-strains. [196] Moreover, these anodic peaks are highly overlapping in the subsequent charge process (desodiation), indicating a good reversible ability of the 2D MoS_2 electrode. From the second to fifth cathodic scan, previous peaks at 0.89 and 0.68 V have vanished, instead showing a weak reduction peak at 0.91 V, which is not fully understood at this time due to the lack of work on the reversible mechanism of MoS_2 as the anode in SIBs.

Figure 5.1c displays the CV curves of the 2D MoS_2 electrode with a 5%FEC additive. Three dominant irreversible cathodic peaks were located at 1.24, 0.83, and 0.65 V in the first sodiation process that can be assigned to the side

reactions of FEC-containing compounds and intercalation of Na into MoS_2 followed by a subsequent conversion reaction of $NaMoS_2$. [189] Again, these peaks are well-consistent with the voltage plateaus at 1.3, 0.87, and 0.72 V in the first discharge process, as shown in **Figure 5.1d**. There are four oxidation peaks at 1.33, 1.82, 2.28, and 2.61 V observed in the following anodic scan, which is highly similar to that of MoS_2 without FEC additive except for a new anodic peak at 2.28 V. Interestingly, compared to **Figure 5.1a**, a similar phenomenon also occurred in the subsequent cathodic scan (2nd to 5th), showing a new enhanced reduction peak at 2.35 V. The reason for that is still unclear for the moment.

Next, a long-cycling profile of 2D MoS_2 electrode with and without FEC at a current density of 0.05 A g^{-1} was compared, as shown in **Figure 5.1e**. The MoS_2 electrode in the FEC-free electrolyte delivered an initial discharge capacity of 794 mAh g^{-1} with an ICE of 53.6% and rapidly declined to 370 mAh g^{-1} at cycle 10. Afterwards, the capacity gradually degraded to 194 mAh g^{-1} but CE continuously increased to 94% after 100 cycles with a capacity retention rate of 39.6% (from the second cycle). Nevertheless, the MoS_2 in the 5% FEC-containing electrolyte exhibited a discharge capacity of 828 mAh g^{-1} with a CE of 56% in the first cycle, which then grew from 497 (2nd cycle 2) to 543 mAh g^{-1} till cycle 20, followed by a gently decrease to 433 mAh g^{-1} at end of cycle 100. The capacity retention is 87%, exhibiting superior cycling stability. This enhanced capacity with FEC additive could be owing to the FEC modifying the surface passivation layer, including the SEI films. [191 197]

The rate performance of the 2D MoS_2 electrode with and without FEC additive was evaluated, and is presented in **Figure 5.1f**. As we can see from that, the rate capability of 2D MoS_2 at various current densities was highly improved by the addition of FEC, in particular at high rates (e.g. 0.5, 1.0, and 2.0 A g^{-1}).

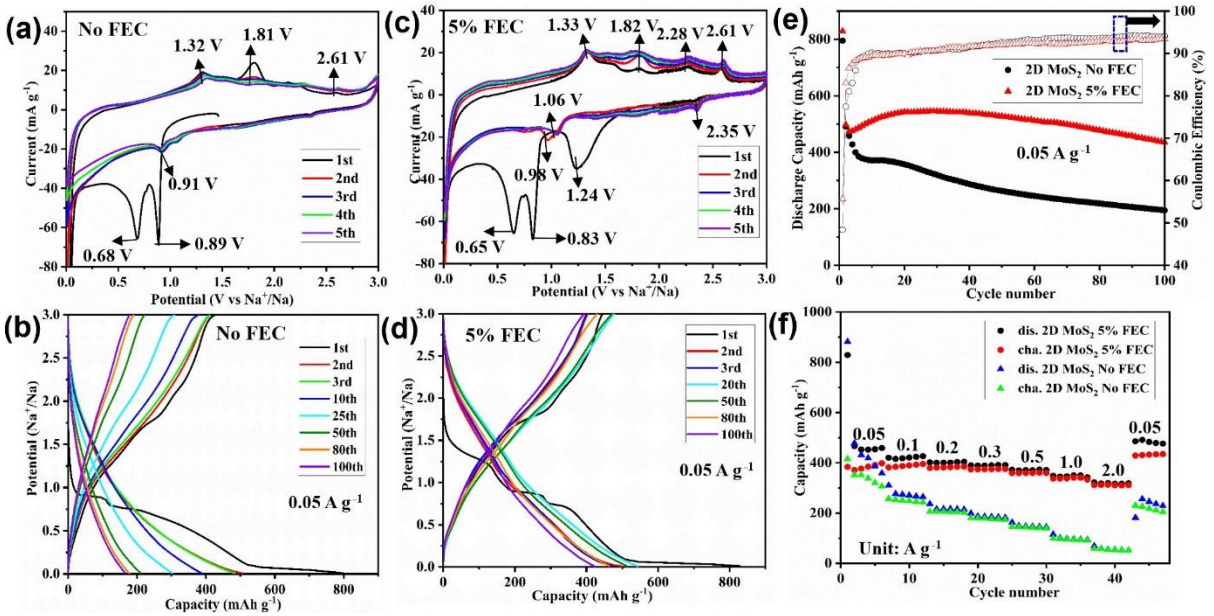

Figure 5.1 Electrochemical measurements of 2D MoS_2 electrode (a) and (b) are the CV curves at a sweep rate of 0.1 mV s^{-1} and voltage profile of 2D MoS_2 electrode without FEC electrolyte additive at a current density of 0.05 A g^{-1}, respectively; (c) and (d) are the CV curves at a sweep rate of 0.1 mV s^{-1} and voltage profile of 2D MoS_2 electrode at a current density of 0.05 A g^{-1} with FEC electrolyte additive, respectively (e) the comparison cycling performance of 2D MoS_2 electrode with and without FEC electrolyte additive at a current density of 0.05 A g^{-1}, (f) the rate performances of 2D MoS_2 electrodes.

Finally, the 2D MoS_2 electrode was cycled at 0.5 and 1.0 A g^{-1} in the FEC additive electrolyte for 500 and 300 cycles, respectively, as shown in **Figure 5.2**. **Figure 5.2a** shows that the MoS_2 electrode delivers an initial capacity of 420 mAh g^{-1} with an extremely low ICE of 40%, which rapidly fades to 188 mAh g^{-1} at cycle 150, and eventually tends to be stabilized around 171 mAh g^{-1} after 500 cycles. Moreover, when 2D MoS_2 is cycled at 1.0 A g^{-1}, the discharge capacity decreases quickly from 368 mAh g^{-1} (1st cycle) to 66 mAh g^{-1} at cycle 150; a capacity of 30 mAh g^{-1} can only be obtained after 300 cycles, as present in **Figure 5.2b**. This poor cycling stability of 2D MoS_2 at high rates is commonly ascribed to the insufficient electronic conductivity and severe volume expansion of MoS_2.

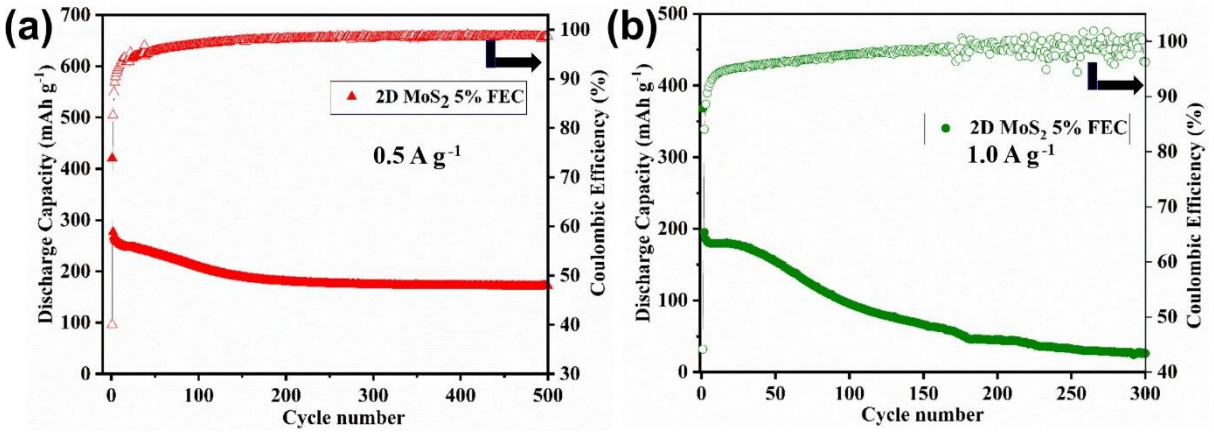

Figure 5.2 (a) and (b) are cycling performances of 2D MoS_2 electrodes with FEC additive at the current densities of 0.5 and 1.0 A g^{-1}, respectively.

5.3.2 Influence of FEC electrolyte additive on the electrochemical performance of $Ti_3C_2T_x$ electrode

The influence of the FEC electrolyte additive on the electrochemical performance of the $Ti_3C_2T_x$ electrode was also evaluated. **Figure 5.3a** shows the first five CV curves of $Ti_3C_2T_x$ electrode without FEC additive, only one broad reduction peak at 0.54 V was observed in the first cathodic scan, which is commonly assigned to irreversible reactions on the surface of the electrodes, including the formation of SEI layer and possible side reactions between Na^+ and surface functional groups of $Ti_3C_2T_x$. [198] And this cathodic peak is in good agreement with the voltage plateau at 0.6 V in the discharge profile (**Figure 5.3b**). There is one oxidation peak at 2.8 V observed in the initial anodic scan and tends to shrink regarding peak intensity, which is quite different from the previous work. [199] In addition, this peak is coupled with a reduction peak at 2.66 V in the subsequent cathodic scan, here, one can speculate that the pair of broad anodic/cathodic peaks located at 2.8/2.66 V is associated with Na^+ insertion/extraction from the electrolyte-derivate compounds. [200] This can be further confirmed by the coulombic efficiency of over 100% in the cycling test (see **Figure 5.3e**)

Figure 5.3c presents the initial five CV curves of the $Ti_3C_2T_x$ electrode in the FEC electrolyte additive. Three broad cathodic peaks at 1.23, 0.69, and 0.39 V were observed in the first sodiation process, which are ascribed to the reduction reaction of FEC-containing compounds and intercalation of Na^+ with $Ti_3C_2T_x$ layer and formation SEI, respectively. Compared to the CV of $Ti_3C_2T_x$ FEC-free electrode (**Figure 5.3a)**, apart from the anodic peak at 2.8 V, a new reduction peak at 2.0 was noticed in the first desodiation process, which is paired with the reduction peak at 0.73V and is associated with the Na^+ extraction from the

$Ti_3C_2T_x$ layer. It is worth noticing that the anodic peaks at 2.0 and 2.8 V shifted to higher potential upon cycling, indicating an activation process of the $Ti_3C_2T_x$ electrode. [201]

Cyclic stability of the $Ti_3C_2T_x$ electrode with and without FEC additive was evaluated at a current density of 0.05 A g^{-1} for 100 cycles, as shown in **Figure 5.3e**. Both of $Ti_3C_2T_x$ electrodes exhibited a closely similar initial discharge capacity of 420 mAh g^{-1} and ICE of 33%, indicating that the FEC does not help to improve the initial capacity loss. However, the discharge capacity of the FEC-free $Ti_3C_2T_x$ electrode quickly declines from 218 (2nd cycle) to 82 mAh g^{-1} at cycle 30, and then tends to have remained at this value till the 100th cycle. Meanwhile, the coulombic efficiency was gently increased from 76% at cycle 2 to 82% at cycle 20, then suddenly expanded to 96% at cycle 40, followed by a gradual increase to 100.1% till cycle 84 and finally stabilized at 101.2% afterwards. The extra charge capacity is supposed to be caused by the decomposition of electrolyte-derivate compounds. On the contrary, the $Ti_3C_2T_x$ electrode can exhibit excellent cycling stability in the FEC additive electrolyte. The discharge capacity rapidly decreased from 182 (2nd cycle) to 158 mAh g^{-1} at cycle 5 and slightly faded to 150 mAh g^{-1} till the 100th cycle, with a capacity retention of 82.4%. As expected, the rate performance of the $Ti_3C_2T_x$ electrode was significantly improved by the FEC electrolyte additive at various current rates.

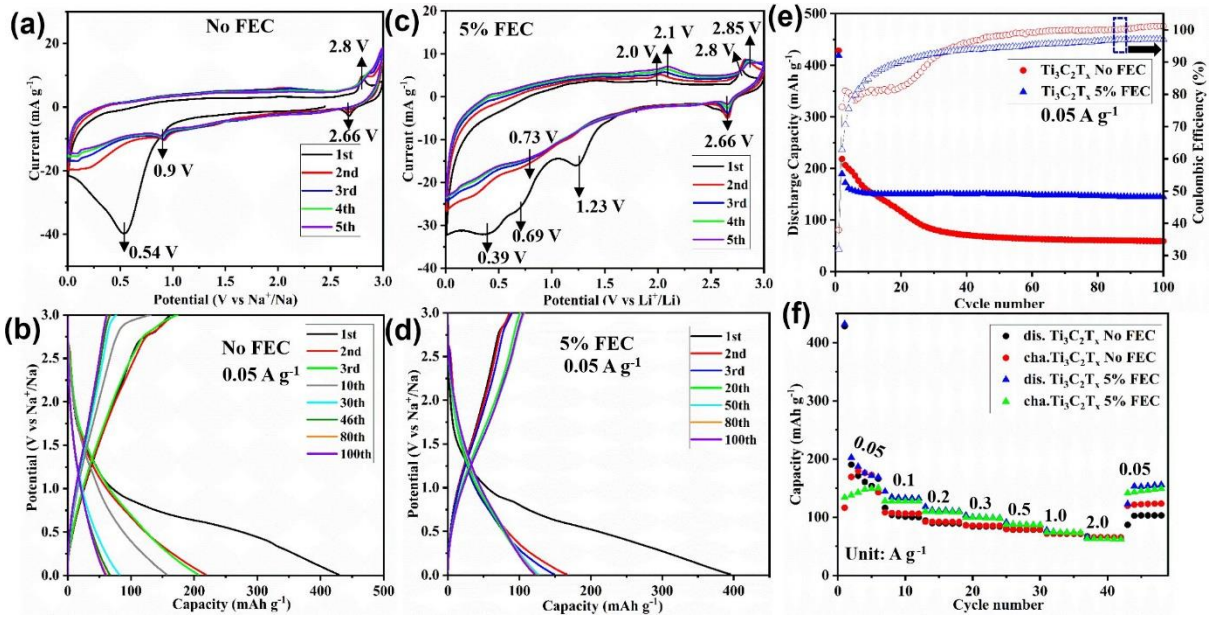

Figure 5.3 Electrochemical measurements of $Ti_3C_2T_x$ electrode (a) and (b) are the CV curves at a sweep rate of 0.1 mV s^{-1} and voltage profile of $Ti_3C_2T_x$ electrode without FEC electrolyte additive at a current density of 0.05 A g^{-1}, respectively; (c) and (d) are the CV curves at a sweep rate of 0.1 mV s^{-1} and voltage profile of $Ti_3C_2T_x$ electrode at a current density of 0.05 A g^{-1} with FEC electrolyte additive, respectively; (e) the comparison cycling performance of

$Ti_3C_2T_x$ electrode with and without FEC electrolyte additive at a current density of 0.05 A g^{-1}, (f) the rate performances of $Ti_3C_2T_x$ electrodes.

Similar to the case of the 2D MoS_2 electrode, the $Ti_3C_2T_x$ electrodes were cycled at 0.5 and 1.0 A g^{-1} for 500 and 1000 cycles, respectively, to determine if the FEC additive can still result in a stable cycling life-span at higher current densities, as presented in **Figure 5.4**. **Figure 5.4a** shows that the $Ti_3C_2T_x$ electrode exhibits a discharge capacity of 139 mAh g^{-1} at 0.5 A g^{-1} after 500 cycles, with a capacity retention of 82%. As expected, a reversible sodiation capacity of 93 mAh g^{-1} at 1.0 A g^{-1} can still be achieved after 1000 cycles for the $Ti_3C_2T_x$ electrode, with a capacity retention rate of up to 76%. Both electrodes show an ultra-stable CE evolution, indicating that a robust SEI layer was formed. As a result, the exceptional capacity retention of the $Ti_3C_2T_x$ electrode can be due to its mechanical strength and the optimized SEI layer by FEC additive. In summary, 1 M $NaClO_4$ in EC/PC with 5% FEC was therefore selected as the exclusive electrolyte for further experiments.

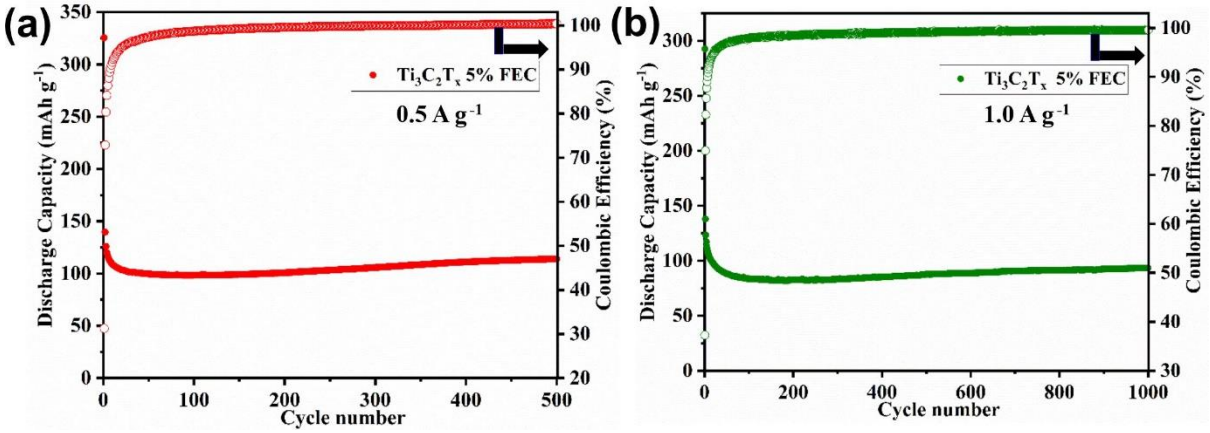

Figure 5.4 (a) and (b) are cycling performances of the $Ti_3C_2T_x$ electrodes with FEC electrolyte additive at the current densities of 0.5 and 1.0 A g^{-1}, respectively.

5.3.3 Electrochemical performance of 2D $MoS_2/Ti_3C_2T_x$-mixed heterostructure

The 2D MoS_2 electrodes have shown a high sodium storage capacity but poor cycling stability, whereas $Ti_3C_2T_x$ electrodes exhibited an excellent life-span, but demonstrate only moderate capacity, in particular at high rates. To address this issue, the 2D $MoS_2/Ti_3C_2T_x$-mixed heterostructure was made by spraying the conventional mixture of 2D MoS_2 and $Ti_3C_2T_x$ suspensions. The electrochemical sodium storage behavior of the $MoS_2/Ti_3C_2T_x$-mixed heterostructure is firstly evaluated by CV measurement, as displayed in **Figure 5.5a**. As can be seen from that, the initial five CV curves of $MoS_2/Ti_3C_2T_x$-

mixed electrode were featured with all characteristic peaks of 2D MoS_2 electrodes in FEC additive electrolyte (**Figure 5.1c**), indicating that the same sodiation/desodiation process occurs to the mixed electrode. Note that the initial three reduction peaks at 1.15, 0.8, and 0.62 V are well consistent with the voltage plateaus at 1.24, 0.88, and 0.73 V in the discharge profile (see **Figure 5.5b**). The cycling performance of the $MoS_2/Ti_3C_2T_x$-mixed electrode at 0.05 A g^{-1} was evaluated, shown in **Figure 5.5c**.

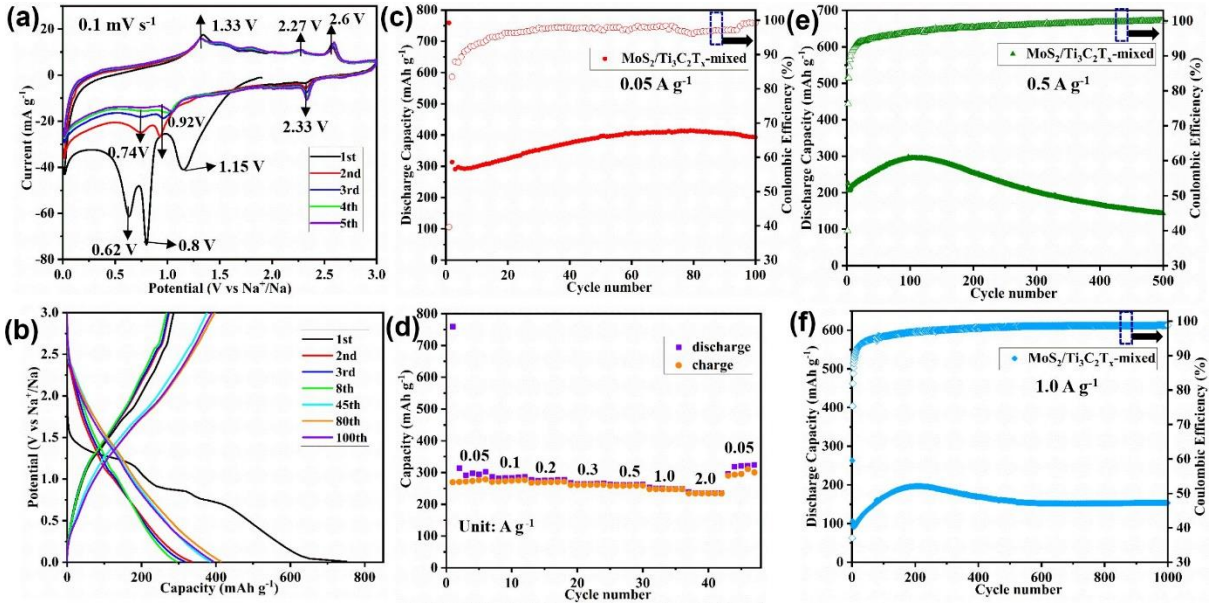

Figure 5.5 Electrochemical measurements of $MoS_2/Ti_3C_2T_x$-mixed heterostructure (a) and (b) are the CV curves at a sweep rate of 0.1 mV s^{-1} and voltage profile of $MoS_2/Ti_3C_2T_x$-mixed heterostructure with FEC electrolyte additive at a current density of 0.05 A g^{-1}, respectively; (c) the cycling performance of $MoS_2/Ti_3C_2T_x$-mixed heterostructure at a current density of 0.05 A g^{-1} with FEC electrolyte additive, (d) the rate performances of $MoS_2/Ti_3C_2T_x$-mixed heterostructure, (e) and (f) are the cycling performance of $MoS_2/Ti_3C_2T_x$-mixed heterostructure at a current density of 0.5 and 1.0 A g^{-1}, respectively.

The electrode delivers an initial discharge capacity of 759 mAh g^{-1} with an ICE of 39.6%, which slightly decreases from 313 to 294 mAh g^{-1} in the first five cycles, followed by a continuous increases to 413 mAh g^{-1} till cycle 80 and a gradual decline to 393 mAh g^{-1}, showing a capacity retention rate of 125.5%. The capacity growth with increasing cycles has been observed in the case of LIBs, which is attributed to the exposure of a large number of electrochemically active sites with cycling. [136] [202]

Compared to the 2D MoS_2 alone electrode, the 2D $MoS_2/Ti_3C_2T_x$-mixed one exhibits relatively lower specific capacity at a rate range of 0.05-2.0 A g^{-1}, but the reversible capacities only gently decreased from 291 to 235 mAh g^{-1} when the current increased from 0.05 to 2.0 A g^{-1} (**Figure 5.5d**). Subsequently, the

cycling stabilities of $MoS_2/Ti_3C_2T_x$-mixed heterostructures were further investigated at 0.5 and 1.0 A g^{-1} for 500 and 1000 cycles, respectively, presented in **Figure 5.5e** and **f**. Both electrodes show a highly similar tendency regarding discharge capacity and CE. For instance, the $MoS_2/Ti_3C_2T_x$-mixed electrode shows a steady discharge capacity growth at 0.5 A g^{-1} in around the 100th cycle, then a constant capacity decrease is observed in the rest of the cycles. A continuous capacity increase was noticed in the initial hundreds of cycles at 0.05, 0.5, and 1.0 A g^{-1}, which are ascribed to the activation processes of the electrodes because of their intrinsic sluggish reaction kinetics. The subsequent capacity loss results from the volume expansion of the MoS_2 component due to repetitive insertion/extraction of Na^+.

In summary, the $MoS_2/Ti_3C_2T_x$-mixed heterostructure can enhance the cycling stability of MoS_2 at low current density but still cannot effectively suppress the volume expansion of the MoS_2 layer at high rates. Hence, a more rational design of $MoS_2/Ti_3C_2T_x$ heterostructures is desired.

5.3.4 Electrochemical performance of 2D $(MoS_2/Ti_3C_2T_x)x3$ heterostructure

According to the results of **chapter 3**, the $(MoS_2/Ti_3C_2T_x)x3$ heterostructure featured with a terminal layer of $Ti_3C_2T_x$ can better buffer the volume expansion of MoS_2 component, especially at high rates. As a result, the $(MoS_2/Ti_3C_2T_x)x3$ electrode was directly used as anode for SIBs. **Figure 5.6a** and **b** show the first five CV curves and voltage profiles of the $(MoS_2/Ti_3C_2T_x)x3$ electrode for 100 cycles, respectively, which are similar to the electrochemical behavior of pure MoS_2 electrode (reference to **Figure 5.1b** and **c**).

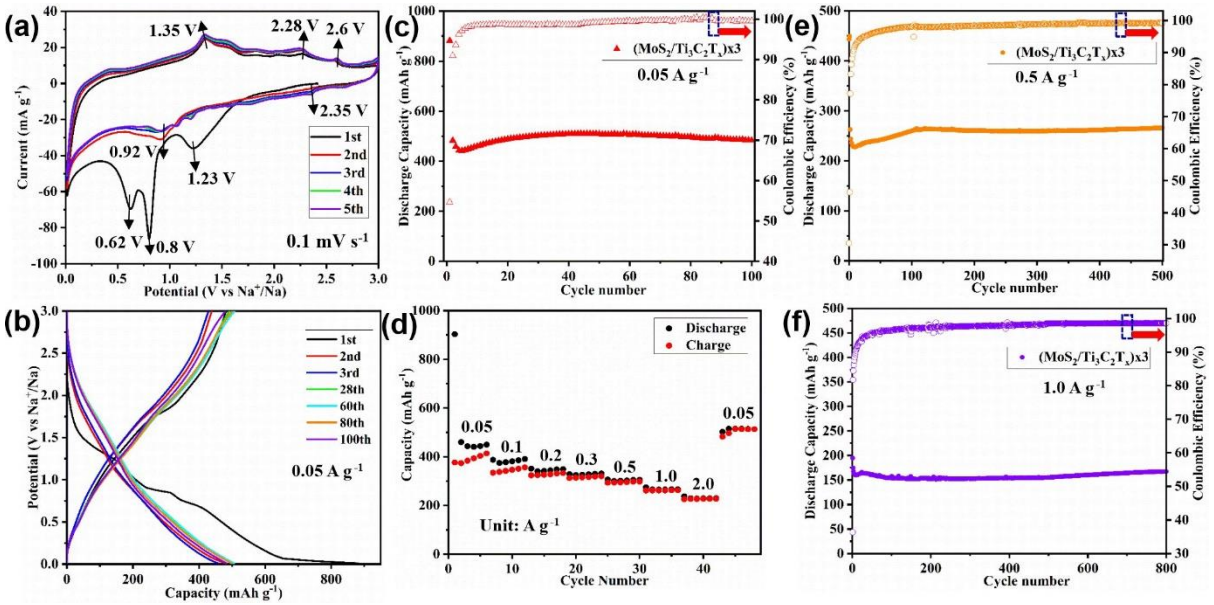

Figure 5.6 Electrochemical measurements of $(MoS_2/Ti_3C_2T_x)x3$ heterostructure (a) and (b) are the CV curves at a sweep rate of 0.1 mV s^{-1} and voltage profile of $(MoS_2/Ti_3C_2T_x)x3$ heterostructure with FEC electrolyte additive at a current density of 0.05 A g^{-1}, respectively; (c) the cycling performance of $(MoS_2/Ti_3C_2T_x)x3$ heterostructure at a current density of 0.05 A g^{-1} with FEC electrolyte additive, (d) the rate performances of $(MoS_2/Ti_3C_2T_x)x3$ heterostructure, (e) and (f) are the cycling performance of $(MoS_2/Ti_3C_2T_x)x3$ heterostructure at the current densities of 0.5 and 1.0 A g^{-1}, respectively.

Figure 5.6c displays the cycling performance of the $(MoS_2/Ti_3C_2T_x)x3$ electrode at 0.05 A g^{-1} for 100 cycles, the discharge capacity slightly decreases from 482 (2nd cycle) to 442 mAh g^{-1} (5th cycle) after an initial discharge capacity of 881 mAh g^{-1}. After that, the capacity steadily rises to 503 mAh g^{-1} at cycle 30, which then tends to be stabilized at around 490 mAh g^{-1} till the end of cycling, demonstrating that the capacity and cycling stability of the heterostructure was highly improved when compared with the single 2D MoS_2 electrode.

Figure 5.6d shows the rate performance of $(MoS_2/Ti_3C_2T_x)x3$ heterostructure. The reversible capacities of 440 and 230 mAh g^{-1} were achieved at 0.05 and 2.0 A g^{-1}, respectively. This capacity retention with increasing current rates is not as good as that of pure MoS_2 electrodes with FEC, in particular at high rates from 0.5 to 2.0 A g^{-1}. This can be attributed to the degraded conductivity of the heterostructure due to the partial oxidation of $Ti_3C_2T_x$ nanosheets (reference to the XPS analysis in **chapter 4**) during the spray deposition process.

Figure 5.6e shows the cycling test of $(MoS_2/Ti_3C_2T_x)x3$ conducted at a large current of 0.5 A g^{-1}. The discharge capacity decreased from an initial value of 449 to 228 mAh g^{-1} at the 10th cycle, followed by continuously increasing to 265 mAh g^{-1} till cycle 110 and stayed at this level after 500 cycles. The capacity rise is related to the activation process of the heterostructure, which is supposed to result from the insufficient transportation of electrons and ions and thereby leads to a sluggish reaction kinetic. Moreover, this can be further reflected by cycling $(MoS_2/Ti_3C_2T_x)x3$ electrode at a higher current density, an obvious capacity loss was observed with increasing current from 0.5 to 1.0 A g^{-1}. However, after 1000 cycles, $(MoS_2/Ti_3C_2T_x)x3$ heterostructure can still deliver a reversible capacity of 167 mAh g^{-1} with a capacity retention of 96% (the discharge capacity of the secondary is 174 mAh g^{-1}), and the average capacity loss rate per cycle is only 0.08%.

To sum up, compared to the pure MoS_2 electrode and $MoS_2/Ti_3C_2T_x$-mixed heterostructure, $(MoS_2/Ti_3C_2T_x)x3$ heterostructure does not show capacity fluctuations during the long-term cycling at various current rates, which is

ascribed to the terminal layer of $Ti_3C_2T_x$ that can better buffer the volume changes of MoS_2 component due to its excellent mechanical strength. On the one hand, $(MoS_2/Ti_3C_2T_x)$x3 heterostructure exhibits exceptional cycling stability due to its well-designed order structure. On the other hand, a moderate capacity at high rates (e.g. 0.5 and 1.0 A g^{-1}) was also observed, which might be caused by the insufficient electrical conductivity of the MoS_2 and partial oxidized $Ti_3C_2T_x$ layers. For this reason, the $(MoS_2/Ti_3C_2T_x)$x3 heterostructure indeed exhibits poor rate performance, thus the reaction kinetics of the electrode needs to be further improved by enhancing the transportation of ions and electrons between MoS_2 or $Ti_3C_2T_x$ nanosheets.

5.3.5 Electrochemical performance of 2D $(MoS_2/Ti_3C_2T_x/CNTs)$x3 heterostructure

Inspired by the 2D $(MoS_2/Ti_3C_2T_x/CNTs)$x3 heterostructure delivering superior lithium storage performance because of its robust structure and remarkable electronic conductivity, $(MoS_2/Ti_3C_2T_x/CNTs)$x3 electrode was also tested as anode material for SIBs. As depicted in **Figure 5.7a**, the first five CV curves of $(MoS_2/Ti_3C_2T_x/CNTs)$x3 were measured in the potential range of 0.01- 3.0 V at 0.1 mV s^{-1}. In the first cathodic sweep, two obvious and one broad reduction peak at 1.06, 0.78, and 0.6 V can be observed. The first one (1.06 V) could be associated with the irreversible side reactions of FEC-containing compounds, which have been observed in all electrodes in this chapter. The other two peaks could correspond to the intercalation of Na^+ insertion into MoS_2 and the formation of Na_xMoS_2 and further reduction of that to metallic Mo and Na_2S. The peaks at 1.06 and 0.78 V are well-consistent with voltage plateaus around 0.92 and 0.8 V in the discharge/charge profile (**Figure 5.7b**). Impressively, there is no pronounced oxidation peak noticed in the subsequent anodic scan, which is most likely due to the Na^+ being trapped in the host structure. This can be further confirmed by the charge curve profiles without voltage plateaus (**Figure 5.7b**). Notably, the previous three reduction peaks disappear and a new peak at 0.88 V emerges in the following cathodic cycles (2nd to 5th), attributing to the deeper intercalation of Na^+ into MoS_2. The shift of the cathodic peak position could be related to the formation of a SEI film in the first cycle, which is consistent with previous reports. [203-205]

The cycling performance of $(MoS_2/Ti_3C_2T_x/CNTs)$x3 heterostructure was performed at 0.05 A g^{-1} for 100 cycles, as shown in **Figure 5.7c**. The electrode delivers an initial discharge capacity of 963 mAh g^{-1} with a quite low ICE of 43.3%, which rapidly fall to 256 mAh g^{-1} at the 10th cycle and retained a

reversible capacity of 205 mAh g^{-1} after 100 cycles. Surprisingly, except for the first few cycles, a much lower specific capacity of ($MoS_2/Ti_3C_2T_x$/CNTs)x3 heterostructure was obtained during the cycling when compared with pure MoS_2 (**Figure 5.1e**), $MoS_2/Ti_3C_2T_x$-mixed (**Figure 5.5c**), and ($MoS_2/Ti_3C_2T_x$)x3 electrodes (**Figure 5.6c**), indicating that the addition of CNTs does not favor to enhance the capacity of $MoS_2/Ti_3C_2T_x$ heterostructure, which may be due to the large radius of Na^+ (1.02 Å) that cannot be intercalated comfortably into the layer structure. [206] This is quite different from the previous reports, [207-209] which is not fully understood at this time.

Finally, the rate performance of ($MoS_2/Ti_3C_2T_x$/CNTs)x3 electrode was also evaluated at various current densities ranging from 0.05 to 2.0 A g^{-1} (**Figure 5.6d**). As can be seen, the average specific capacities of the ($MoS_2/Ti_3C_2T_x$/CNTs)x3 electrode are significantly lower than those of pure MoS_2 (**Figure 5.1f**), $MoS_2/Ti_3C_2T_x$-mixed (**Figure 5.5d**), and ($MoS_2/Ti_3C_2T_x$)x3 electrodes (**Figure 5.6d**), Noticeably, the capacity could not return to the initial values when the current density is relaxed to 0.05 A g^{-1}. As a result, the ($MoS_2/Ti_3C_2T_x$/CNTs)x3 heterostructure not only does not improve the rate performance of the electrodes, but also reduces the cell capacity, which is significantly different from the case of LIBs.

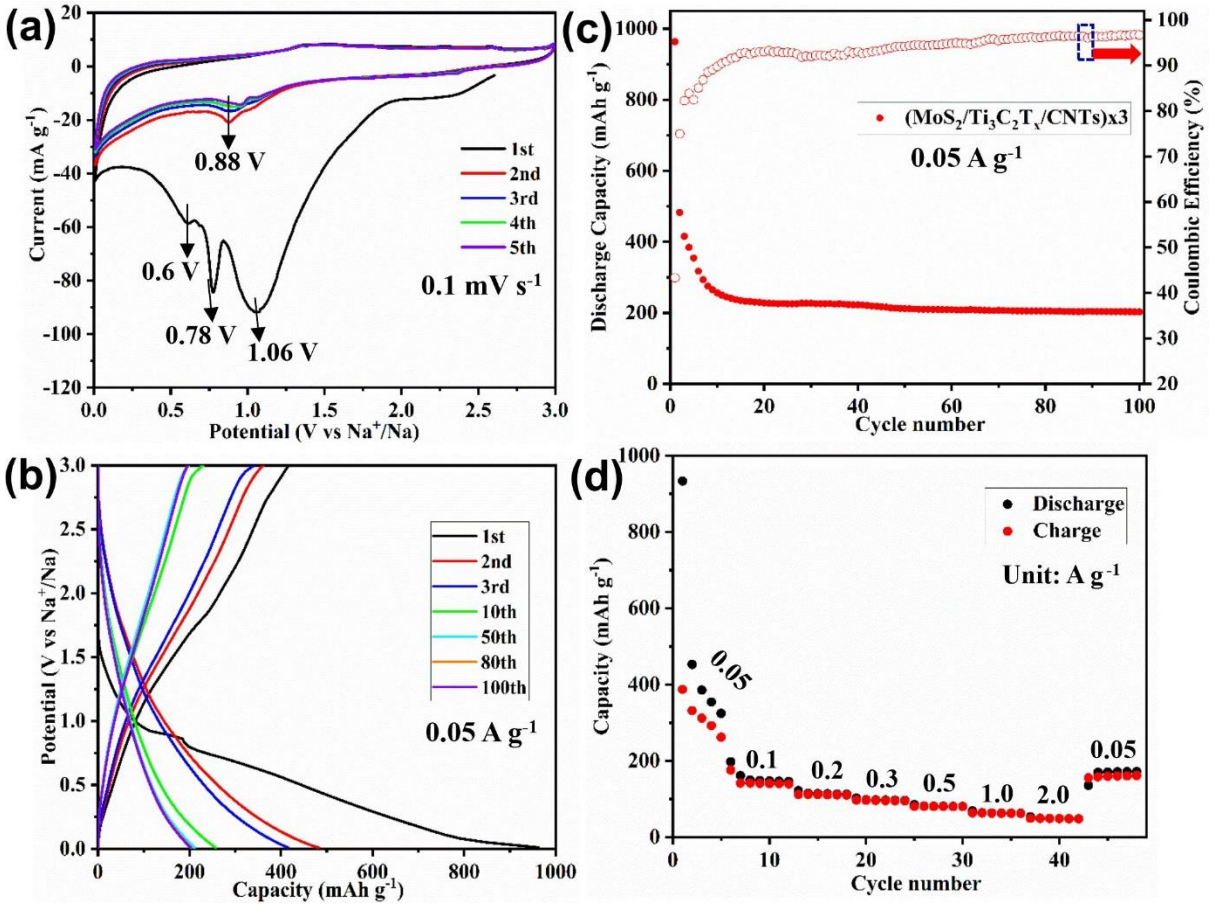

Figure 5.7 Electrochemical measurements of $(MoS_2/Ti_3C_2T_x/CNTs)x3$ heterostructure (a) and (b) are the CV curves at a sweep rate of 0.1 mV s^{-1} and voltage profile of $(MoS_2/Ti_3C_2T_x/CNTs)x3$ heterostructure with FEC electrolyte additive at a current density of 0.05 A g^{-1}, respectively; (c) the cycling performance of $(MoS_2/Ti_3C_2T_x/CNTs)x3$ heterostructure at a current density of 0.05 A g^{-1} with FEC electrolyte additive, (d) the rate performances of $(MoS_2/Ti_3C_2T_x/CNTs)x3$ heterostructure.

5.4 Conclusions

In summary, the influences of FEC electrolyte additive (5 wt. %) on the sodium storage of 2D MoS_2 and $Ti_3C_2T_x$ electrodes were firstly explored. It is found that the capacity and cycling stability of both electrodes were remarkably improved by the FEC additive due to it modifying the surface passivation layer (more various organic compounds but less concentration of inorganic salts), including the SEI film (main inorganic slats). To address the serious volume expansion of the 2D MoS_2 electrode, especially at high rates, three rationally designed types of $MoS_2/Ti_3C_2T_x$ heterostructures were constructed by the same spray deposition technique in chapter 3, which are denoted as $MoS_2/Ti_3C_2T_x$-mixed, $(MoS_2/Ti_3C_2T_x)x3$, and $(MoS_2/Ti_3C_2T_x/CNTs)x3$ heterostructures. Among them, the well-defined stacking $(MoS_2/Ti_3C_2T_x)x3$ heterostructure exhibits improved specific capacity and cycling stability, which is significantly superior to the $MoS_2/Ti_3C_2T_x$-mixed electrode that features with randomly stacking of MoS_2 and $Ti_3C_2T_x$ nanosheets. However, the rate performance of $(MoS_2/Ti_3C_2T_x)x3$ remains a challenge. To this end, $(MoS_2/Ti_3C_2T_x/CNTs)x3$ heterostructure was constructed and aims to further improve the rate capability, but it cannot be used as anode for SIBs, like LIBs, which might be because the large radius of Na^+ (1.02 Å) cannot be intercalated comfortably into the CNTs or engineered $Ti_3C_2T_x/CNTs$ layer structure. Therefore, further work on applying $MoS_2/Ti_3C_2T_x$ heterostructures as anode materials for SIBs is expected in the future.

6 Conclusions and Outlook

In this thesis, the 2D MoS_2, $Ti_3C_2T_x$ electrodes, and several different 2D $MoS_2/Ti_3C_2T_x$ heterostructures with and without CNTs matrix were successfully manufactured by the scalable layer-by-layer spray deposition technique. Thereafter, their structural and morphological properties were further revealed by a variety of techniques (e.g. SEM, XRD). Finally, all as-prepared electrodes have been comprehensively investigated as anode materials for LIBs and SIBs.

Firstly, the 2D MoS_2 electrode was prepared by spraying with the few-layers 2D MoS_2 nanosheets that have been manufactured by scalable liquid-phase exfoliation. The controversial question of reversibility/irreversibility of conversion reaction of the MoS_2-based electrodes was addressed by *ex-situ* Raman. The studies revealed that, in 2D MoS_2 electrodes, conversion processes are indeed reversible, where nanostructure played a key role. Cycling of the 2D MoS_2 electrodes at high current rates (0.75-3.0 C) revealed an intriguing phenomenon consisting of a continuously increasing capacity after ca. 100-200 cycles. This phenomenon was comprehensively addressed by a variety of electrochemical and microscopy methods that revealed underlying physical activation mechanisms that involved a range of profound changes in electrode structure and SEI films. Activation mechanisms delivered a capacitive electrode of a superior rate performance and cycling stability, as compared to the corresponding pristine electrodes, and to MoS_2 electrodes previously reported.

To further address the unexpected activation of 2D MoS_2 electrodes induced by the high-rate lithiation process, three well-defined 2D $MoS_2/Ti_3C_2T_x$ heterostructures were prepared by spray deposition, which are denoted as $(Ti_3C_2T_x/MoS_2)xn$ (n = 1, 2, 3, 4 and 8), $(MoS_2/Ti_3C_2T_x)x3$, and $MoS_2/Ti_3C_2T_x$-mixed heterostructure. They are featured with the terminal layer of MoS_2, $Ti_3C_2T_x$, and a mixture of both nanosheets, respectively. When tested as anodes for LIBs, all as-prepared heterostructures exhibit enhanced electrochemical performance in terms of capacity, rate capability, and cycling stability compared with single MoS_2 or $Ti_3C_2T_x$ nanosheets. The influences of the terminal layers of the above 2D $MoS_2/Ti_3C_2T_x$ heterostructures on the lithium storage performances were systematically investigated by various electrochemical methods. These results demonstrate that the $(MoS_2/Ti_3C_2T_x)x3$ heterostructure with a terminal layer of $Ti_3C_2T_x$ can better buffer the volume expansion of the MoS_2 component, especially at high rates, but much more cycles of activation process were still required to achieve a high and stable capacity. To solve this issue, carbon nanotubes matrix (CNTs) were incorporated into $(MoS_2/Ti_3C_2T_x)x3$ electrode to obtain $(MoS_2/Ti_3C_2T_x/CNTs)x3$ heterostructure.

As expected, it exhibits a superior reversible capacity of 578 mAh g^{-1} (after 1000 cycles) at 1.0 A g^{-1}, and 532, 347 mAh g^{-1} at the 2000th cycle at 2.0 and 5.0 A g^{-1}, respectively. Moreover, the (MoS_2/$Ti_3C_2T_x$/CNTs)x3 heterostructure also delivers comparable specific capacities of 180 (0.1 C) and 158 mAh g^{-1} (1.0 C) when coupled in a full cell with the commercial $LiNi_{0.6}Co_{0.2}Mn_{0.2}O_2$ (NCM622) cathode. Finally, we argue that the addition of CNTs is not only facilitating electron and ion transport but also act as a substrate to prevent the aggregation of the terminal $Ti_3C_2T_x$ layer, thus rendering the robust SEI layer formation, which was eventually confirmed by *ex-situ* SEM and EIS.

In the end, inspired by the studies of 2D MoS_2 and $Ti_3C_2T_x$ electrodes as well as their different 2D MoS_2/$Ti_3C_2T_x$ heterostructures as anodes for LIBs, , they have been applied directly as anodes for SIBs to determine if the combination of $Ti_3C_2T_x$ MXene and MoS_2 can result in enhanced electrochemical sodium storage. The improvement of capacity and cycling stability for 2D MoS_2 and $Ti_3C_2T_x$ electrodes in the FEC-containing electrolyte was firstly verified, which can attribute to the FEC modifying the surface passivation layer, including the SEI films. Therefore, the electrolyte with FEC additive was selected for further electrochemical experiments on the (MoS_2/$Ti_3C_2T_x$)x3, MoS_2/$Ti_3C_2T_x$-mixed, and (MoS_2/$Ti_3C_2T_x$/CNTs)x3 heterostructures. Among them, the (MoS_2/$Ti_3C_2T_x$)x3 heterostructure with ordered stacking structure exhibits improved specific capacity and cycling stability, which is significantly superior to the MoS_2/$Ti_3C_2T_x$-mixed electrode that features with randomly stacking of MoS_2 and $Ti_3C_2T_x$ nanosheets, which is consistent with the case of LIBs. However, the (MoS_2/$Ti_3C_2T_x$/CNTs)x3 heterostructure, aiming to further improve the rate capability of the (MoS_2/$Ti_3C_2T_x$)x3 electrode, cannot be used as an anode for SIBs, like LIBs, which is most likely ascribed to the large radius of Na^+ that cannot be intercalated stably into the CNTs or $Ti_3C_2T_x$/CNTs layer structure.

In summary, manufacturing film electrodes via layer-by-layer spray deposition is a promising strategy for large-scale energy storage systems. The changes in morphology and structure of the electrodes play an important role in the battery's cycling life due to the volume expansion of 2D MoS_2, especially at high rates. In this thesis, the reaction mechanism of 2D MoS_2 electrodes was explored only by *ex-situ* Raman. This process requires opening the cell in the glove box, which is not favorable for air-sensitive products. Therefore, future work should address a comprehensive understanding of the conversion reaction mechanism of 2D MoS_2 through *in-situ* Raman and more advanced characterization techniques such *as in-situ* XAS and XPS.

Rationally designing the composites with complementary properties in a well-defined robust architecture is an attractive strategy to suppress the intrinsic volume changes of MoS_2-based electrodes. The 2D (MoS_2/$Ti_3C_2T_x$/CNTs)x3 heterostructures, made by stacking MoS_2/CNTs and $Ti_3C_2T_x$/CNTs matrix on top of each other at the nanoscale, have shown high capacity, excellent rate performances, and superior cycling stability as anodes for LIBs. The results show that the interfaces between MoS_2/CNTs and $Ti_3C_2T_x$/CNTs stacking layers are critical for buffering the stress accumulation and volume expansion of the MoS_2 layers. In spite of this, the crystal structures evolution of the (MoS_2/$Ti_3C_2T_x$/CNTs)x3 heterostructure could not be extensively investigated by the conventional XRD due to the poor crystallinity of the electrode. As a result, further work on that needs to be performed by synchrotron radiation diffraction, which is capable of providing information on crystal structural changes.

Since the effects of FEC on the long-term cycling stability of the 2D MoS_2 and $Ti_3C_2T_x$ electrodes for SIBs have been investigated, it is also interesting to study the influence of FEC electrolyte additive on surface morphology by SEM/EDX and SEI composition by XPS. Additionally, further research could address the side reactions and the role of the individual electrolyte solvent in SIBs by *in-situ* techniques (Raman, XPS, and XAS). This could guide researchers toward strategies for more effective electrolyte optimization. And the reasons behind why (MoS_2/$Ti_3C_2T_x$/CNTs)x3 heterostructure cannot be used directly as an anode for SIBs are also expected to be explored.

7 References

1. Armand, M.; Tarascon, J. M., Building Better Batteries. *Nature* **2008,** *451*, 652-657.
2. Figgener, J.; Stenzel, P.; Kairies, K.-P.; Linßen, J.; Haberschusz, D.; Wessels, O.; Angenendt, G.; Robinius, M.; Stolten, D.; Sauer, D. U., The Development of Stationary Battery Storage Systems in Germany – A Market Review. *Journal of Energy Storage* **2020,** *29*, 101153.
3. Soloveichik, G. L., Battery Technologies for Large-scale Stationary Energy Storage. *Annu Rev Chem Biomol Eng* **2011,** *2*, 503-527.
4. Durmus, Y. E.; Zhang, H.; Baakes, F.; Desmaizieres, G.; Hayun, H.; Yang, L.; Kolek, M.; Küpers, V.; Janek, J.; Mandler, D.; Passerini, S.; Ein-Eli, Y., Side by Side Battery Technologies with Lithium‐Ion Based Batteries. *Advanced Energy Materials* **2020,** *10*, 2000089.
5. Dunn, B.; Kamath, H.; Tarascon, J. M., Electrical Energy Storage for the Grid: A Battery of Choices. *Science* **2011,** *334*, 928-935.
6. Armand, J.-M. T. a. M., Issues and Challenges Facing Rechargeable Lithium Batteries. *Nature* **2001,** *414*, 359-367.
7. Kang, K.; Meng, Y. S.; Breger, J.; Grey, C. P.; Ceder, G., Electrodes with High Power and High Capacity for Rechargeable Lithium Batteries. *Science* **2006,** *311*, 977-980.
8. Hwang, J. Y.; Myung, S. T.; Sun, Y. K., Sodium-ion Batteries: Present and Future. *Chem Soc Rev* **2017,** *46*, 3529-3614.
9. Pan, H.; Hu, Y.-S.; Chen, L., Room-Temperature Stationary Sodium-ion Batteries for Large-scale Electric Energy Storage. *Energy & Environmental Science* **2013,** *6*, 2338-2360.
10. Hu, Z.; Liu, Q.; Chou, S. L.; Dou, S. X., Advances and Challenges in Metal Sulfides/Selenides for Next-Generation Rechargeable Sodium-Ion Batteries. *Adv Mater* **2017,** *29*, 1700606.
11. He, H.; Sun, D.; Tang, Y.; Wang, H.; Shao, M., Understanding and Improving the Initial Coulombic Efficiency of High-capacity Anode Materials for Practical Sodium Ion Batteries. *Energy Storage Materials* **2019,** *23*, 233-251.
12. Anasori, B.; Lukatskaya, M. R.; Gogotsi, Y., 2D Metal Carbides and Nitrides (MXenes) for Energy Storage. *Nature Reviews Materials* **2017,** *2*, 16098.
13. Wang, X.; Weng, Q.; Yang, Y.; Bando, Y.; Golberg, D., Hybrid Two-dimensional materials in Rechargeable Battery Applications and Their Microscopic Mechanisms. *Chem Soc Rev* **2016,** *45*, 4042-4073.
14. Aslam, M. K.; Niu, Y.; Xu, M., MXenes for Non-Lithium-Ion (Na, K, Ca, Mg, and Al) Batteries and Supercapacitors. *Advanced Energy Materials* **2020,** *11*, 2000681.
15. Sun, S.; Liao, C.; Hafez, A. M.; Zhu, H.; Wu, S., Two-dimensional MXenes for energy storage. *Chemical Engineering Journal* **2018,** *338*, 27-45.
16. Xie, Y.; Dall'Agnese, Y.; Naguib, M.; Gogotsi, Y.; Barsoum, M. W.; Zhuang, H. L.; Kent, P. R., Prediction and Characterization of MXene Nanosheet Anodes for Non-lithium-ion Batteries. *ACS Nano* **2014,** *8*, 9606-9615.
17. Pomerantseva, E.; Gogotsi, Y., Two-dimensional Heterostructures for Energy Storage. *Nat Energy* **2017,** *2*, 17089.
18. Liu, J.; Liu, X. W., Two-dimensional Nanoarchitectures for Lithium Storage. *Adv Mater* **2012,** *24*, 4097-111.

19. Kim, S. J.; Naguib, M.; Zhao, M.; Zhang, C.; Jung, H.-T.; Barsoum, M. W.; Gogotsi, Y., High Mass Loading, Binder-free MXene Anodes for High Areal Capacity Li-ion Batteries. *Electrochimica Acta* **2015,** *163*, 246-251.
20. Xie, Y.; Naguib, M.; Mochalin, V. N.; Barsoum, M. W.; Gogotsi, Y.; Yu, X.; Nam, K. W.; Yang, X. Q.; Kolesnikov, A. I.; Kent, P. R., Role of Surface Structure on Li-ion Energy Storage Capacity of Two-dimensional Transition-metal Carbides. *J Am Chem Soc* **2014,** *136*, 6385-6394.
21. Jiang, H.; Ren, D.; Wang, H.; Hu, Y.; Guo, S.; Yuan, H.; Hu, P.; Zhang, L.; Li, C., 2D Monolayer MoS_2-Carbon Interoverlapped Superstructure: Engineering Ideal Atomic Interface for Lithium Ion Storage. *Adv Mater* **2015,** *27*, 3687-3695.
22. Liu, Y.; He, X.; Hanlon, D.; Harvey, A.; Khan, U.; Li, Y.; Coleman, J. N., Electrical, Mechanical, and Capacity Percolation Leads to High-Performance MoS_2/Nanotube Composite Lithium Ion Battery Electrodes. *ACS Nano* **2016,** *10*, 5980-5990.
23. Chen, C.; Xie, X.; Anasori, B.; Sarycheva, A.; Makaryan, T.; Zhao, M.; Urbankowski, P.; Miao, L.; Jiang, J.; Gogotsi, Y., MoS_2-on-MXene Heterostructures as Highly Reversible Anode Materials for Lithium-Ion Batteries. *Angew Chem Int Ed Engl* **2018,** *57*, 1846-1850.
24. Li, M.-Y.; Chen, C.-H.; Shi, Y.; Li, L.-J., Heterostructures Based on Two-dimensional Layered Materials and Their Potential Applications. *Materials Today* **2016,** *19*, 322-335.
25. Gogotsi, Y.; Huang, Q., MXenes: Two-Dimensional Building Blocks for Future Materials and Devices. *ACS Nano* **2021,** *15*, 5775-5780.
26. Geim, A. K.; Grigorieva, I. V., Van der Waals heterostructures. *Nature* **2013,** *499*, 419-425.
27. Zhang, C. J.; Park, S. H.; Ronan, O.; Harvey, A.; Seral-Ascaso, A.; Lin, Z.; McEvoy, N.; Boland, C. S.; Berner, N. C.; Duesberg, G. S.; Rozier, P.; Coleman, J. N.; Nicolosi, V., Enabling Flexible Heterostructures for Li-Ion Battery Anodes Based on Nanotube and Liquid-Phase Exfoliated 2D Gallium Chalcogenide Nanosheet Colloidal Solutions. *Small* **2017,** *13*, 1701677.
28. Wu, Y., Lithium-ion Batteries Fundamentals and Applications. *CRC Press:* **2015**; 582.
29. Li, F., Wen, Lei, Cheng, Hui ming, *Novel Electrochemical Energy Storage Devices*. Wiley: **2021**; 336
30. Kubota, K.; Dahbi, M.; Hosaka, T.; Kumakura, S.; Komaba, S., Towards K-ion and Na-ion Batteries as "Beyond Li-ion". *Chem Rec* **2018,** *18*, 459-479.
31. Korthauer, R., Lithium-Ion Batteries: Basics And Applications. *Springer Nature:* **2018**; 412.
32. Goodenough, J. B.; Park, K. S., The Li-Ion Rechargeable Battery: A Perspective. *J Am Chem Soc* **2013,** *135*, 1167-1176.
33. Wang, W.; Li, W.; Wang, S.; Miao, Z.; Liu, H. K.; Chou, S., Structural Design of Anode Materials for Sodium-ion Batteries. *Journal of Materials Chemistry A* **2018,** *6*, 6183-6205.
34. Liu, Z. G.; Du, R.; He, X. X.; Wang, J. C.; Qiao, Y.; Li, L.; Chou, S. L., Recent Progress on Intercalation-Based Anode Materials for Low-cost Sodium-ion Batteries. *ChemSusChem* **2021,** *14*, 3724-3743.
35. Dambournet, D.; Belharouak, I.; Amine, K., Tailored Preparation Methods of TiO_2 Anatase, Rutile, Brookite: Mechanism of Formation and Electrochemical Properties. *Chemistry of Materials* **2009,** *22*, 1173-1179.
36. Lu, J.; Chen, Z.; Pan, F.; Cui, Y.; Amine, K., High-Performance Anode Materials for Rechargeable Lithium-ion Batteries. *Electrochemical Energy Reviews* **2018,** *1*, 35-53.

37. Goriparti, S.; Miele, E.; De Angelis, F.; Di Fabrizio, E.; Proietti Zaccaria, R.; Capiglia, C., Review on Recent Progress of Nanostructured Anode Materials for Li-ion Batteries. *Journal of Power Sources* **2014,** *257*, 421-443.
38. Yi, T. F.; Yang, S. Y.; Xie, Y., Recent Advances of $Li_4Ti_5O_{12}$ as A Promising Next Generation Anode Material for High Power Lithium-ion Batteries. *Journal of Materials Chemistry A* **2015,** *3*, 5750-5777.
39. Zhou, L. M.; Zhang, K.; Hu, Z.; Tao, Z. L.; Mai, L. Q.; Kang, Y. M.; Chou, S. L.; Chen, J., Recent Developments on and Prospects for Electrode Materials with Hierarchical Structures for Lithium-ion Batteries. *Advanced Energy Materials* **2018,** *8*, 1701415.
40. Chang, H.; Wu, Y.-R.; Han, X.; Yi, T.-F., Recent Developments in Advanced Anode Materials for Lithium-ion Batteries. *Energy Materials* **2021,** *1*, 100003.
41. Yang Yu-Fei, Y. J.-L., Pan Feng Cui Yi, From Intercalation to Alloying Chemistry: Structural Design of Silicon Anodes for the Next Generation of Lithium-ion Batteries. *Chinese J. Struct. Chem.* **2020,** *39*, 16-19.
42. Luo, L. L.; Wu, J. S.; Xu, J. M.; Dravid, V. P., Atomic Resolution Study of Reversible Conversion Reaction in Metal Oxide Electrodes for Lithium-ion Battery. *ACS Nano* **2014,** *8*, 11560-11566.
43. Geng, P. B.; Zheng, S. S.; Tang, H.; Zhu, R. M.; Zhang, L.; Cao, S.; Xue, H. G.; Pang, H., Transition Metal Sulfides Based on Graphene for Electrochemical Energy Storage. *Advanced Energy Materials* **2018,** *8*, 1703259.
44. Xie, X.; Makaryan, T.; Zhao, M.; Van Aken, K. L.; Gogotsi, Y.; Wang, G., MoS_2 Nanosheets Vertically Aligned on Carbon Paper: A Freestanding Electrode for Highly Reversible Sodium-ion Batteries. *Advanced Energy Materials* **2016,** *6*, 1502161.
45. Sun, L.; Song, G. S.; Sun, Y. F.; Fu, Q.; Pan, C. X., One-step Construction of 3D N/P-Codoped Hierarchically Porous Carbon Framework In-situ Armored Mn_3O_4 Nanoparticles for High-performance Flexible Supercapacitors. *Electrochimica Acta* **2020,** *333*, 135496.
46. Yu, L.; Wang, L. P.; Liao, H.; Wang, J.; Feng, Z.; Lev, O.; Loo, J. S. C.; Sougrati, M. T.; Xu, Z. J., Understanding Fundamentals and Reaction Mechanisms of Electrode Materials for Na-Ion Batteries. *Small* **2018,** *14*, e1703338.
47. Dong, Y. F.; Li, Y.; Shi, H. D.; Qin, J. Q.; Zheng, S. H.; He, R. H.; Wu, Z. S., Graphene Encapsulated Iron Nitrides Confined in 3D Carbon Nanosheet Frameworks for High-rate Lithium Ion Batteries. *Carbon* **2020,** *159*, 213-220.
48. Wei, Z.; Wang, L.; Zhuo, M.; Ni, W.; Wang, H.; Ma, J., Layered tin sulfide and selenide anode materials for Li- and Na-ion batteries. *Journal of Materials Chemistry A* **2018,** *6*, 12185-12214.
49. Xie, D.; Xia, X.; Wang, Y.; Wang, D.; Zhong, Y.; Tang, W.; Wang, X.; Tu, J., Nitrogen-Doped Carbon Embedded MoS_2 Microspheres as Advanced Anodes for Lithium-and Sodium-ion Batteries. *Chemistry* **2016,** *22*, 11617-23.
50. Zhang, H.; Zhao, H.; Khan, M. A.; Zou, W.; Xu, J.; Zhang, L.; Zhang, J., Recent Progress in Advanced Electrode Materials, Separators and Electrolytes for Lithium Batteries. *Journal of Materials Chemistry A* **2018,** *6*, 20564-20620.
51. Zhang, X.; Ju, Z.; Zhu, Y.; Takeuchi, K. J.; Takeuchi, E. S.; Marschilok, A. C.; Yu, G., Multiscale Understanding and Architecture Design of High Energy/Power Lithium-Ion Battery Electrodes. *Advanced Energy Materials* **2020,** *11*, 2000808.
52. Dieringa, H., Applications: Magnesium-based Metal Matrix Composites *MMCs*. **2013**; 317-341.

53. Gutierrezmiravete, E.; Lavernia, E. J.; Trapaga, G. M.; Szekely, J.; Grant, N. J., A Mathematical-Model of the Spray Deposition Process. *Metall Trans A* **1989,** *20*, 71-85.
54. Huang, C.; Grobert, N.; Watt, A. A. R.; Johnston, C.; Crossley, A.; Young, N. P.; Grant, P. S., Layer-by-Layer Spray Deposition and Unzipping of Single-wall Carbon Nanotube-based Thin Film Electrodes for Electrochemical Capacitors. *Carbon* **2013,** *61*, 525-536.
55. Huang, C.; Zhang, J.; Snaith, H. J.; Grant, P. S., Engineering the Membrane/Electrode Interface To Improve the Performance of Solid-State Supercapacitors. *ACS Appl Mater Interfaces* **2016,** *8*, 20756-20765.
56. Huang, C.; Young, N. P.; Zhang, J.; Snaith, H. J.; Grant, P. S., A Two Layer Electrode Structure for Improved Li Ion Diffusion and Volumetric Capacity in Li Ion Batteries. *Nano Energy* **2017,** *31*, 377-385.
57. Mendoza-Sánchez, B.; Coelho, J.; Pokle, A.; Nicolosi, V., A Study of the Charge Storage Properties of a $MoSe_2$ Nanoplatelets/SWCNTs Electrode in a Li-ion Based Electrolyte. *Electrochimica Acta* **2016,** *192*, 1-7.
58. Wang, W. Z. Z. L., Scanning Microscopy for Nanotechnology. *Springer New York*, NY: **2007**; 522.
59. Joseph Goldstein, D. N., David Joy, CharlesLyman, Patrick Echlin, Eric Lifshin, Linda Sawyer, JosephMichael, Scanning electron microscopy and x-ray microanalysis 3rd edition By Joseph Goldstein Dale. *Springer*: **2017**; 550.
60. Michler, G. H., Electron Microscopy of Polymers. *Springer-Verlag Berlin Heidelberg*: **2008**; 473.
61. E.'Sobol, J. F. M. W. F. S. P.; Bomben, K. D., Handbook of X-ray Photoelectron Spectroscopy. **1992**.
62. Stevie, F. A.; Donley, C. L., Introduction to X-ray Photoelectron Spectroscopy. *Journal of Vacuum Science & Technology A* **2020,** *38*.
63. Thommes, M.; Kaneko, K.; Neimark, A. V.; Olivier, J. P.; Rodriguez-Reinoso, F.; Rouquerol, J.; Sing, K. S. W., Physisorption of Gases, with Special Reference to The Evaluation of Surface Area and Pore Size Distribution (IUPAC Technical Report). *Pure and Applied Chemistry* **2015,** *87*, 1051-1069.
64. de Lange, M. F.; Lin, L. C.; Gascon, J.; Vlugt, T. J.; Kapteijn, F., Assessing the Surface Area of Porous Solids: Limitations, Probe Molecules, and Methods. *Langmuir* **2016,** *32*, 12664-12675.
65. Ambroz, F.; Macdonald, T. J.; Martis, V.; Parkin, I. P., Evaluation of the BET Theory for the Characterization of Meso and Microporous MOFs. *Small Methods* **2018,** *2*, 1800173.
66. Kim, T.; Choi, W.; Shin, H.-C.; Choi, J.-Y.; Kim, J. M.; Park, M.-S.; Yoon, W.-S., Applications of Voltammetry in Lithium Ion Battery Research. *Journal of Electrochemical Science and Technology* **2020,** *11*, 14-25.
67. Azzarello, E.; Masi, E.; Mancuso, S., Electrochemical Impedance Spectroscopy. **2012**; 205-223.
68. Lukács, Z.; Kristóf, T., A Generalized Model of The Equivalent Circuits in The Electrochemical Impedance Spectroscopy. *Electrochimica Acta* **2020,** *363*, 137199.
69. Stephenson, T.; Li, Z.; Olsen, B.; Mitlin, D., Lithium Ion Battery Applications of Molybdenum Disulfide (MoS_2) Nanocomposites. *Energy & Environmental Science* **2014,** *7*, 209-231.
70. Butler, S. Z.; Hollen, S. M.; Cao, L.; Cui, Y.; Gupta, J. A.; Gutiérrez, H. R.; Heinz, T. F.; Hong, S. S.; Huang, J.; Ismach, A. F.; Johnston-Halperin, E.; Kuno, M.; Plashnitsa, V. V.;

Robinson, R. D.; Ruoff, R. S.; Salahuddin, S.; Shan, J.; Shi, L.; Spencer, M. G.; Terrones, M.; Windl, W.; Goldberger, J. E., Progress, Challenges, and Opportunities in Two-dimensional Materials Beyond Graphene. *ACS Nano* **2013,** *7*, 2898-2926.
71. Thomas, N.; Mathew, S.; Nair, K. M.; O'Dowd, K.; Forouzandeh, P.; Goswami, A.; McGranaghan, G.; Pillai, S. C., 2D MoS_2: Structure, Mechanisms, and Photocatalytic Applications. *Materials Today Sustainability* **2021,** *13*, 100073.
72. Chhowalla, M.; Shin, H. S.; Eda, G.; Li, L.-J.; Loh, K. P.; Zhang, H., The Chemistry of Two-dimensional Layered Transition Metal Dichalcogenide Nanosheets. *Nature Chemistry* **2013,** *5*, 263-275.
73. Stephenson, T.; Li, Z.; Olsen, B.; Mitlin, D., Lithium ion Battery Applications of Molybdenum Disulfide (MoS_2) Nanocomposites. *Energy & Environmental Science* **2014,** *7*, 209-231.
74. Huang, X.; Zeng, Z.; Zhang, H., Metal Dichalcogenide Nanosheets: Preparation, Properties and Applications. *Chemical Society Reviews* **2013,** *42*, 1934-1946.
75. Nicolosi, V.; Chhowalla, M.; Kanatzidis, M. G.; Strano, M. S.; Coleman, J. N., Liquid Exfoliation of Layered Materials. *Science* **2013,** *340*, 1226419.
76. Mendoza-Sánchez, B.; Gogotsi, Y., Synthesis of Two-Dimensional Materials for Capacitive Energy Storage. *Advanced Materials* **2016,** *28*, 6104-6135.
77. Zhao, X.; Mendoza-Sanchez, B.; Dobson, P. J.; Grant, P. S., The Role of Nanomaterials in Redox-based Supercapacitors for Next Generation Energy Storage Devices. *Nanoscale* **2011,** *3*, 839-855.
78. Mendoza-Sánchez, B.; Rasche, B.; Nicolosi, V.; Grant, P. S., Scaleable Ultra-thin and High Power Density Graphene Electrochemical Capacitor Electrodes Manufactured by Aqueous Exfoliation and Spray Deposition. *Carbon* **2013,** *52*, 337-346.
79. Coelho, J.; Mendoza-Sánchez, B.; Pettersson, H.; Pokle, A.; McGuire, E. K.; Long, E.; McKeon, L.; P. Bell, A.; Nicolosi, V., Manganese Oxide Nanosheets and A 2D Hybrid of Graphene–manganese Oxide Nanosheets Synthesized by Liquid-phase Exfoliation. *2D Materials* **2015,** *2*, 025005.
80. Mendoza-Sánchez, B.; Coelho, J.; Pokle, A.; Nicolosi, V., A 2D Graphene-manganese Oxide Nanosheet Hybrid Synthesized by a Single Step Liquid-phase Co-exfoliation Method for Supercapacitor Applications. *Electrochimica Acta* **2015,** *174*, 696-705.
81. Qiu, Y.; Chen, Y., Capacitance Performance of Sub-2 nm Graphene Nanochannels in Aqueous Electrolyte. *Journal of Physical Chemistry C* **2015,** *119*, 23813-23819.
82. Backes, C.; Higgins, T. M.; Kelly, A.; Boland, C.; Harvey, A.; Hanlon, D.; Coleman, J. N., Guidelines for Exfoliation, Characterization and Processing of Layered Materials Produced by Liquid Exfoliation. *Chemistry of Materials* **2016,** *29*, 243-255.
83. Coleman, J. N.; Lotya, M.; O'Neill, A.; Bergin, S. D.; King, P. J.; Khan, U.; Young, K.; Gaucher, A.; De, S.; Smith, R. J.; Shvets, I. V.; Arora, S. K.; Stanton, G.; Kim, H. Y.; Lee, K.; Kim, G. T.; Duesberg, G. S.; Hallam, T.; Boland, J. J.; Wang, J. J.; Donegan, J. F.; Grunlan, J. C.; Moriarty, G.; Shmeliov, A.; Nicholls, R. J.; Perkins, J. M.; Grieveson, E. M.; Theuwissen, K.; McComb, D. W.; Nellist, P. D.; Nicolosi, V., Two-dimensional Nanosheets Produced by Liquid Exfoliation of Layered Materials. *Science* **2011,** *331*, 568-571.
84. O'Neill, A.; Khan, U.; Coleman, J. N., Preparation of High Concentration Dispersions of Exfoliated MoS_2 with Increased Flake Size. *Chemistry of Materials* **2012,** *24*, 2414-2421.

85. Bang, G. S.; Nam, K. W.; Kim, J. Y.; Shin, J.; Choi, J. W.; Choi, S. Y., Effective Liquid-phase Exfoliation and Sodium Ion Battery Application of MoS_2 Nanosheets. *ACS Appl Mater Interfaces* **2014,** *6*, 7084-7089.
86. Li, H.; Zhang, Q.; Yap, C. C. R.; Tay, B. K.; Edwin, T. H. T.; Olivier, A.; Baillargeat, D., From Bulk to Monolayer MoS_2: Evolution of Raman Scattering. *Advanced Functional Materials* **2012,** *22*, 1385-1390.
87. Mukhopadhyay, I.; Kawasaki, S.; Okino, F.; Govindaraj, A.; Rao, C. N. R.; Touhara, H., Electrochemical Li Insertion into Single-walled Carbon Nanotubes Prepared by Graphite Arc-discharge Method. *Physica B: Condensed Matter* **2002,** *323*, 130-132.
88. Liang, K. S.; Chianelli, R. R.; Chien, F. Z.; Moss, S. C., Structure of Poorly Crystalline MoS_2 — A modeling study. *Journal of Non-Crystalline Solids* **1986,** *79*, 251-273.
89. De la Rosa, M. P.; Texier, S.; Berhault, G.; Camacho, A.; Yácaman, M. J.; Mehta, A.; Fuentes, S.; Montoya, J. A.; Murrieta, F.; Chianelli, R. R., Structural Studies of Catalytically Stabilized Model and Industrial-supported Hydrodesulfurization Catalysts. *Journal of Catalysis* **2004,** *225*, 288-299.
90. Wang, L.; Xu, Z.; Wang, W.; Bai, X., Atomic Mechanism of Dynamic Electrochemical Lithiation Processes of MoS_2 Nanosheets. *J Am Chem Soc* **2014,** *136*, 6693-6697.
91. Zhu, Z.; Tang, Y.; Leow, W. R.; Xia, H.; Lv, Z.; Wei, J.; Ge, X.; Cao, S.; Zhang, Y.; Zhang, W.; Zhang, H.; Xi, S.; Du, Y.; Chen, X., Approaching the Lithiation Limit of MoS_2 While Maintaining Its Layered Crystalline Structure to Improve Lithium Storage. *Angew Chem Int Ed Engl* **2019,** *58*, 3521-3526.
92. Wang, Y.; Ma, Z.; Chen, Y.; Zou, M.; Yousaf, M.; Yang, Y.; Yang, L.; Cao, A.; Han, R. P., Controlled Synthesis of Core-Shell Carbon@MoS_2 Nanotube Sponges as High-Performance Battery Electrodes. *Adv Mater* **2016,** *28*, 10175-10181.
93. Xiao, J.; Choi, D.; Cosimbescu, L.; Koech, P.; Liu, J.; Lemmon, J. P., Exfoliated MoS_2 Nanocomposite as an Anode Material for Lithium Ion Batteries. *Chemistry of Materials* **2010,** *22*, 4522-4524.
94. Chen, S.; Wang, L.; Shao, R.; Zou, J.; Cai, R.; Lin, J.; Zhu, C.; Zhang, J.; Xu, F.; Cao, J.; Feng, J.; Qi, J.; Gao, P., Atomic Structure and Migration Dynamics of MoS_2/Li_xMoS_2 Interface. *Nano Energy* **2018,** *48*, 560-568.
95. Li, Z.; Ottmann, A.; Sun, Q.; Kast, A. K.; Wang, K.; Zhang, T.; Meyer, H.-P.; Backes, C.; Kübel, C.; Schröder, R. R.; Xiang, J.; Vaynzof, Y.; Klingeler, R., Hierarchical MoS_2–carbon Porous Nanorods Towards Atomic Interfacial Engineering for High-performance Lithium Storage. *Journal of Materials Chemistry A* **2019,** *7*, 7553-7564.
96. Zhang, L.; Sun, D.; Kang, J.; Feng, J.; Bechtel, H. A.; Wang, L. W.; Cairns, E. J.; Guo, J., Electrochemical Reaction Mechanism of the MoS_2 Electrode in a Lithium-Ion Cell Revealed by in Situ and Operando X-ray Absorption Spectroscopy. *Nano Lett* **2018,** *18*, 1466-1475.
97. Spanier, T. L. a. J. E., A Comprehensive Multiphonon Spectral Analysis in MoS_2. *2D Materials* **2015,** *2*, 035003.
98. Lee, C.; Yan, H.; Brus, L. E.; Heinz, T. F.; Hone, J.; Ryu, S., Anomalous Lattice Vibrations of Single- and Few-layer MoS_2. *ACS Nano* **2010,** *4*, 2695-700.
99. Frey, G. L.; Tenne, R.; Matthews, M. J.; Dresselhaus, M. S.; Dresselhaus, G., Raman and Resonance Raman Investigation of MoS_2 Nanoparticles. *Physical Review B* **1999,** *60*, 2883-2892.

100. Jimenez Sandoval, S.; Yang, D.; Frindt, R. F.; Irwin, J. C., Raman Study and Lattice Dynamics of Single Molecular Layers of MoS_2. *Phys Rev B Condens Matter* **1991,** *44*, 3955-3962.
101. Calandra, M., Chemically Exfoliated Single-layer MoS_2: Stability, Lattice Dynamics, and Catalytic Adsorption From First Principles. *Physical Review B* **2013,** *88*, 245428.
102. Yang, D.; Sandoval, S. J.; Divigalpitiya, W. M. R.; Irwin, J. C.; Frindt, R. F., Structure of Single-molecular-layer MoS_2. *Physical Review B* **1991,** *43*, 12053-12056.
103. Du, G.; Guo, Z.; Wang, S.; Zeng, R.; Chen, Z.; Liu, H., Superior Stability and High Capacity of Restacked Molybdenum Disulfide as Anode Material for Lithium-ion Batteries. *Chem Commun* **2010,** *46*, 1106-8.
104. An, S. J.; Li, J.; Daniel, C.; Mohanty, D.; Nagpure, S.; Wood, D. L., The State of Understanding of the Lithium-ion-battery Graphite Solid Electrolyte Interphase (SEI) and Its Relationship to Formation Cycling. *Carbon* **2016,** *105*, 52-76.
105. Laruelle, S.; Grugeon, S.; Poizot, P.; Dolle, M.; Dupont, L.; Tarascon, J. M., On the Origin of The Extra Electrochemical Capacity Displayed by MO/Li Cells at Low Potential. *Journal of the Electrochemical Society* **2002,** *149*, A627-A634.
106. Chen, C.; Ding, N.; Wang, L.; Yu, Y.; Lieberwirth, I., Some New Facts on Electrochemical Reaction Mechanism for Transition Metal Oxide Electrodes. *Journal of Power Sources* **2009,** *189*, 552-556.
107. Li, Y.; Fu, Z.-Y.; Su, B.-L., Hierarchically Structured Porous Materials for Energy Conversion and Storage. *Advanced Functional Materials* **2012,** *22*, 4634-4667.
108. Chen, Y. M.; Yu, X. Y.; Li, Z.; Paik, U.; Lou, X. W., Hierarchical MoS_2 Tubular Structures Internally Wired by Carbon Nanotubes as A Highly Stable Anode Material for Lithium-ion Batteries. *Sci Adv* **2016,** *2*, e1600021.
109. Shi, Z.-T.; Kang, W.; Xu, J.; Sun, Y.-W.; Jiang, M.; Ng, T.-W.; Xue, H.-T.; Yu, D. Y. W.; Zhang, W.; Lee, C.-S., Hierarchical Nanotubes Assembled from MoS_2-carbon Monolayer Sandwiched Superstructure Nanosheets for High-performance Sodium Ion Batteries. *Nano Energy* **2016,** *22*, 27-37.
110. Zhang, Q.; Pei, J.; Chen, G.; Bie, C.; Sun, J.; Liu, J., Porous $Co_3V_2O_8$ Nanosheets with Ultrahigh Performance as Anode Materials for Lithium Ion Batteries. *Advanced Materials Interfaces* **2017,** *4*, 1700054.
111. Cao, B.; Liu, Z.; Xu, C.; Huang, J.; Fang, H.; Chen, Y., High-rate-induced capacity evolution of mesoporous C@SnO_2@C hollow nanospheres for ultra-long cycle lithium-ion batteries. *Journal of Power Sources* **2019,** *414*, 233-241.
112. Wang, X.; Guan, H.; Chen, S.; Li, H.; Zhai, T.; Tang, D.; Bando, Y.; Golberg, D., Self-Stacked Co_3O_4 Nanosheets for High-performance Lithium Ion Batteries. *Chem Commun* **2011,** *47*, 12280-12282.
113. Yang, C.; Feng, J.; Lv, F.; Zhou, J.; Lin, C.; Wang, K.; Zhang, Y.; Yang, Y.; Wang, W.; Li, J.; Guo, S., Metallic Graphene-Like VSe_2 Ultrathin Nanosheets: Superior Potassium-Ion Storage and Their Working Mechanism. *Adv Mater* **2018,** *30*, e1800036.
114. Adpakpang, K.; Patil, S. B.; Oh, S. M.; Kang, J.-H.; Lacroix, M.; Hwang, S.-J., Effective Chemical Route to 2D Nanostructured Silicon Electrode Material: Phase Transition from Exfoliated Clay Nanosheet to Porous Si Nanoplate. *Electrochimica Acta* **2016,** *204*, 60-68.
115. Edge, J. S.; O'Kane, S.; Prosser, R.; Kirkaldy, N. D.; Patel, A. N.; Hales, A.; Ghosh, A.; Ai, W.; Chen, J.; Yang, J.; Li, S.; Pang, M.-C.; Bravo Diaz, L.; Tomaszewska, A.; Marzook,

M. W.; Radhakrishnan, K. N.; Wang, H.; Patel, Y.; Wu, B.; Offer, G. J., Lithium Ion Battery Degradation: What You Need to Know. *Physical Chemistry Chemical Physics* **2021,** *23*, 8200-8221.
116. Liu, X.; Zhu, X.; Pan, D., Solutions for The Problems of Silicon-carbon Anode Materials for Lithium-ion Batteries. *R Soc Open Sci* **2018,** *5*, 172370.
117. Choi, C.; Ashby, D. S.; Butts, D. M.; DeBlock, R. H.; Wei, Q.; Lau, J.; Dunn, B., Achieving High Energy Density and High Power Density with Pseudocapacitive Materials. *Nature Reviews Materials* **2020,** 5, 5-19.
118. Augustyn, V.; Simon, P.; Dunn, B., Pseudocapacitive Oxide Materials for High-rate Electrochemical Energy Storage. *Energy & Environmental Science* **2014,** *7*, 1597.
119. Choi, C.; Ashby, D. S.; Butts, D. M.; DeBlock, R. H.; Wei, Q. L.; Lau, J.; Dunn, B., Achieving High Energy Density and High Power Density with Pseudocapacitive Materials. *Nature Reviews Materials* **2020,** *5*, 5-19.
120. Mukhopadhyay, A.; Tokranov, A.; Xiao, X.; Sheldon, B. W., Stress Development Due to Surface Processes in Graphite Electrodes for Li-ion Batteries: A first report. *Electrochimica Acta* **2012,** *66*, 28-37.
121. Nadimpalli, S. P. V.; Sethuraman, V. A.; Bucci, G.; Srinivasan, V.; Bower, A. F.; Guduru, P. R., On Plastic Deformation and Fracture in Si Films During Electrochemical Lithiation/Delithiation Cycling. *Journal of The Electrochemical Society* **2013,** *160*, A1885-A1893.
122. Muller, G. A.; Cook, J. B.; Kim, H. S.; Tolbert, S. H.; Dunn, B., High Performance Pseudocapacitor Based on 2D Layered Metal Chalcogenide Nanocrystals. *Nano Lett* **2015,** *15*, 1911-1917.
123. Fang, Y.; Yu, X. Y.; Lou, X. W. D., Formation of Hierarchical Cu-Doped $CoSe_2$ Microboxes via Sequential Ion Exchange for High-Performance Sodium-Ion Batteries. *Adv Mater* **2018,** *30*, e1706668.
124. Choi, W.; Shin, H.-C.; Kim, J. M.; Choi, J.-Y.; Yoon, W.-S., Modeling and Applications of Electrochemical Impedance Spectroscopy (EIS) for Lithium-ion Batteries. *Journal of Electrochemical Science and Technology* **2020,** *11*, 1-13.
125. Zheng, Y.; Seifert, H. J.; Shi, H.; Zhang, Y.; Kübel, C.; Pfleging, W., 3D Silicon/Graphite Composite Electrodes for High-energy Lithium-ion Batteries. *Electrochimica Acta* **2019,** *317*, 502-508.
126. Boukamp, B. A., A Nonlinear Least-squares Fit Procedure for Analysis of Immittance Data of Electrochemical Systems. *Solid State Ionics* **1986,** *20*, 31-44.
127. Nobili, F.; Dsoke, S.; Mancini, M.; Tossici, R.; Marassi, R., Electrochemical Investigation of Polarization Phenomena and Intercalation Kinetics of Oxidized Graphite Electrodes Coated with Evaporated Metal Layers. *Journal of Power Sources* **2008,** *180*, 845-851.
128. Levi, M. D.; Aurbach, D., Impedance of A Single Intercalation Particle and of Non-Homogeneous, Multilayered Porous Composite Electrodes for Li-ion Batteries. *J Phys Chem B* **2004,** *108*, 11693-11703.
129. Gogotsi, Y.; Anasori, B., The Rise of MXenes. *ACS Nano* **2019,** *13*, 8491-8494.
130. Alhabeb, M.; Maleski, K.; Anasori, B.; Lelyukh, P.; Clark, L.; Sin, S.; Gogotsi, Y., Guidelines for Synthesis and Processing of Two-dimensional Titanium Carbide ($Ti_3C_2T_x$ MXene). *Chemistry of Materials* **2017,** *29*, 7633-7644.

131. Shahzad, F.; Alhabeb, M.; Hatter, C. B.; Anasori, B.; Man Hong, S.; Koo, C. M.; Gogotsi, Y., Electromagnetic Interference Shielding with 2D Transition Metal Carbides (MXenes). *Science* **2016,** *353*, 1137-1140.
132. Naguib, M.; Kurtoglu, M.; Presser, V.; Lu, J.; Niu, J.; Heon, M.; Hultman, L.; Gogotsi, Y.; Barsoum, M. W., Two-dimensional Nanocrystals Produced by Exfoliation of Ti_3AlC_2. *Adv Mater* **2011,** *23*, 4248-4253.
133. Tang, Q.; Zhou, Z.; Shen, P., Are MXenes Promising Anode Materials for Li ion Batteries? Computational Studies on Electronic Properties and Li Storage Capability of Ti_3C_2 and $Ti_3C_2X_2$ (X = F, OH) Monolayer. *J Am Chem Soc* **2012,** *134*, 16909-16916.
134. Naguib, M.; Come, J.; Dyatkin, B.; Presser, V.; Taberna, P.-L.; Simon, P.; Barsoum, M. W.; Gogotsi, Y., MXene: A Promising Transition Metal Carbide Anode for Lithium-ion Batteries. *Electrochemistry Communications* **2012,** *16*, 61-64.
135. Novoselov, K. S.; Mishchenko, A.; Carvalho, A.; Castro Neto, A. H., 2D Materials and Van der Waals Heterostructures. *Science* **2016,** *353*, aac9439.
136. Zhao, M.-Q.; Torelli, M.; Ren, C. E.; Ghidiu, M.; Ling, Z.; Anasori, B.; Barsoum, M. W.; Gogotsi, Y., 2D Titanium Carbide and Transition Metal Oxides Hybrid Electrodes for Li-ion Storage. *Nano Energy* **2016,** *30*, 603-613.
137. Liu, Y. T.; Zhang, P.; Sun, N.; Anasori, B.; Zhu, Q. Z.; Liu, H.; Gogotsi, Y.; Xu, B., Self-Assembly of Transition Metal Oxide Nanostructures on MXene Nanosheets for Fast and Stable Lithium Storage. *Adv Mater* **2018,** *30*, e1707334.
138. Lukatskaya, M. R.; Mashtalir, O.; Ren, C. E.; Dall'Agnese, Y.; Rozier, P.; Taberna, P. L.; Naguib, M.; Simon, P.; Barsoum, M. W.; Gogotsi, Y., Cation Intercalation and High Volumetric Capacitance of Two-dimensional Titanium Carbide. *Science* **2013,** *341*, 1502-1505.
139. Lipatov, A.; Alhabeb, M.; Lukatskaya, M. R.; Boson, A.; Gogotsi, Y.; Sinitskii, A., Effect of Synthesis on Quality, Electronic Properties and Environmental Stability of Individual Monolayer Ti_3C_2 MXene Flakes. *Advanced Electronic Materials* **2016,** *2*, 1600255.
140. Backes, C.; Szydlowska, B. M.; Harvey, A.; Yuan, S.; Vega-Mayoral, V.; Davies, B. R.; Zhao, P. L.; Hanlon, D.; Santos, E. J.; Katsnelson, M. I.; Blau, W. J.; Gadermaier, C.; Coleman, J. N., Production of Highly Monolayer Enriched Dispersions of Liquid-exfoliated Nanosheets by Liquid Cascade Centrifugation. *ACS Nano* **2016,** *10*, 1589-601.
141. Wu, E.; Wang, J.; Zhang, H.; Zhou, Y.; Sun, K.; Xue, Y., Neutron Diffraction Studies of $Ti_3Si_{0.9}Al_{0.1}C_2$ Compound. *Materials Letters* **2005,** *59*, 2715-2719.
142. Zhang, T.; Pan, L.; Tang, H.; Du, F.; Guo, Y.; Qiu, T.; Yang, J., Synthesis of Two-dimensional $Ti_3C_2T_x$ MXene using HCl+LiF Etchant: Enhanced Exfoliation and Delamination. *Journal of Alloys and Compounds* **2017,** *695*, 818-826.
143. Halim, J.; Cook, K. M.; Naguib, M.; Eklund, P.; Gogotsi, Y.; Rosen, J.; Barsoum, M. W., X-ray Photoelectron Spectroscopy of Select Multi-layered Transition Metal Carbides (MXenes). *Applied Surface Science* **2016,** *362*, 406-417.
144. Persson, I.; Naslund, L. A.; Halim, J.; Barsoum, M. W.; Darakchieva, V.; Palisaitis, J.; Rosen, J.; Persson, P. O. A., On The Organization and Thermal Behavior of Functional Groups on Ti_3C_2 MXene Surfaces in Vacuum. *2D Materials* **2018,** *5*, 015002.
145. Okubo, M.; Sugahara, A.; Kajiyama, S.; Yamada, A., MXene as a Charge Storage Host. *Acc Chem Res* **2018,** *51*, 591-599.
146. Luo, J.; Tao, X.; Zhang, J.; Xia, Y.; Huang, H.; Zhang, L.; Gan, Y.; Liang, C.; Zhang, W., Sn^{4+} Ion Decorated Highly Conductive Ti_3C_2 MXene: Promising Lithium-ion Anodes

with Enhanced Volumetric Capacity and Cyclic Performance. *ACS Nano* **2016,** *10*, 2491-2499.
147. Cheng, R.; Hu, T.; Zhang, H.; Wang, C.; Hu, M.; Yang, J.; Cui, C.; Guang, T.; Li, C.; Shi, C.; Hou, P.; Wang, X., Understanding the Lithium Storage Mechanism of $Ti_3C_2T_x$ MXene. *The Journal of Physical Chemistry C* **2018,** *123*, 1099-1109.
148. Naguib, M.; Halim, J.; Lu, J.; Cook, K. M.; Hultman, L.; Gogotsi, Y.; Barsoum, M. W., New Two-dimensional Niobium and Vanadium Carbides as Promising Materials for Li-ion Batteries. *J Am Chem Soc* **2013,** *135*, 15966-15969.
149. Ren, C. E.; Zhao, M. Q.; Makaryan, T.; Halim, J.; Boota, M.; Kota, S.; Anasori, B.; Barsoum, M. W.; Gogotsi, Y., Porous Two-dimensional Transition Metal Carbide (MXene) Flakes for High-performance Li-ion Storage. *Chemelectrochem* **2016,** *3*, 689-693.
150. Kim, J.; Lee, Z., Phase Transformation of Two-dimensional Transition Metal Dichalcogenides. *Applied Microscopy* **2018,** *48*, 43-48.
151. George, C.; Morris, A. J.; Modarres, M. H.; De Volder, M., Structural Evolution of Electrochemically Lithiated MoS_2 Nanosheets and the Role of Carbon Additive in Li-ion Batteries. *Chem Mater* **2016,** *28*, 7304-7310.
152. Zhang, R.; Qin, Y.; Liu, P.; Jia, C.; Tang, Y.; Wang, H., How Does Molybdenum Disulfide Store Charge: A Minireview. *ChemSusChem* **2020,** *13*, 1354-1365.
153. Fang, X.; Yu, X.; Liao, S.; Shi, Y.; Hu, Y.-S.; Wang, Z.; Stucky, G. D.; Chen, L., Lithium Storage Performance in Ordered Mesoporous MoS_2 Electrode Material. *Microporous and Mesoporous Materials* **2012,** *151*, 418-423.
154. Fang, X.; Hua, C.; Guo, X.; Hu, Y.; Wang, Z.; Gao, X.; Wu, F.; Wang, J.; Chen, L., Lithium Storage in Commercial MoS_2 in Different Potential Ranges. *Electrochimica Acta* **2012,** *81*, 155-160.
155. Wang, L.; Zhang, Q.; Zhu, J.; Duan, X.; Xu, Z.; Liu, Y.; Yang, H.; Lu, B., Nature of Extra Capacity in MoS_2 Electrodes: Molybdenum Atoms Accommodate with Lithium. *Energy Storage Materials* **2019,** *16*, 37-45.
156. Zhu, Z.; Xi, S.; Miao, L.; Tang, Y.; Zeng, Y.; Xia, H.; Lv, Z.; Zhang, W.; Ge, X.; Zhang, H.; Wei, J.; Cao, S.; Chen, J.; Du, Y.; Chen, X., Unraveling the Formation of Amorphous MoS_2 Nanograins During the Electrochemical Delithiation Process. *Advanced Functional Materials* **2019,** *29*, 1904843.
157. Wang, Q.; Li, J. H., Facilitated Lithium Storage in MoS_2 Overlayers Supported on Coaxial Carbon Nanotubes. *J Phys Chem C* **2007,** *111*, 1675-1682.
158. Zhang, R.; Li, H.; Sun, D.; Luan, J.; Huang, X.; Tang, Y.; Wang, H., Facile Preparation of Robust Porous MoS_2/C Nanosheet Networks as Anode Material for Sodium Ion Batteries. *Journal of Materials Science* **2018,** *54*, 2472-2482.
159. Xia, Q.; Tan, Q. Q., MoS_2 Nanosheets Strongly Coupled with Cotton-derived Carbon Microtubes for Ultrafast Sodium Ion Insertion. *Materials Letters* **2018,** *228*, 285-288.
160. Chao, Y. F.; Jalili, R.; Ge, Y.; Wang, C. Y.; Zheng, T.; Shu, K. W.; Wallace, G. G., Self-assembly of Flexible Free-standing 3D Porous MoS_2-reduced Graphene Oxide Structure for High-performance Lithium-ion Batteries. *Advanced Functional Materials* **2017,** *27*, 1700234.
161. Ma, Y.; Ma, Y.; Bresser, D.; Ji, Y.; Geiger, D.; Kaiser, U.; Streb, C.; Varzi, A.; Passerini, S., Cobalt Disulfide Nanoparticles Embedded in Porous Carbonaceous Micro-polyhedrons Interlinked by Carbon Nanotubes for Superior Lithium and Sodium Storage. *ACS Nano* **2018,** *12*, 7220-7231.

162. Kim, H.; Choi, W.; Yoon, J.; Um, J. H.; Lee, W.; Kim, J.; Cabana, J.; Yoon, W. S., Exploring Anomalous Charge Storage in Anode Materials for Next-generation Li Rechargeable Batteries. *Chem Rev* **2020,** *120*, 6934-6976.
163. Pang, J.; Mendes, R. G.; Bachmatiuk, A.; Zhao, L.; Ta, H. Q.; Gemming, T.; Liu, H.; Liu, Z.; Rummeli, M. H., Applications of 2D MXenes in Energy Conversion and Storage Systems. *Chem Soc Rev* **2019,** *48*, 72-133.
164. Zhao, T.; Shu, H.; Shen, Z.; Hu, H.; Wang, J.; Chen, X., Electrochemical Lithiation Mechanism of Two-dimensional Transition-metal Dichalcogenide Anode Materials: Intercalation versus Conversion Reactions. *The Journal of Physical Chemistry C* **2019,** *123*, 2139-2146.
165. Mashtalir, O.; Naguib, M.; Mochalin, V. N.; Dall'Agnese, Y.; Heon, M.; Barsoum, M. W.; Gogotsi, Y., Intercalation and Delamination of Layered Carbides and Carbonitrides. *Nat Commun* **2013,** *4*, 1716.
166. Han, X.; Lu, L.; Zheng, Y.; Feng, X.; Li, Z.; Li, J.; Ouyang, M., A Aeview on The Key Issues of The Lithium Ion Battery Degradation Among The Whole Life Cycle. *eTransportation* **2019,** *1*, 100005.
167. Li, C.; Sarapulova, A.; Pfeifer, K.; Dsoke, S., Effect of Continuous Capacity Rising Performed by FeS/Fe_3C/C Composite Electrodes for Lithium-ion Batteries. *ChemSusChem* **2020,** *13*, 986-995.
168. Vetter, J.; Novák, P.; Wagner, M. R.; Veit, C.; Möller, K. C.; Besenhard, J. O.; Winter, M.; Wohlfahrt-Mehrens, M.; Vogler, C.; Hammouche, A., Ageing mechanisms in Lithium-ion Batteries. *Journal of Power Sources* **2005,** *147*, 269-281.
169. Dylla, A. G.; Henkelman, G.; Stevenson, K. J., Lithium Insertion in Nanostructured TiO_2(B) Architectures. *Accounts Chem Res* **2013,** *46*, 1104-1112.
170. Mashtalir, O.; Lukatskaya, M. R.; Zhao, M. Q.; Barsoum, M. W.; Gogotsi, Y., Amine-Assisted Delamination of Nb_2C MXene for Li-ion Energy Storage Devices. *Adv Mater* **2015,** *27*, 3501-3506.
171. Halim, J.; Kota, S.; Lukatskaya, M. R.; Naguib, M.; Zhao, M.-Q.; Moon, E. J.; Pitock, J.; Nanda, J.; May, S. J.; Gogotsi, Y.; Barsoum, M. W., Synthesis and Characterization of 2D Molybdenum Carbide (MXene). *Advanced Functional Materials* **2016,** *26*, 3118-3127.
172. Xu, E. Z.; Zhang, Y.; Wang, H.; Zhu, Z. F.; Quan, J. J.; Chang, Y. J.; Li, P. C.; Yu, D. B.; Jiang, Y., Ultrafast Kinetics Net electrode Assembled via $MoSe_2$/MXene Heterojunction for High-performance Sodium-ion Batteries. *Chemical Engineering Journal* **2020,** *385*, 123839.
173. Chao, D.; Liang, P.; Chen, Z.; Bai, L.; Shen, H.; Liu, X.; Xia, X.; Zhao, Y.; Savilov, S. V.; Lin, J.; Shen, Z. X., Pseudocapacitive Na-ion Storage Boosts High Rate and Areal Capacity of Self-branched 2D Layered Metal Chalcogenide Nanoarrays. *ACS Nano* **2016,** *10*, 10211-10219.
174. Augustyn, V.; Come, J.; Lowe, M. A.; Kim, J. W.; Taberna, P. L.; Tolbert, S. H.; Abruna, H. D.; Simon, P.; Dunn, B., High-rate Electrochemical Energy Storage Through Li^+ Intercalation Pseudocapacitance. *Nature Materials* **2013,** *12*, 518-522.
175. Wang, J.; Polleux, J.; Lim, J.; Dunn, B., Pseudocapacitive Contributions to Electrochemical Energy Storage in TiO_2 (anatase) Nanoparticles. *J Phys Chem C* **2007,** *111*, 14925-14931.

176. Zhang, X.; Chen, X.; Ren, H.; Diao, G.; Chen, M.; Chen, S., Bowl-like C@MoS_2 Nanocomposites as Anode Materials for Lithium-ion Batteries: Enhanced Stress Buffering and Charge/Mass Transfer. *ACS Sustainable Chemistry & Engineering* **2020,** *8*, 10065-10072.
177. Landi, B. J.; Ganter, M. J.; Cress, C. D.; DiLeo, R. A.; Raffaelle, R. P., Carbon Nanotubes for Lithium Ion Batteries. *Energy & Environmental Science* **2009,** *2*, 638.
178. Zhao, Z.; Tian, G.; Sarapulova, A.; Melinte, G.; Gomez-Urbano, J. L.; Li, C.; Liu, S.; Welter, E.; Etter, M.; Dsoke, S., Mechanism Study of Carbon Coating Effects on Conversion-type Anode Materials in Lithium-ion Batteries: Case Study of $ZnMn_2O_4$ and ZnO-MnO Composites. *ACS Appl Mater Interfaces* **2019,** *11*, 29888-29900.
179. Li, T.; Yuan, X.-Z.; Zhang, L.; Song, D.; Shi, K.; Bock, C., Degradation Mechanisms and Mitigation Strategies of Nickel-rich NMC-Based Lithium-ion Batteries. *Electrochemical Energy Reviews* **2019,** *3*, 43-80.
180. Manthiram, H.-H. S. a. A., Impact of Microcrack Generation and Surface Degradation on Nickel-rich Layered $Li[Ni_{0.9}Co_{0.05}Mn_{0.05}]O_2$ Cathode for Lithium-ion Batteries. *Chem. Mater* **2017,** *29*, 8486–8493.
181. Zhou, H.; Xin, F.; Pei, B.; Whittingham, M. S., What Limits the Capacity of Layered Oxide Cathodes in Lithium Batteries? *ACS Energy Letters* **2019,** *4*, 1902-1906.
182. Chen, S.; Shen, L.; van Aken, P. A.; Maier, J.; Yu, Y., Dual-functionalized Double Carbon Shells Coated Silicon Nanoparticles for High Performance Lithium-ion Batteries. *Adv Mater* **2017,** *29*, 1605650.
183. Ma, Y.; Ma, Y.; Kim, G. T.; Diemant, T.; Behm, R. J.; Geiger, D.; Kaiser, U.; Varzi, A.; Passerini, S., Superior Lithium Storage Capacity of α-MnS Nanoparticles Embedded in S-Doped Carbonaceous Mesoporous Frameworks. *Advanced Energy Materials* **2019,** *9*, 1902077.
184. You, L.; Tang, J.; Wu, Q.; Zhang, C.; Liu, D.; Huang, T.; Yu, A., $LiFePO_4$-coated $LiNi_{0.6}Co_{0.2}Mn_{0.2}O_2$ for Lithium-ion Batteries with Enhanced Cycling Performance at Elevated Temperatures and High Voltages. *Rsc Adv* **2020,** *10*, 37916-37922.
185. Wu, Y.; Li, M.; Wahyudi, W.; Sheng, G.; Miao, X.; Anthopoulos, T. D.; Huang, K. W.; Li, Y.; Lai, Z., Performance and Stability Improvement of Layered NCM Lithium-ion Batteries at High Voltage by a Microporous Al_2O_3 Sol-gel Coating. *ACS Omega* **2019,** *4*, 13972-13980.
186. Liu, T.; Zhang, Y.; Jiang, Z.; Zeng, X.; Ji, J.; Li, Z.; Gao, X.; Sun, M.; Lin, Z.; Ling, M.; Zheng, J.; Liang, C., Exploring Competitive Features of Stationary Sodium Ion Batteries for Electrochemical Energy Storage. *Energy & Environmental Science* **2019,** *12*, 1512-1533.
187. Wu, Y.; Yu, Y., 2D Material as Anode for Sodium Ion Batteries: Recent Progress and Perspectives. *Energy Storage Materials* **2019,** *16*, 323-343.
188. Xiong, X.; Luo, W.; Hu, X.; Chen, C.; Qie, L.; Hou, D.; Huang, Y., Flexible Membranes of MoS_2/C Nanofibers by Electrospinning as Binder-free Anodes for High-performance Sodium-ion Batteries. *Sci Rep* **2015,** *5*, 9254.
189. Ahmed, B.; Anjum, D. H.; Hedhili, M. N.; Alshareef, H. N., Mechanistic Insight into the Stability of HfO_2-Coated MoS_2 Nanosheet Anodes for Sodium Ion Batteries. *Small* **2015,** *11*, 4341-4350.
190. Hou, T.; Yang, G.; Rajput, N. N.; Self, J.; Park, S.-W.; Nanda, J.; Persson, K. A., The Influence of FEC on The Solvation Structure and Reduction Reaction of $LiPF_6$/EC Electrolytes and Its Implication for Solid Electrolyte Interphase Formation. *Nano Energy* **2019,** *64*, 103881.

191. Komaba, S.; Ishikawa, T.; Yabuuchi, N.; Murata, W.; Ito, A.; Ohsawa, Y., Fluorinated Ethylene Carbonate as Electrolyte Additive for Rechargeable Na batteries. *ACS Appl Mater Interfaces* **2011,** *3*, 4165-4168.
192. Ponrouch, A.; Goñi, A. R.; Palacín, M. R., High Capacity Hard Carbon Anodes for Sodium Ion Batteries In Additive Free Electrolyte. *Electrochemistry Communications* **2013,** *27*, 85-88.
193. Park, J.; Kim, J.-S.; Park, J.-W.; Nam, T.-H.; Kim, K.-W.; Ahn, J.-H.; Wang, G.; Ahn, H.-J., Discharge mechanism of MoS_2 for sodium ion battery: Electrochemical Measurements and Characterization. *Electrochimica Acta* **2013,** *92*, 427-432.
194. David, L.; Bhandavat, R.; Singh, G., MoS_2/Graphene Composite Paper for Sodium-ion Battery Electrodes. *ACS Nano* **2014,** *8*, 1759-1770.
195. Li, J.; Wang, H.; Wei, W.; Meng, L., Advanced MoS_2 and Graphene Heterostructures as High-performance Anode for Sodium-ion Batteries. *Nanotechnology* **2019,** *30*, 104003.
196. González, J. R.; Alcántara, R.; Tirado, J. L.; Fielding, A. J.; Dryfe, R. A. W., Electrochemical Interaction of Few-layer Molybdenum Disulfide Composites vs Sodium: New Insights on the Reaction Mechanism. *Chemistry of Materials* **2017,** *29*, 5886-5895.
197. Wang, J.; Luo, C.; Gao, T.; Langrock, A.; Mignerey, A. C.; Wang, C., An advanced MoS_2 /Carbon Anode for High-performance Sodium-ion Batteries. *Small* **2015,** *11*, 473-481.
198. Wu, Y.; Nie, P.; Wang, J.; Dou, H.; Zhang, X., Few-Layer MXenes Delaminated via High-energy Mechanical Milling for Enhanced Sodium-ion Batteries Performance. *ACS Appl Mater Interfaces* **2017,** *9*, 39610-39617.
199. Kajiyama, S.; Szabova, L.; Sodeyama, K.; Iinuma, H.; Morita, R.; Gotoh, K.; Tateyama, Y.; Okubo, M.; Yamada, A., Sodium-ion Intercalation Mechanism in MXene Nanosheets. *ACS Nano* **2016,** *10*, 3334-3341.
200. Wu, Y. T.; Nie, P.; Jiang, J. M.; Ding, B.; Dou, H.; Zhang, X. G., MoS_2-Nanosheet-Decorated 2D Titanium Carbide (MXene) as High-performance Anodes for Sodium-ion Batteries. *Chemelectrochem* **2017,** *4*, 1560-1565.
201. Xie, X.; Kretschmer, K.; Anasori, B.; Sun, B.; Wang, G.; Gogotsi, Y., Porous $Ti_3C_2T_x$ MXene for Ultrahigh-rate Sodium-ion Storage with Long Cycle Life. *ACS Applied Nano Materials* **2018,** *1*, 505-511.
202. Zeng, G. B.; Shi, N.; Hess, M.; Chen, X.; Cheng, W.; Fan, T. X.; Niederberger, M., A General Method of Fabricating Flexible Spinel-type Oxide/Reduced Graphene Oxide Nanocomposite Aerogels as Advanced Anodes for Lithium-ion Batteries. *ACS Nano* **2015,** *9*, 4227-4235.
203. Yang, T.; Liang, J.; Sultana, I.; Rahman, M. M.; Monteiro, M. J.; Chen, Y.; Shao, Z.; Silva, S. R. P.; Liu, J., Formation of Hollow MoS_2/Carbon Microspheres for High Capacity and High Rate Reversible Alkali-ion Storage. *Journal of Materials Chemistry A* **2018,** *6*, 8280-8288.
204. Huang, H.; Cui, J.; Liu, G.; Bi, R.; Zhang, L., Carbon-coated $MoSe_2$/MXene Hybrid Nanosheets for Superior Potassium Storage. *ACS Nano* **2019,** *13*, 3448-3456.
205. Zhao, X.; Cai, W.; Yang, Y.; Song, X.; Neale, Z.; Wang, H.-E.; Sui, J.; Cao, G., $MoSe_2$ Nanosheets Perpendicularly Grown on Graphene with Mo–C Bonding for Sodium-ion Capacitors. *Nano Energy* **2018,** *47*, 224-234.
206. Ruhul Amin, P. R. K. a. I. B., Carbon Nanotubes: Applications to Energy Storage Devices. *IntechOpen:* **2002**; 23.

207. Xia, X.; Chao, D.; Zhang, Y.; Zhan, J.; Zhong, Y.; Wang, X.; Wang, Y.; Shen, Z. X.; Tu, J.; Fan, H. J., Generic Synthesis of Carbon Nanotube Branches on Metal Oxide Arrays Exhibiting Stable High-rate and Long-cycle Sodium-ion Storage. *Small* **2016,** *12*, 3048-3058.
208. Feng, J. M.; Dong, L.; Li, X. F.; Li, D. J.; Lu, P. Y.; Hou, F.; Liang, J.; Dou, S. X., Hierarchically Stacked Reduced Graphene Oxide/Carbon Nanotubes for As High Performance Anode for Sodium-ion Batteries. *Electrochimica Acta* **2019,** *302*, 65-70.
209. Luo, X.-F.; Yang, C.-H.; Peng, Y.-Y.; Pu, N.-W.; Ger, M.-D.; Hsieh, C.-T.; Chang, J.-K., Graphene Nanosheets, Carbon Nanotubes, Graphite, and Activated Carbon as Anode Materials for Sodium-ion Batteries. *Journal of Materials Chemistry A* **2015,** *3*, 10320-10326.

8 Appendix

8.1 Abbreviations, Constants, and Symbols

2D	Two-dimensional
TMDs	Transition metal dichalcogenides
BET	Brunauer-Emmett-Teller
BJH	Barrett-Joyner-Halenda
SSA	Specific surface area
CE	Coulombic efficiency
CMC	Carboxymethyl cellulose
CA	Cellulose acetate
CV	Cyclic voltammetry
CNTs	Carbon nanotubes
DMC	Dimethyl carbonate
PC	Propylene carbonate
PTFE	Polytetrafluoroethylene
EEC	Electrical equivalent circuit
EC	Ethylene carbonate
EDS	Electrolyte-derived surface
EVs	Electric vehicles
HEVs	Hybrid electric vehicles
AC	Alternating current
DC	Direct current
et al.	*et alii / et aliae / et alia*
FEC	Fluoroethylene carbonate
GCPL	Galvanostatic cycling with potential limitation
LIBs	Lithium-ion batteries
SIBs	Sodium-ion batteries
OCV	Open-circuit voltage
PVdF	Polyvinylidene fluoride
NMP	1-methyl-2-pyrrolidinone
IPA	2-propanol

PEI	Polyethyleneimine
SEI	Solid electrolyte interphase
SEM	Scanning electron microscopy
TEM	Transmission electron microscopy
HRTEM	High-resolution transmission electron microscopy
SAED	Selected area electron diffraction
XPS	X-ray photoelectron spectroscopy
XRD	X-ray diffraction
ICDD	International Centre for Diffraction Data
UV-vis	Ultraviolet-visible (UV-Vis) spectroscopy
EIS	Electrochemical impedance spectroscopy
LBL	Layer-by-layer
LPE	Liquid-phase exfoliation
LCC	Liquid cascade centrifugation
MILD	Minimally intensive layer delamination
C	C-rate
CPE	Constant phase element
CPE_{int}	Capacitance at the electrode/electrolyte interface
R_{wp}	Weighted profile R-factor
R_{CT}	Resistance of charge transfer
R_{el}	Resistance of electrolyte systems
R_{SEI}	Resistance of solid electrolyte interface
W*o*	Open circuit terminus Warburg element
V_{rms}	Root mean square of voltage
ΔG	Non-standard Gibbs free energy / J
ΔG^0	Standard Gibbs free energy / J
n	Number of electrons transferred in an electrode reaction
F	Faraday constant (96485.3 C/mol)
E	Cell voltage under non-standard conditions / V
φ	The phase shift
θ	Bragg angle
ν	Scan rate

f	Frequency of microwave radiation
j	The imaginary unit
Z	The impedance
Z'	The real part of the impedance
Z''	The imaginary part of the impedance

8.2 List of Figures

9 Publications

1. **Tianzhu Liu,** Georgian Melinte, Oleksandr Dolotko, Michael, Knapp, Beatriz Mendoza Sanchez, Activation of 2D MoS_2 Electrodes Induced by High-rate Lithiation Processes, submitted to ***Journal of Energy Chemistry***.
2. **Tianzhu Liu**, Christopher Shuck, Vanessa Trouillet, Georgian Melinte, Michael Knapp, Yury Gogotsi, Beatriz Mendoza Sanchez, Engineering 2D $MoS_2/Ti_3C_2T_x$/CNTs Heterostructures via Layer-by-Layer Spray Deposition as Highly Stable Anode for Lithium-ion Batteries, getting ready to submit to a journal.
3. Lihua Zhu, **Tianzhu Liu**, Frieder Scheiba, Suya Liu, Vanessa Trouillet, Andreas Stoll, Angelina Sarapulpva, Weibo Hua, Sylvio Indris, Helmut Ehrenberg, Understanding the Catalytic Mechanism in a Co_3O_4-Catalyzed Li-O_2 Battery, ***Catalysis Science and Technology***, under review.
4. Lihua Zhu, **Tianzhu Liu,** Frieder Scheiba, Wu Wang, Guiying Tian, Helmut Ehrenberg, Synergistic Effects of DBBQ and LiI as Dual Soluble Catalysts to Enhance the Performance of Lithium-Oxygen Batteries, getting ready to submit to a journal.